UNIVERSITAT POLITÈCNICA
DE CATALUNYA
BARCELONATECH

PhD program in Construction Engineering

Structural behaviour and plastic design of carbon and stainless steel frames in fire

Doctoral thesis by:

Guillermo Segura Valdivieso

Thesis advisors:

Enrique Mirambell Arrizabalaga

Itsaso Arrayago Luquin

Escola Tècnica Superior d'Enginyeria de Camins, Canals i Ports de Barcelona
Department of Civil and Environmental Engineering

Barcelona, July 2023

SEGURA VALDIVIESO GUILLERMO -

Firmado digitalmente por SEGURA VALDIVIESO GUILLERMO - Fecha: 2023.10.02 19:28:10 +02'00'

MIRAMBELL ARRIZABALAGA, ENRIQUE (AUTENTICACIÓN)

Firmado digitalmente por MIRAMBELL ARRIZABALAGA, ENRIQUE (AUTENTICACIÓN) Fecha: 2023.10.04 13:19:23 +02'00'

ARRAYAGO LUQUIN ITSASO -

Digitally signed by ARRAYAGO LUQUIN ITSASO - Date: 2023.10.03 11:19:40 +02'00'

ABSTRACT

This thesis investigates the response of carbon and stainless steel frames in fire, and proposes new and more efficient approaches for their design. The investigation is mainly focused on one bay frames comprised by rectangular hollow sections (RHS) classified as Class 1 (i.e., plastic sections) and full-strength welded joints. In order to evaluate the behaviour of carbon and stainless steel frames under fire situation, advanced finite element models are developed aiming to reproduce both the global and local scale behaviour of these structures at elevated temperatures, besides being capable of modelling explicitly the welded joints in the frame discretization. Before using them systematically, the numerical models are validated against different laboratory tests, covering the different types of failure investigated at elevated temperatures (i.e., joint failure, local or member buckling, and structural system collapse).

Based on these numerical models, a preliminary parametric study is presented, in which the performance of carbon and stainless steel frames at elevated temperatures is assessed, and the main factors conditioning the frames' response are identified. From these preliminary results, a set of knowledge gaps are identified, which are subsequently addressed throughout the different chapters of this thesis.

First, an exhaustive parametric study on welded joints is carried out on both carbon and stainless steel tubular members under bending moment forces, which allows assessing the accuracy of the formulation prescribed in current European standards, and from which a new formulation for estimating the bending moment resistance of welded joints between RHS members is presented. The obtained results show a clear improvement compared to current design specifications, especially for stainless steel joints, as the new formulation accounts for strain hardening effects.

Subsequently, an extensive parametric study on carbon and stainless steel frames with plastic cross-sections and full-strength welded joints considering different techniques for modelling the connections is carried out, from which the influence of welded joints on the frame response is analysed, both at room temperature and under fire situation. The results demonstrate that frames modelled with explicit joints and with simplified rigid joints exhibited similar responses for the two design scenarios, confirming that joints classified as full-strength can be modelled as perfectly rigid joints for numerical purposes under fire situation too, as prescribed in European structural codes for room temperature.

Based on the previous findings, the redistribution capacity of carbon and stainless steel frames under room temperature and fire conditions is studied numerically. The results obtained from the extensive finite element parametric study confirm the internal force redistribution capacity of carbon and stainless steel frames with plastic cross-sections and full-strength joints at room temperature, and demonstrate that these structures exhibit sufficient redistribution capacity to fail through the formation of plastic collapse mechanisms in fire situation too. This fact suggests the possibility of developing more accurate formulations for estimating the resistance of carbon and stainless steel frames under fire situation.

Finally, two new methods for determining the time fire resistance of carbon and stainless steel frames are presented: fire design based on advanced numerical models and new analytical plastic approach. For the first design approach based on FE analysis, a set of failure criteria are presented; the collapse is defined in an objective manner by limiting the displacement and displacement rates described by the frames. The second proposed method is a new analytical design approach based on global plastic analysis; this methodology is capable of taking into account the redistribution capacity of carbon and stainless steel structures in fire, as well as the second order effects derived from the horizontal drift of the frames and the overstrength provided by strain hardening for stainless steel structures. The two proposed methods are shown to improve significantly the accuracy of the estimated time fire resistances, demonstrating that a new and more effective way of designing steel structures is possible.

Taking benefit from these new approaches, more efficient designs for carbon and stainless steel structures in fire situations can be achieved, allowing the design of unprotected stainless steel frames that meet the current fire safety requirements due to their unique mechanical and thermal properties at elevated temperatures. This feature, combined with the exceptional corrosion resistance and ductility, poise these alloys as excellent alternatives to more traditional structural materials in the paradigm of making the construction sector safer and more sustainable.

ACKNOWLEDGEMENTS

I would like to express my deepest gratitude to my supervisors Prof. Enrique Mirambell and Prof. Itsaso Arrayago for their invaluable guidance, support, and constant encouragement throughout this thesis. Their expertise, knowledge and dedication have made this journey a constant learning experience, for which I am really grateful.

Likewise, I would like to thank Prof. Esther Real, her constant support made this thesis possible, and to Prof. Sheida Afshan, from the University of Southampton, for her willingness to share her knowledge with me.

I would also like to thank Isabel Gonzalez de León for all the days spent working in our theses, she made this journey way more entertaining, and to Adrià Jiménez, who was always ready to answer all my questions.

This thesis would have not been possible out of the framework of MINECO (Spain) Project BIA2016-75678-R, AEI/FEDER, UE "Comportamiento estructural de pórticos de acero inoxidable. Seguridad frente a acciones accidentales de sismo y fuego" and the support of Secretaria d'Universitats i Recerca de la Generalitat de Catalunya (Spain) and the European Social Fund through the FI-AGAUR 2020 grant. Their collaboration is hereby acknowledged.

Finally, I would like to express my most sincere gratitude to my parents, who allowed me to get this far, to my sister who has always put up with me and to Marta, for her unconditional support and continuous encouragement on do what I like. This thesis is dedicated to them.

PUBLICATIONS

The peer-review publications developed in the framework of this thesis are listed below.

Journal publications

Segura, G.; Pournaghshband, A.; Afshan, S.; Mirambell, E. *Numerical simulation and analysis of stainless steel frames at high temperature*. Engineering structures, 227, 111446, 2021.

Segura, G.; Arrayago, I.; Mirambell, E. *New proposal for the bending moment capacity of tubular T-joints in carbon steel and stainless steel structures.* Thin-Walled structures, 187, 110667, 2023.

Segura, G.; Arrayago, I.; Mirambell, E. *Plastic redistribution capacity of stainless steel frames in fire.* Journal of Constructional Steel Research, 208, 108019, 2023.

Segura, G.; Arrayago, I.; Mirambell, E. *A new plastic global analysis approach for the fire design of steel and stainless steel structures.* Submitted to Engineering Structures.

Conference publications

Segura, G.; Afshan, S.; Mirambell, E.; Real, E. *Numerical analysis of stainless steel frames subject to fire*. Congress of Numerical Methods in Engineering (CMN19), Guimaraes (Portugal) 2019.

Segura, G.; Pournaghshband, A.; Afshan, S.; Mirambell, E. *Influence of the degree of utilization on the structural behaviour of stainless steel frames subject to fire*. Eurosteel2020, Sheffield (UK) 2021.

Segura, G.; Arrayago, I.; Mirambell, E. *Influence of welded joints modelling on the structural response of steel frames under fire situation*. Stability and Ductility in Steel Structures (SDSS2022), Aveiro (Portugal) 2022.

Segura, G.; Arrayago, I.; Mirambell, E. *Influence of welded joints modelling on the structural response of stainless steel frames under fire situation*. 6th International Experts Seminar: Stainless Steel in Structures, London (UK) 2022.

CONTENTS

CHAPTER 1

Introduction

1.1. Background

Accidental fire events in buildings are a catastrophic event that have always been a threat to human life and property, causing thousands of deaths and material loses estimated in billions of euros each year. The safety of the occupants depends on many factors that are defined in the design and construction of buildings. Much can be done to reduce the probability of occurrence, but it is impossible to prevent all major fires.

Given that fires will always occur, there are many strategies for reducing their impact, being one of them the design of structures which will not collapse prematurely when exposed to fire. Structural performance in the fire condition is an important design consideration for all materials, but for steel structures it represents a major issue because the strength of this material reduces significantly at elevated temperatures. Structural steelwork will generally need protection if the resistance of an unprotected member cannot be justified.

Figure 1.1. Fire and smoke billows from the north tower of New York's World Tarde Center, 11th of September, 2001. (AP Photo / David Karp)

In the recent years, many advances have been done in terms of the fire design of steel structures aiming for safer and more efficient structural designs, by taking advantage of the new calculation techniques offered by the advances in commercial software for advanced numerical methods on structural behaviour.

In parallel, the use of stainless steel as a structural material has increased in recent years thanks to the unique combination of its mechanical properties, durability, and aesthetics. In particular, stainless steel offers excellent advantages as resistant material, such as its high ductility, the increase in strength due to strain hardening, its good fatigue resistance, and its good fire behaviour. The main socio-economic and environmental advantages are related to its excellent durability, low maintenance cost, high residual value, and its added value in the circular economy, thus guaranteeing environmental safety and the rational use of the planet's resources in the construction industry (Nethercot and Gardner 2002). In the recent years, studies have been carried out on the structural behaviour of stainless steel elements, the results of which have enabled progress to be made in the development of design guides and regulations for the calculation of structures with this material. However, this progress has been rather scarce on the global analysis of stainless steel structures in general, and on frames in particular.

Research advances as well as the continuous development of powerful numerical tools allow to foresee a future in which numerical methods will provide a new design approach for carbon and stainless steel structures under fire situation, assessing the response of structures as whole systems. Furthermore, in

conjunction with the emergence of stainless steel as a structural material, it may provide an innovative way of addressing fire design, by building structures with enough fire resistance that may not require additional fire protection to fulfil current safety requirements.

1.2. Research objectives

1.2.1. General objectives

This thesis aims to investigate the structural behaviour of carbon and stainless steel frames in fire as a whole system, and to identify the main factors affecting the response of such structures at elevated temperatures for the development of novel design recommendations for a safe and efficient design of carbon and stainless steel structures in fire.

1.2.2. Specific objectives

Multiple specific objectives have been defined in order to achieve the general objective formulated in this thesis. These specific objectives are presented below, which have been addressed in the different chapters included in this document:

- To study the behaviour of carbon and stainless steel frames in fire as whole systems, and to determine whether the constitutive law of stainless steel (characterized by strain hardening and nonlinearity) leads to responses different from those obtained with traditional carbon steel.
- To develop advanced finite element models capable of accurately reproducing the response of carbon and stainless steel frames at both room and elevated temperatures, and to calibrate these against experimental results.

- Based on advanced FE models, to identify the main factors affecting the response of carbon and stainless steel frames at elevated temperatures.
- To assess the design specifications provided in the current and upcoming European codes for the design of welded joints between carbon and stainless steel rectangular hollow sections, and to develop new design approaches for such joints to provide efficient and safe designs if necessary, accounting for the particular features of each material.
- To determine the influence of joints on the response of carbon and stainless steel frames with plastic (Class 1) cross-sections, and to assess the joints' redistribution capacity under fire situation, as well as their influence on the overall fire resistance of the frame.
- To identify the redistribution capacity of carbon and stainless steel frames that are capable of developing plastic collapse mechanisms at room temperature in fire, and to determine if carbon and stainless steel frames can redistribute enough internal forces to develop plastic collapse mechanism at elevated temperatures when fulfilling the requirements needed for such capability at room temperature.
- To develop a new design proposal for the assessment of the fire resistance of carbon and stainless steel frames in fire based on advanced numerical methods supported on finite element (FE) analysis.
- To propose a new analytical design proposal for estimating the fire resistance of carbon and stainless steel frames with plastic (Class 1) cross-sections accounting for their capacity of developing plastic collapse mechanism at elevated temperatures due to the redistribution capacity of internal forces, and accounting for the overstrength provided by strain hardening in stainless steel structures.

1.3. Methodology

The methodology adopted in this thesis in order to reach the objectives listed in the previous section is briefly presented herein.

1. Literature review. Review of the current research in fire design for carbon and stainless steel, including previous experimental programmes, constitutive equations at elevated temperatures, codified design guidance, and alternative design methods.
2. Development and validation of advanced FE models to reproduce the complex response of carbon and stainless steel frames in fire, including possible local effects and the response of the joints comprising the structure.
   2.1. Validation of the numerical models reproducing connections against experimental data on welded joints.

2.2. Validation of the numerical models reproducing local and member buckling at elevated temperatures against experimental data on columns subjected to fire.

2.3. Validation of the numerical models reproducing the overall response of carbon and stainless steel frames in fire against tests on steel systems in fire.

3. Systematic use of the validated FE models to carry out parametric studies in order to identify the influence of the key parameters in the structural behaviour of carbon and stainless steel members and frames at room and elevated temperatures.

4. Preliminary study on carbon and stainless steel frames in fire.

4.1. Assessment of the behaviour of carbon and stainless steel frames in fire.

4.2. Introduction of a set of failure criteria to define the collapse of carbon steel frames in fire based on advanced numerical methods (i.e., FE analysis).

4.3. Identification of the main parameters governing the response of carbon and stainless steel frames under fire situation.

4.4. Evaluation of the influence of the heating profile (i.e., 3 vs 4 faces exposed to fire) on the overall structural response.

4.5. Assessment of the main differences between carbon and stainless steel frames in fire.

5. Analysis of welded joints between rectangular hollow section (RHS) members.

5.1. Assessment of the response of typical welded joints between RHS members and their failure modes and the accuracy of existing predictive expressions.

5.2. Development of new design expressions (if necessary) for carbon and stainless steel RHS connections failing due to chord face yielding by analysing multiple yield line mechanisms feasible for this failure mode.

5.3. Statistical validation of the new formulation.

6. Analysis of the influence of the joint modelling techniques in the response of carbon and stainless steel frames.

6.1. Development of advanced FE models with two alternative joint modelling techniques for welded joints.

6.2. Assessment of the influence of the joint modelling technique on the frame response at room temperature and in fire situation.

6.3. Determination of the redistribution capacity of welded joints at room temperature and in fire situation.

6.4. Evaluation of the redistribution capacity of carbon and stainless steel frames with plastic cross-sections at elevated temperatures.

7. Revision and extension of the preliminary failure criteria for carbon and stainless steel frames for the fire design of systems based on advanced numerical methods.

8. Development of a new simplified design method for fire design based on plastic global analysis.

8.1. Conduct a large parametric study to extend the available database on carbon and stainless steel frames at room temperature and in fire.
8.2. Development of a new simplified design method for fire design based on plastic global analysis.
8.3. Validation of the proposed analytical approach at room temperature against ultimate frame capacities obtained from advanced numerical methods.
8.4. Application and assessment of the proposed new design approach for fire design against the results obtained by means of FE nonlinear analysis for carbon and stainless steel frames.

1.4. Financial support

The author of the thesis acknowledges the support of the Secretaria d'Universitats i Recerca de la Generalitat de Catalunya (Spain) and the European Social Fund. This thesis has been developed in the frame of MINECO (Spain) Project BIA2016-75678-R, AEI/FEDER, UE "Comportamiento estructural de pórticos de acero inoxidable. Seguridad frente a acciones accidentales de sismo y fuego"

1.5. Thesis outline

This first chapter presents a brief introduction containing an overview of fire events in building construction and its catastrophic effects, along with a review to the increase use of stainless steel alloys as structural materials and their application in the construction industry. Then, the general and specific research objectives addressed in this thesis are presented. Finally, the financial support and the outline of the document are provided.

Chapter 2 presents a brief review of the literature that is relevant to this research. The review is intended to give an overview of the important topics, with most of the literature being introduced and discussed at the relevant chapters throughout the thesis.

The description and validation of the developed numerical models for the assessment of the response of carbon and stainless steel frames in fire, using the general-purpose software ABAQUS, is presented in Chapter 3. The three different numerical analysis needed to determine the response of such structures in fire are presented, and the validation of the numerical models is carried out against experimental tests reported in the literature.

Chapter 4 presents a comprehensive numerical investigation on carbon and stainless steel frames with plastic (Class 1) cross-sections, from which the main parameters governing the response of such structures are identified and their overall response is analysed. Additionally, some conclusions on the performance of stainless steel frames in fire, when compared to carbon steel frames, are also provided.

The revision of the design provision for estimating the resistance of welded joints between rectangular hollow section members is presented in Chapter 5 with the aim of providing clear guidance on their strength classification. An extensive parametric study is first presented, both for carbon and stainless steel joints, and a new design proposal to estimate the resistance of such joints is developed, which has the capacity of considering strain hardening effects on stainless steel joints.

In Chapter 6, the assessment of the influence of rigid and full-strength joints on the frame response at room temperature and under fire situation is presented. The response of a set of multiple frame geometries is assessed using two joint modelling techniques: explicitly modelled connections and numerical rigid joints. This study is carried out at room temperature and at elevated temperature, both for carbon and stainless steel structures, to establish the basis of the studies carried out in the next chapters.

The redistribution capacity of carbon and stainless steel frames at elevated temperatures is assessed and determined in Chapter 7. A new proposal for estimating the bending resistance of stainless steel cross-sections in fire is also presented, based on the resistance estimation provided by the Continuous Strength Method (CSM) at room temperature, which will be codified in the upcoming European codes.

Chapter 8 provides a detailed description of the development of a new analytical design methodology to estimate the fire resistance of carbon and stainless steel frames accounting for their redistribution capacity and their ability to develop plastic collapse mechanism at elevated temperatures. Additionally, new failure criteria are proposed to determine the collapse of carbon and stainless steel frames in fire when using advanced design methods based on FE analysis.

Finally, Chapter 9 summarises the findings of the different research works carried out in this thesis, as well as the possible areas for future research.

Additionally, Annex A provides detailed calculation on how to obtain the new formulation presented in Chapter 5 for estimating the bending moment resistance of welded joints between rectangular hollow sections. Likewise, Annexes B to D contain detailed calculations on how to estimate the frame resistance based on a first and second order plastic global analysis, both at room temperature and at elevated temperatures.

CHAPTER 2

Literature review

2.1. Introduction

This chapter provides an overview of the current knowledge on carbon and stainless steel structures in fire, and reviews the main European design guides and specifications concerning this topic. Firstly, the most important models for describing the stress–strain response of carbon and stainless steel are presented, including stress–strain models at elevated temperatures. This is followed by an introduction to fire, the main physical phenomena governing this accidental action, and how fire is treated in the current and upcoming structural design codes. Finally, a summary of the design guidelines for fire design according to European provisions is presented.

2.2. Material models for carbon steel

The stress–strain relationship commonly assumed for carbon steel at room temperature corresponds to an ideal elasto-plastic material, where the Young's modulus (E) defines the stress–strain relationship

of the material up to reaching the yield stress (f_y) at the corresponding yield strain (ε_y), followed by a horizontal plateau, as Figure 2.1 shows.

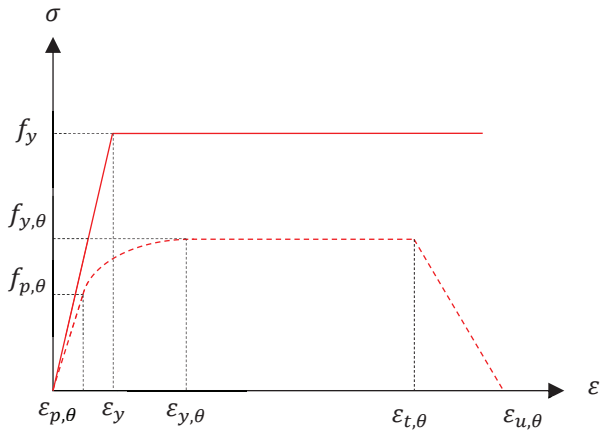

Figure 2.1. Schematic stress–strain relationship of carbon steel at room temperature (solid line) and at elevated temperatures (dashed line).

This bilinear stress–strain model (Eq. 2.1-Eq. 2.2) is codified in prEN 1993-1-14 (2021) for the design of structural steel at room temperature.

$$\sigma = E \cdot \varepsilon \qquad for\ \varepsilon \leq \varepsilon_y \qquad \text{Eq. 2.1}$$

$$\sigma = f_y \qquad for\ \varepsilon_y < \varepsilon < \varepsilon_t \qquad \text{Eq. 2.2}$$

Under fire situation, the upcoming version of prEN 1993-1-2 (2021) includes an elasto-plastic stress–strain relationship dependant on the temperature (θ) (see Figure 2.1), that includes a nonlinear branch after the proportionality limit f_p and a decaying zone up to the ultimate strain ($\varepsilon_{u,\theta}$). This stress–strain relationship is reproduced in Eq. 2.3-Eq. 2.6 where the Young's modulus (E_θ), the yield stress ($f_{y,\theta}$) and the proportional limit ($f_{p,\theta}$) are temperature dependant and can be calculated based on their corresponding reduction factors at elevated temperatures ($k_{E,\theta}$, $k_{y,\theta}$, $k_{p,\theta}$), which are also provided in prEN 1993-1-2 (2021) (i.e., $f_{y,\theta}$=$f_y \cdot k_{y,\theta}$).

$$\sigma_\theta = E_\theta \cdot \varepsilon_\theta \qquad for\ \varepsilon_\theta \leq \varepsilon_{p,\theta} \qquad \text{Eq. 2.3}$$

$$\sigma_\theta = f_{p,\theta} - c + \left(\frac{b}{a}\right) \cdot \sqrt{a^2 - \left(\varepsilon_{y,\theta} - \varepsilon_\theta\right)^2} \qquad for\ \varepsilon_{p,\theta} < \varepsilon_\theta < \varepsilon_{y,\theta} \qquad \text{Eq. 2.4}$$

$$\sigma_\theta = f_{y,\theta} \qquad for\ \varepsilon_{y,\theta} \leq \varepsilon_\theta \leq \varepsilon_{t,\theta} \qquad \text{Eq. 2.5}$$

$$\sigma_\theta = f_{y,\theta} \cdot \left(1 - \frac{\varepsilon_\theta - \varepsilon_{t,\theta}}{\varepsilon_{u,\theta} - \varepsilon_{t,\theta}}\right) \qquad for\ \varepsilon_{t,\theta} \leq \varepsilon_\theta \leq \varepsilon_{u,\theta} \qquad \text{Eq. 2.6}$$

In these equations the parameters a, b and c can be calculated as per Eq. 2.7-Eq. 2.9.

$$a^2 = \left(\varepsilon_{y,\theta} - \varepsilon_{p.\theta}\right) \cdot \left(\varepsilon_{y,\theta} - \varepsilon_{p,\theta} + c/E_\theta\right) \quad \text{Eq. 2.7}$$

$$b^2 = c \cdot \left(\varepsilon_{y,\theta} - \varepsilon_{p.\theta}\right) \cdot E_\theta + c^2 \quad \text{Eq. 2.8}$$

$$c = \frac{\left(f_{y,\theta} - f_{p,\theta}\right)^2}{\left(\varepsilon_{y,\theta} - \varepsilon_{p.\theta}\right) \cdot E_\theta - 2 \cdot \left(f_{y,\theta} - f_{p,\theta}\right)} \quad \text{Eq. 2.9}$$

2.3. Material models for stainless steel

Stainless steel is an alloy of iron, carbon, nickel and chromium in addition to molybdenum and manganese in few quantities. Stainless steel obtains its corrosion resistance from chromium – with a minimum content of 10.5% – has a great affinity for oxygen, reacting with it and creating a protector layer and avoiding the reaction of iron with oxygen and preventing the corrosion.

The quantity of each metal in the alloy provides the stainless steel with different properties. The prEN 1993-1-2 (2021) regulates the properties of the stainless steel depending on its chemical composition and sorting them in different grades. The upcoming European design code for the design of structural stainless steel provides design guidelines for the three main families of stainless steel used in construction industry:

- Austenitic stainless steel: with a 17-18% of chromium and an 8-11% of nickel provides a high corrosion resistance, high ductility, are easily cold formed and welded.
- Ferritic stainless steel: the most used ferritic stainless steels usually contain a percentage of chromium between 10.5% and 18%. They have nearly no nickel and show lower ductility than austenitic stainless steels, but maintain the corrosion resistance.
- Duplex stainless steel: also known as austenitic-ferritic stainless steels are a mix between austenitic and ferritic stainless steel. Usually contain a 20-26% of chromium, from 1% to 8% of nickel, less than a 5% of molybdenum and less than 0.3% of nitrogen.

In contrast to the perfect elasto-plastic stress–strain behaviour assumed for carbon steel, stainless steel alloys exhibit a highly nonlinear stress–strain relationship even at low strain values. This nonlinear relationship – also characterized by a significant strain hardening – plays a major role on the response of stainless steel structures, which means that most of the knowledge acquired for carbon steel structures included in EN 1993-1-1 (2005) is not directly applicable to the design of stainless steel structures.

Among the constitutive models developed to describe the nonlinear stress–strain behaviour of stainless steel, the two-stage Ramberg-Osgood model is the most commonly used, and it has been featured in

EN 1993-1-4 (2006), the Design Manual for Structural Stainless Steel (SCI 2017) and the upcoming prEN 1993-1-4 (2021). The codified version of this stress–strain model for room temperature is reproduced in Eq. 2.10-Eq. 2.11.

$$\varepsilon = \frac{\sigma}{E} + 0.002 \cdot \left(\frac{\sigma}{f_y}\right)^n \qquad for\ \sigma \leq f_y \qquad \text{Eq. 2.10}$$

$$\varepsilon = \frac{\sigma - f_y}{E_{0.2}} + \left(\varepsilon_u - \varepsilon_{0.2} - \frac{f_u - f_y}{E_{0.2}}\right)\left(\frac{\sigma - f_y}{f_u - f_y}\right)^m + \varepsilon_{0.2} \qquad for\ f_y < \sigma \leq f_u \qquad \text{Eq. 2.11}$$

The yield stress (f_y) is usually assumed to be the stress corresponding to a 0.2% plastic strain ($\varepsilon_{0.2}$), as recommended by EN 1993-1-4 (2006) and prEN 1993-1-4 (2021) at room temperature. $E_{0.2}$ is the tangent modulus of the stress–strain curve at the yield point and can be calculated as per Eq. 2.12, f_u is the ultimate tensile strength of the material, ε_u is the corresponding ultimate strain that can be estimated according to Eq. 2.13 – with C_3 being a material parameter shown in Table 2.1 –, and n and m are the nonlinear coefficients. The nonlinear parameter n ranges from 7 to 14 depending on the stainless steel grade – for austenitic its nominal value is equal to 7, for ferritic is equal to 14 and for duplex is 8 –, and the parameter m can be estimated from Eq. 2.14.

$$E_{0.2} = \frac{E}{1 + 0.002 \cdot n \cdot \frac{E}{f_y}} \qquad \text{Eq. 2.12}$$

$$\varepsilon_u = C_3 \cdot \left(1 - \frac{f_y}{f_u}\right) \qquad \text{Eq. 2.13}$$

$$m = 1 + 2.8 \cdot \frac{f_y}{f_u} \qquad \text{Eq. 2.14}$$

Table 2.1. Material model coefficients.

Stainless steel	C_1	C_2	C_3
Austenitic	0.10	0.16	1.00
Duplex	0.10	0.16	1.00
Ferritic	0.40	0.45	0.60

As an alternative to the two-stage Ramberg-Osgood model represented in Figure 2.2, the upcoming prEN 1993-1-4 (2021) for stainless steel structures allows using the bilinear elastic-linear hardening material model based on previous studies of the Continuous Strength Method (CSM), also represented in Figure 2.2. This stress–strain relationship must be used in conjunction with strain limits that restricts the amount of strain hardening the cross-section is capable of use before failing due to local buckling.

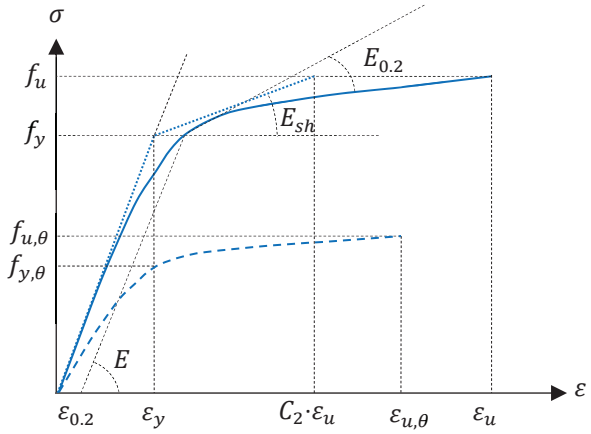

Figure 2.2. Schematic stress–strain relationship of stainless steel at room temperature represented by the two-stage Ramberg-Osgood (solid line) and the CSM bilinear curve (dotted line), along with the stress–strain curve at elevated temperatures (dashed line).

The current reduction factors ruling the stress–strain relationship of stainless steel alloys at elevated temperatures are based on the studies carried out by Manninen and Säynäjäkangas (2012) and Gardner et al. (2010), and have been codified in prEN 1993-1-4 (2021). The stress–strain curve for stainless steel at elevated temperatures is similar to its constitutive behaviour at room temperature (Eq. 2.10-Eq. 2.11), and can be described using the model reproduced in Eq. 2.15-Eq. 2.16.

$$\varepsilon_\theta = \frac{\sigma_\theta}{E_\theta} + 0.002 \cdot \left(\frac{\sigma_\theta}{f_{0.2,\theta}}\right)^{n_\theta} \qquad for\ \sigma_\theta \le f_{0.2,\theta} \qquad \text{Eq. 2.15}$$

$$\varepsilon_\theta = \frac{\sigma_\theta - f_{0.2,\theta}}{E_{0.2,\theta}} + \left(\varepsilon_{u,\theta} - \varepsilon_{0.2,\theta} - \frac{f_{u,\theta} - f_{0.2,\theta}}{E_{0.2,\theta}}\right)\left(\frac{\sigma_\theta - f_{0.2,\theta}}{f_{u,\theta} - f_{0.2,\theta}}\right)^{m_\theta} + \varepsilon_{0.2,\theta} \qquad for\ f_{0.2,\theta} < \sigma_\theta \le f_{u,\theta} \qquad \text{Eq. 2.16}$$

The main difference between the codified curve at elevated temperatures and the room temperature curve – besides being temperature dependant – is that while the 0.2% proof stress ($f_{0.2,\theta}$) is also used as the yield stress ($f_{y,\theta}$) for computing the stress–strain curve, for calculating the ultimate strain ($\varepsilon_{u,\theta}$) at elevated temperatures (see Eq. 2.13) the proof stress corresponding to a 2.0% plastic strain ($f_{2.0,\theta}$) is employed.

Moreover, the nonlinear parameters (n_θ, m_θ) may adopt different values at elevated temperatures than at room temperature. Nevertheless, and according to prEN 1993-1-2 (2021), the n_θ parameter can be taken equal to its room temperature value (i.e., equal to 7, 8 or 14 for austenitic, duplex and ferritic stainless steels, respectively), whereas the nonlinear exponent m_θ should be estimated as per Eq. 2.17.

However, the bilinear stress–strain curve based on the CSM formulation has not been extended to elevated temperatures yet.

$$1.5 \leq m_\theta = \frac{\ln\left(\frac{0.02 - \varepsilon_{0.2,\theta} - \left[\frac{f_{2.0,\theta} - f_{0.2,\theta}}{E_{0.2,\theta}}\right]}{\varepsilon_{u,\theta} - \varepsilon_{0.2,\theta} - \left[\frac{f_{u,\theta} - f_{0.2,\theta}}{E_{0.2,\theta}}\right]}\right)}{\ln\left(\frac{f_{2.0,\theta} - f_{0.2,\theta}}{f_{u,\theta} - f_{0.2,\theta}}\right)} \leq 5 \qquad \text{Eq. 2.17}$$

2.4. Fire

Fire is defined as the rapid oxidation of a material in an exothermic chemical reaction of combustion (Fire Design of Steel Structures (Franssen and Vila Real 2010)). This chemical process releases heat, light and it is an irreversible phenomenon. Combustion can only appear if the following conditions are present at the same time: (a) the necessary heat to provide a temperature high enough to reach the activation energy of the material in order to start the chemical reaction, (b) the fuel material required to have an exothermic reaction when oxidizing, (c) enough oxygen to maintain the combustion reaction, and (d) a chain reaction that enables the continuity of the combustion reaction without the need of the initial heat source.

In fire engineering, the physical phenomenon of fire is divided in four typical stages (Fire Design of Steel Structures (Franssen and Vila Real 2010)): (a) ignition, (b) growth, (c) fully-development, and (d) decay. The evolution of the gas temperature θ_g during these four stages over time is represented in Figure 2.3, along with the flashover point and the nominal ISO-834 curve EN 1991-1-2 (2002).

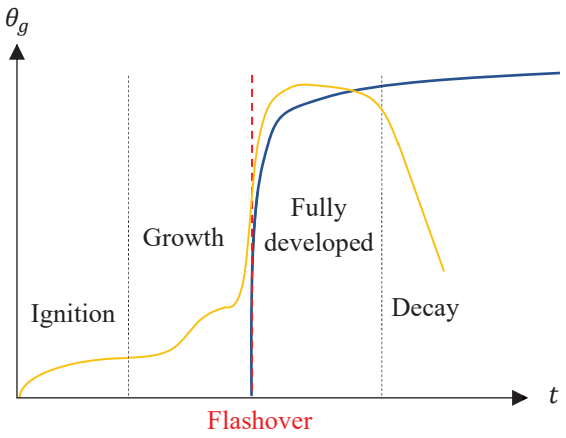

Figure 2.3. Temperature evolution of the gas temperature in a real fire (yellow line) and its 4 typical stages, along with the nominal temperature–time curve ISO-834 (blue line).

The development of the gas temperature over time varies depending on many factors, which may be different for each fire scenario. The current European code for actions on structures exposed to fire (EN 1991-1-2 (2002)) provides the designer with multiple tools to calculate the gas temperature evolution, from nominal temperature–time curves to advanced fire models based on Computational

Fluid Dynamics (CFD), where the fire compartment is divided into cells in which the Navier-Stokes equations are formulated and solved.

The nominal temperature–time curves included in EN 1991-1-2 (2002) are used for common design purposes and are different from the natural fire curve: they are characterized by starting after the flashover point and by not allowing for the decay of the temperature as the combustible material is consumed. Current codes provide multiple normalised curves depending on the type of fire the structure may need to withstand (i.e., hydrocarbon curve, external fire curve or standard curve). The ISO-834 curve corresponds to the standard temperature–time curve that should be used for design purposes for hypothetical fires that develop in fully ignited compartments without openings, and it is also shown in Figure 2.3. It can be noted that the ISO-834 curve is a rather conservative approximation to real fire curves, but it provides a solid basis to assess the response of carbon and stainless steel frames under the fire effect. The evolution of the gas temperature θ_g according to the standard ISO-834 temperature–time curve can be calculated from Eq. 2.18.

$$\theta_g = 20 + 345 \cdot \log_{10}(8 \cdot t + 1) \qquad \text{Eq. 2.18}$$

In this equation, t is the time elapsed after the flashover point in minutes. Once the temperature evolution of the gas surrounding the structure is determined, the heat transfer between the gas and the structure is governed by three physical phenomena: (a) radiation, (b) conduction, and (c) convection. Radiation is expelled by any body with a temperature higher than the absolute zero, and the neat heat flux ($\dot{h}_{net,r}$) between the gas and the steel structure can be described by means of the Stephan-Boltzmann law, reproduced in Eq. 2.19.

$$\dot{h}_{net,r} = \phi \varepsilon_g \varepsilon_s \sigma \left[\left(\theta_g + 273\right)^4 - (\theta_s + 273)^4 \right] \qquad \text{Eq. 2.19}$$

Therefore, ϕ stands for the configuration factor, which represents the fraction of radiation leaving the gas surface that is incident on the steel surface, and ε_g and ε_s are the emissivities of the gas and the steel, respectively. The gas emissivity (ε_g) should be considered equal to 1.0, while the steel emissivity (ε_s) depends on the type of steel used; for carbon steel grades is usually equal to 0.7, whereas for stainless steel alloys a value of 0.4 is recommended in prEN 1993-1-2 (2021). The coefficient σ is the Stephan-Boltzmann constant (σ=5.67·10^{-8} W/m^2°K^{-4}), and θ_g and θ_s stand for the temperature of the gas and the steel, respectively.

Additionally, an element subjected to a fire on any of its faces experiences the physical phenomenon known as convection, produced by the air motion. This phenomenon produces a net convective heat flux $\dot{h}_{net,c}$ and it is described by the Newton's law, which is reproduced by Eq. 2.20.

$$\dot{h}_{net,c} = \alpha_c \cdot (\theta_g - \theta_s) \quad \text{Eq. 2.20}$$

In this equation, α_c is the convective coefficient, with a value of 25 W/m^2°K for carbon and stainless steel structures. Convection heat transfer is the main source of temperature increase at the early fire stages, whereas radiation starts playing a main role in the heat transfer at high temperatures.

The whole heat transfer phenomenon can be described as a transient problem, and is governed by the Fourier's heat transfer equation (see Eq. 2.21).

$$\rho_s c_s \frac{\partial \theta}{\partial t} - \nabla \cdot (\lambda_c \nabla \theta) = \dot{q}_V \quad \text{Eq. 2.21}$$

Furthermore, ρ_s is the steel density (7850 kg/m^3) and c_s is the specific heat of the steel, varying its value with the temperature and $\dot{q}_V$ denotes the heat source. Moreover, conduction heat flux appears due to a difference of temperature within an element. Assuming an isotropic material, conductive heat flux depends on the thermal conductivity coefficient λ_c [W/m°K] and it is proportional to the gradient of the temperature as per Eq. 2.22. The conductivity coefficient (λ_c) value depends on the steel grade and the temperature of it.

$$q = -\lambda_c \nabla \theta \quad \text{Eq. 2.22}$$

2.5. Design under fire situation

In contrast to other persistent or transient actions that should be considered during the design of a structure at room temperature, fire is considered as an accidental action by the current European codes (EN 1990 (2002)). Consequently, the combination of actions to be adopted for fire design is different to that used for other types of actions at room temperature at Ultimate Limit State (ULS). The combination of actions given for the persistent and transient ULS design situation is given in Eq. 2.23.

$$E_d = \sum_i \gamma_{G,i} G_{k,i} + \gamma_{Q,1} \cdot Q_{k,1} + \sum_j \gamma_{Q,j} \psi_{0,j} Q_{k,j} \quad \text{Eq. 2.23}$$

In this equation, $\gamma_{G,i}$, $\gamma_{Q,1}$ and $\gamma_{Q,j}$ are the partial factors for the permanent action ($G_{k,i}$), the leading variable action ($Q_{k,1}$), and the accompanying variable actions ($Q_{k,j}$), respectively, and $\psi_{0,\mathrm{j}}$ is the combination factor for the combination value of the accompanying variable actions in the persistent situation. Alternatively, for fire design scenarios the combination of actions for the accidental design situation should be considered as per in Eq. 2.24.

$$E_{fi,d} = \sum_i G_{k,i} + \psi_{1,1} \cdot Q_{k,1} + \sum_j \psi_{2,j} Q_{k,j} \qquad \text{Eq. 2.24}$$

Likewise, $G_{k,i}$ represents the characteristic value of the permanent actions, $\psi_{1,1}\cdot Q_{k,1}$ is the frequent value of the leading variable action, and $\psi_{2,j}\cdot Q_{k,j}$ is the quasi-permanent value of the accompanying variable actions. It should be mentioned that although some national annexes adopt the quasi-permanent value of the leading variable ($\psi_{2,1}\cdot Q_{k,1}$) in the combination of actions for accidental fire situations, the Spanish code (CTE (2006)) conservatively assumes the frequent value ($\psi_{1,1}\cdot Q_{k,1}$).

Therefore, the use of combinations of actions that are different at room temperature and in fire situation means that for fire design structures are subjected to design loads below their ultimate capacity. The ratio between the design load applied onto the structure when the fire starts ($E_{fi,d}$) and the ultimate capacity of the structure for an elapsed time under fire situation of 0 seconds ($R_{fi,d,0}$) is defined as the degree of utilisation (μ_0), which plays a major role on the response of structures under fire situation.

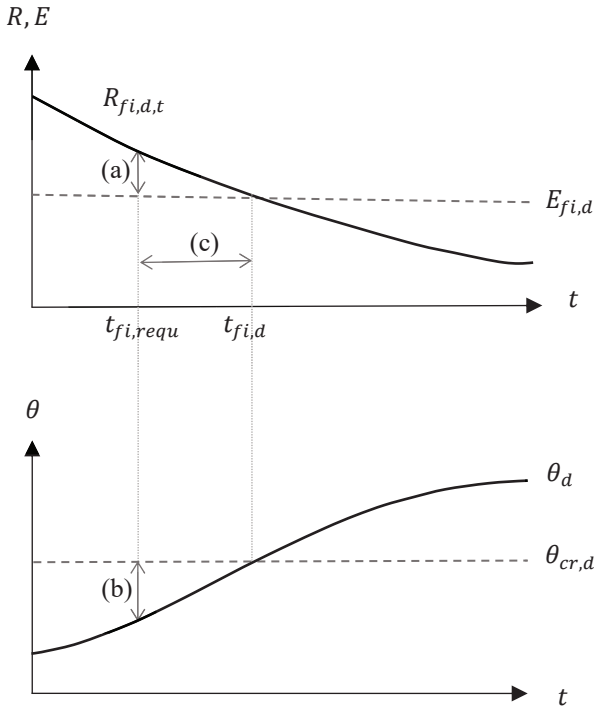

Figure 2.4. Load (a), temperature (b), and time (c) domains of the resistance of structures for a nominal fire (Fire Design of Steel Structures (Franssen and Vila Real 2010)).

Note that the fire resistance of carbon steel and stainless steel structures can be expressed in the three domains illustrated in Figure 2.4 (Fire Design of Steel Structures (Franssen and Vila Real 2010)): (a) in terms of resistances, where the design resistance ($R_{fi,d,t}$) should be higher than the design effect of the action ($E_{fi,d}$) under fire situation after the required duration ($t_{fi,requ}$) of fire exposure (i.e., $E_{fi,d} \leq R_{fi,d,t}$); (b) in terms of the corresponding critical temperature of the structure $\theta_{cr,d}$ (i.e., its collapse temperature), assuming that the cross-section is uniformly heated as current structural codes recommend for design purposes; or (c) in terms of the time that the structure can withstand the fire based on the standard ISO-834 (EN 1991-1-2 (2002)) air temperature curve $t_{fi,d}$ (i.e., the failure time) relative to the required fire resistance time $t_{fi,requ}$.

Moreover, the temperature evolution of an unprotected carbon or stainless steel member under fire situation can be estimated based on the analytical formulation provided in prEN 1993-1-2 (2021), given in (Eq. 2.25).

$$\Delta\theta_{s,t} = k_{sh} \cdot \frac{A_m/V}{c_a \rho} \dot{h}_{net,d} \Delta t \qquad \text{Eq. 2.25}$$

In this equation, $\Delta\theta_{s,t}$ is the temperature increment [°C] of the steel member corresponding to a time increment of Δt [s]. The parameter k_{sh} is the correction factor for the shadow effect – where the geometry of the cross-section is considered –, the ratio A_m/V is the so-called section factor (S_m=A_m/V) [m^{-1}] and compares the area exposed to the fire effect (A_m) to the member volume (V) per unit of length, c_a is the specific heat, ρ is the steel density, and $\dot{h}_{net,d}$ is the neat heat flux per unit of area [W/m^2]. The neat heat flux is the sum of the radiative heat flux (see Eq. 2.19) and the convective heat flux (see Eq. 2.20).

Although the equation codified in prEN 1993-1-2 (2021) for the temperature evolution of steel members (Eq. 2.25) is a simplified approximation to the real heat transfer problem, since the conductive heat transfer is disregarded because the temperature along the steel cross-section must be assumed to be uniform when employing this formulation, it has demonstrated a great accuracy. Another requirement when employing this formulation for design purposes is, according to prEN 1993-1-2 (2021), that the time increment (Δt) adopted must not exceed 5 seconds to avoid instabilities on the temperature evolution, usually derived from the radiative heat transfer, which is a fourth order equation.

2.5.1. Material response at elevated temperatures

Carbon and stainless steel are known to lose their mechanical properties at elevated temperatures. Therefore, the upcoming European code for fire design (prEN 1993-1-2 (2021)) provides a set of reduction factors $k_{i,\theta}$ for carbon steel and for the most used stainless steel grades to account for this

degradation. A comparison between the reduction factors for the yield stress (f_y) and the Young's modulus (E) of carbon steel and the stainless steels is shown in Figure 2.5. It should be pointed out that the different stainless steel families (austenitic, ferritic and duplex) are separated in different classes (i.e., austenitic I, austenitic II, austenitic III, etc.), grouping multiple grades with similar reduction factors when necessary, e.g. the subclass austenitic I is comprised by the austenitic stainless steel grades EN 1.4301, EN 1.4307 and EN 1.4318.

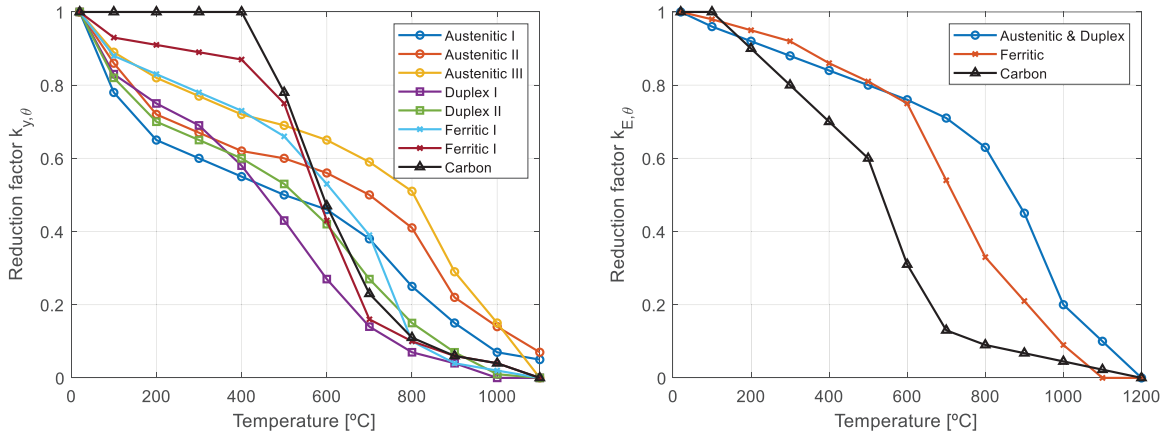

Figure 2.5. Evolution of the reduction factor of (a) the yield stress and the (b) Young's modulus for carbon steel and for the stainless steel grades reported in prEN 1993-1-2 (2021).

As shown in Figure 2.5(a), carbon steel retains higher values of the yield stress (f_y) at low-to-intermediate temperatures (i.e., θ_s<500°C) compared to all stainless steel grades, but at intermediate-to-high temperatures stainless steel grades are capable of retaining a higher portion of the yield stress, especially after carbon steel loses most of it after its phase change (~735°C). This different performance can provide a competitive advantage to structures made of stainless steel under fire situation, since with an adequate fire design unprotected stainless steel structures may be able to withstand the fire effect long enough to fulfil national codes for fire safety. However, if an inadequate fire design is carried out, it may lead to low critical temperatures (θ_{cr}) and insufficient time fire resistances (TFR). It should be noted, however, that in the upcoming European code for fire design (prEN 1993-1-2 (2021)),the reduction factors for the Young's modulus do not distinguish between subclasses of stainless steels, and it only differentiates between ferritic and austenitic/duplex stainless steel alloys. Nevertheless, Figure 2.5(b) highlights the capacity of all types of stainless steel alloys to retain higher stiffness proportions at elevated temperatures compared to carbon steel, contributing to a higher stability of these structures in fire.

Moreover, the thermal properties of carbon steel and stainless steel change with the temperature. The European code for fire design (prEN 1993-1-2 (2021)) provides a set of formulations to calculate the main thermal material properties, which are reproduced below. The evolution of the thermal conductivity [W/m°K] of carbon steel (λ_c) can be estimated as per Eq. 2.26-Eq. 2.27.

$$\lambda_c = 54 - 3.33 \cdot 10^{-2} \qquad for\ 20℃ \leq \theta < 800℃ \qquad \text{Eq. 2.26}$$

$$\lambda_c = 27.3 \qquad for\ 800℃ \leq \theta \leq 1200℃ \qquad \text{Eq. 2.27}$$

The specific heat [J/kg°K] of carbon steel (c_a) at different temperatures can be calculated according to Eq. 2.28-Eq. 2.31. As stated before, carbon steel suffers a phase change at around 735℃, which is reflected on the evolution of its specific heat (c_a), as its value spikes near that temperature.

$$c_a = 425 + 7.73 \cdot 10^{-1}\theta - 1.36 \cdot 10^{-3}\theta^2 + 2.22 \cdot 10^{-6}\theta^3 \qquad for\ 20℃ \leq \theta < 600℃ \qquad \text{Eq. 2.28}$$

$$c_a = 666 + \frac{13002}{738 - \theta} \qquad for\ 600℃ \leq \theta < 735℃ \qquad \text{Eq. 2.29}$$

$$c_a = 545 + \frac{17820}{\theta - 731} \qquad for\ 735℃ \leq \theta < 900℃ \qquad \text{Eq. 2.30}$$

$$c_a = 650 \qquad for\ 900℃ \leq \theta \leq 1200℃ \qquad \text{Eq. 2.31}$$

Among other properties that vary with the temperature, one can also find the thermal expansion coefficient (α [℃$^{-1}$]), which relates the member expansion per unit of length ($\Delta l = \alpha \cdot \Delta\theta \cdot l$) with the temperature increase. Since its value varies with temperature, the upcoming European code for fire design (prEN 1993-1-2 (2021)) gives the relative thermal expansion ($\Delta l/l$) of carbon steel instead of the coefficient of thermal expansion (α) for convenience, which is given in Eq. 2.32-Eq. 2.34.

$$\Delta l/l = 1.2 \cdot 10^{-5}\theta + 0.4 \cdot 10^{-8}\theta^2 - 2.416 \cdot 10^{-4} \qquad for\ 20℃ \leq \theta < 750℃ \qquad \text{Eq. 2.32}$$

$$\Delta l/l = 1.1 \cdot 10^{-2} \qquad for\ 750℃ \leq \theta < 860℃ \qquad \text{Eq. 2.33}$$

$$\Delta l/l = 2 \cdot 10^{-5}\theta - 6.2 \cdot 10^{-3} \qquad for\ 860℃ \leq \theta \leq 1200℃ \qquad \text{Eq. 2.34}$$

Likewise, the temperature evolution of the thermal and mechanical properties of the main families of stainless steel are codified and reported in Annex C of prEN 1993-1-2 (2021), and are reproduced in Eq. 2.35 to Eq. 2.41.

$$\lambda_c = 14.6 + 1.27 \cdot 10^{-2}\theta \qquad for\ austenitic\ and\ duplex \qquad \text{Eq. 2.35}$$

$$\lambda_c = 20.4 + 2.28 \cdot 10^{-2}\theta - 1.54 \cdot 10^{-5}\theta^2 \qquad for\ ferritic \qquad \text{Eq. 2.36}$$

$$c_a = 450 + 0.28 \cdot \theta - 2.91 \cdot 10^{-4}\theta^2 + 1.34 \cdot 10^{-7}\theta^3 \quad for\ austenitic\ and\ duplex \quad \text{Eq. 2.37}$$

$$c_a = 430 + 0.26 \cdot \theta \quad for\ ferritic \quad \text{Eq. 2.38}$$

$$\frac{\Delta l}{l} = \frac{(16.54 + 3.58 \cdot 10^{-3}\theta) \cdot (\theta - 20)}{10^6} \quad for\ austenitic \quad \text{Eq. 2.39}$$

$$\frac{\Delta l}{l} = \frac{(12.98 + 4.14 \cdot 10^{-3}\theta) \cdot (\theta - 20)}{10^6} \quad for\ duplex \quad \text{Eq. 2.40}$$

$$\frac{\Delta l}{l} = \frac{(9.87 + 3.89 \cdot 10^{-3}\theta) \cdot (\theta - 20)}{10^6} \quad for\ ferritic \quad \text{Eq. 2.41}$$

2.5.2. Cross-section resistance and member-based fire design

One of the domains in which the fire resistance of structure can be expressed is in terms of loads or resistances. Most of current European fire codes for structural design are devoted to express the fire resistance of a structure in these terms, and prEN 1993-1-2 (2021) is not an exception. Consequently, most of the formulations and equations prescribed in prEN 1993-1-2 (2021) and introduced in this section are similar to those to be used at room temperature, but with some particularities to account for the material degradations that occur at elevated temperatures.

The first difference when designing a steel structure under fire situation is that the cross-section classification material parameter ε suffers a modification. The parameter ε relates the yield stress (f_y) of the considered steel to a reference yield stress (S235), as per $\varepsilon=\sqrt{235/f_y}$, and is used for cross-section classification as it denotes how prone to local buckling a steel cross-section is depending on its yield stress. For fire design, this parameter ε_{fi} should be calculated as per in Eq. 2.42; this modification makes it possible to adopt the same maximum width-to-thickness limits for Class 1, 2 and 3 compression parts reported in prEN 1993-1-1 (2019) for room temperature.

$$\varepsilon_{fi} = \sqrt{\frac{235}{f_y} \cdot \frac{k_{E,\theta}}{k_{y,\theta}}} \quad \text{Eq. 2.42}$$

The reason for this modification is that the susceptibility of carbon and stainless steel cross-sections to local buckling depends on the temperature, because the mechanical properties influencing the yield stress and the critical buckling stress (Eq. 2.49) vary with the temperature. For simplicity, equation Eq. 2.43 can be employed for classifying carbon steel cross-sections instead of adopting Eq. 2.42, since the additional term 0.85 works as a lower bound to the $k_{E,\theta}/k_{y,\theta}$ ratios exhibited by carbon steel at elevated temperatures. This simplified equation (Eq. 2.43) is not as accurate as the previous equation (Eq. 2.42), although it eliminates the need to recalculate the cross-section class for each temperature increase.

$$\varepsilon_{fi} = 0.85 \cdot \sqrt{\frac{235}{f_y}} \qquad \text{Eq. 2.43}$$

Likewise, for stainless steel cross-sections, Eq. 2.44 may be used as a simplification.

$$\varepsilon_{fi} = \frac{\sqrt{235/f_y}}{\xi_\theta} \qquad \text{Eq. 2.44}$$

In this equation, ξ_θ should be taken equal to 1.0 for the subclasses austenitic I and II, duplex I and II and ferritic I; and equal to 1.1 for the subclasses austenitic III and ferritic II.

Based on this, cross-sections can be classified as plastic (Class 1), compact (Class 2), semi-compact (Class 3) and slender (Class 4) cross-section according to prEN 1993-1-1 (2016) or prEN 1993-1-2 (2021). This classification identifies when local buckling will develop based on the geometric ratio c/t, where c stands for the straight length of the plate comprising the cross-section and t for the plate thickness, and the parameter ε. Figure 2.6 shows the typical moment–curvature curves for the different cross-section classes.

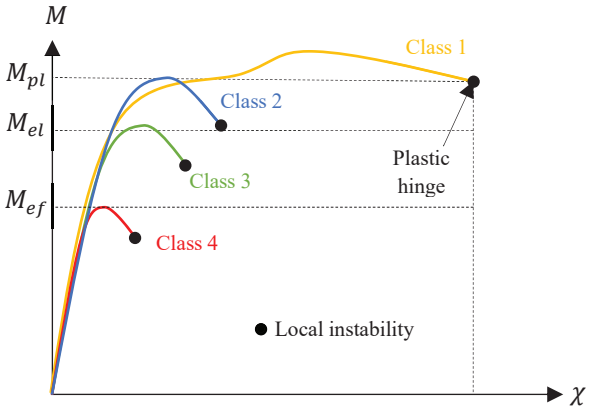

Figure 2.6. Typical moment–curvature (M–χ) curves for steel and stainless steel cross-sections depending on their Class.

As shown in Figure 2.6, Class 4 cross-section exhibit local instabilities before reaching the yield stress at any of its fibres, whereas Class 3 cross-sections are able to reach the elastic bending moment (i.e., M_{el}=W_{el}·f_y, where W_{el} is the elastic section modulus) before suffering from local buckling. The main difference between Class 2 and Class 1 cross-section is the rotation capacity: Class 2 cross-sections reach their maximum curvature shorty after reaching the plastic bending moment (i.e., M_{pl}=W_{pl}·f_y, where W_{pl} is the plastic section modulus), whereas Class 1 cross-section exhibit a great rotation capacity after reaching the plastic bending moment M_{pl}. This is why Class 1 cross-sections are considered to be able to develop plastic hinges (concentrating all the rotation at one cross-section) and allow the use of global plastic analysis approaches.

The CSM bilinear curve (Eq. 2.10-Eq. 2.11) can be used in conjunction with the strain limits (ε_{csm}) – Eq. 2.45 – and their corresponding stress levels (f_{csm}) – Eq. 2.46 – to predict the cross-section resistance based on the deformation capacity of the cross-section prior to local buckling (i.e., the cross-section slenderness $\overline{\lambda}_p$). In contrast to the current resistance prediction based on the cross-section Class (Figure 2.6), the CSM provides a continuum approach to assess the influence of the cross-section slenderness on the cross-section resistance.

$$\frac{\varepsilon_{csm}}{\varepsilon_y} = \begin{cases} \dfrac{0.25}{\bar{\lambda}_p^{\,3.6}} \leq \min\left(\Omega, C_1 \cdot \dfrac{\varepsilon_u}{\varepsilon_y}\right) & for\ \bar{\lambda}_p \leq 0.68 \\ \left(1 - \dfrac{0.222}{\bar{\lambda}_p^{1.05}}\right) \cdot \dfrac{1}{\bar{\lambda}_p^{1.05}} & for\ 0.68 < \bar{\lambda}_p \leq 1.00 \end{cases} \quad \text{Eq. 2.45}$$

$$f_{csm} = f_y + E_{sh} \cdot \varepsilon_y \cdot \left(\frac{\varepsilon_{csm}}{\varepsilon_y} - 1\right) \quad \text{Eq. 2.46}$$

In this equation, C_1 is a material coefficient shown in Table 2.1, E_{sh} is the strain hardening modulus, taken as shown in Eq. 2.47 with C_2 being another material coefficient shown in Table 2.1, and $\overline{\lambda}_p$ is the relative local slenderness of the cross-section, which can be calculated as per Eq. 2.48. On top of that, the maximum strain ε_{csm} is limited by the parameter Ω, which is a project specific parameter that is usually assumed to be equal to 15 (prEN 1993-1-4 (2021)).

$$E_{sh} = \frac{f_u - f_y}{C_2 \varepsilon_u - \varepsilon_y} \quad \text{Eq. 2.47}$$

$$\overline{\lambda}_p = \sqrt{\frac{f_y}{\sigma_{cr}}} \quad \text{Eq. 2.48}$$

Likewise, σ_{cr} is the elastic critical local buckling stress of the plates conforming the cross-section, which can be determined by Eq. 2.49 or numerically using finite strip or finite element methods.

$$\sigma_{cr} = \frac{k_\sigma \pi^2 E t^2}{12 \cdot (1 - v^2)\overline{b}^2} \quad \text{Eq. 2.49}$$

Furthermore, k_σ being the buckling coefficient dependant on the boundary conditions and loading state of the plate, t the plate thickness, $\overline{b}$ the straight width of the plate, and v the Poisson's coefficient of the material, equal to 0.3 for stainless steel and carbon steel.

It should be noted that the deformation limit (Ω) was originally adopted to adhere with the ductility requirements in the current version of EN 1993-1-1 (2005), where the ultimate deformation is required to be at least 15 times the corresponding yield strain (i.e., $\varepsilon_u \geq 15 \cdot \varepsilon_y$). However, this ductility

requirement is no longer included in the new version of the code prEN 1993-1-1 (2019), which implies that it may be susceptible to change. In this regard, some recent studies (Walport et al. 2023) have already adopted higher values of the Ω limit.

Noticeably, this discrete cross-section classification is useful for bilinear materials as carbon steel, where the moment–curvature up to the plastic bending moment is rather bilinear, but for nonlinear material such as stainless steel, the applicability of this classification is more complex and unable to account for strain hardening effects. For this reason, international research groups (Afshan and Gardner 2013, Zhao et al. 2017), led by the team at the Imperial College in London, have developed the Continuous Strength Method (CSM) to provide a continuous approach to this phenomenon, where the ultimate strain of cross-sections can be calculated depending directly on their relative local slenderness ($\bar{\lambda}_p$), as shown in Eq. 2.45. Therefore, the ultimate CSM bending capacity of the cross-section can be calculated based on the bilinear material model with linear hardening described in Section 2.3, the as per in Eq. 2.50.

$$M_{csm} = \frac{\varepsilon_{csm}}{\varepsilon_y} \cdot W_{el} \cdot f_y \qquad for\ \varepsilon_{csm}/\varepsilon_y < 1.0$$
$$M_{csm} = W_{pl} f_y \cdot \left[1 + \frac{E_{sh}}{E} \cdot \frac{W_{el}}{W_{pl}} \cdot \left(\frac{\varepsilon_{csm}}{\varepsilon_y} - 1\right) - \left(1 - \frac{W_{el}}{W_{pl}}\right) \cdot \left(\frac{\varepsilon_{csm}}{\varepsilon_y}\right)^{-\alpha}\right] \qquad for\ \varepsilon_{csm}/\varepsilon_y \geq 1.0 \qquad \text{Eq. 2.50}$$

In these equations, α is a CSM bending parameter that depends on the cross-section type (i.e., hollow section, I-section, T-section) and their aspect ratio and ranges from 1.0 to 2.0.

The traditional resistance equations used at room temperature for designing cross-sections under axial, shear and bending moment loads can also be used for fire design by adopting the partial safety factor for fire design ($\gamma_{M,fi}$=1.0) instead of the corresponding partial safety factor (γ_{Mi}), and by reducing the yield stress according to its temperature ($f_{y,\theta}$=$k_{y,\theta}$·f_y). It should be noted that for the fire design of stainless steel structures the upcoming prEN 1993-1-2 (2021) recommends the use of the 2.0% proof stress ($f_{2.0}$) as the basic characteristic for material strength (i.e., yield stress f_y), including the cross-section classification. By using $f_{2.0}$ instead of $f_{0.2}$ as the yield stress, it is possible to take advantage of the characteristic strain hardening of stainless steel alloys in a simple and efficient way when designing under fire situation. However, this approach for fire design is not consistent with the upcoming European code (prEN 1993-1-2 (2021)) for the design of stainless steel structures at room temperature, in which the yield stress (f_y) is assumed to be equal to the 0.2% proof stress ($f_{0.2}$). Thus, depending on which design code is employed (prEN 1993-1-2 (2021) or prEN 1993-1-4 (2021)), different resistance estimations can be obtained at room temperature. Note that the $f_{2.0}/f_{0.2}$ ratio at room temperature ranges from 1.12 to 1.31 depending on the stainless steel grade considered according to prEN 1993-1-2 (2021).

In terms of member-based resistance, the prEN 1993-1-2 (2021) provides specific formulation for calculating the flexural buckling resistance ($N_{b,fi,t,Rd}$) and the lateral-torsional buckling resistance ($M_{b,fi,t,Rd}$) under elevated temperatures. The main difference between these specific formulations and the ones provided in prEN 1993-1-1 (2019) for room temperature lies in the shape of the buckling curves.

2.5.3. Composite structures in fire

Composite cross-sections benefit from the combined effect of concrete and steel working together, taking advantage of the composite action against fire situations too. A concrete filled tube column with an embedded steel section (or steel reinforcement) is a clear example of the benefits this type of structural members can provide against fire. Where the inner steel section is protected from the fire effect by a concrete core, the temperature increase of the steel section is delayed as shown in Figure 2.7 and the fire resistance of such structural members is increased. Likewise, the external steel tube contributes to the confinement of the concrete core, increasing its compressive strength, and avoids the spalling of the concrete outer layers. Moreover, the concrete core prevents deformations on the embedded steel section and the external steel tube, avoiding local and global buckling effects, and thus leading to thinner steel cross-sections and more economical designs.

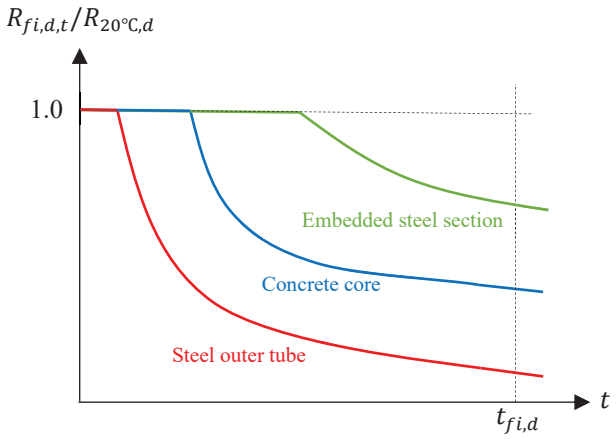

Figure 2.7. Resistance evolution over time of the main components conforming a concrete filled tube with encased steel section when exposed to fire (Espinós 2012).

The response of composite structures in fire is a complex phenomenon characterized by being highly nonlinear. The EN 1994-1-2 (2005), the standard that regulares the fire design of composite structures, allows designing these structures based on advanced calculation models, since traditional analytical methods can only provide approximated estimations of the actual fire resistance of composite structures (Lie 1984 and Han 2001). Nevertheless, recent research efforts have developed innovative simplified methods based on advanced numerical studies for assessing the temperature evolution of composite cross-sections (Medall et al. 2022), proposed simplified calculation models for assessing the fire resistance of composite columns (Espinós et al. 2012), or to assess the influence of stainless steel tubes in the response of composite cross-sections in fire (Tan et al. 2020).

2.5.4. System-based fire design

Research efforts on carbon and stainless steel structures have shifted from the traditional approaches (Young 2008, Todini et al. 2013, Lopes et al. 2012, Zhao et al. 2016, Kucukler et al. 2020) focused on the analysis of isolated elements (i.e., member-based approaches) to studying the global response of structures (Couto et al. 2013, Walport et al. 2019, Liu et al. 2018, González-de-León et al. 2022, Yun et al. 2022) as whole systems (i.e., system-based approaches) thanks to the advances in commercial finite element software and the development of system-based direct design approaches (Zhang et al. 2016). However, the existing system-based approaches (Arrayago and Rasmussen 2022(a), Arrayago et al. 2022, Arrayago and Rasmussen 2022(b)) were developed based on analyses carried out on carbon and stainless steel structures at room temperature, and still need to be adapted to the design of structures under fire situation.

For this reason, the simplified design methods prescribed in the upcoming version of European codes (prEN 1993-1-2 (2021)) for fire design base the resistance of whole carbon and stainless steel structures on the resistance of their critical member, hence disregarding the capacity for redistributing internal forces of Class 1 (plastic) cross-sections. Only when the advanced design methods featured in prEN 1993-1-2 (2021) are employed – those based on advanced numerical finite element (FE) models – the redistribution capacity of the designed structures can be considered at elevated temperatures.

According to prEN 1993-1-2 (2021), advanced design methods shall consider any potential failure mode of the structure, or otherwise they shall be prevented by appropriate means. Moreover, advanced design methods shall consider the increase of temperature of the structure according to the theory of heat transfer and the influence of the temperature increase on the structural mechanical response, but both analyses may be carried out independently. The main drawback when employing these advanced design methods for fire design is, however, that no guidelines are given to assess the failure of the structure from the results of the numerical analysis, leaving to the designer's experience the assessment of the structure's collapse under fire situation.

2.5.4.1. Influence of second order effects

Second order effects produced by the deformation of structures shall be considered in the design calculations when they are assumed to significantly affect their response and resistance. However, according to the upcoming European codes (prEN 1993-1-1 (2019) and prEN 1993-1-4 (2021)) the influence of second order effects in carbon steel structures may be small enough to be disregarded in some situations, for which a first order analysis would be suitable. Based on this, a set of conditions in the form of equations Eq. 2.51-Eq. 2.52 are codified in prEN 1993-1-1 (2019) for classifying structures as non-sway or sway. Equation Eq. 2.51 is to be used to assess the influence of the second order effects

produced by non-sway buckling modes of a structural member, while Eq. 2.52 checks the influence of second order effects produced by in-plane global sway modes.

$$\alpha_{cr,ns} = \frac{F_{cr,ns}}{F_d} \geq 25 \quad \text{Eq. 2.51}$$

$$\alpha_{cr,sw} = \frac{F_{cr,sw}}{F_d} \geq 10 \quad \text{Eq. 2.52}$$

In these equations, $\alpha_{cr,ns}$ and $\alpha_{cr,sw}$ stand for the factors by which the design value of the loading would have to be increased to cause elastic instabilities following a non-sway mode or a sway mode, respectively. $F_{cr,ns}$ is the corresponding minimum elastic critical load for an in-plane or out-of-plane non-sway member buckling mode, while $F_{cr,sw}$ is the minimum elastic critical load for an in-plane global sway mode. The design value of the loading on the structure is denoted by F_d.

When Eq. 2.51 is fulfilled means that the members conforming the structure are not prone to buckling thus the design checks can be skipped, otherwise the influence of the second order effects produced by the non-sway buckling modes of the members conforming the structure should be considered.

Alternatively, if Eq. 2.52 is fulfilled the structure is classified as a non-sway structure, in which the influence of the second order effects produced by the global sway of the structure have a negligible impact on the structure's response (differences in design forces are below 10%), and according to prEN 1993-1-1 (2019) may be ignored for design purposes. When Eq. 2.52 is not met, the influence of global second order effects is significant and should be considered appropriately.

However, Eq. 2.51 and Eq. 2.52 should only be employed to assess the influence of the second order effects if an elastic global analysis is going to be employed. When using plastic global analysis Eq. 2.51 and Eq. 2.52 should apply for the system before forming the last plastic hinge or should be checked for each individual system along the formation of the different plastic hinges, up to the design loading. Alternatively, current European code EN 1993-1-1 (2005) provides a modified version of Eq. 2.52 with a more restrictive requirement when employing plastic global analysis, as shown in Eq. 2.53.

$$\alpha_{cr,sw} = \frac{F_{cr,sw}}{F_d} \geq 15 \quad \text{Eq. 2.53}$$

For stainless steel structures, the upcoming European design code provides a specific formulation to assess the influence of the second order effects produced by sway global modes, as material nonlinearities result in a reduction of the structural stiffness and hence in a further amplification of second order effects. The codified equation, given in Eq. 2.54, is a slight modification of Eq. 2.52 and

it has been introduced in prEN 1993-1-4 (2021) with the aim of addressing the reduction of stiffness described by stainless steel alloys at elevated strains (i.e., $\varepsilon \geq \varepsilon_y$), as shown in Figure 2.2.

$$\alpha_{cr,sw,mod} = \frac{K_s}{K} \cdot Y \cdot \alpha_{cr,sw} \geq 10 \qquad \text{Eq. 2.54}$$

In this equation, K_s/K is the ratio of the secant lateral stiffness at the design value of the loading on the structure (F_d) to the initial lateral stiffness of the structure due to the influence of plasticity (obtained according to a first order plastic analysis). Alternatively, the ratio K_s/K may be expressed in terms of displacements as Δ_{el}/Δ_{pl}, where Δ_{el} is the lateral drift of the structure corresponding to a load equal to the design value of the loading on the structure (F_d) following a first order elastic analysis, and Δ_{pl} is the corresponding lateral drift of the structure at a load of F_d based on a plastic global analysis. The parameter Y is an additional coefficient to consider the additional loss of stiffness of the structure due to the further loss of stiffness due to second order effects. Conversely to carbon steel structures Eq. 2.54 can be used for assessing the influence of the second order effects despite the global analysis employed (i.e., elastic or plastic) for stainless steel structures.

Currently, under fire situation, there is not specific formulation on how to consider the influence of second order effects at elevated temperatures for carbon or stainless steel structures, despite the fact that the reduction of stiffness on carbon and stainless steel alloys at elevated temperatures is acknowledged in European fire codes prEN 1993-1-2 (2021), as shown in Figure 2.5(b).

2.5.4.2. Joint classification

When using system-based approaches for structural design, the correct response and strength of the joints must be ensured beforehand, unless the joint response is explicitly considered in the analysis, e.g., through the definition of the moment–rotation diagrams. In this regard, the current and upcoming European codes for joint design (EN 1993-1-8 (2005) and prEN 1993-1-8 (2020)) provide guidelines on how to model the joint response depending on two parameters: the joint resistance $M_{j,Rd}$ and the joint initial stiffness $S_{j,ini}$.

For elastic global analysis, joints should be classified according to their rotational stiffness (prEN 1993-1-8 (2020)) based on their moment–rotation response (M–ϕ). The classification of the joints is carried out based on the criteria shown in Figure 2.8: (a) rigid joints, if $S_{j,ini} \geq k_b \cdot E \cdot I_b/L_b$; (b) semi-rigid; and (c) nominally pinned, if $S_{j,ini} \geq 0.5 \cdot E \cdot I_b/L_b$, where $S_{j,ini}$ is the initial rotational stiffness of the joint, I_b is the second moment of inertia of the beam and column respectively, L_b is the span of beam, and k_b is the mean value of I_b/L_b for all the beams at the top of that storey.

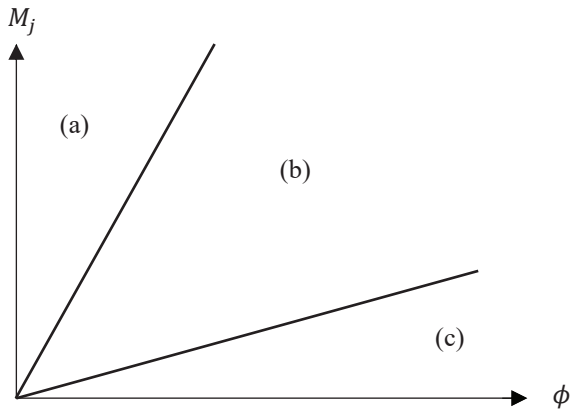

Figure 2.8. Classification of joints based on their initial joint rotational stiffness ($S_{j,ini}$).

For global plastic (rigid-plastic) analysis, the joint classification is based on the joint resistance: (a) full-strength joints, if $M_{j,Rd} \geq \min(M_{c,pl,Rd}, M_{b,pl,Rd})$ for top column joints; (b) partial-strength joints; (c) nominally pinned joints, if $M_{j,Rd} < 0.25 \cdot \min(M_{c,pl,Rd}, M_{b,pl,Rd})$, where $M_{c,pl,Rd}$ and $M_{b,pl,Rd}$ are the plastic bending resistance of the column and the beam, respectively.

For advanced design methods (i.e., elastic-plastic global analysis), joints are classified based on both previous criteria (i.e., stiffness and resistance). A summary on how to consider the influence of the joint's response on the structural analysis, depending on the type of analysis carried out, can be found in Table 2.2 (prEN 1993-1-8 (2020)).

Table 2.2. Type of joint model (prEN 1993-1-8 (2020)).

	Method of global analysis			Type of joint model
	Elastic	Rigid-plastic	Elastic-plastic	
Joint classification	Nominally pinned	Nominally pinned	Nominally pinned	Simple
	Rigid	Full-strength	Rigid and full-strength	Continuous
	Semi-rigid	Partial-strength	Semi-rigid and partial-strength Semi-rigid and full-strength Rigid and partial-strength	Semi-continuous

CHAPTER 3

Finite element modelling

3.1. Introduction

In this section, the finite element (FE) models developed to assess the response of carbon and stainless steel frames at room temperature and under fire situation are described comprehensively. Furthermore, this section presents the validation of the developed FE model against experimental data of carbon and stainless steel structures at room and elevated temperatures. The FE analysis package Abaqus version 2020 (Abaqus 2020) was used to develop the analysis of all the structural models used throughout this thesis.

As recommended by prEN 1993-1-2 (2021), the advanced design methods based on FE models should consider the loss of mechanical properties of carbon and stainless steel structures at elevated temperatures; hence, the mechanical response of the structure must be directly influenced by the changes of the temperature field over time. Therefore, and in order to correctly reproduce the response of carbon and stainless steel frames under fire situation by means of FE numerical methods, two different analyses should be carried out: a heat transfer analysis and a mechanical analysis. Moreover,

the fire resistance of a structure is remarkably influenced by the degree of utilisation (μ_0) (Segura et al. 2021) which indicates the percentage of the ultimate load (P_u) that the structure is withstanding when the fire starts, as described in Section 2.5. Consequently, a prior mechanical analysis should also be carried out at room temperature in order to determine the ultimate load (P_u) of the frame and allow the definition of load levels corresponding to different degrees of utilisation.

3.2. Heat transfer analysis

The heat transfer analysis is governed by three physical phenomena (i.e., radiation, convection, and conduction) that rule the heat transmission between the heated air and the structure, as explained in Section 2.4. Radiation and convection were modelled by a set of boundary conditions applied onto the external faces of the cross-sections affected by the fire effect, which simulated the heat transfer between the heated air and the structure. These external conditions included the emissivity coefficient (ε_g, ε_s) and the convective coefficient (α_c), which were adopted as recommended by prEN 1993-1-2 (2021) for the corresponding steel or stainless steel grades analysed as shown in Table 3.1. The evolution of the temperature for the gas surrounding the structure was modelled according to the standardized ISO-834 curve (Eq. 2.18). Conductivity (λ_c) and the remaining material properties influencing the heat transfer analysis – i.e., specific heat (c_a) and density (ρ) – were introduced in the FE model as recommended in prEN 1993-1-2 (2021) for each specific material. The adopted values of these material properties are shown in Table 3.1, alongside with the values of the thermal expansion ($\Delta l/l$) – despite this property only affects the thermo-mechanical analysis (Section 3.3) –.

Table 3.1. Adopted values of the main thermal properties of carbon and stainless steel.

Material property	Carbon steel	Stainless steel
ε_g	1.0	1.0
ε_s	0.7	0.4
α_c [W/m^2°C]	25.0	25.0
λ_c [W/m°C]	Eq. 2.26-Eq. 2.27	Eq. 2.35-Eq. 2.36
c_a [J/kg°C]	Eq. 2.28-Eq. 2.31	Eq. 2.37-Eq. 2.38
ρ [kg/m^3]	7850	7850
$\Delta l/l$	Eq. 2.32-Eq. 2.34	Eq. 2.39-Eq. 2.41

Moreover, in order to correctly model the heat transfer problem by means of numerical methods, a time increment (Δt) equal to 5 seconds was employed to avoid instabilities on the problem-solving convergence, which is in accordance with the recommendations provided in prEN 1993-1-2 (2021). The heat transfer problem was treated as a transient heat transfer problem and solved by means of the Newton-Raphson method, where the time increments considered in the numerical model had a real physical meaning. Figure 3.1 shows the temperature field of a stainless steel frame after being exposed 20 minutes to the standardized ISO-834 curve.

Figure 3.1. Temperature field [°C] of a stainless steel frame subjected to fire in its interior faces after 20 minutes.

It should be noted that the radiative heat flux appearing inside the hollow in the beam and columns was also considered. It was modelled as an idealized cavity radiation: all elements facing the column or beam cavity suffer an additional radiative heat flux between them and the air temperature in the cavity. The temperature of the air inside the cavity is computed as the mean temperature of all the elements facing the defined cavity. This additional heat transfer flux has a strong influence on the temperature development of structural members not heated up isotropically (e.g., only three sides of the cross-section are subject to fire).

3.3. Thermo-mechanical analysis

Considering that the fire response of structures is directly influenced by the applied initial load or the degree of utilisation (μ_0) (Segura et al. 2021), the resistance of the structure at room temperature (P_u) must be estimated before assessing the structural response under fire situation. This initial mechanical analysis at room temperature was solved by means of the arc-length method, which allowed to obtain the peak of the load–displacement curve – assumed to be the ultimate load or resistance of the system (P_u) – and the post-peak response of the structure.

Once the ultimate load at room temperature (P_u) was estimated, a certain degree of utilisation could be defined as per $P_{fi,Ed}=\mu_0 \cdot P_u$ in order to analyse the structure under fire situation. Following the prEN 1993-1-2 (2021) recommendations, the response of carbon and stainless steel structures was modelled by means of the sequential thermo-mechanical analysis, where the heat transfer analyses were carried out beforehand in order to determine the temperature field evolution necessary to feed the mechanical analysis.

Carbon and stainless steel frames were subjected to an initial load corresponding to a pre-defined degree of utilisation (μ_0) that was maintained constant, while the temperature fields – obtained in the prior heat transfer analyses – were updated at different time steps until the frames could no longer withstand the applied loads due to the loss of their mechanical properties, and the time fire resistance was reached. It should be noted that the thermal elongations ($\Delta l/l$) occurring due to the increase of temperature were also explicitly considered in the mechanical analyses as shown in Table 3.1 following prEN 1993-1-2 (2021) recommendations.

3.4. General modelling assumptions

As recommended in the Abaqus manual (Abaqus 2020), the stress–strain curves at room temperature were introduced in the numerical models as user-defined true stress (σ_{true}) and logarithmic true plastic strain (ε_{true}^{pl}) relationships, calculated as shown in Eq. 3.1 and Eq. 3.2 from the engineering material properties. The engineering stresses (σ_{nom}) and strains (ε_{nom}) were obtained from the corresponding material models prescribed for stainless steel or carbon steel in prEN 1993-1-14 (2021). For stainless steel alloys the two-stage Ramberg-Osgood material model described in Section 2.3 was adopted in order to model the nonlinear stress–strain relationship and consider strain hardening effects (see Eq. 2.10-Eq. 2.11).

$$\sigma_{true} = \sigma_{nom}(1 + \varepsilon_{nom}) \quad \text{Eq. 3.1}$$

$$\varepsilon_{true}^{pl} = \ln(1 + \varepsilon_{nom}) - \sigma_{true}/E \quad \text{Eq. 3.2}$$

Likewise, material properties at elevated temperatures were also input as user-defined stress–strain curves (see Eq. 2.15-Eq. 2.17) by means of the temperature-dependent true stress ($\sigma_{true,\theta}$) and logarithmic plastic strains ($\varepsilon_{true,\theta}^{pl}$), using the reduction factors for the Young's modulus ($k_{E,\theta}$), the yield stress ($k_{\mathrm{y},\theta}$) and the ultimate tensile strength ($k_{u,\theta}$) obtained from prEN 1993-1-2 (2021). The main material properties at room temperature (E, f_y, f_u) for stainless steel were obtained from Afshan et al. (2019), while the corresponding values at elevated temperatures (E_θ, $f_{y,\theta}$, $f_{u,\theta}$) and the remaining material properties (n, m, $\varepsilon_{0.2}$, ε_u, $E_{0.2}$) at room and at elevated temperatures (n_θ, m_θ, $\varepsilon_{0.2,\theta}$, $\varepsilon_{u,\theta}$, $E_{0.2,\theta}$) were calculated as described in Section 2.3.

For carbon steel structures, the base material properties (E, f_y) were obtained from prEN 1993-1-1 (2019), and the engineering stresses (σ_{nom}) and strains (ε_{nom}) were calculated as Eq. 2.1-Eq. 2.2 and introduced into the numerical model as true stress (σ_{true}) and logarithmic true plastic strain (ε_{true}^{pl}), as per Eq. 3.1 and Eq. 3.2. Likewise, the stress–strain curves at elevated temperatures were computed as per Eq. 2.3-Eq. 2.9 and introduced to the numerical model using Eq. 3.1 and Eq. 3.2.

Unless otherwise specified, the local and member initial geometric imperfections of cross-section and members, as well as residual stresses, were not included in the developed finite element models, since they have been shown to have a low influence on the final response of these types of frames and their influence diminishes at elevated temperatures (Ng and Gardner 2007). Likewise, the analysed frames throughout this thesis were subjected to loading cases that featured gravity loads and significantly high horizontal loads, where the explicit modelling of global initial geometric imperfections was not necessary according to prEN 1993-1-1 (2019).

The mechanical boundary conditions (i.e., fixed or pinned supports) were included in the numerical models by restraining the appropriate degrees of freedom of sets of reference points, which were connected to the nodes comprising the end surfaces of the members through kinematic couplings. Likewise, the point loads were applied onto reference points, also connected to sets of surfaces, while the distributed loads were applied as uniformly distributed onto the corresponding surfaces with a fixed direction and without considering surface deformations.

Joints, and their mechanical responses, were introduced into the FE models using two different joint modelling techniques: explicitly modelled joints and numerically perfect rigid joints. For the first type (i.e., explicitly modelled joints, shown in Figure 3.2(a)), representing actual frame joints, the welds connecting the beams and the columns were explicitly included in the FE discretization of the model, assuming that the welding material was equivalent to the carbon or stainless steel alloy defined for the connected members. For the idealized connections (i.e., numerical joint model, shown in Figure 3.2(b)), perfectly rigid joints were implemented in the numerical models by connecting the beam and column ends via multiple strings with very high stiffnesses for all the degrees of freedom.

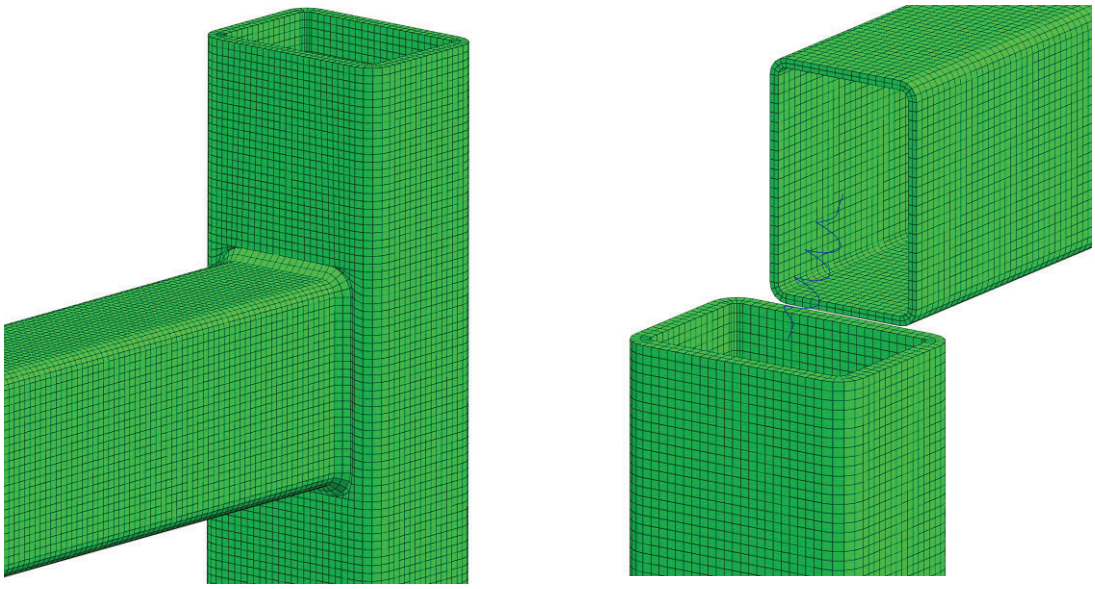

(a) (b)

Figure 3.2. Joint modelling techniques employed: (a) explicitly modelled joints and (b) numerically modelled joints.

3.5. Validation of the FE models

The developed numerical models were assessed and validated against multiple laboratory tests, both at room and elevated temperatures:

- The first numerical model validation focused on reproducing the failure of a set of welded joints connecting multiple stainless steel members with hollow sections at room temperature. The tests were reported in Feng and Young (2008) and Feng et al. (2019).

- The second laboratory test reproduced by means of the developed numerical model was carried out by Rossi (2012). This experimental programme comprised a stainless steel column subjected to high temperatures under anisothermal conditions (i.e., evolutive non-uniform temperature), which was tested applying a fixed axial vertical load. The failure of the stainless steel column occurred in a combination of global flexural and local buckling modes due to the loss of mechanical properties at elevated temperatures.

- The final FE model validation covered the main structural typologies studied throughout this thesis and their main failure modes, i.e., steel systems, in which the laboratory tests carried out by Rubert and Schaumann (1982) were reproduced. This experimental programme reported a set of 18 carbon steel frames, with different geometric configurations and loading cases, tested under anisothermal conditions until failure.

It is worth noting that the laboratory tests reproduced by means of the developed FE models covered the main structural typologies analysed throughout this thesis, as well as the different potential failure modes. The results reported in the following sub-sections confirm and demonstrate the capability of the numerical model developed for this investigation to correctly reproduce the response of carbon and stainless steel members, connections and frames at room temperature and under fire situation in terms of predicted ultimate capacities, failure modes and load–displacement histories.

3.5.1. Joint failure

In order to assess the accuracy of the developed numerical models on welded joints conforming steel and stainless steel frames, a total of 12 stainless steel Rectangular Hollow Section (RHS) joint tests reported in the literature (Feng and Young 2008, Feng et al. 2019) were reproduced. Feng and Young (2008) tested several T-joints between stainless steel RHS specimens, four of which failed exhibiting the purely chord face failure modes that the developed numerical model aims to reproduce. Furthermore, Feng et al. (2019) reported the experimental results of 18 stainless steel connections

between hollow members with different inclined angles, although for the validation of the FE model only the connections with 90º angles were reproduced: four T-joints and five X-joints.

The key parameters of the reproduced tests on RHS joints are presented in Table 3.2, including the chord and brace dimensions. The specimen IDs define the joint typology according to the following labelling system: the first letter X or T indicates the connection type (X-connection or T-connection), while the second part defines the chord (C) geometry as $Ch_0 \times t_0$, where h_0 is the chord height and t_0 is the chord thickness, and the third part defines the brace (B) geometry as $Bh_1 \times t_1$, where h_1 is the brace height for RHS members –or the brace diameter (d_1) for CHS specimens– and t_1 is the brace thickness. Note that all these geometric properties are defined in Figure 3.3. The additional term -R stands for those tests that were repeated with the same geometry. In addition, l_0 and l_1 are the chord and brace member lengths, respectively.

Table 3.2. Geometric parameters of the laboratory tests reproduced in the validation of the FE model.

Specimen ID	Chord				Brace				Ref.
	b_0 [mm]	h_0 [mm]	t_0 [mm]	l_0 [mm]	b_1 [mm]	h_1/d_1 [mm]	t_1 [mm]	l_1 [mm]	
T-C140×3-B40×2	80.2	140.3	3.14	740	40.4	40.0	2.02	99	Feng (2008)
T-C140×3-B40×2-R	80.3	140.2	3.09	742	40.3	40.3	1.61	98	Feng (2008)
T-C160×3-B40×2	80.6	160.5	2.96	842	40.3	40.1	1.96	99	Feng (2008)
T-C140×3-B50×1.5	80.4	140.0	3.13	738	50.2	50.5	1.56	122	Feng (2008)
T-C80×2-B40×4	80.2	80.4	2.02	438	40.2	40.2	3.93	97	Feng (2008)
T-C150×3-B108×3	150.2	150.2	3.01	900	-	108.4	3.04	325	Feng (2019)
T-C150×3-B133×3	149.9	149.9	3.02	900	-	132.1	3.09	400	Feng (2019)
T-C200×4-B108×3	200.1	200.1	3.96	1200	-	108.8	2.88	325	Feng (2019)
T-C200×4-B133×3	199.8	199.8	3.82	1200	-	131.2	2.84	400	Feng (2019)
X-C150×3-B108×3	149.9	149.9	2.96	900	-	108.4	3.05	325	Feng (2019)
X-C150×3-B133×3	149.8	149.8	2.96	900	-	131.7	3.00	400	Feng (2019)
X-C150×3-B133×3-R	149.8	149.8	2.96	900	-	131.8	2.99	400	Feng (2019)
X-C200×4-B108×3	199.9	199.9	3.97	1200	-	108.4	3.06	325	Feng (2019)
X-C200×4-B133×3	199.4	199.4	3.98	1200	-	131.4	3.02	400	Feng (2019)

All the tests reproduced numerically in this study corresponded to stainless steel joints, characterized by a highly nonlinear response and significant strain hardening. Hence, the two-stage Ramberg-Osgood material model (Eq. 2.10-Eq. 2.11) was used to describe the stress–strain relationship. The main basic material parameters (E, f_y, f_u) necessary for the Ramberg-Osgood model were reported in the original papers (Feng and Young 2008, Feng et al. 2019), and are reproduced in Table 3.3, whereas the remaining parameters (n, m, $E_{0.2}$) were obtained by means of the predictive expressions given in prEN 1993-1-14 (2021) and presented in Section 2.3.

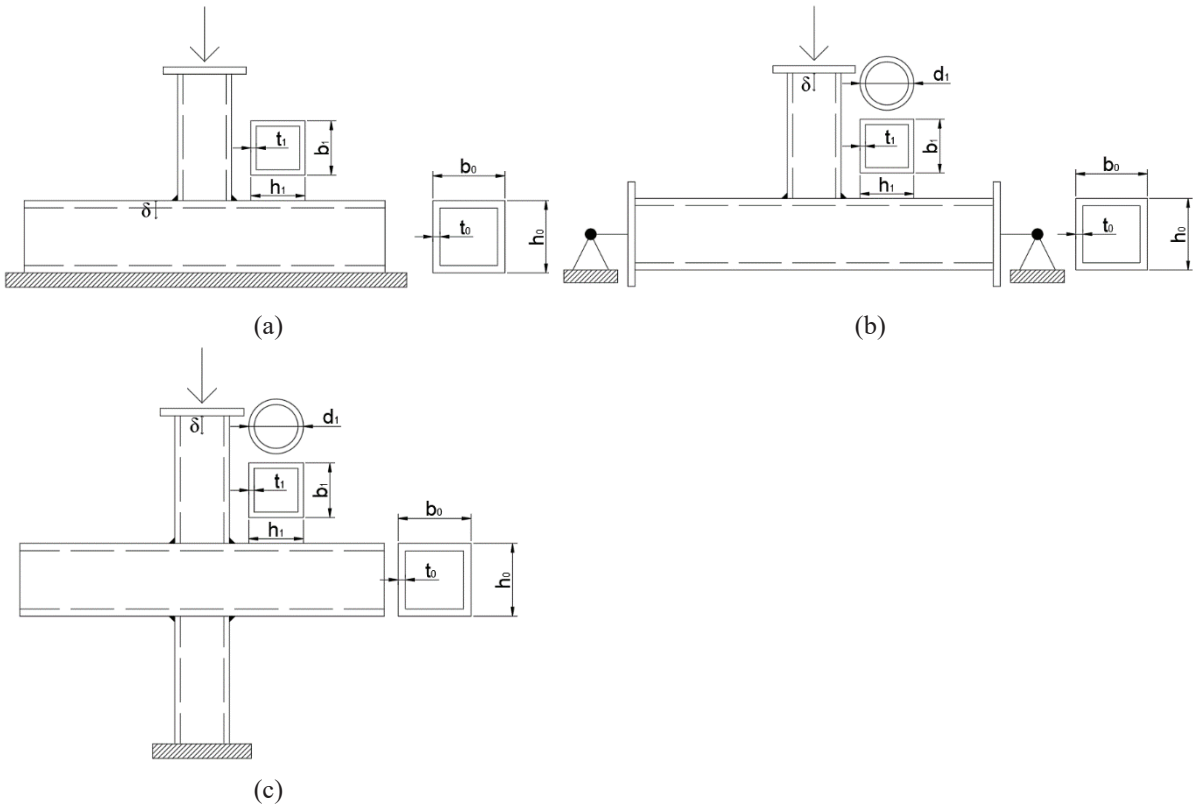

Figure 3.3. Schemes of the reproduced laboratory tests: (a) T-joints from Feng and Young (2008) , (b) T-joints from Feng et al. (2019), and (c) X-joints from Feng et al. (2019).

Table 3.3. Material parameters of the reproduced laboratory tests for the validation of the FE model.

Specimen ID	Chord			Brace			Ref.
	E [GPa]	$f_{0.2}$ [MPa]	f_u [MPa]	E [GPa]	$f_{0.2}$ [MPa]	f_u [MPa]	
T-C140×3-B40×2	212	486	736	216	707	827	Feng (2008)
T-C140×3-B40×2-R	212	486	736	216	707	827	Feng (2008)
T-C160×3-B40×2	208	536	766	216	707	827	Feng (2008)
T-C140×3-B50×1.5	212	486	736	200	662	770	Feng (2008)
T-C80×2-B40×4	201	398	608	196	565	725	Feng (2008)
T-C150×3-B108×3	207	430	780	233	441	750	Feng (2019)
T-C150×3-B133×3	207	430	780	229	434	753	Feng (2019)
T-C200×4-B108×3	188	423	758	233	441	750	Feng (2019)
T-C200×4-B133×3	188	423	758	229	434	753	Feng (2019)
X-C150×3-B108×3	207	430	780	233	441	750	Feng (2019)
X-C150×3-B133×3	207	430	780	229	434	753	Feng (2019)
X-C150×3-B133×3-R	207	430	780	229	434	753	Feng (2019)
X-C200×4-B108×3	188	423	758	233	441	750	Feng (2019)
X-C200×4-B133×3	188	423	758	229	434	753	Feng (2019)

The load versus vertical displacement curves obtained by means of the numerical analyses are compared with those measured in the laboratory tests (Feng and Young 2008) in Figure 3.4. Note that the vertical displacements shown in Figure 3.4(a) correspond to the top flange indentation of the chord measured 20 mm away from the brace faces, as reported by the original authors (Feng and Young 2008), while in

Figure 3.4(b) and Figure 3.4(c) the vertical displacements were measured at the top cross-section of the braces. As it can be seen from Figure 3.4, and despite the uncertainties associated to this type of tests, the numerical load–displacements histories are in good agreement with the test results, indicating the suitability of the developed FE models to reproduce the behaviour of welded joints between RHS members for different configurations.

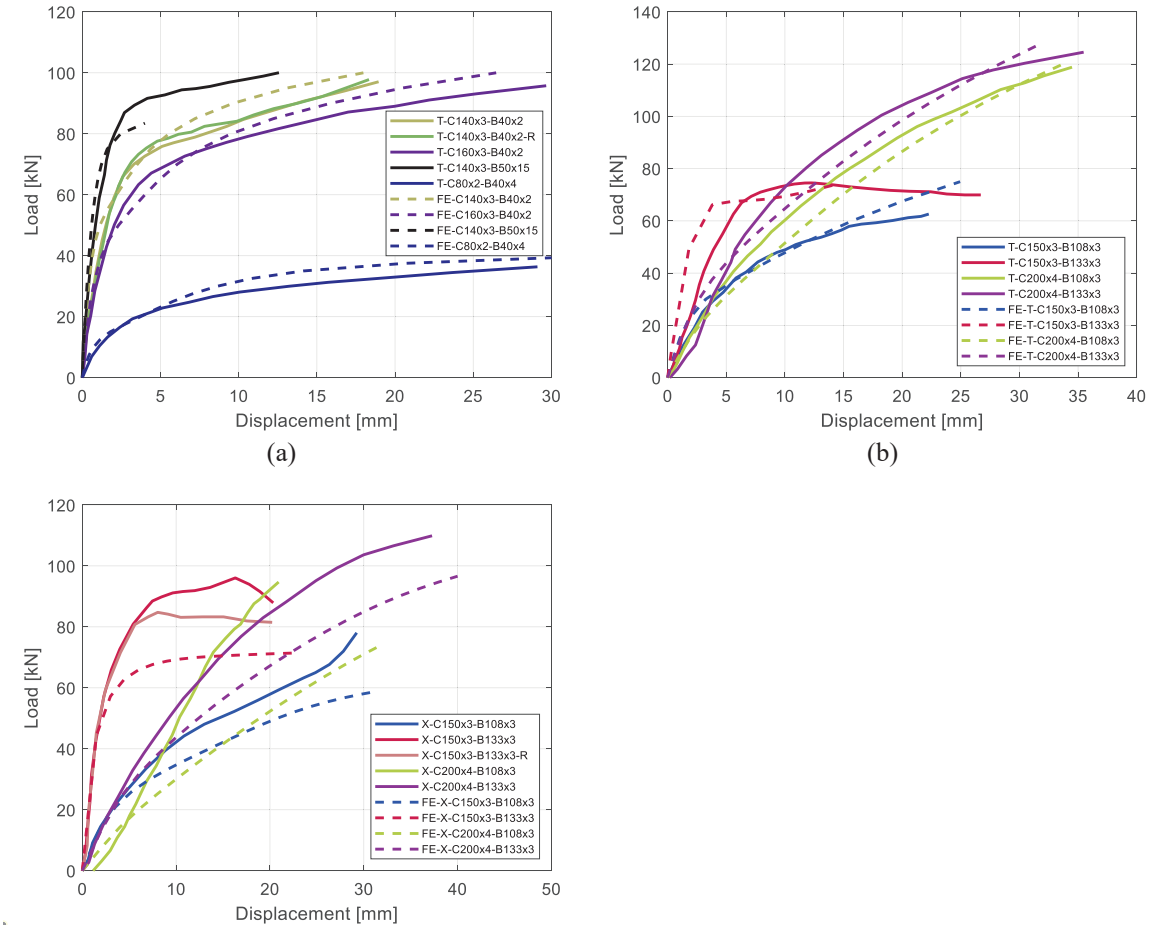

Figure 3.4. Comparison of experimental and numerical load–displacement curves for model validation: (a) T-joints from Feng and Young (2008), (b) T-joints from Feng et al. (2019), and (c) X-joints from Feng et al. (2019).

Likewise, Table 3.4 reports the ultimate loads of the experimental tests besides the ultimate loads obtained by means of the finite element analyses (FE) and the comparison thereof (i.e., N_{Test}/N_{FE} ratios). The numerical results reported in Table 3.4 show a very good agreement with the laboratory tests in terms of predicted ultimate joint capacities, with a mean value of the ultimate numerical-to-test loads equal to 1.04 and a coefficient of variation (COV) of 0.125, further demonstrating the suitability of the developed FE model to reproduce the failure of the chord face due to yielding in RHS member joints.

Table 3.4. Comparison of the experimental and FE results for the validation of the FE model.

Specimen ID	N_{Test} [kN]	N_{FE} [kN]	N_{Test}/N_{FE}
T-C140×3-B40×2	59.6	62.0	0.96
T-C140×3-B40×2-R	59.5	62.0	0.96
T-C160×3-B40×2	46.3	44.4	1.04
T-C140×3-B50×1.5	68.7	78.9	0.87
T-C80×2-B40×4	16.7	16.7	1.00
T-C150×3-B108×3	31.6	34.1	0.93
T-C150×3-B133×3	53.6	67.1	0.80
T-C200×4-B108×3	42.8	35.6	1.20
T-C200×4-B133×3	51.4	48.6	1.06
X-C150×3-B108×3	25.5	23.9	1.07
X-C150×3-B133×3	75.9	62.9	1.21
X-C150×3-B133×3-R	74.8	62.9	1.19
X-C200×4-B108×3	23.7	20.1	1.18
X-C200×4-B133×3	36.0	31.6	1.14
		Mean	1.04
		COV	0.125

3.5.2. Local and member failure at elevated temperatures

The most common stainless steel sections used in construction are the cold-formed hollow sections. While these types of sections are not susceptible to torsional lateral buckling, they can fail in flexural buckling modes as other steel members. With the objective of calibrating the developed numerical model for local and member failure at elevated temperatures, the response of an 80×80×3 Square Hollow Section (SHS) column with a height of 2.5 m was numerically reproduced. This column was tested at the University of Liège by Rossi (2012).

This anisothermal test subjected the stainless steel column to fire (following the standard ISO-834 curve) at its four faces while a constant axial load was applied, increasing the temperature until failure. The aim of this test was to obtain the critical temperature of the column, and consequently, the time fire resistance of the member. The test specimen was fixed at both ends to prevent cross-sectional deformation, lateral displacements, rotations, and warping. The applied load was equal to 78 kN, and was the equivalent load corresponding to a degree of utilisation μ_0=0.3. The failure mode observed in the laboratory after the completing of the test was a combination of flexural and local buckling of the column, and it is shown in Figure 3.5.

The FE model was developed as specified in Section 3 with shell elements (S4R), the main material properties was obtained from (Afshan 2013) and the remaining parameters (n, m, $E_{0.2}$) were obtained by means of the predictive expressions given in prEN 1993-1-14 (2021) and presented in Section 2.3.

Figure 3.5. Different points of view of the column after the laboratory test (Rossi 2012).

Only the transverse out of plane displacements were impeded in order to trigger the failure mode in the desired plane. Since a combination of local buckling and global buckling failure modes was observed in the laboratory tests, both local and global geometric imperfection were introduced in the numerical model, following the amplitudes reported in (Afshan 2013). The shapes of the imperfections were obtained from a prior linear buckling analysis, and the corresponding global and local modes were input in the FE model. Figure 3.6 shows the deformed shape of the specimen obtained by means of the numerical model, which was very similar to that observed experimentally.

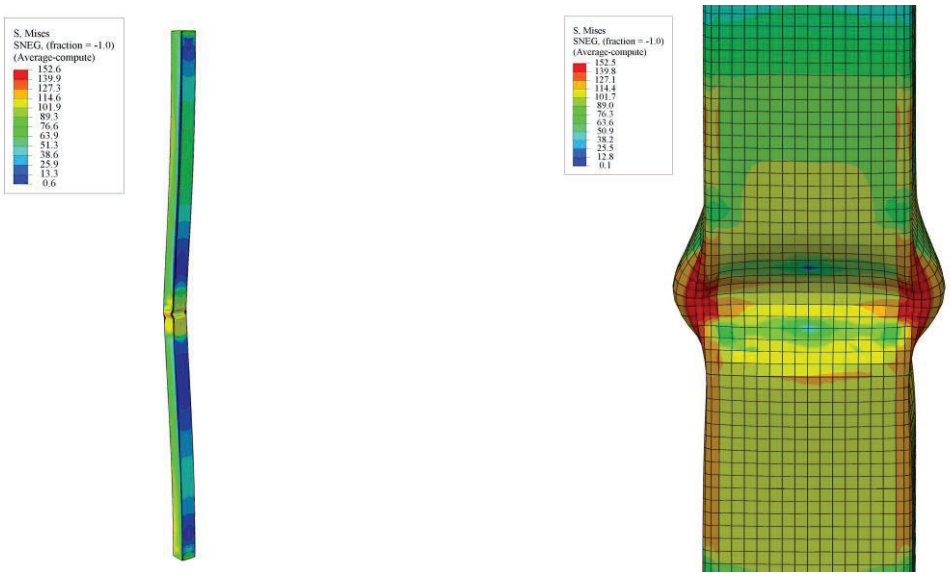

(a) (b)

Figure 3.6. Von Mises stress [MPa] distribution before failure obtained by means of the FE model of (a) the whole column and (b) the mid part where the local buckling developed.

A very good agreement can be observed from the comparison between the experimental and numerical axial displacement–temperature curves shown in Figure 3.7. Likewise, the FE model predicted a critical furnace temperature of 712°C, which corresponded to a critical temperature (θ_{crit}) of the specimen of

681℃, whereas the critical furnace temperature measured from the experimental results was 708℃, resulting in a relative error below 1%.

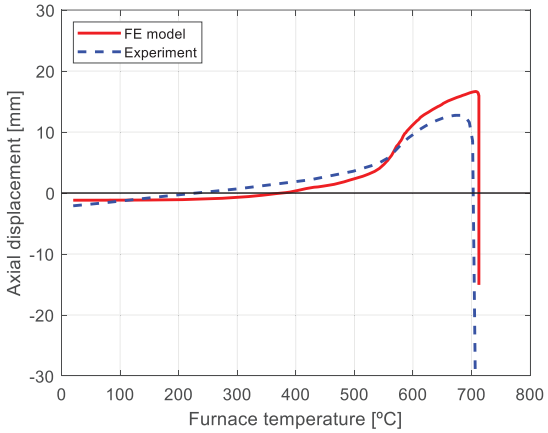

Figure 3.7. Axial displacement versus furnace temperature curve obtained in the laboratory test and by means of the FE model.

3.5.3. Structural system behaviour at elevated temperatures

Due to the complexity of performing structural system tests at elevated temperatures, the availability of experimental results on frames subjected to fire is very scarce or non-existent, both for carbon steel and stainless steel. Since no experimental fire tests for stainless steel frames have been reported in the literature as far as the author knows, the results of fire tests on I-section carbon steel frames conducted by Rubert and Schaumann (1986) were used for the validation of the numerical models developed in this thesis for structural systems. The tests included three different frame configurations, namely EHR, EGR and ZSR frame series, subjected to combined vertical and horizontal load cases, as shown in Figure 3.8(a)-(c), respectively.

All the structural members of the tested frames were IPE 80 profiles of carbon steel St37 grade. The torsional displacement and out-of-plane deformations of the frame structural elements were precluded by means of suitable restraints at the locations on the frames marked with a cross "×" in Figure 3.8.

The key details of the tested frames, including the loadings and geometries, are reported in Table 3.5, and are described hereafter. All the EHR and EGR frames were heated completely and uniformly, except for the EGR7 and EGR8 frames, where their beam members were left unheated. For all the ZSR frames, only one bay, as marked in Figure 3.8(c), was heated. Note that in Table 3.5 L and H are the frame width (one bay) and height, respectively, f_y is the measured yield stress at room temperature, F_1 and F_2 are the applied point loads, as shown in Figure 3.8, μ_0 is the degree of utilisation, and θ_{crit} is the experimentally measured failure (critical) temperature.

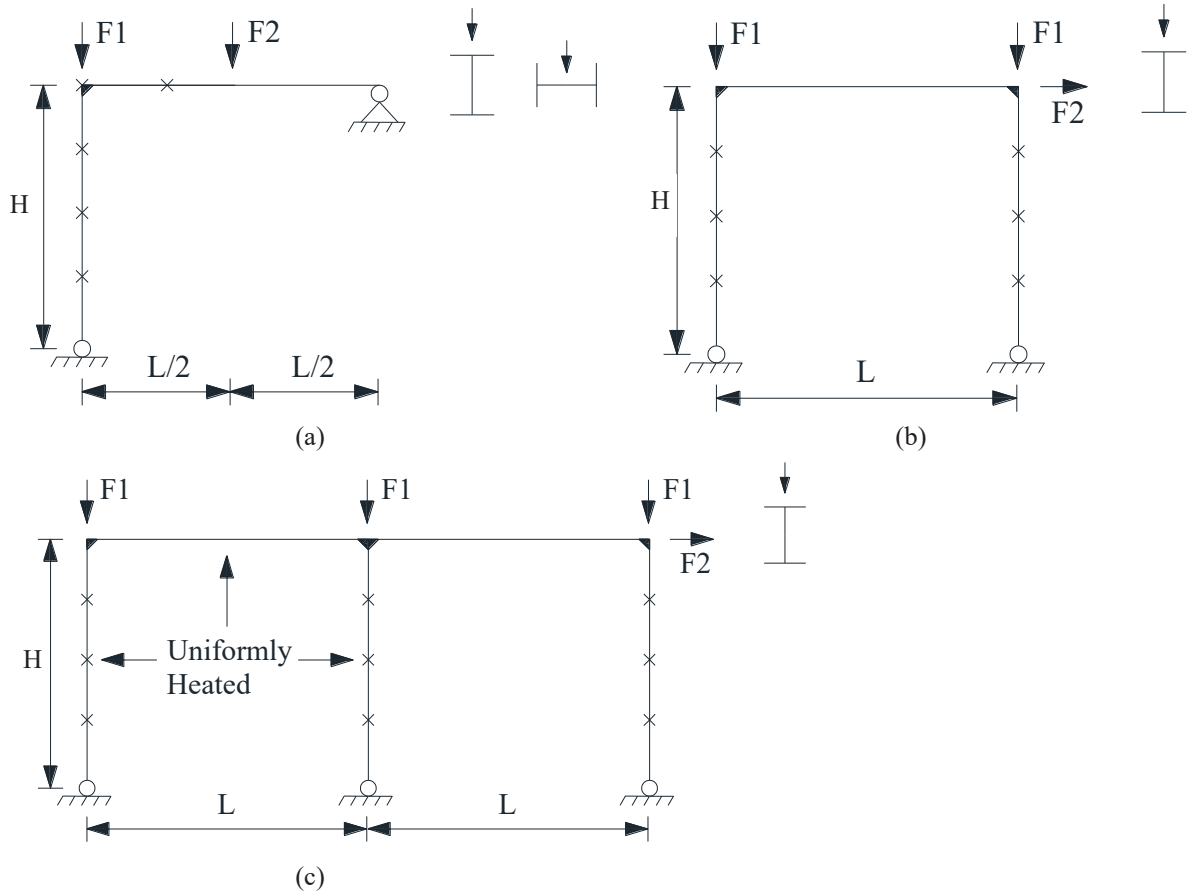

Figure 3.8. Schematic definition of the carbon steel frames tested at elevated temperature in Rubert and Schaumann (1986): (a) Frame HER, (b) Frame EGR, and (c) Frame ZSR.

Table 3.5. Key details of the tested frames from Rubert and Schaumann (1986).

Frame	L [mm]	H [mm]	F_1 [kN]	F_2 [kN]	μ_0	θ_{crit} [°C]	f_y [MPa]	Remarks	
EHR1	1190	1170	56	14	0.38	600	395	Major axis bending	All members fully heated
EHR2	1240	1170	84	21	0.59	530	395		
EHR3	1240	1170	112	28	0.82	475	382		
EHR4	1250	1500	20	5	0.59	562	389	Minor axis bending	
EHR5	1250	1500	24	6	0.71	460	389		
EHR6	1250	1500	27	6.7	0.79	523	389		
EGR1b	1220	1170	65	2.5	0.55	533	382	Major axis bending	All members fully heated
EGR1c	1220	1170	65	2.5	0.55	515	382		
EGR2	1220	1170	40	1.6	0.34	612	385		
EGR3	1220	1170	77	3.0	0.66	388	385		
EGR4	1220	1170	77	3.0	0.63	424	412		
EGR5	1220	1170	88	3.4	0.72	335	412		
EGR6	1220	1170	88	3.4	0.72	350	412		
EGR7	1220	1170	68.5	2.6	0.65	454	320		Cold beam
EGR8	1220	1170	77	3.0	0.70	464	385		
ZSR1	1200	1180	74.0	2.9	0.60	547	355	Major axis bending	Partly heated
ZSR2	1200	1180	84.5	3.3	0.66	479	380		
ZSR3	1200	1180	68.5	68.5	0.50	574	432		

The degree of utilisation (μ_0) adopted in the tests, defined as the ratio of the applied load in the fire situation (i.e., F_1 or F_2) to the load-bearing capacity at room temperature ($F_{1,u}$ or $F_{2,u}$), ranged between 0.34 and 0.82. The design load-bearing capacity of the frames at room temperature (i.e., $F_{1,u}$ and $F_{2,u}$) were determined by Rubert and Schaumann (1986) using a second order analysis, considering the yielding of the cross-sections and geometric nonlinearities. The experimental critical temperature θ_{cr} was defined in (Rubert and Schaumann 1986) as the temperature at which the beam midspan deflection reached a limiting maximum value of $L/60$. The FE predicted and experimentally obtained failure temperatures, θ_{FE} and θ_{Test}, respectively, of the modelled carbon steel frames are presented in Table 3.6.

Table 3.6. FE and test critical temperatures.

Frame	θ_{FE} [°C]	θ_{Test} [°C]	$\theta_{FE}/\theta_{Test}$
EHR1	627	600	1.04
EHR2	559	530	1.06
EHR3	474	475	1.00
EHR4	578	562	1.03
EHR5	545	460	1.18
EHR6	522	523	1.00
EGR1b	509	533	0.96
EGR1c	509	515	0.99
EGR2	600	612	0.98
EGR3	425	388	1.10
EGR4	445	424	1.05
EGR5	371	335	1.11
EGR6	371	350	1.06
EGR7	456	454	1.00
EGR8	453	464	0.98
ZSR1	542	547	0.99
ZSR2	507	479	1.06
ZSR3	600	574	1.05
		Mean	1.04
		COV	0.053

These two temperatures (θ_{FE} and θ_{Test}) refer to the temperatures in which the beam midspan vertical deflections reached the limiting values of $L/60$. As reported in Table 3.6, the ratio of the FE-to-test failure temperature ranged from 0.96 to 1.11, except for the EHR5 specimen, where this ratio was greater and equal to 1.18. It was reported by the authors in (Rubert and Schaumann 1986) that the EHR5 frame was in the plastic range prior to undergoing elevated temperatures. The mean value and the coefficient of variation (COV) of the FE-to-test critical temperatures were 1.035 and 0.053, respectively, showing a very good overall estimation of the failure temperatures.

Finally, Figures 3.9(a) and (b) show the comparison between the FE and test displacement–temperature responses of the EHR3 and ZSR1 frames, respectively. The displacements were measured as shown in Figure 3.9, at the beam midspan and column mid-height for EHR frames and at the joints for ZSR frames. The trend of the increase in the predicted displacements with temperature agrees well with the measured results, and the predictive accuracy of the developed FE models is therefore considered appropriate. Hence, the described modelling approach may reliably be used for the parametric numerical modelling investigation of similar carbon steel and stainless steel frames at elevated temperatures.

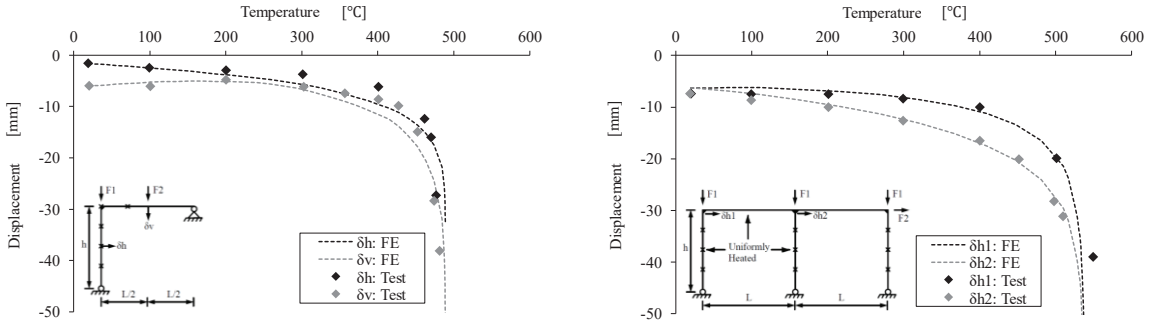

(a) (b)

Figure 3.9. Comparison of test and FE displacement versus temperature responses for (a) Frame EHR3 and (b) Frame ZSR1.

CHAPTER 4

Behaviour of carbon and stainless steel frames under fire situation

4.1. Introduction

Following on from the realization of the many benefits of design based on whole frame behaviour in fire of carbon steel structures and building on the existing body of knowledge on fire performance of stainless steel structures at member level, this preliminary study aims to investigate the global structural behaviour of carbon and stainless steel frame assemblies in fire. A thorough numerical investigation studying the structural behaviour of two-dimensional carbon and stainless steel frames is carried out at elevated temperatures, based on finite element simulations able to capture the combined effects of material degradation with temperature and the interaction between the individual frame elements. The effect of key behavioural parameters including frame type, degree of utilisation, material grade and heating profile is investigated through an extensive parametric study, which will serve as reference background knowledge to identify the main existing drawbacks for the implementation of advanced system-based design of carbon and stainless steel frames in fire and state the research questions that will be addressed in the following chapters of this thesis.

This chapter first presents the finite element parametric study carried out to assemble a reference database on the performance of carbon and stainless steel frames, which is subsequently used to assess

the influence of several basic design parameters such as the failure criteria, influence of second order effects (i.e., sway and non-sway structural classification), and the comparison between the performance of carbon and stainless steel frames.

4.2. Reference database: FE parametric study

4.2.1. Investigated parameters

The numerical parametric modelling was conducted to study the structural performance of stainless steel frames in fire and make comparative analysis with carbon steel frames. The analysed stainless steel frames were made of the austenitic EN 1.4301 and EN 1.4571 grades, and carbon steel frames were made of S275 steel. The geometry and loading configuration of the modelled frames are shown in Figure 4.1. The frame members were all hot-finished RHS 180×100×8 cross-sections, classified as Class 1 according to the EN 1993-1-4 (2006) and EN 1993-1-1 (2005) cross-section classification limits.

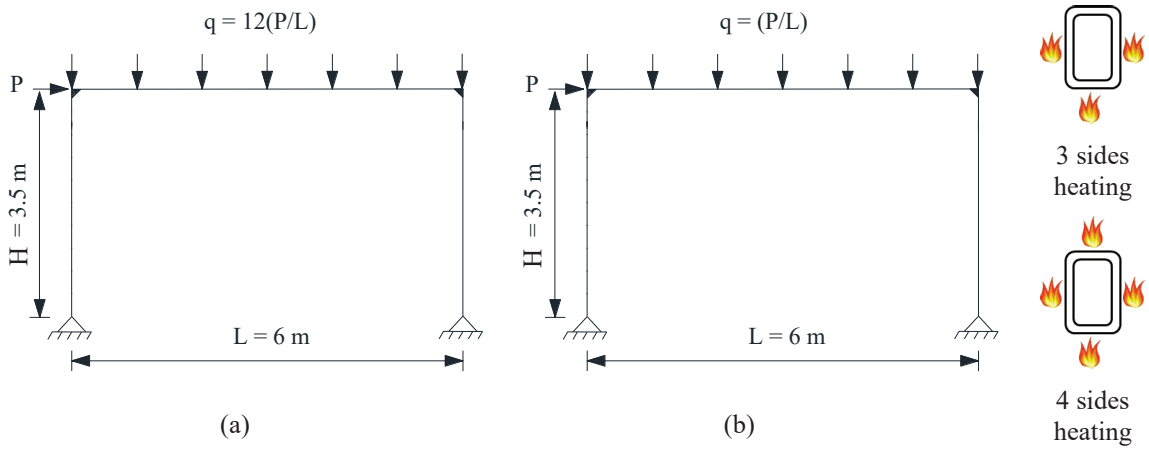

Figure 4.1: Geometry and loading for (a) sway and (b) non-sway frames subjected to heating on three and four sides.

For each stainless steel grade, two series of frames, namely sway and non-sway frames, were considered in the parametric study. As a preliminary study, the elastic buckling load factor α_{cr} was calculated according to the provisions given in the current EN 1993-1-1 (2005) for carbon steel structures, introduced as per Eq. 2.53. For plastic global analysis, these limits are $F_{cr}/F_{Ed} \geq 15$ for non-sway frames and $F_{cr}/F_{Ed} < 15$ for sway frames.

Sway and non-sway type frames were achieved through the adoption of different applied load combinations on the modelled frames. Sway frames had an applied total vertical ($q \cdot L$) to horizontal (P) load ratio of $R = q \cdot L/P = 12$, resulting in an elastic buckling load factor of α_{cr}=6.1 and α_{cr}=6.8 for the stainless steel (both EN 1.4301 and EN 1.4571) and carbon steel models, respectively. For the non-sway frames, the load ratio was defined as R=1, with elastic buckling load factors of α_{cr}=19.5 for

stainless steel frames and α_{cr}=23.9 for carbon steel structures. The elastic critical buckling loads (P_{cr}) were determined by conducting a linear eigenvalue buckling analysis of the frames subjected to the applied loading conditions at room temperature, and taking the eigenvalue corresponding to the lowest global sway buckling mode.

The applied design loads (P_{Ed}) of the frames were assumed to be equal to the system resistances, and were determined by conducting geometrically and materially nonlinear analyses with imperfections (i.e., GMNIA) at room temperature, and which are reported in Table 4.1. Using a first order plastic analysis, the sway frames were designed to form combined collapse mechanisms in failure, where the overall strength of the frames was tested as the strength of the columns and the beams is involved, whereas the frames classified as non-sway were designed to fail describing a traditional sway collapse mechanism. The predicted plastic collapse loads (P_{GPA}) according to an analytical first order plastic global analysis of the frames are reported in Table 4.1. Considering that the study was a first approach to the response of stainless steel frames under fire situation, the bending resistance of the stainless steel cross-sections was preliminarily calculated as the traditional plastic bending resistance (M_{pl}=$W_{pl} \cdot f_y$), using the 0.2% proof stress $f_{0.2}$ as the yield stress for the plastic global analysis and, therefore, neglecting the effect of strain hardening in the predicted resistances.

Table 4.1. P_{GMNIA}, P_{cr}, P_{GPA} loads of the modelled frames at room temperature depending on their material and loading ratio (R).

Steel grade	R	P_{GMNIA} [kN]	P_{cr} [kN]	P_{PGA} [kN]	α_{cr}=P_{cr}/P_{GMNIA}
EN 1.4301	12	11.6	70.9	10.5	6.1
	1	41.4	807.2	37.4	19.5
EN 1.4571	12	11.6	70.9	10.5	6.1
	1	41.4	807.2	37.4	19.5
S275	12	11.0	74.4	10.3	6.8
	1	35.4	847.6	36.7	23.9

Based on the applied design loads P_{Ed}, the modelled frames were subjected to a range of degrees of utilisation (μ_0) of 0.2, 0.3, 0.4, 0.5, 0.6 and 0.7. For each case, two different heating profiles were considered, including heating of all the four sides of the frame members and heating of only three faces of the frame members, as shown in Figure 4.1. In total, 72 frames were modelled and analysed, as summarised in Table 4.2.

Table 4.2.Summary of investigated parameters.

Steel grade	Frame type	Heating profile	Degree of utilization μ_0
EN 1.4301	Sway and non-sway	3 sides, 4 sides	0.2, 0.3, 0.4, 0.5, 0.6 and 0.7
EN 1.4571	Sway and non-sway	3 sides, 4 sides	0.2, 0.3, 0.4, 0.5, 0.6 and 0.7
S275	Sway and non-sway	3 sides, 4 sides	0.2, 0.3, 0.4, 0.5, 0.6 and 0.7

4.2.2. Specific details of FE models

The features and validation of the numerical models employed for modelling the frames are described in detail in Section 3, and in this subsection only the particularities of the FE models employed to assess the response of the presented frames will be highlighted.

The 4-noded S4R and DS4 shell elements, from the Abaqus (2020) element library, were employed to create the structural and thermal analyses models, respectively, and were used in all the numerical simulations presented in this section. A uniform mesh size of 5mm×5mm was used based on a mesh sensitivity analysis.

The stress–strain model for carbon steel provided in EN 1993-1-2 (2002) was adopted to describe the elevated temperature behaviour of the material. The EN 1993-1-2 (2002) strength, stiffness reduction factors and thermal properties, together with the room temperature yield stress f_y=275 MPa and Young's modulus E=210 GPa, were used to construct stress–strain curves at elevated temperatures. For stainless steel alloys assessed in this section, the stress–strain curve at elevated temperature provided in the Design Manual for Structural Stainless Steel (SCI 2007) was adopted, along with the thermal material properties proposed in it. The base mechanical material properties at room temperature of stainless steel were obtained from (Afshan et al. 2019), while thermal material properties given in the Design Manual for Structural Stainless Steel (SCI 2007) were adopted.

Moreover, rigid body coupling was used at the end cross-sections of the beam and the column members to restrain the degrees of freedom of all the nodes on the cross-sections to that of their corresponding concentric reference point. The beam and column members were connected via rigid body constraints at their ends to provide full continuity, simulating the numerical joint modelling approach described in Section 3.

4.3. Failure criteria

As explained in Section 4.2.1, the sway frames were designed to fail forming a combined collapse mechanism (i.e., plastic hinges forming at the beam mid-span and at the beam-to-column junction), while the non-sway frames were design to form a sway collapse mechanism (i.e., plastic hinges forming at the beam-to-column joints). Figure 4.2 illustrates the frame failure mechanisms for each type of frame, together with the deformed shape responses obtained from the corresponding FE models.

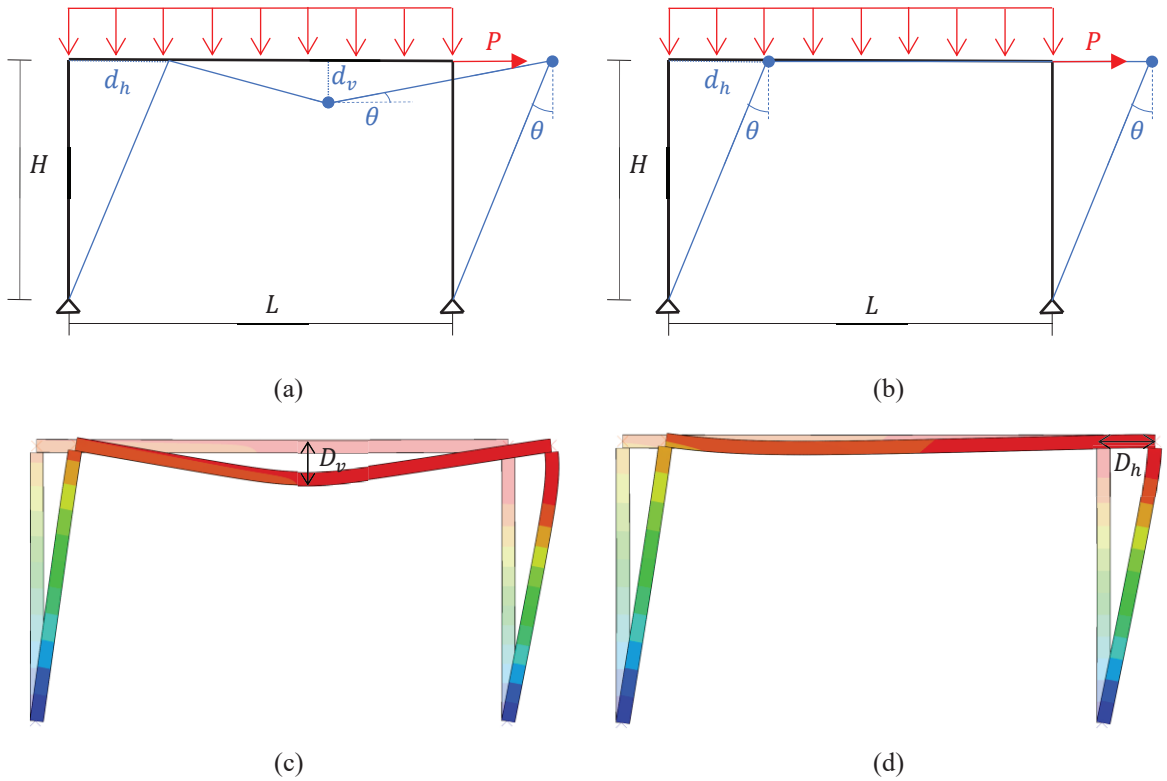

Figure 4.2. Predicted frame failure mechanisms from first order plastic global analyses of (a) the combined collapse mechanism, and (b) the sway collapse mechanism. Corresponding FE deformed shapes for frames with loading ratios of (c) R=12 and (d) R=1.

In contrast to the analyses carried out at room temperature, where the ultimate load of the frame can be identified as the peak load of the corresponding load–displacement curve, under fire situation the failure of the frame cannot be easily identified. For this reason, a new set of failure criteria are proposed below in order to compare the fire resistance between frames (with different materials, geometries and loads) in an objective manner.

Considering the different deformed shape responses of the analysed frames, suitable failure criteria in terms of the maximum deflection reached at elevated temperature needed to be first established. EN 1363-1 (2020) sets out distinct failure criteria for carbon steel flexural elements (i.e., beams) and vertically loaded elements (i.e., columns) in fire, which are given in terms of limiting deflections and deflection rates over time, as well as of limiting vertical contractions and vertical contraction rates, respectively. The limiting deflection (D) and limiting rate of deflection (dD/dt) requirements given in EN 1363-1 (2020) for flexural carbon steel members are presented in Eq. 4.1 and Eq. 4.2, respectively, where L is the member length and d is the height of the cross-section.

$$D_v = \frac{L^2}{400 \cdot d} \ [mm] \qquad \text{Eq. 4.1}$$

$$\frac{dD_v}{dt} = \frac{L^2}{9000 \cdot d} \ [mm/min] \qquad \text{Eq. 4.2}$$

The failure criteria presented in Eq. 4.1 and Eq. 4.2 were conceived to be used in laboratory tests to ensure safety and avoid sudden failures for security purposes. However, the assessment of the presented frames correspond to a situation of Ultimate Limit State (ULS). Therefore, based on the EN 1363-1 (2020) performance criteria for flexural members, two sets of modified limiting deflection and rate of deflection were preliminarily defined in this thesis: one for frames describing large horizontal displacements and another for frames describing large vertical displacements.

These two sets were fully compatible with the observed deformation shape responses shown in Figure 4.2. The proposed limits related to the vertical deflection (D_v) and the rate of vertical deflection over time (dD_v/dt) are given by Eq. 4.3 and Eq. 4.4, respectively, where L is taken as the frame span. Alternatively, for frames describing large horizontal displacements, the proposed limits were set in terms of the horizontal deflection (D_h) and the rate of horizontal deflection (dD_h/dt), and are given by Eq. 4.5 and Eq. 4.6, respectively, where H is taken as the frame height. The definitions of deflections D_v and D_h are illustrated in Figure 4.2(c) and Figure 4.2(d), while h_0 and h_1 stand for the cross-sectional height of the column and the beam, respectively.

For predominant vertical displacements:

$$D_v = \frac{L^2}{400 \cdot h_1}\ [mm] \qquad \text{Eq. 4.3}$$

$$\frac{dD_v}{dt} = \frac{L^2}{9000 \cdot h_1} \cdot 10\mu_0\ [mm/min] \qquad \text{Eq. 4.4}$$

For predominant horizontal displacements:

$$D_h = 2\frac{H^2}{400 \cdot h_0}\ [mm] \qquad \text{Eq. 4.5}$$

$$\frac{dD_h}{dt} = \frac{H^2}{9000 \cdot h_0} \cdot 10\mu_0\ [mm/min] \qquad \text{Eq. 4.6}$$

Note that the proposed horizontal deflection limit (D_h) is double of the corresponding limit for the vertical deflection because the horizontal deflection is measured at the top of the column and not at mid-height. The deflection rates were observed to be highly dependent on the degree of utilisation (μ_0), because frames subjected to high initial loads exhibit lower time fire resistance, but reach similar ultimate displacements, resulting in higher displacements rates than those subjected to low initial loads, as results presented in Section 4.6 prove. Therefore, applying the same deflection rate limit to frames with different degrees of utilisation did not seem reasonable and the comparison between them would not be direct, nor accurate. To solve this problem, and in order to not further reduce the displacement limit, the normalised degree of utilisation ($10{\cdot}\mu_0$) was tentatively included in the definition of the deflection rate limits shown in Eq. 4.4 and Eq. 4.6, allowing for higher deflection rate limits for higher

degrees of utilisation, and hence allowing a more realistic comparison of the failure temperatures across the entire range of utilisation ratios.

In this preliminary study, the failure of the frames under the applied loads was considered to occur when both failure criteria had been exceeded (i.e., Eq. 4.3 and Eq. 4.4 for frames describing large vertical displacements, and Eq. 4.5 and Eq. 4.6 for frames with predominantly horizontal displacements).

The suitability of the failure criteria was assessed against the laboratory tests carried out by Rubert and Schaumann (1986) on carbon steel frames at elevated temperatures by reassessing their collapse temperatures using the failure criteria presented in Eq. 4.3-Eq. 4.6. Note that these same frames were also used for validating the FE model in Section 3.5.3, where the detailed information on the geometry, loads and materials used can be found. The obtained results are shown in Table 4.3 and exhibit a good agreement with the critical temperatures obtained by Rubert and Schaumann (1986), suggesting the suitability of the proposed failure criteria.

Table 4.3. Critical temperatures of the validation frames obtained applying the defined failure criteria (θ_{FE}) and compared to the test critical temperatures (θ_{Test}).

Frame	μ_0	D_v [mm]	dD_v/dt [mm/min]	h [mm]	dD_h/dt [mm/min]	θ_{FE} [°C]	θ_{Test} [°C]	$\theta_{FE}/\theta_{Test}$
EHR1	0.38	88.5	486.8	85.6*	470.6	637	600	1.06
EHR2	0.59	96.1	528.6	85.6*	470.6	566	530	1.07
EHR3	0.82	96.1	326.7	85.6*	290.9	489	475	1.03
EHR4	0.59	97.7	644.5	140.6	928.1	639	562	1.14
EHR5	0.71	97.7	615.2	140.6	885.9	615	460	1.34
EHR6	0.79	97.7	703.1	140.6	1012.5	598	523	1.14
EGR1b	0.55	93.0	669.8	85.6	616.0	506	533	0.95
EGR1c	0.55	93.0	604.7	85.6	556.1	506	515	0.98
EGR2	0.34	93.0	651.2	85.6	598.9	596	612	0.97
EGR3	0.66	93.0	353.5	85.6	162.6	421	388	1.09
EGR4	0.63	93.0	548.8	85.6	252.4	441	424	1.04
EGR5	0.72	93.0	762.8	85.6	350.8	366	335	1.09
EGR6	0.72	93.0	548.8	85.6	504.8	366	350	1.05
EGR7	0.65	93.0	660.5	85.6	607.4	450	454	0.99
EGR8	0.70	93.0	734.9	85.6	675.9	449	464	0.97
ZSR1	0.60	90.0	540.0	87.0	522.2	506	547	0.93
ZSR2	0.66	90.0	594.0	87.0	574.4	450	479	0.94
ZSR3	0.50	90.0	450.0	87.0	435.1	574	574	1.00

*The horizontal deflection limit (D_h) is measured at the middle of the column due to their failure mechanism of this frame. Therefore, the limit has not been doubled for this model as shown in Eq. 4.5.

The time fire resistance (TFR) and critical temperature (θ_{cr}) at failure were determined for the carbon and stainless steel frames analysed in the parametric study following the proposed failure criteria (Eq. 4.3-Eq. 4.6), and are reported in Table 4.4 and Table 4.5.

Table 4.4. TFR [min] and critical temperatures (θ_{cr}) [°C] of the modelled frames with R=12 (classified as non-sway frames) corresponding to their predominant deflection D and deflection rate dD/dt criteria.

Steel grade	μ_0	R=12; 3 sides				R=12; 4 sides			
		D_v		dD_v/dt		D_v		dD_v/dt	
		TFR	θ_{cr}	TFR	θ_{cr}	TFR	θ_{cr}	TFR	θ_{cr}
S275	0.2	**34**	**789**	31	758	**32**	**793**	29	757
	0.3	**26**	**718**	23	702	**22**	**717**	19	689
	0.4	**21**	**679**	20	654	**19**	**688**	17	655
	0.5	**19**	**641**	18	612	**17**	**656**	16	628
	0.6	**17**	**600**	16	569	**15**	**624**	14	591
	0.7	**15**	**557**	14	529	**14**	**594**	13	570
EN 1.4301	0.2	**60**	**931**	59	926	**60**	**937**	58	929
	0.3	**43**	**868**	43	864	**42**	**875**	41	870
	0.4	**34**	**808**	24	807	**32**	**824**	32	819
	0.5	26	720	**27**	**735**	**26**	**771**	26	771
	0.6	20	593	**22**	**640**	21	696	**22**	**710**
	0.7	15	467	**17**	**526**	15	563	**17**	**615**
EN 1.4571	0.2	102	1017	**103**	**1020**	102	1019	**102**	**1020**
	0.3	71	960	**73**	**963**	71	963	**72**	**965**
	0.4	53	909	**55**	**916**	54	917	**55**	**920**
	0.5	42	861	**42**	**862**	43	878	**43**	**881**
	0.6	**31**	**775**	31	772	**33**	**828**	32	823
	0.7	22	638	**24**	**683**	**26**	**768**	26	767

Table 4.5. TFR [min] and critical temperatures (θ_{cr}) [°C] of the modelled frames with R=1 (classified as sway frames) corresponding to their predominant deflection D and deflection rate dD/dt criteria.

Steel grade	μ_0	R=1; 3 sides				R=1; 4 sides			
		D_v		dD_v/dt		D_v		dD_v/dt	
		TFR	θ_{cr}	TFR	θ_{cr}	TFR	θ_{cr}	TFR	θ_{cr}
S275	0.2	**30**	**742**	20	667	**28**	**746**	16	645
	0.3	**22**	**687**	18	631	**21**	**710**	15	610
	0.4	**18**	**630**	17	599	**18**	**674**	14	583
	0.5	**16**	**572**	15	564	**16**	**633**	13	570
	0.6	14	515	**14**	**535**	**14**	**593**	12	539
	0.7	12	449*	**13**	**509**	**13**	**548**	12	522
EN 1.4301	0.2	43	866	**46**	**882**	**51**	**908**	43	880
	0.3	29	758	**33**	**800**	**34**	**834**	29	798
	0.4	15	467	**28**	**740**	**26**	**765**	24	737
	0.5	11	339	**24**	**683**	19	654	**20**	**676**
	0.6	8	261	**18**	**562**	12	460	**15**	**560**
	0.7	7	199	**14**	**448**	8	285	**11**	**404**
EN 1.4571	0.2	77	973	**84**	**987**	**84**	**990**	82	985
	0.3	47	883	**61**	**933**	57	926	**58**	**930**
	0.4	31	777	**47**	**884**	42	877	**44**	**882**
	0.5	14	444	**39**	**842**	33	826	**35**	**842**
	0.6	10	329	**32**	**787**	23	725	**30**	**805**
	0.7	8	252	**26**	**708**	14	529	**22**	**716**

For the frames that were subjected to fire on three sides of the cross-sections, where its temperature distribution was non-uniform the critical temperature was taken as the average temperature of the cross-section corresponding to the specified failure time. Moreover, the frames with loading ratios R=1 (classified as non-sway frames) failed describing sway collapse mechanisms and, thus, the horizontal displacements were the predominant deflections, so Eq. 4.5 and Eq. 4.6 were used to determine the frame failure. On the contrary, frames under a loading ratio of R=12 (classified as sway frames) failed describing the combined collapse mechanism, for which the vertical displacement was predominant and, in consequence, Eq. 4.3 and Eq. 4.4 were employed for assessing the frame collapse under fire situation. In addition, Table 4.4 and Table 4.5 reports the obtained critical temperature and time fire resistance of the analysed frames according to each of the corresponding failure criterion (deflection and deflection rate limit), where the definitive (limiting) collapse temperature and time at failure are bolded.

4.4. Effect of the non-uniform heating on the frame response

To understand the effect of the non-uniform heating on the response of the frames, the temperature fields of the studied frames were obtained from the heat transfer analysis models. Note that the thermal response depends on the thermal properties of the material, the cross-section geometry, and the heating profile (i.e., heating on the four sides or the three interior sides of the frame members). Figure 4.3 shows the temperature–time response of the analysed carbon and stainless steel frames during the first 40 minutes of exposure to the ISO-834 curve in terms of (a) the temperature (θ) evolution of the frames subjected to fire in its 4 sides, and (b) the maximum (θ_{max}) and minimum (θ_{min}) temperature of the frames subjected to fire in its 3 sides. Note that as both stainless steel grades, EN 1.4301 and EN 1.4571, exhibit the same thermal properties, according to the values specified in (Structural Design Manual (SCI 2017)), their temperature development was identical and thus the curves are overlapped.

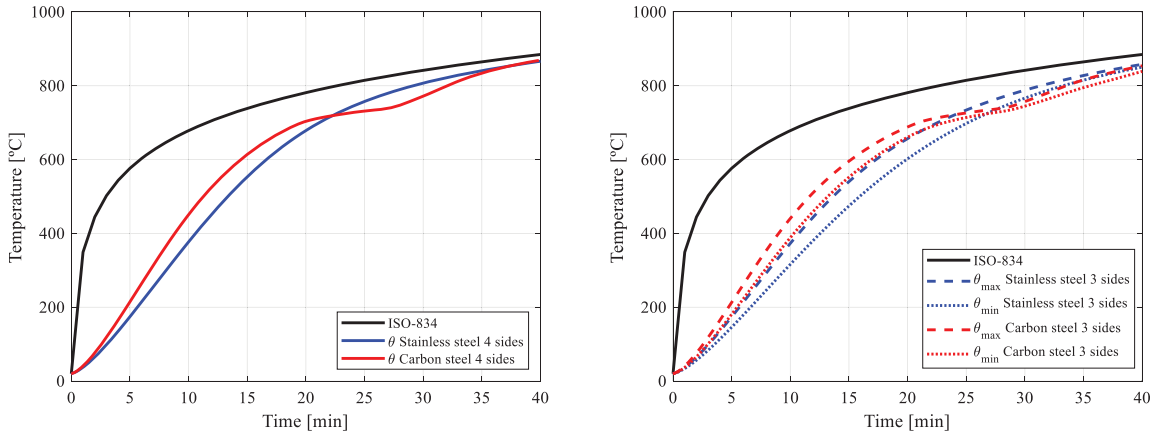

(a) (b)

Figure 4.3. Temperature–time development of the carbon steel and stainless steel frames (a) subjected to fire in its 4 sides and (b) 3 sides.

As shown in Figure 4.3(a), carbon steel frames gain temperature at a faster rate than stainless steel frames at the early stages of fire, but when carbon steel undergoes a phase change around the 735°C, the specific heat of the material increases abruptly, thereby making frames made of carbon and stainless steel have a similar temperature evolution henceforth. More detailed information can be found in Section 2.5.1.

The temperature gradient for the frames subjected to fire on the three interior sides may also be observed in Figure 4.3(b), where a significant difference between the minimum and the maximum temperature of the cross-section was evident. Since the maximum temperatures of these frames do not represent the real temperature of the cross-section, the average frame temperature was used to analyse these frames. In addition, a temperature difference was evident between the frames subjected to fire on all four sides of the cross-section and the frames exposed to fire on the three interior sides, as one would expect, difference that was larger at the early stages of fire, and smaller at higher temperatures.

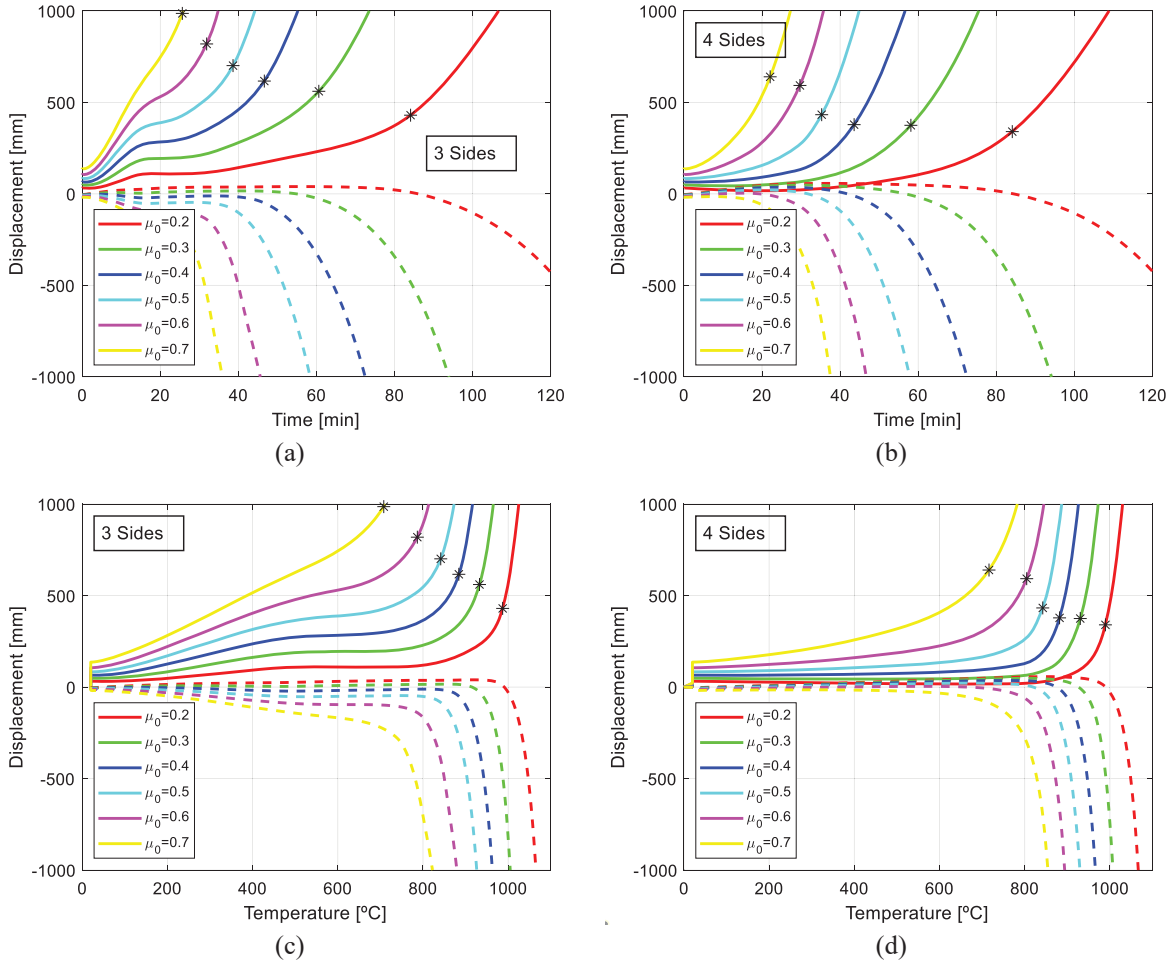

Figure 4.4. Horizontal (solid line) and vertical (dashed line) displacements versus (a) time with 3 sides heating profile, (b) time with 4 sides heating profile, (c) temperature with 3 sides heating profile and (d) temperature with 3 sides heating profile for EN 1.4571 stainless steel non-sway frames (R=1).

Figure 4.4 shows the displacement–time and displacement–temperature responses for the EN 1.4571 stainless steel frames subjected to heating on four sides and three interior sides, where the TFR and critical temperatures corresponding to the proposed failure criteria are marked with an asterisk (*). Prior to the start of runaway deflections at high temperatures, the frames heated on three sides show larger vertical and horizontal deflections than the frames with heating at the four sides. This could be due to the additional bending moments generated in the members by the temperature gradient across the depth of the cross-section. At high temperatures, when the temperature distributions become more uniform across the cross-section, frames with both heating profiles show similar responses.

Despite the different heating profiles, the resulting TFR and θ_{cr} of the frames showed slight differences, with the frames with heating on three interior sides showing marginally lower failure temperatures (θ_{cr}), due to the additional bending moments, but higher TFRs, due to the slower heating rates, see Table 4.4 and Table 4.5. For other types of structures, in which the imposed thermal displacements may be restrained, additional internal forces and bending moments may be induced and ought to be considered when checking the overall structure and its elements. If these additional internal forces and bending moments are not considered in the structural fire design, the designed structure may collapse earlier than expected.

4.5. Sway vs non-sway response

The non-sway (R=1) and sway (R=12) frames were designed to form sway collapse mechanisms and combined collapse mechanisms, respectively; these failure modes were indeed observed for all the analysed frames once their critical temperatures were reached. With the aim of assessing the influence of the lateral stability (or the susceptibility to second order effects) in the performance of portal frames in fire, Figure 4.5 compares the displacement–temperature response of EN 1.4301 stainless steel sway and non-sway frames.

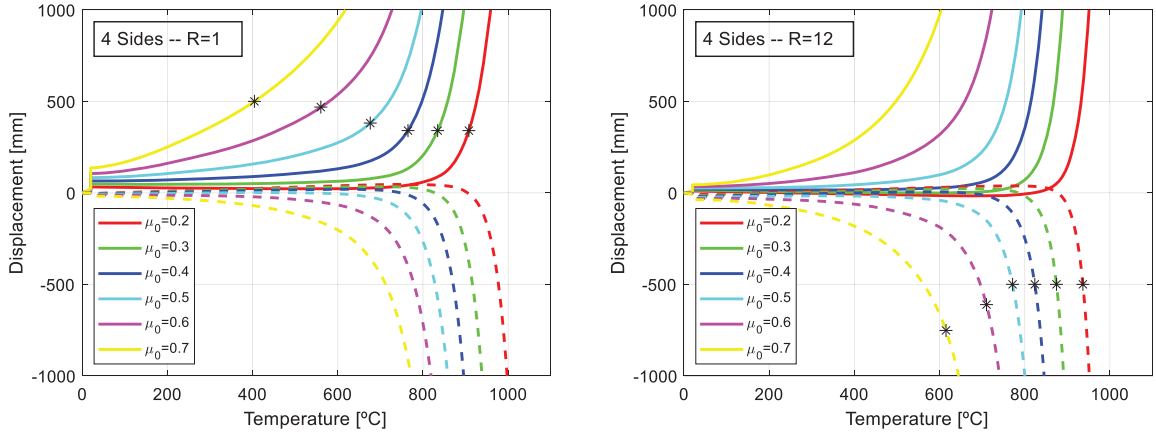

(a) (b)

Figure 4.5. Horizontal (solid line) and vertical (dashed line) displacements versus temperature for EN 1.4301 stainless steel frames under a loading ratio of (a) R=1 (non-sway) and (b) R=12 (sway).

For the two frames the vertical displacement is initially downwards due to the loads applied at room temperature, which starts to decrease as the temperature increases and the beams start to expand. At high temperatures, however, the increasing downward mechanical deflection, which is controlled by the reduced material stiffness due to the increased temperature, overtakes the thermal expansion and the deflection starts to runaway until the applied load can no longer be sustained, and the frame failure mechanisms are formed. Moreover, no major differences could be observed in terms of response under fire situation of the analysed frames based on the influence of their second order effects (i.e., sway or non-sway classification).

Figure 4.6 shows the variation of the TFR and critical temperature (θ_{cr}) at failure of the analysed frames, determined according to the criteria set out in Section 4.3, with the degree of utilisation (μ_0), alongside with the tendency curves obtained by fitting a quadratic curve to the results obtained. Note that the results are presented separately for the different materials and for sway (R=12) and non-sway (R=1) frames, and that the data presented in Figure 4.6 belong to frames with heating on 3 and 4 sides, exhibiting very similar responses. As expected, the time fire resistance and temperature at failure decrease with increasing degrees of utilisation for both sway (R=12) and non-sway (R=1) frames, both for stainless steel and carbon steel materials. The results also suggest that the obtained TFRs for the frames classified as sway were slightly higher than their non-sway counterparts. However, these preliminary results cannot lead to premature conclusions.

Moreover, it can be seen that TFRs seem to increase exponentially for very low degrees of utilisation (μ_0), whereas the critical temperature (θ_{cr}) does not follow a similar trend with μ_0. Nevertheless, further research needs to be done to arrive at sound and more general conclusions, since this preliminary study is a first approach to the response of this type of structures.

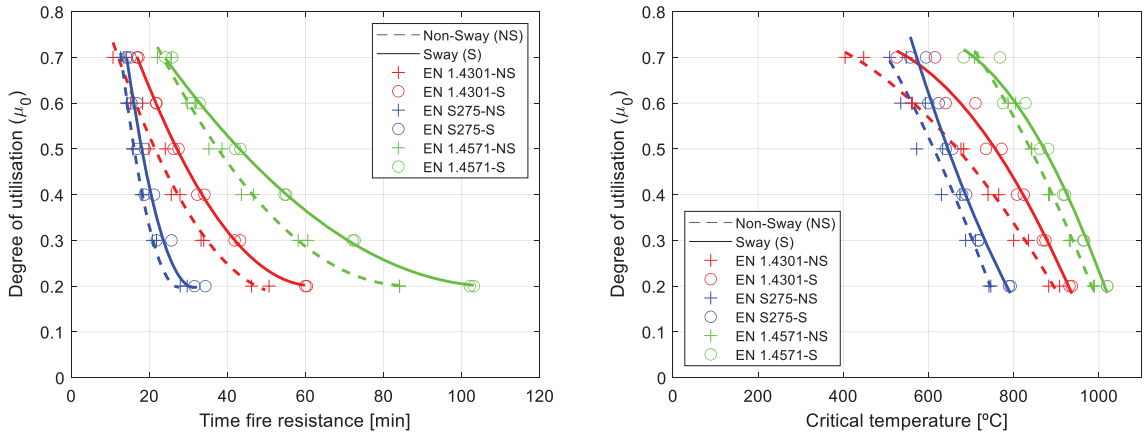

Figure 4.6. Variation of (a) TFR and (b) critical temperature of the analysed frames with the degree of utilisation.

4.6. Carbon and stainless steel

The time–displacement and temperature–displacement of carbon steel and stainless steel non-sway frames are shown in Figure 4.7, while those of sway frames are shown in Figure 4.8. In the two cases, both carbon steel and stainless steel frames are shown to exhibit similar response trends.

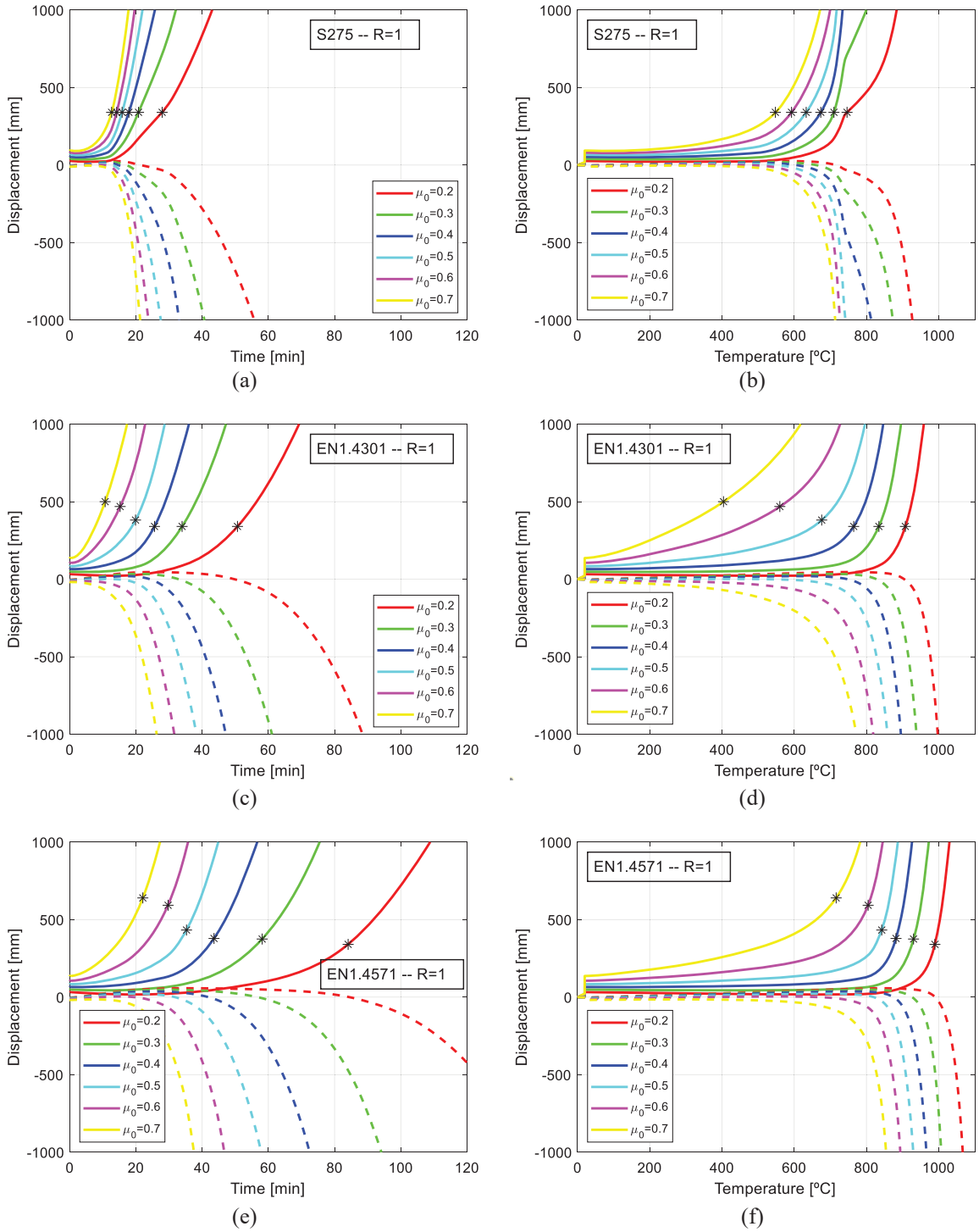

Figure 4.7. Horizontal (solid line) and vertical (dashed line) displacements versus time and temperature for non-sway frames subjected to fire on 4 sides: (a) and (b) for S275, (c) and (d) for EN 1.4301, and (e) and (f) for EN 1.4571.

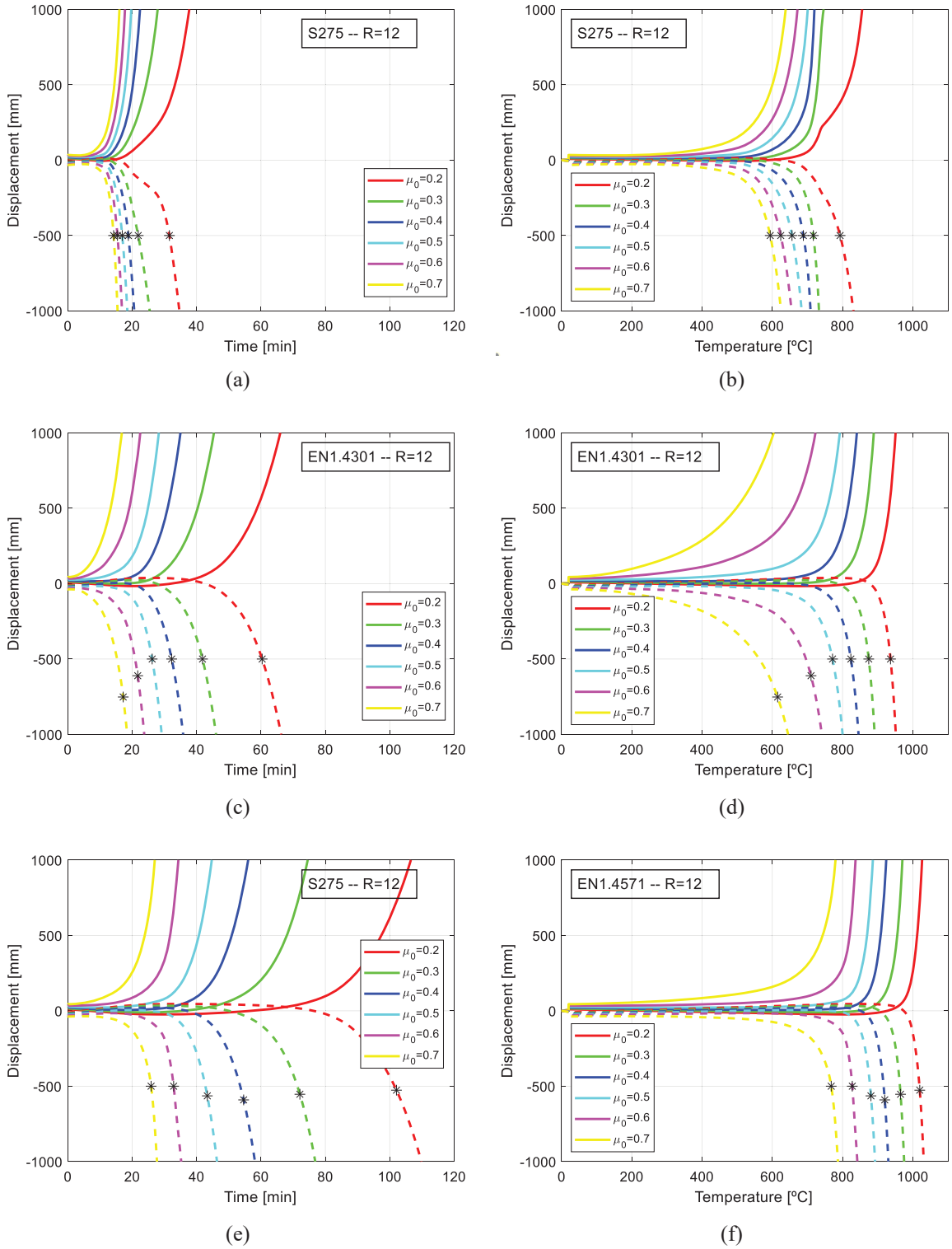

Figure 4.8. Horizontal (solid line) and vertical (dashed line) displacements versus time and temperature for sway frames subjected to fire on 4 sides: (a) and (b) for S275, (c) and (d) for EN 1.4301, and (e) and (f) for EN 1.4571.

The ratios of the stainless steel-to-carbon steel time fire resistances (TFR_{ss}/TFR_{cs}) and critical temperatures ($\theta_{cr,ss}/\theta_{cr,cs}$) for all the analysed frame configurations are presented in Table 4.6.

Table 4.6. Comparison of failure times and critical temperatures for stainless steel and carbon steel frames.

Steel grade	μ_0	Sway 3 sides		Sway 4 sides		Non-sway 3 sides		Non-sway 4 sides	
		$\frac{TFR_{ss}}{TFR_{cs}}$	$\frac{\theta_{cr,ss}}{\theta_{cr,cs}}$	$\frac{TFR_{ss}}{TFR_{cs}}$	$\frac{\theta_{cr,ss}}{\theta_{cr,cs}}$	$\frac{TFR_{ss}}{TFR_{cs}}$	$\frac{\theta_{cr,ss}}{\theta_{cr,cs}}$	$\frac{TFR_{ss}}{TFR_{cs}}$	$\frac{\theta_{cr,ss}}{\theta_{cr,cs}}$
EN 1.4301	0.2	1.76	1.18	1.88	1.18	1.53	1.19	1.82	1.22
	0.3	1.65	1.21	1.91	1.22	1.50	1.16	1.62	1.17
	0.4	1.62	1.19	1.68	1.20	1.56	1.17	1.44	1.14
	0.5	1.42	1.15	1.53	1.18	1.50	1.19	1.25	1.07
	0.6	1.29	1.07	1.47	1.14	1.29	1.05	1.07	0.94
	0.7	1.13	0.94	1.21	1.04	1.08	0.88	0.85	0.74
EN 1.4571	0.2	3.03	1.29	3.19	1.29	2.80	1.33	3.00	1.33
	0.3	2.81	1.34	3.27	1.35	2.77	1.36	2.76	1.31
	0.4	2.62	1.35	2.89	1.34	2.61	1.40	2.44	1.31
	0.5	2.21	1.34	2.53	1.34	2.44	1.47	2.19	1.33
	0.6	1.82	1.29	2.20	1.33	2.29	1.47	2.14	1.36
	0.7	1.60	1.23	1.86	1.29	2.00	1.39	1.69	1.31

Both stainless steel grades generally show higher TFRs and critical temperatures than the equivalent carbon steel frames. This is due to the combination of three phenomena: (a) the lower heating rate of stainless steel, (b) the different stress–strain behaviour of the two materials at elevated temperatures, and (c) the higher retention of strength and stiffness of stainless steel alloys after the temperature of 600℃, the reader is referred to Section 2.5.1 for more details. Carbon steel frames with high degrees of utilisation (i.e., $\mu_0 \geq 0.6$), however, seem to exhibit improved fire resistances over the EN 1.4301 stainless steel frames. This is due to the fact that carbon steel does not see its yield stress reduced until 400℃, whereas both the yield stress and the ultimate tensile stress of stainless steels start to reduce at 100℃ – see Figure 2.5 for subgroup Austenitic I in Section 2.5.1 for more details. As a result, for high degrees of utilisation, where the critical temperature is usually lower, carbon steel frames may perform better than some stainless steel alloys under certain fire scenarios. Nevertheless, stainless steel grades such as the EN 1.4571 austenitic grade seem to outperform carbon steel frames for all degrees of utilisation, as one may expect due to the superior elevated temperature strength and stiffness retention ratios shown in Figure 2.5 for this grade (included in the subgroup Austenitic III) in Section 2.5.1.

Finally, Figure 4.9 plots the critical temperatures (θ_{cr}) of the analysed frames for different degrees of utilisation (μ_0). The reduction factors for the proportional limit ($k_{p,\theta}$) and the yield stress ($k_{y,\theta}$) for S275 carbon steel according to prEN 1993-1-2 (2021) are also depicted, along with the reduction factors for the 0.2% proof stress ($k_{0.2,\theta}$) and the ultimate tensile stress ($k_{u,\theta}$) for EN 1.4301 and EN 1.4571

stainless steels given in (Structural Design Manual (SCI 2017)). From the results shown in Figure 4.9, the critical temperatures of the frames follow the same trend as the strength reduction factors of the corresponding materials. This suggests that the analysed frames are forming complete plastic failure mechanisms for all the degrees of utilisation before collapsing, and exploiting all the resistance provided by the material and the frame design. It should be pointed out that the frame members analysed in this chapter were not prone to premature failure by global or local instabilities, hence their critical temperatures seem to follow the strength reduction factors; otherwise, the failure of the frames would have occurred before the development of the plastic collapse mechanisms and the obtained critical temperatures would have not followed these trends.

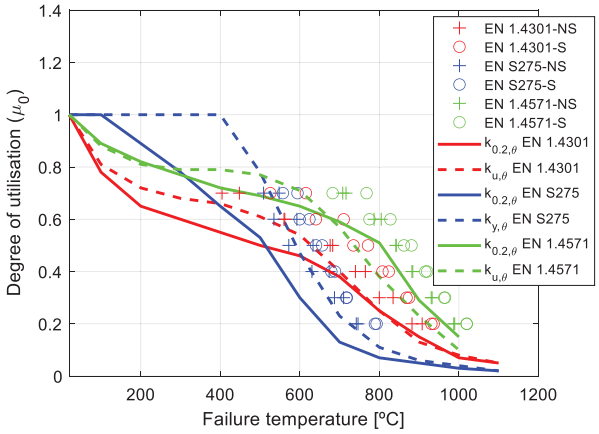

Figure 4.9. Comparisons between the failure temperatures of the analysed frames and the elevated temperature strength reduction factors of the materials.

This observation could be confirmed based on the Von Misses stress distributions of the analysed frames, which are shown in Figure 4.10 for a typical sway and non-sway frames, where the plastic hinges (or plastic zones) developing at each of the analysed frames could be clearly identified. The zones highlighted in grey correspond to elements surpassing the yield stress of the material ($f_{y,\theta}$ or $f_{0.2,\theta}$). The deformed shapes and the yielded parts described by the frames shown in Figure 4.10 were fully consistent with the theoretical plastic collapse mechanisms assumed for each of them in Figure 4.2, suggesting that the analysed frames were able to develop plastic collapse mechanisms before failure under fire situation.

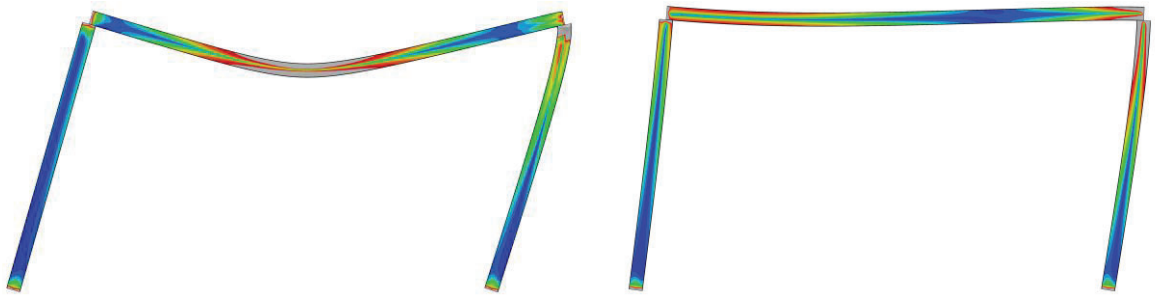

(a) (b)

Figure 4.10. Von Misses stress distribution on the deformed shape just before collapsing of: (a) sway EN 1.4571 frame with μ_0=0.7, and (b) non-sway S275 frame with μ_0=0.3.

4.7. Concluding remarks

The preliminary study presented in this chapter was carried out with the aim of identifying the main knowledge gaps on the response of carbon and stainless steel Class 1 frames under fire situation. The effect of key behavioural parameters including frame type (i.e., sway and non-sway), degree of utilisation, material grade, and heating profile was investigated through an extensive parametric finite element study and, based on the analysis of these results, the following conclusions and knowledge gaps can be drawn, which have been used as reference for the results and proposals presented in this thesis.

- The new failure criteria for estimating the time fire resistance of carbon and stainless steel frames in an objective way is provided in this section. Moreover, it has been validated for carbon steel frames against experimental data of laboratory tests carried out on carbon steel frames obtained from the literature. However, its applicability on stainless steel frames has to be assessed.
- The different heating profiles applied at the frames were found to not be critical on the fire performance of the frames, as the results of this study showed slight difference in the TFRs and critical temperatures (θ_{cr}) only. In general, frames with heating on three interior sides exhibited marginally lower critical temperatures, due to the additional bending moments induced by their non-uniform temperature profiles, but higher TFRs due to the slower heating rates.
- The proposed performance criteria for sway and non-sway frames, defined in terms of limiting deflections and limiting rates of deflection, were validated against experimental tests on carbon steel frames reported in the literature with excellent results, and were preliminarily adopted for the analysis of carbon and stainless steel frames in this chapter. Nevertheless, the proposed failure criteria – despite providing a rigorous and objective method for determining the frame resistance under fire situation –, have yet to be validated for stainless steel frames.
- Moreover, the TFRs and critical temperatures (θ_{cr}) were found to reduce with increasing degrees of utilisation for both sway and non-sway frames, and both for stainless steel and carbon steel materials. The two stainless steel grades considered in this study generally showed higher TFRs and critical temperatures than the S275 carbon steel frames: EN 1.4571 stainless steel frames outperformed S275 carbon steel frames at all degrees of utilisation, while EN 1.4301 stainless steel frames reached higher TFRs and critical temperatures for mid-to-low degrees of utilisation ($\mu_0 \leq 0.5$) only.
- The joints in the analysed portal frames were modelled as full-strength rigid joints, as required for performing global plastic analyses, but their influence on the frame response under fire situation is yet unknown and must be tackled carefully, as it may affect the plastic redistribution capacity of the structure. Preliminarily, the analysed carbon and stainless steel frames were found to be able to form plastic collapse mechanisms before failure, with significant plastic

redistribution, but this redistribution capacity has yet to be assessed at elevated temperatures, where the joints may play a major role.

- Finally, the loss of mechanical properties at elevated temperatures may lead to the premature failure of the joints and amplified horizontal displacements, increasing the influence of second order effects at elevated temperatures. This means that the criteria given for classifying frames as sway and non-sway at room temperature have yet to be validated for elevated temperatures.

CHAPTER 5

Bending moment resistance of welded joints

5.1. Introduction

In the recent years, most of the well-established design provisions for carbon steel structures under different loading conditions are being reassessed for stainless steel structures – being hollow sections the most commonly used product types – to evaluate their applicability to these alloys, which exhibit a significantly different stress–strain response (Dundu and Van Tonder 2014, Bock et al. 2015). This includes the provisions codified for joints, where the resistance, the maximum rotation capacity and the increment of internal forces resulting from strain hardening and the nonlinear material response are under investigation (Feng and Young 2015, Elflah et al. 2019(a), Elflah et al. 2019(b)).

Comprehensive design guidance for steel tubular joints is available in design codes and guides (EN 1993-1-8 (2005), prEN 1993-1-8 (2020), ANSI/AISC 360 (2010), CIDECT: Design Guide for Rectangular Hollow Section (Packer et al. 2009), CIDECT: Design Guide for Circular Hollow Section (Wardenier et al. 2008), ISO 14346 (2013), IIW (2008)), although these design guidelines generally cover normal strength carbon steel members at room temperature. Therefore, previous researchers

focused their studies on adapting these design guidelines to high-strength steels, stainless steels and to carbon steel members under elevated temperatures. Lan et al. (2018) studied the response of welded joints between high-strength steel members, concluding that high-strength steel welded joints show on average a resistance lower than that corresponding to normal-strength steel joints, in terms of the yield stress. Likewise, Feng and Young (2008) and Feng et al. (2019) assessed the response of stainless steel welded joints, where a new design formulation was proposed for stainless steel X-joints and T-joints under axial loading. Furthermore, Ozyurt et al. (2014), Ozyurt and Wang (2015 and 2019) studied the response of welded steel joints under elevated temperatures and proposed to use the room temperature formulation for the prediction of their strength, but multiplying it by different material reduction coefficients for elevated temperatures depending on the loading type: for welded joints under tensile forces the yield stress reduction coefficient ($k_{y,\theta}$) was proposed, for welded joints under compression forces, the Young's modulus reduction coefficient ($k_{E,\theta}$), and for welded joints under bending moment the average between the yield stress reduction coefficient ($k_{y,\theta}$) and the Young's modulus reduction coefficient ($k_{E,\theta}$) was recommended.

The failure of welded T-joints between tubular members under pure bending moment can be classified in four different failure modes: chord face failure, chord side wall failure, chord punching shear or brace failure, in addition to the local buckling failure of the brace or the chord comprising the joint (Hollow Sections in Structural Applications (Wardenier 2001)). Brace failure and chord punching shear failure may both occur due to an initial fracture that leads to the rupture and detach of one member from the other. The occurrence of the remaining failure modes depends on the joint geometry, being chord face failure the predominant failure mode for rectangular hollow section (RHS) joints when the ratio of the brace width (b_1) over the chord width (b_0) is lower than 0.85 (i.e., β=b_1/b_0≤0.85). Alternatively, for joints with β=1.0, the expected failure mode is chord side wall failure, although failure may also occur due to the overlapping of multiple failure modes. In order to clarify the notation, the chord and brace members will be referred to with subscripts 0 and 1, respectively.

The first formulation developed for hollow member joints exhibiting chord face failure modes was the Ring model proposed by Togo (1967), devoted to welded joints between circular hollow sections (CHS) under axial loading. The capacity (N_{Rk}) of the welded joints according to this model is given by Eq. 5.1, in which B_e is the effective length, d_0, d_1 and t_0 are the chord diameter, the brace diameter and the chord thickness, respectively, c_1 is a calibrated constant, β is equal to d_1/d_0, k_n is a parameter that considers the previously existing stresses on the chord and m_{pl}=$f_y t_0^2/4$ is the plastic moment per unit length, where f_y is the yield stress of the chord.

$$N_{Rk} = \frac{8B_e/d_0}{1 - c_1\beta} k_n m_{pl} \qquad \text{Eq. 5.1}$$

Afterwards, Johansen developed the yield line models for plates (Yield-line formulae for slabs (CRC Press 1972)), which were later used for analysing the behaviour of chord face failure modes (Wardenier 1982, Zhao 1992, Packer 1978, Yu 1997). This method is based on the principle of virtual works (PVW), where the work produced by the external forces is equated to the work produced by the internal forces ($\sum W_{ext}$=$\sum W_{int}$). This methodology was adapted to welded joints between tubular members under axial loads by Wardenier (1982), as shown in Eq. 5.2: $N \cdot \delta$ is the work produced by the external force, where N is the axial load applied and δ is the virtual displacement along the direction of the force N, and $m_{pl} \cdot l_i$ is the internal work produced by each of the yield lines defined in the model, where m_{pl} is the plastic moment per unit of length – calculated as indicated above – and l_i is the length of the corresponding yield line.

$$N \cdot \delta = \sum_i m_{pl} \cdot l_i \qquad \text{Eq. 5.2}$$

Wardenier (1982) defined the plastic line mechanism presented in Figure 5.1(a) for welded joints between RHS members and derived the expression given in Eq. 5.3 to estimate the chord face failure axial resistance, where η=h_1/b_0 and β=b_1/b_0, being h_1 and b_1 the brace cross-section height and width, respectively, and b_0 the chord width. This formulation was first implemented in the CIDECT recommendations (Packer et al. (2009)) and was subsequently included in EN 1993-1-8 (2005), prEN 1993-1-8 (2020) and ANSI/AISC 360 (2010).

$$N_{Rd} = \frac{8}{(1-\beta)}\left(\eta + 2\sqrt{1-\beta}\right)k_n m_{pl} \qquad \text{Eq. 5.3}$$

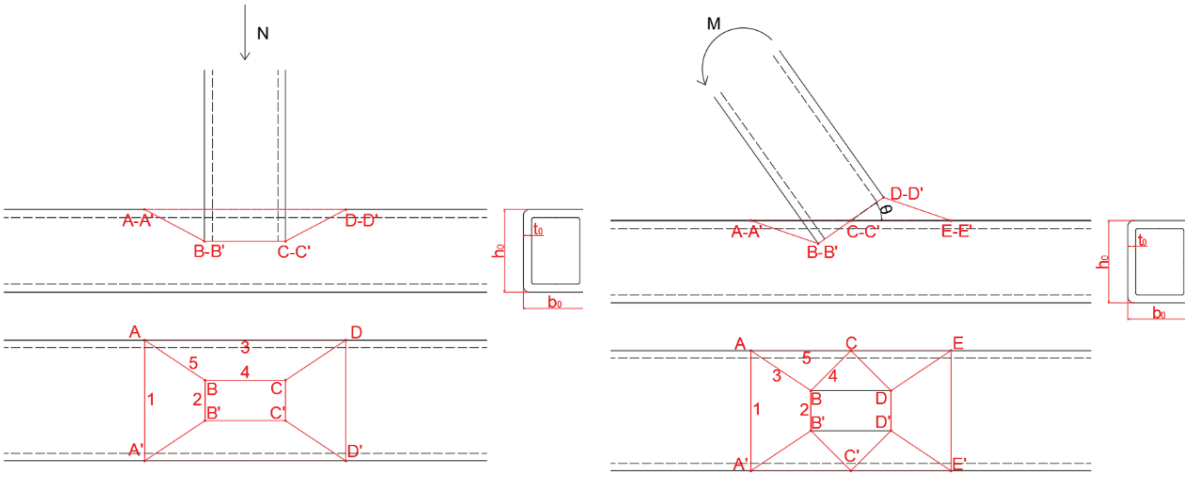

(a) (b)

Figure 5.1. Yield line mechanism proposed by Wardenier (1982) for welded RHS joints: (a) under axial compression load, and (b) under bending moment

Likewise, a similar methodology was followed in (Wardenier 1982) to derive a design expression to estimate the bending resistance of welded joints between RHS members. From the yield line mechanism shown in Figure 5.1(b), and adapting the PVW to welded joints under bending moment and joint rotations (θ) as per in Eq. 5.4, Wardenier (1982) proposed the formulation shown in Eq. 5.5 to estimate the bending resistance (M_{Rk}) of welded joints between RHS members. This formulation is also included in the CIDECT recommendations (Packer et al. (2009)) and was subsequently included in EN 1993-1-8 (2005), prEN 1993-1-8 (2020) and ANSI/AISC 360 (2010).

$$M \cdot \theta = M \cdot (2\delta/h_1) = \sum_i m_{pl} \cdot l_i \quad \text{Eq. 5.4}$$

$$M_{Rk} = f_y h_1 {t_0}^2 \left(\frac{1}{2\eta} + \frac{2}{\sqrt{1-\beta}} + \frac{\eta}{1-\beta}\right) k_n \quad \text{Eq. 5.5}$$

Note that since Eq. 5.5 is based on the principle of the virtual works, M_{Rk} only represents an upper bound of the joint resistance, because other yield line patterns (i.e., failure mechanisms) could provide lower bending capacities for certain joint geometries.

As demonstrated in Section 4, carbon and stainless steel frames failed describing global plastic failure mechanisms, redistributing internal forces before reaching their critical temperature. This means that if a real structure was assessed joints would have to provide enough resistance and redistribution capacity to form the plastic mechanisms. In terms of numerical modelling, and according to prEN 1993-1-8 (2020), joints classified as full-strength can be modelled as perfectly rigid joints. This simplification, which is commonly used at room temperature, has yet to be proven to be appropriate also at elevated temperatures. Therefore, having design expressions that accurately predict the ultimate resistance of the joints is fundamental for efficient designs. This becomes even more important as the chord thickness (t_0) – i.e., the column thickness – is the geometric parameter that has the maximum impact on the bending resistance of the joint (see the t_0^2 term in Eq. 5.5). However, increasing this parameter in order to design full-strength joints and obtain the full benefit of Class 1 cross-sections (i.e., plastic redistribution capacity) will heavily increase the overall cost of the structure.

While carbon steel structures are commonly designed with open sections (such as angle sections, channel sections, T- and I-sections), stainless steel structural elements are commonly designed using RHS sections due to the excellent strength-to-weight ratios exhibited by these product types (Gardner 2019), while frames subjected to bending forces usually present b_1/b_0 ratios lower than 0.85, leading to chord face failure mechanisms.

Some preliminary finite element (FE) models carried out on joints between RHS members showed that the equation for estimating their resistance (i.e., Eq. 5.5) prescribed in prEN 1993-1-8 (2020) and in

ANSI/AISC 360 (2010) was not accurate enough for common geometries that may be used in the design of one bay Class 1 frames for building construction, which is further evidenced in this section. For carbon steel frames, the current resistance predictions for welded joints were found to underestimate the actual joint capacities by up to 33% of the joint bending resistance, while for stainless steel joints current estimations underestimated the joint bending resistance up to 50%.

To overcome these inaccuracies, the present study focuses on the resistance and response of welded joints between RHS members under bending forces. This study employs the developed FE models described in Section 3 to develop a parametric numerical study, which have been validated against previous laboratory tests (Feng and Young 2008, Feng et al. 2019) in Section 3.5.1. Subsequently, the obtained results are analysed and compared to the formulation prescribed in prEN 1993-1-8 (2020) and ANSI/AISC 360 (2010), while a new formulation based on an alternative yield line mechanism that also involves some parameters that the current formulation dismisses (i.e., the external radius of the chord and the throat thickness of the weld). This new formulation is presented and assessed afterwards for carbon steel, and is later assessed and adapted to austenitic stainless steel. The statistical validation of the new proposal is also presented.

5.2. Parametric analysis

5.2.1. Specific information of the FE models

Due to the complexity of the reproduced phenomenon (chord face failure), all joint elements (chords, braces and welds) were modelled by means of the solid element C3D10 available in the Abaqus (2020) library, which was selected in order to exactly reproduce the actual geometry of the welded connections. Nevertheless, shell elements have also been known to correctly reproduce the response of this type of joints (Feng et al. 2020). The chord and brace lengths depended on the studied case, because both lengths were optimized in order to reduce the computational cost while ensuring a sufficient length in order to avoid local effects produced by the applied loads or the boundary conditions. Boundary conditions were modelled by means of a set of reference points (RP) that constrained the degrees of freedom of the associated surfaces, which are shown in Figure 5.2.

Failure mechanisms based on plastic lines are known to exhibit very high mesh sensitivity (Feng et al. 2019). Since the resistance of a plastic line (m_{pl}) corresponds to the plastic bending moment of section cut with a depth equal to t_0, the mesh needs to be fine enough to reproduce this phenomenon correctly. If the mesh is too coarse, the internal forces required to form a plastic line will differ from m_{pl} and therefore the obtained joint resistance will not match the actual resistance. With this in mind, an exhaustive mesh sensitivity study was carried out. Figure 5.3 presents the mesh sensitivity analysis for

one of the modelled joints and different mesh sizes (8 mm, 6 mm, 4 mm, 3.5 mm, 3 mm, 2.5 mm, 2 mm and 1.8 mm).

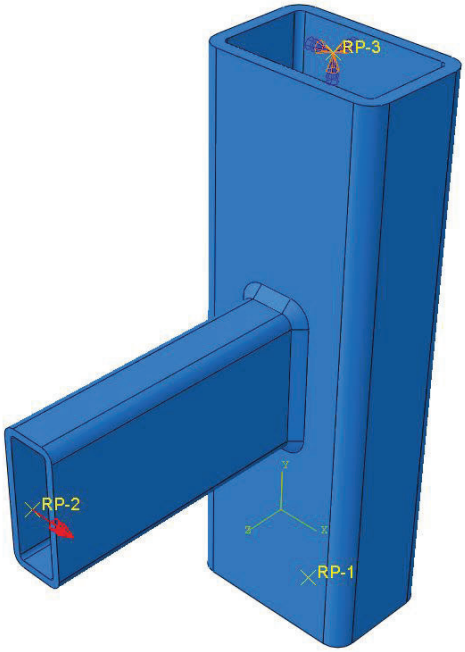

Figure 5.2. General layout of the developed FE model, with boundary conditions and loading features

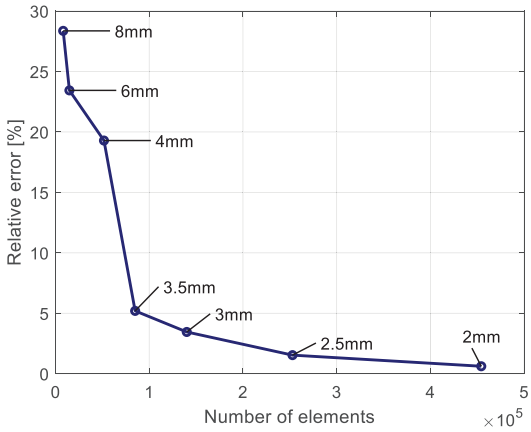

Figure 5.3. Mesh sensitivity study to establish the FE analysis framework

As it can be seen in Figure 5.3, the first mesh fine enough to reproduce the response of the analysed joint with a relative error below 5%, compared to the model with the finest mesh, is the model with a mesh size of 3 mm (which included 140,052 elements). Therefore, all the joints analysed in this study were modelled with element sizes ranging between 3 mm and 3.5 mm.

5.2.2. Investigated parameters

The validated FE model was used to reproduce welded joints between RHS members subjected to bending systematically for a wide range of member cross-section geometries. Note that the present study focuses on the resistance of RHS welded joints showing chord face failure modes in bending. A

total of 444 advanced FE models of RHS joints were analysed under pure bending conditions (243 corresponded to carbon steel joints, while 201 featured stainless steel alloys), and the main parameters investigated in this study are defined in Figure 5.4. The parametric study was divided in three groups, with the first group being focused on assessing the influence of the main geometric parameters such as the width of the chord (b_0), the thickness of the chord (t_0) and the height of the brace (h_1) on the bending resistance. A summary of the joint parameter ranges analysed is given in Table 5.1. This first group of FE models was comprised of a total of 185 analyses, where the remaining geometric parameters were fixed: the brace width was set as b_1=60 mm, the brace thickness as t_1=8 mm, the chord height as h_0=130 mm, the external radius of the brace equal to R_1=12 mm and the external radius of the chord as R_0=21 mm. The throat thickness of the welds was a=8 mm, equal to the brace thickness (t_1) as recommended in Hollow Sections in Structural Applications (Wardenier 2001).

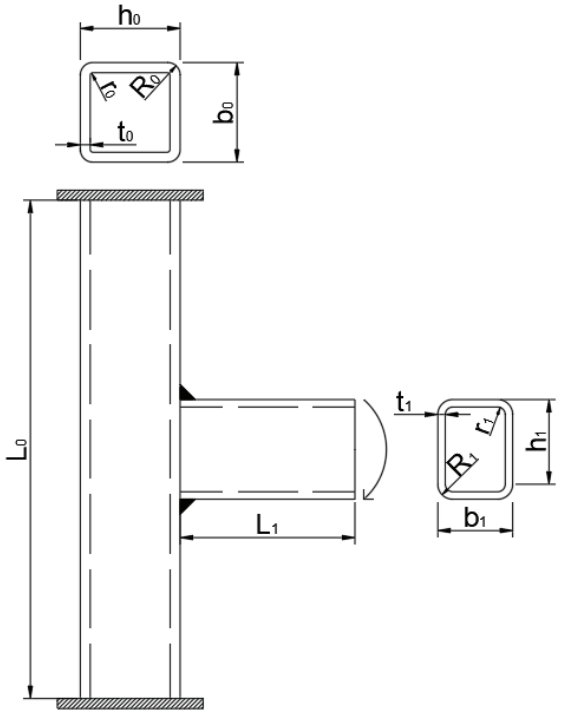

Figure 5.4. Definition of the main geometric parameters investigated in the parametric study.

Table 5.1. Summary of the joint parameter ranges analysed in the first group of analyses of the parametric study.

t_0 [mm]	b_0 [mm]	h_1 [mm]
6.3	130	80, 90, 100, 110, 120, 130, 140, 150, 160, 170, 180, 190, 200, 210, 220
8	110, 130, 150, 175, 200	80, 90, 100, 110, 120, 130, 140, 150, 160, 170, 180, 190, 200, 210, 220
10	130	80, 90, 100, 110, 120, 130, 140, 150, 160, 170, 180, 190, 200, 210, 220
12.5	130	80, 90, 100, 110, 120, 130, 140, 150, 160, 170, 180, 190, 200, 210, 220
14	120, 130, 150, 175, 200	80, 90, 100, 110, 120, 130, 140, 150, 160, 170, 180, 190, 200, 210, 220

The second part of the parametric study focused on assessing the influence of the geometric parameters that the current formulation (Eq. 5.5) does not include and whether their influence should be explicitly considered when proposing a potential new formulation. A total of 58 advanced FE models were studied, where the influence of the external radius of the chord (R_0) was assessed along with the effect of the throat thickness (a) of the weld. The results of this second part of the parametric study will be presented in Section 5.3, but their particular influence on the joint response will be discussed in Section 5.4 along with the introduction of the new formulation. The third and last part of the parametric study was devoted to stainless steel joints, and was focused on one of the most commonly used austenitic stainless steel grades, EN 1.4301 (prEN 1993-1-4 (2021)). A total of 201 of the 243 joints analysed for carbon steel were re-analysed using the EN 1.4301 austenitic grade as material in order to calibrate the new formulation for stainless steel alloys also. A summary of the main material parameters used in the parametric study for carbon and stainless steel alloys is presented in Table 5.2.

Table 5.2. Main material parameters adopted in the parametric study.

Grade	E [GPa]	f_y or $f_{0.2}$ [MPa]	f_u [MPa]
S275	210	275	280
EN 1.4301	200	280	580

All the analysed cross-sections were classified as Class 1 (i.e., plastic sections) according to prEN 1993-1-1 (2019) and prEN 1993-1-4 (2021), so that joint failure did not occur due to local buckling neither at the chord nor at the brace. Due to the large variability of geometries between the chord and the braces, some of the analysed welded joints were designed with bending resistances higher than the corresponding plastic bending moment capacities of the braces, meaning that in a FE analysis the maximum resisted bending moment would have been the plastic moment capacity of the brace. In order to avoid this, and since this study focuses on the resistance of the chord face, when this response was expected the brace was modelled as a perfectly elastic beam; this allowed the braces to deform elastically and at the same time the FE analyses to reach the bending moment resistance of the joint. The FE models of the parametric study were solved by means of the Newton-Raphson method with load increments.

5.3. Behaviour of welded RHS joints in bending

5.3.1. General joint response

As it has already been introduced in Section 5.1, the objective of this study is to investigate the bending resistance of welded joints between RHS members exhibiting chord face failure modes, thus all the analysed joints met the geometric criterion of $\beta \leq 0.85$. Based on the results obtained from the parametric study, the typical failure of these joints started with some local yielding near the two brace flanges, which was then extended until the final yield line mechanism was fully developed and the joints failed.

Figure 5.5 shows the in-plane stresses (horizontal and vertical) of the chord face just before failure for a typical welded joint, where the areas in grey and black indicate the yielded zones.

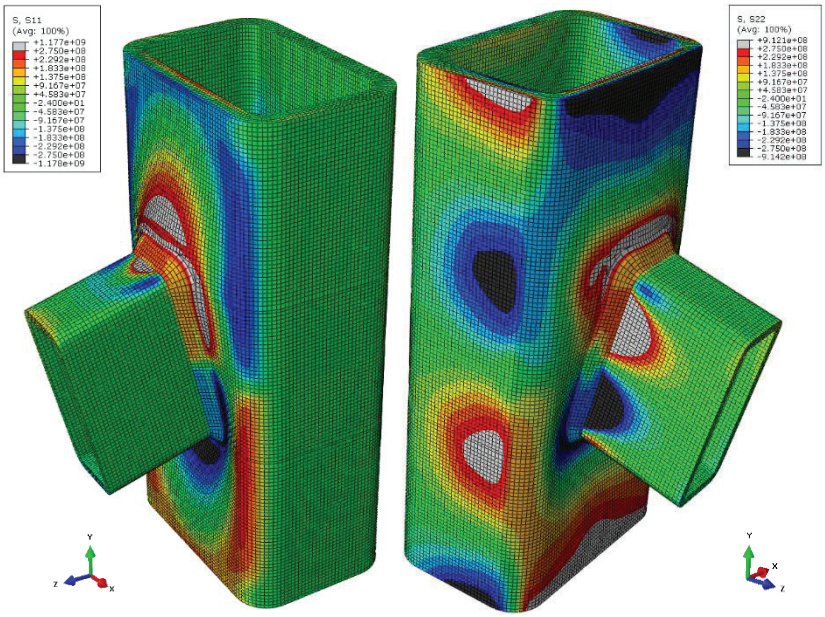

Figure 5.5. Representation of the horizontal S11 (over X axis) and vertical S22 (over Y axis) stresses for a typical welded joint between RHS members under bending moment.

The moment–rotation diagram of welded joints that failed exhibiting a chord face failure is characterized by describing, as mentioned before, a continuously increasing curve without a clear peak load. This can be confirmed with Figure 5.6, where the bending moment is plotted against the joint rotation for several analysed joints. The joint rotation was calculated as the difference between the out-of-plane displacement of the mid points in lines B-B' and D-D' shown in Figure 5.1(b) divided by the distance between them. Note that in order to specify a certain specimen, all the analysed joints have been identified with an ID according to the following criterion: $b_0 \times h_0 \times t_0$-$b_1 \times h_1 \times t_1$. In those cases in which the external radius (R_0) or the throat thickness (a) of the weld is different to that specified in Section 3, a third part is added: -RX or -WX, where X is the value of external radius of the chord, identified with R, or the value of the throat thickness of the weld, specified after W.

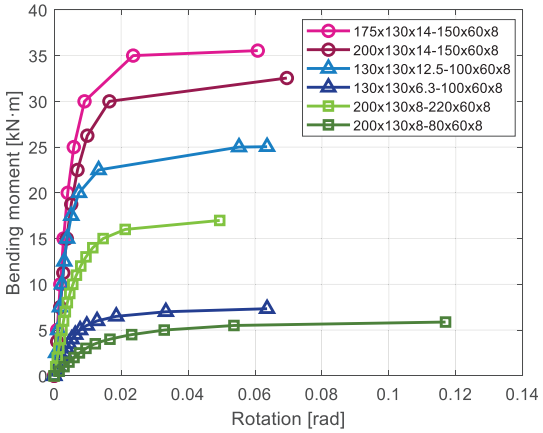

Figure 5.6. Moment–rotation diagrams for several RHS joints under bending moment.

Some conclusions can be extracted from the curves shown in Figure 5.6: joints with wider chords exhibit lower flexural resistances, whereas connections with thicker chords provide higher bending moment resistances, and increasing the lever arm also results in an increase of the joint resistance. All these phenomena are correctly reproduced by the formulation prescribed in current and upcoming European codes (EN 1993-1-8 (2005) and prEN 1993-1-8 (2020)) and ANSI/AISC 360 (2010), given in Eq. 5.5. Each of the numerical moment–rotation curves plotted in Figure 5.6 was ended at a certain maximum value of joint rotation (θ_{max}).

Regarding the definition of the ultimate loads in welded RHS joints, it should be noted that chord side wall failure is generally characterized by load–displacement curves with explicit peaks, which can be assumed to be the joint resistance as long as this peak load is reached for a displacement value smaller than 3% of the brace width (b_0), referred to as $U_{3\%}$, according to Zhao (2000). When the peak load corresponds to a higher displacement, the resistance of the joint shall be assumed as the load corresponding to a displacement equal to 3% of b_0 (Zhao 2000), and is referred to as $N_{3\%}$. Conversely, the chord face plastic failure does not result in a clear peak on the load–displacement curve, and for this reason Lu et al. (1994) defined an objective failure criterion for RHS tubular T-joints. The failure load was defined as the axial load corresponding to a chord face indentation equal to 3% of b_0, as per chord side wall failure modes. This failure load definition is included in the CIDECT recommendations (Packer et al. (2001)) for Ultimate Limit States (ULS). Nevertheless, it should be pointed out that recent studies carried out by Kožich et al. (2022) suggest that using a failure criterion based on maximum principal strains might predict the resistance of welded joints between RHS members more appropriately.

Under bending moment, the maximum rotation has been defined as the rotation equivalent to an out-of-plane displacement of the mid points in B-B' and D-D' represented in Figure 5.1(b) equal to 3% of b_0, divided by the distance between them. Therefore, the maximum rotation (θ_{max}) depends on the joint geometry. Larger rotations are allowed for wider chords and braces with shorter height, whereas for narrower chords and braces with larger height the maximum rotation is smaller, as it can be seen in Figure 5.6. Based on this, the bending moment resistance of the joint according to the FE models (M_{FE}) was defined as the bending moment corresponding to the maximum rotation (θ_{max}) for each analysed joint.

5.3.2. Comparison with code predictions

Current and upcoming European and US (EN 1993-1-8 (2005), prEN 1993-1-8 (2020) and ANSI/AISC 360 (2010)) codes provide formulations for estimating the resistance of welded joints between hollow section members under different loading cases and for multiple geometric configurations. Since this study focuses on RHS welded T-joints under pure bending moment, the

resistance estimated by the prEN 1993-1-8 (2020) and ANSI/AISC 360 (2010) provisions is given by Eq. 5.5. Based on this equation, and using the numerical results obtained for the failure condition just presented in Section 5.3.1 in terms of maximum rotation, a comparison between the theoretical bending resistances and the FE-predicted results is shown in Figure 5.7 for different ranges of the β=b_1/b_0 parameter.

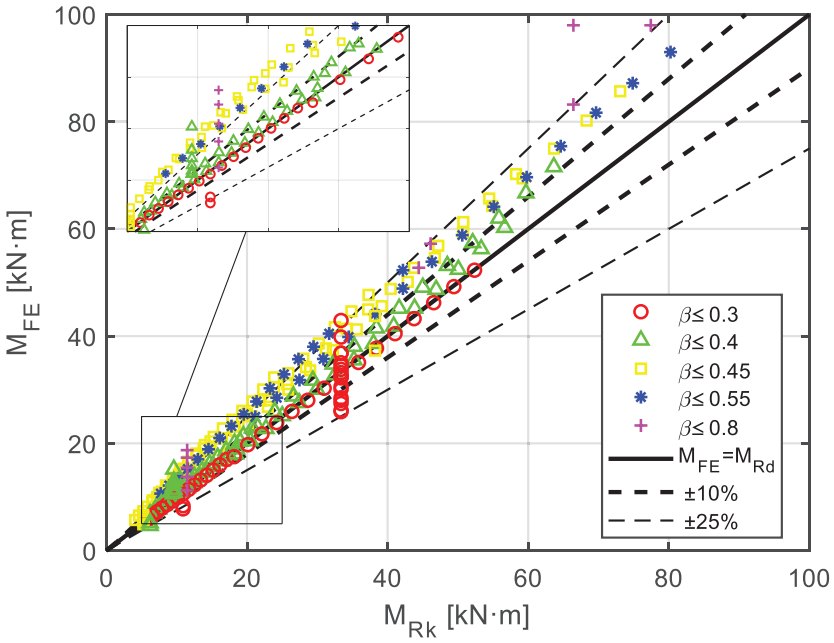

Figure 5.7. Comparison between the bending resistance of the analysed joints (M_{FE}) and the estimation of the resistance (M_{Rk}) with the current formulation (Eq. 5.5).

From Figure 5.7 it can be seen that the current formulation prescribed in prEN 1993-1-8 (2020) and ANSI/AISC 360 (2010) (i.e., Eq. 5.5) provides a conservative estimation of the joint resistance since the numerical resistances are typically equal or higher than the predicted strengths on most of the studied cases. Moreover, this comparison also shows that the numerically obtained bending moment resistances differ more from the analytically estimated values as the β-values increase, even surpassing the +10% and +25% intervals, as shown in Figure 5.7. This could mean that the assumed yield line mechanism (see Figure 5.1(b)) may correspond to the mechanism with the lowest associated energy for the welds with lower values of β, but that for higher β-values (always below β≤0.85) failure may occur with a different yield line mechanism.

On top of that, Figure 5.7 also shows a few sets of numerical results that are displayed describing a vertical straight line: these results correspond to the second part of the parametric study, where the influence of the geometric parameters that the current formulation dismisses (i.e., the chord external radius (R_0) and the throat thickness (a) of the weld) was assessed. Each of these data sets describing a straight line correspond to a certain overall joint geometry, where only one of these geometric parameters was modified. Although the numerical resistance of the joint (M_{FE}) is

noticeably affected by the value of these parameters (R_0 and a), this influence is not taken into account by the current formulation (Eq. 5.5) and hence the same analytical resistance (M_{Rk}) is predicted for the different cases in each set. Therefore, another possible reason behind the overly conservative estimations observed for the prEN 1993-1-8 (2020) and ANSI/AISC360 (2010) formulation may be that it neglects the effect of the external chord radius (R_0) and considers the width of the yield line mechanism equal to the chord width (b_0). Disregarding the fact that the actual free width available at the chord faces to develop the yield line mechanism is at most the flat length between the ends of the external radii of the chords, and that the yield lines A-C-E depicted in Figure 5.1(b) do not form at the edges of the chord widths but at the edges of the external radius of the chord. This hypothesis can be supported thanks to Figure 5.5, where the stresses corresponding to the yield lines A-C-E are over the edges of the chord radius instead of at the flat chord width face regions. It is true that the current formulation was developed to be used for truss structures, where this simplification can be reasonable due to the size of the typical elements conforming such truss structures, but neglecting the influence of these parameters in larger cross-sections similar to those considered in this study may lead to overconservative estimations of the joint resistance. It should be highlighted that the range of β-values analysed in this study is between 0.30 and 0.75, even though the chord face failure is known to be the predominant failure mode for β-values up to 0.85 according to prEN 1993-1-8 (2020). The main reason for this shorter range of β values is that, when the chord radius and the weld are explicitly incorporated in the FE model, there is not enough space to fit chord and brace width combinations resulting in higher values of β for the analysed joints.

The assessment of the accuracy of the formulation included in prEN 1993-1-8 (2020) and ANSI/AISC 360 (2010) for all the analysed carbon joints is presented in Table 5.3, where the mean value and COV of the M_{FE}/M_{EN} ratios are reported for two different ranges of β-values (with M_{EN} being the strength predicted by Eq. 5.5). The results of the entire dataset are also presented. As it can be seen from these ratios, the current formulation shows a good agreement with the carbon steel FE results for the lower values of β (i.e., β<0.45) with 88% of them accomplishing the criterion of $M_{FE}/M_{EN}\in$[0.90,1.15], and showing a mean M_{FE}/M_{EN} ratio of 1.03 with a low scatter, whereas for higher values of β the current formulation is found to underestimate the actual resistance of the joints as a mean M_{FE}/M_{EN} ratio of 1.27 is obtained, with only 3% of the joints meeting the criterion of $M_{FE}/M_{EN}\in$[0.90,1.15]. Considering these results, and that the explicit consideration of the external radius of the chord in the FE models may be causing yield line pattern mechanisms different from that assumed when developing the formulation proposed in (Wardenier 1986) for the high range of β-values, these joints are further investigated in Section 5.4.

Table 5.3 Assessment of the accuracy of the current formulation (Eq. 5.5) and the new yield line mechanism (Eq. 5.7) to predict the resistance of RHS joints under bending moment.

Material	Range of $\beta=b_1/b_0$	n	M_{FE}/M_{EN} (Eq. 5.5)*			M_{FE}/M_{NEW} (Eq. 5.7)†		
			Mean	∈[0.90,1.15]	COV	Mean	∈[0.90,1.15]	COV
S275	β<0.45	122	1.03	88%	0.10	1.13	50%	0.10
	β>0.45	121	1.27	3%	0.09	1.06	82%	0.09
	Total	243	1.15	46%	0.14	1.09	66%	0.10
EN 1.4301	β<0.45	97	1.23	28%	0.11	1.12	92%	0.03
	β>0.45	94	1.62	1%	0.05	1.09	94%	0.06
	Total	201	1.42	15%	0.16	1.10	93%	0.05

*For austenitic stainless steel EN 1.4301, f_y was substituted by $f_{0.2}$ as recommended in prEN 1993-1-4 (2021)

†For austenitic stainless steel EN 1.4301, f_y was substituted by f_{csm} (Eq. 2.46) as explained in Section 2.5.2.

Table 5.4 Assessment of the accuracy of the new approach (Eq. 5.7-Eq. 5.9) to predict the resistance of RHS joints under bending moment.

Material	Range of $\beta=b_1/b_0$	n	M_{FE}/M_{PR} (Eq. 5.7-Eq. 5.8)†			M_{FE}/M_{PR^*} (Eq. 5.7-Eq. 5.9)†		
			Mean	∈[0.90,1.15]	COV	Mean	∈[0.90,1.15]	COV
S275	β<0.45	122	1.06	72%	0.10	1.09	80%	0.06
	β>0.45	121	1.06	82%	0.09	1.09	74%	0.08
	Total	243	1.06	77%	0.10	1.09	77%	0.07
EN 1.4301	β<0.45	97	1.06	97%	0.05	1.06	97%	0.06
	β>0.45	94	1.09	94%	0.06	1.12	88%	0.07
	Total	201	1.07	95%	0.06	1.09	93%	0.07

†For austenitic stainless steel EN 1.4301, f_y was substituted by f_{csm} (Eq. 2.46) as explained in Section 2.5.2.

5.4. New failure mode and design proposal

As it has been highlighted in the previous section, the current formulation for welded RHS joints in bending codified in prEN 1993-1-8 (2020) and ANSI/AISC 360 (2010) provides overconservative estimations of the joint strength for certain geometries. Hence, alternative failure modes resulting from multiple yield line mechanisms were defined and assessed, and the associated bending moment resistances were calculated. Hereunder the mechanism best fitting the numerical results is developed, presented and assessed in the following sub-sections.

5.4.1. Proposal of a new yield line pattern

After an exhaustive study of the chord face failure of welded joints between RHS members under bending moment, the results indicated that the plane defined by the points B-C-D shown in Figure 5.1(b) does not fully develop for certain joint geometries (i.e., high values of β) because the distance between the line A-C-E and the line B-D is insufficient to form a plane, even less if the chord radius is explicitly

considered. In addition, the yield line defined by points A-A' does not necessarily have to be equal to the chord width b_0 according to the FE models investigated. Considering this, a new yield line mechanism compatible with the yielding pattern observed in the FE models is proposed. The geometry of the proposed yield line mechanism is shown in Figure 5.8, while Figure 5.9 shows a typical displacement field of the analysed joints compared to the proposed yield line mechanism.

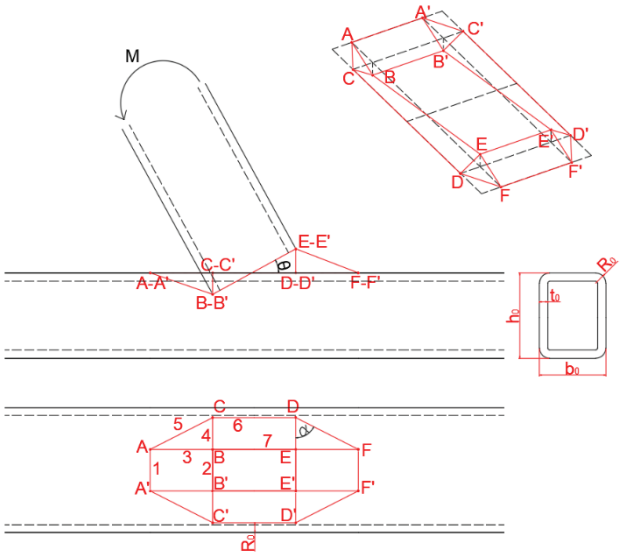

Figure 5.8. Proposed yield line mechanism for RHS joints under bending moment.

Note that in this new mechanism, points B-C-D-E do not form a plane but a ruled surface. As it is clearly shown in Figure 5.9, due to the small distance between the lines B-C and D-E, it is not possible to form a plane, but a ruled surface accurately matches the deformation patterns obtained. Furthermore, it can be also seen from Figure 5.9 that the yield line A-A' has a length shorter than the chord width, and that the yield line C-D is over the end of the external radius of the chord.

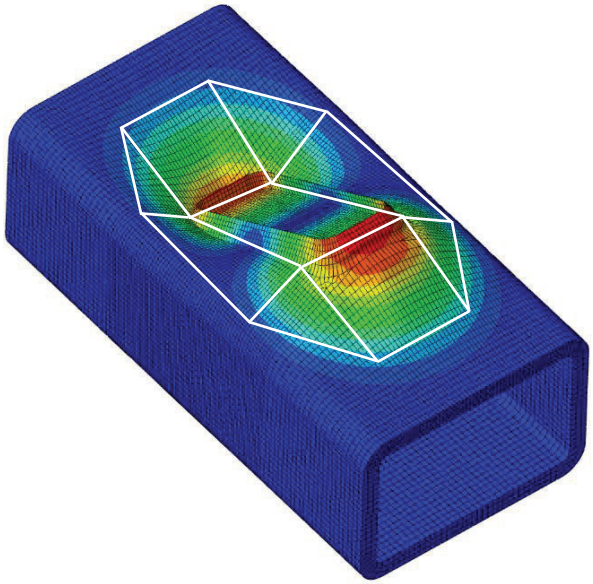

Figure 5.9. Typical displacement field of the analysed joints compared to the proposed yield line mechanism (displacements augmented x2).

From the yield line mechanism geometry presented in Figure 5.8 and Figure 5.9, and based on the principle of virtual works given in Eq. 5.4, the following equation can be obtained (see Annex A).

$$M = f_y \frac{h_1}{2} {t_0}^2 \left[\frac{(b_0 - 2R_0)}{2h_1} + \frac{b_1}{2h_1} + \frac{h_1}{(b_0 - 2R_0) - b_1} + \frac{2b_1}{(b_0 - 2R_0) - b_1} \cot(\alpha) + 2\tan(\alpha) + 2\cot(\alpha) \right] \quad \text{Eq. 5.6}$$

In this equation, α is the in-plane angle between the yield lines D-F and D-E, as shown in Figure 5.8, and has to be calculated in order to obtain the lowest bending moment that triggers that yield line mechanism. Therefore, solving the optimisation problem $dM/d\alpha$=0 and obtaining the solution $\tan(\alpha_0)=1/\sqrt{(1-\beta)}$, Eq. 5.6 can be re-written in terms of the main geometric variables β and η used in current standards as per in Eq. 5.7.

$$M_{Rk} = f_y h_1 {t_0}^2 \left(\frac{1+\beta^*}{4\eta^*} + \frac{2}{\sqrt{1-\beta^*}} + \frac{\eta^*}{2(1-\beta^*)} \right) k_n \quad \text{Eq. 5.7}$$

In this equation, the k_n factor that takes into consideration the previous stress state of the chord face is retained, as in the current formulation (Eq. 5.5). However, it should be noted that all the joints analysed in this study did not have any previous stresses, with the k_n factor adopting a value of 1.0, and hence its accuracy has not been assessed in this study. Moreover, Eq. 5.7 is presented as a function of the adapted geometric variables β^* and η^*, because the width of the presented yield line mechanism (see Figure 5.8) corresponds to the effective flat chord length, limited by the chord radius (R_0) and not by the total width of the chord (b_0), as Figure 5.9 highlights. For this reason, the new formulation (Eq. 5.7) is presented in terms of the geometric parameters $\beta^*=b_1/b_0^*$ and $\eta^*=h_1/b_0^*$, calculated using the effective length $b_0^*=b_0-2R_0$, in order to differentiate them from the current geometric parameters β and η based on the total chord width b_0.

Using the new proposed formulation (i.e., Eq. 5.7), the bending resistance of carbon steel joints can be estimated. The main statistical indicators of the accuracy of the new formulation are presented in Table 5.3, where the mean values and the COVs of the M_{FE}/M_{NEW} ratios are reported. Likewise, the accuracy of the bending moment resistance estimation using the new formulation (Eq. 5.7) can be compared to the accuracy of the current formulation (Eq. 5.5) for the two different ranges of β-values investigated. As it can be seen in Table 5.3, the new formulation shows a better agreement with the FE results than the current formulation included in prEN 1993-1-8 (2020) and ANSI/AISC 360 (2010) for higher values of β (i.e., β>0.45), where 82% of the carbon steel joints meet the $M_{FE}/M_{NEW}\in$[0.90,1.15] criterion and a mean M_{FE}/M_{NEW} ratio of 1.06 is obtained, with a COV of 0.09. Nevertheless, for lower β-values (i.e., β<0.45) the current formulation (Eq. 5.5) shows a better agreement with the FE results. In line with the

initial hypothesis, a yield line mechanism different from the one defined by Wardenier (1986) may develop depending on the geometric parameter β.

5.4.2. Adaptation of the effective length parameter

As it has been presented in Section 5.4.1, the new formulation (Eq. 5.7) was developed in order to fill the gap that the current formulation leaves for joint geometries exhibiting high values of β. As demonstrated above, the resistance estimation for joints with low values of β is negatively affected by the new formulation, where only 50% of the estimations for carbon steel joints fulfil the criterion $M_{FE}/M_{Rk} \in [0.90,1.15]$, whereas with the original formulation (Eq. 5.5) 88% of the results met that criterion, as Table 5.3 highlights. In order to solve this problem, an adaptation of the b_0^* parameter is carried out so that the proposed new formulation can be used with improved accuracy also for joint geometries with smaller β values. Considering that the goal of this adaptation is to diminish the weight the β^* parameter has on Eq. 5.7, but only for lower values of β^*, a logarithmic scale is applied on the effective length (b_0^*) once a certain threshold of the geometric parameter β^* is surpassed, as Eq. 5.8 shows.

$$b_0^* = \begin{cases} b_0 - 2R_0 & for\ b_0 - 2R_0 \leq 2b_1 \\ 2b_1 \cdot \left[1 + \log_{10}\left(\frac{b_0 - 2R_0}{2b_1}\right)\right] & for\ b_0 - 2R_0 > 2b_1 \end{cases} \quad \text{Eq. 5.8}$$

The effective length parameter can be physically understood as follows: the wider the chord is, the lower the bending resistance of the joint becomes. However, the influence of the chord width on the joint resistance starts to diminish once the ratio $b_1/(b_0\text{-}2R_0)$ becomes larger, or the β^*-value is below 0.5. The threshold and the base of the logarithmic scale were calibrated using the numerical results obtained in the parametric study. Note also that due to the new way of calculating the geometric parameter β^* there are some joint geometries that can lead to β^*-values over $\beta^*>0.85$ and close to $\beta^*\approx1$, and thus, in order to avoid discontinuities in Eq. 5.7, the new parameter β^* should have an upper limit of $\beta^*=0.9$.

Figure 5.10 shows the bending resistance obtained by means of numerical models for the same joint geometry for different values of the chord width (b_0), along with the estimations of the bending resistance obtained with the current formulation (Eq. 5.5) and the new yield line pattern (Eq. 5.7) in conjunction with the adapted definition of the effective length (b_0^*) proposed herein (Eq. 5.8). The bending moment resistances are plotted according to the $\beta=b_1/b_0$ value. Figure 5.10 shows that the new formulation provides a better estimation of the joint resistance than the current formulation for higher values of β, as expected. Nevertheless, it can be also seen how the proposed formulation (Eq. 5.7-Eq. 5.8) can be used with relatively good results for joint geometries with low values of β as well.

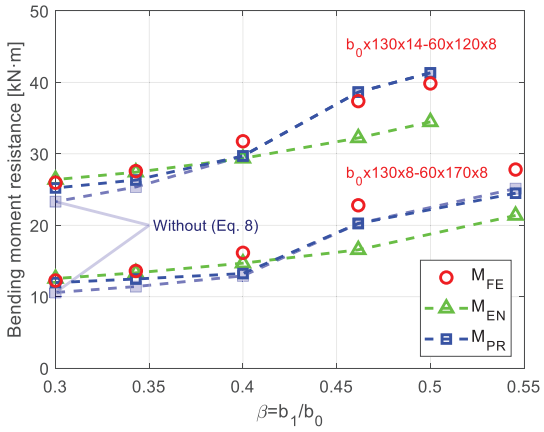

Figure 5.10. Influence of the chord width (b_0) on the bending resistance of joints and corresponding resistance estimations according to current formulation M_{EN} (Eq. 5.5) and the new proposal M_{PR} (Eq. 5.7-Eq. 5.8).

Therefore, the new formulation proposal (Eq. 5.7-Eq. 5.8) was used to estimate the bending resistance (M_{PR}) of the entire set of carbon steel joints, the basic statistical parameters of which are presented in Table 5.4. As it can be seen from these results, the resistance estimations for lower β-values have been improved with the revised definition of the effective length parameter (b_0^*) according to the new M_{FE}/M_{PR} ratio, compared to the previous M_{FE}/M_{NEW} ratio, where 72% of the estimations accomplish the criterion $M_{FE}/M_{PR}\in[0.90,1.15]$ for lower β-values, and resulted in a mean value of 1.06 and a COV value of 0.10 for all the studied joints.

5.4.3. Influence of the chord radius and the weld thickness

One of the goals when developing the new formulation for estimating the bending resistance of welded joints between RHS members was to incorporate the effect of the geometric parameters that the current formulation dismisses and that have been found to influence the joint resistance. As discussed before, the current formulation prescribed in prEN 1993-1-8 (2020) and ANSI/AISC 360 (2010) neglects the effect of the chord radius and the weld thickness in order to facilitate its use and because it was meant to be used for truss structures, in which the influence of these parameters may be dismissed due to their size. But thanks to the second part of the parametric study carried out – focused on assessing the influence of the external radius of the chord (R_0) and the thickness of the weld –, it can be seen the importance of including these parameters in the formulation predicting the joint resistance in frames designed for building construction, as highlighted by Figure 5.7.

Figure 5.11 shows the variation of the joint resistance depending on the chord radius size (R_0) for two different joint geometries. As it can be seen, the numerical results show a great dependency on this parameter, but its influence is not considered in the current formulation (see Eq. 5.5). On the contrary, the proposed formulation (Eq. 5.7-Eq. 5.8) is capable of reproducing this effect even for low β-values, as Figure 5.11 shows for β=0.3 and β=0.4.

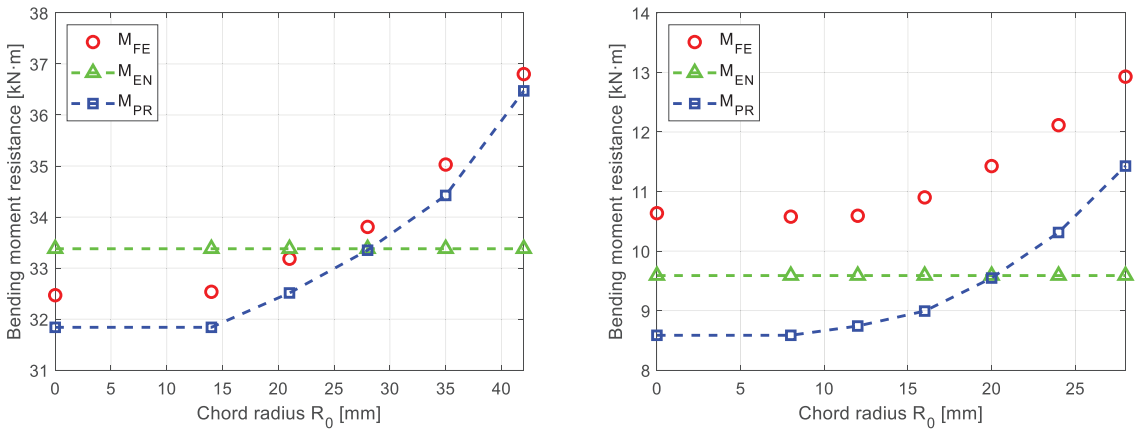

Figure 5.11. Influence of the chord radius (R_0) on the bending resistance of joints and corresponding resistance estimations according to current formulation M_{EN} (Eq. 5.5) and the new proposal M_{PR} (Eq. 5.7-Eq. 5.8) for two study cases: (a) 200x130x14_60x150x8_R and (b) 150x130x8_60x120x8_R.

Likewise, multiple joints in which only the weld thickness was modified were analysed in the parametric study. Figure 5.12(a) shows the variation of the bending resistance of the joints as the weld thickness increases according to the FE models, which show a linear dependency on the weld thickness. According to these results, the new proposed formulation given by Eq. 5.7-Eq. 5.8 seems to overestimate the joint resistance for lower values of the weld thickness (a), whereas for larger welds the proposed formulation is rather conservative.

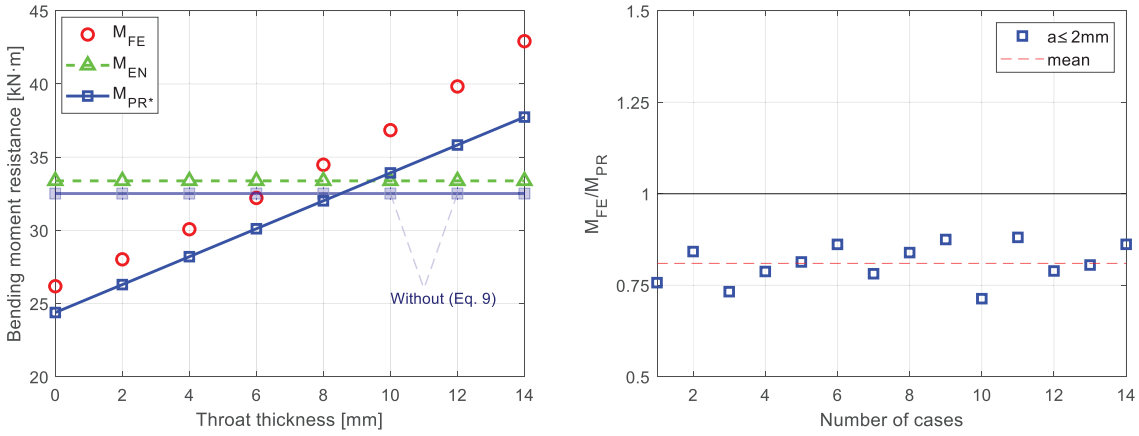

Figure 5.12. Influence of the weld thickness (a) on the bending resistance of joints: (a) numerical resistance M_{FE} and resistance estimations according to the current formulation M_{EN} (Eq. 5.5) and the new proposal M_{PR^*} (Eq. 5.7-Eq. 5.9); (b) M_{FE}/M_{PR} ratio for multiple RHS joints with a throat thickness value of a≤2mm.

Based on this, a linear equation (y=m·a+n) was studied as an additional term f that multiplies the whole joint resistance expression (Eq. 5.7-Eq. 5.8) in order to properly reproduce the influence of the weld thickness (a) also. This linear expression was adjusted as shown in Eq. 5.9.

$$f(a, b_1, b_0, t_0) = 0.75 + \frac{a}{b_1} \cdot \left(\frac{b_0}{t_0}\right)^{\frac{1}{4}} \quad \text{Eq. 5.9}$$

In this equation, the independent term n=0.75 was fitted based on multiple numerical results with null or nearly null weld thicknesses, as Figure 5.12(b) shows. On the contrary, the dependant term $(m \cdot a)$ was calibrated using a least square adjustment method and with the only condition of being a dimensionless variable. As it can be seen in Figure 5.12(a), thanks to multiplying the proposed formulation (Eq. 5.7-Eq. 5.8) by this additional term f defined in Eq. 5.9, the influence of the weld thickness on the joint resistance is correctly reproduced by the analytical estimation M_{PR^*}=$M_{PR} \cdot f(a, b_1, b_0, t_0)$. Nevertheless, it is important to highlight that the proposed formulation (Eq. 5.7-Eq. 5.8) without the additional weld term f (Eq. 5.9) has been proven to correctly estimate the bending resistance based on the results presented in Table 5.4, thus Eq. 5.9 is not necessary when standard weld thicknesses are used (i.e., $a \approx t_1$), but only when unconventional weld thicknesses are considered, in which cases the additional term presented in Eq. 5.9 takes that effect into consideration.

Figure 5.13 presents the assessment of the accuracy of the current formulation (Eq. 5.5), the new proposal (Eq. 5.7-Eq. 5.8) and the new proposal with the additional term f that takes into account the effect of the weld thickness (Eq. 5.7-Eq. 5.9) by comparing the numerical bending resistance of all the analysed carbon steel joints with the strengths predicted by these three formulations, plotted in terms of the parameter η=h_1/b_0. First of all, it can be seen that no clear pattern can be discerned when the results are plotted against the geometric parameter η, confirming that the yield lines mechanisms proposed in this study does not depend on η, but on the parameter β. In Figure 5.13(a) it can be seen how the new proposal (Eq. 5.7-Eq. 5.8) provides more accurate resistance estimations for the analysed carbon steel joints than the current formulation (Eq. 5.5), but it still does not consider the effect of the weld thickness on the joint resistance, as the results highlighted in Figure 5.13(a) evidence. This problem can be solved if the additional term presented in Eq. 5.9 is used for estimating the joint resistance, as Figure 5.13(b) shows. Nevertheless, Eq. 5.9 can be used in all case scenarios without losing much accuracy as Figure 5.13(b) highlights, as the statistical values of the M_{FE}/M_{PR^*} ratio reported in Table 5.4 demonstrate.

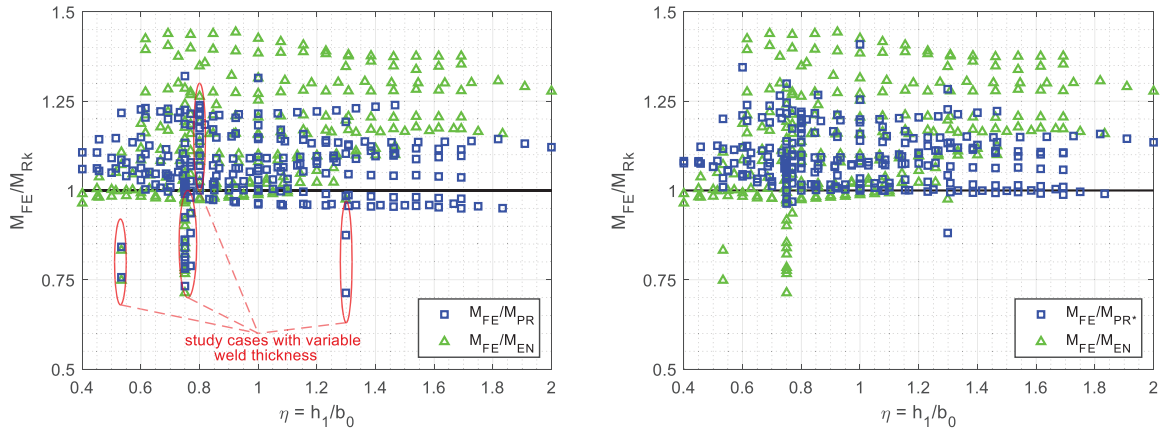

(a) (b)

Figure 5.13 Assessment of the different design approaches in terms of the parameter η for the ratios: (a) M_{FE}/M_{EN} and M_{FE}/M_{PR}; and (b) M_{FE}/M_{EN} and M_{FE}/M_{PR^*}.

5.4.4. Assessment of the new proposal for stainless steel joints

Current and upcoming standards for stainless steel (EN 1993-1-4 (2006) and prEN 1993-1-4 (2021)) do not provide specific formulations for stainless steel joints between tubular members. In fact, according to European stainless steel codes (EN 1993-1-4 (2006) and prEN 1993-1-4 (2021)) the bending resistance of a stainless steel joint between RHS members should be estimated using the formulation currently prescribed for carbon steel (i.e., Eq. 5.5) by substituting the yield stress f_y with the proof stress correspondent to a 0.2% strain ($f_{0.2}$) of stainless steel alloys. As for carbon steel joints, some preliminary studies on stainless steel joints showed that this approach provides overconservative resistance estimations, underestimating by over 50% the joint resistance for certain geometries. Since stainless steel is characterized by a nonlinear stress–strain curve and its inherent strain hardening, determining the yield stress of the material has been a topic of discussion. Even if the proof stress $f_{0.2}$ is conventionally adopted as the yield stress, the CSM formulation could be used to determine the strain limits for plastic zones and predict a design stress that also accounts for strain hardening effects. This approach has been proven to be able to correctly reproduce the local buckling (Afshan and Gardner 2013, Bock et al. 2015) and member buckling (Arrayago et al. 2020(b), Arrayago et al. 2021) of stainless steel structures, and it has been included in the prEN 1993-1-4 (2021) and ANSI/AISC 370 (2021) specifications. For the further details of how the CSM strain limit (ε_{csm}) was calculated the reader is referred to Section 2, where the Eq. 2.45 can be employed if the bilinear stress–strain relationship shown in Figure 2.2 is used, with the corresponding CSM design stress f_{csm} (Eq. 2.46).

A total of 201 EN 1.4301 austenitic stainless steel joints were analysed in order to assess the accuracy of the current formulation (Eq. 5.5), considering both the proof stress $f_{0.2}$, and the accuracy of the different proposed formulations (Eq. 5.7-Eq. 5.8, Eq. 5.7-Eq. 5.9) and using the CSM design stress (f_{csm}) corresponding to the CSM strain limit (ε_{csm}). The different M_{FE}/M_{Rk} ratios reported in the previous sections are also presented for stainless steel joints in Table 5.3 and Table 5.4, where it can be seen that the proposed formulation along with f_{csm} (i.e., combining Eq. 5.7-Eq. 5.8 and Eq. 2.45-Eq. 2.46) provides more accurate bending resistance estimations for stainless steel joints than the current formulation (Eq. 5.5) included in prEN 1993-1-8 (2020) and ANSI/AISC 360 (2010) considering the proof stress $f_{0.2}$, which presents a mean value of the M_{FE}/M_{EN} ratio equal to 1.42 and a COV value equal to 0.16, with only 15% of the estimations fulfilling the criterion of $M_{FE}/M_{EN} \in [0.90,1.15]$.

The moment–rotation curves of stainless steel joints were characterized by describing a nonlinear response with a continuously increasing curve, without the horizontal plateau that carbon steel joints exhibited in Figure 5.6. On top of that, stainless steel structures are known for describing

larger displacements before collapsing (González-de-León et al. 2022), thus applying the same failure criterion used for carbon steel welded joints, defined in terms of the maximum rotation (θ_{max}), may not be appropriate for stainless steel welded joints. Nevertheless, this topic needs further research and in order to assess the accuracy of the resistance estimations obtained with the current formulation (Eq. 5.5) and by means of the new formulation proposed (Eq. 5.7-Eq. 5.8), the same failure criterion presented in Section 5.3.1 was used to determine the numerical resistance (M_{FE}) of the analysed stainless steel joints as well. In any event, this assumption is rather conservative. A comparison between the M_{FE}/M_{EN} and M_{FE}/M_{PR} ratios for the studied stainless steel joints is presented in Figure 5.14.

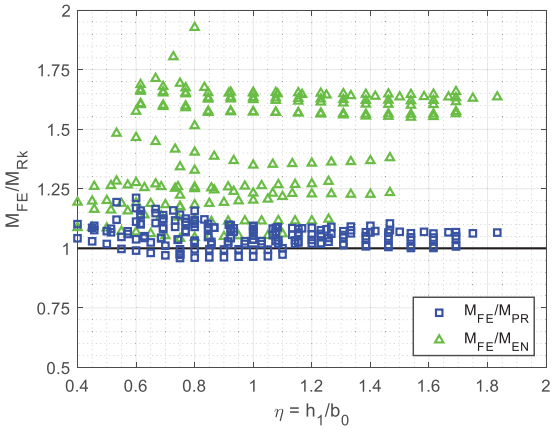

Figure 5.14. Assessment of the different design approaches in terms of the parameter η for ratios M_{FE}/M_{EN} and M_{FE}/M_{PR} for the analysed austenitic stainless steel EN 1.4301 welded joints.

As it can be seen, the current formulation provides overly conservative estimations for the analysed stainless steel joints, underestimating the numerical bending resistance of the joints by more than 50% in many cases. Alternatively, the results show that the new proposal developed (Eq. 5.7-Eq. 5.8) in conjunction with the CSM formulation (Eq. 2.45-Eq. 2.46) provides accurate estimations for the analysed stainless steel joints, as Figure 5.14 highlights and Table 5.3 and Table 5.4 confirms, with a mean value of the M_{FE}/M_{PR} ratio equal to 1.07 and a COV value of 0.06, and with 95% of the estimations lying between the values of M_{FE}/M_{PR}=0.90 and M_{FE}/M_{PR}=1.15.

5.4.5. Statistical validation of the new proposal

In this section, the determination of the partial resistance factor (γ_M) for the proposed formulation (Eq. 5.7-Eq. 5.8) is carried out based on the methodology set out in Annex D of prEN 1990 (2022). This methodology considers: (a) the scatter of the reference data, (b) the statistical uncertainty associated with the number of results available, and (c) the prior statistical knowledge of each basic variable (b_0, R_0, t_0, h_1, b_1, f_y) involved in the formulation. The statistical characterization of these basic variables is material dependant and, for this reason, the partial resistance factor (γ_M) was determined separately for the two materials analysed (i.e., carbon steel and austenitic stainless steel).

The methodology followed to calculate the partial resistance factors begins by comparing the numerical values (r_e=M_{FE}) and the theoretical values (r_t) obtained based on the presented formulation (M_{Rk}), as per in Eq. 5.10.

$$r_e = b r_t \delta \quad \text{Eq. 5.10}$$

In this equation, b is the slope of the r_e/r_t relationship, which can be estimated using Eq. 5.11, and δ is the error term with a mean value of one and a coefficient of variation of V_δ (given in Eq. 5.12). The variable $\bar{\Delta}$ is the mean value of Δ_i=ln($b\delta_i$)=ln$\left(r_{e,i}\right)$-ln$\left(r_{t,i}\right)$. Likewise, s_Δ^2 is the square of the standard deviation of the data set Δ_i.

$$b = \exp\left(\bar{\Delta} + \frac{1}{2} s_\Delta^2\right) \quad \text{Eq. 5.11}$$

$$V_\delta = \sqrt{\exp(s_\Delta^2) - 1} \quad \text{Eq. 5.12}$$

The theoretical values (r_t) depend on the variability of the cross-section geometry (b_0, R_0, t_0, h_1, b_1) and the material properties (f_y), which were considered as recommended in Annex D of prEN 1990 (2022) by means of the coefficients of variation ($V_{x,i}$) of each of the basic variables involved. These coefficients of variation were obtained from Annex E of EN 1993-1-1 (2005) for carbon steel and from previous statistical studies carried out by Arrayago et al. (2020(a)) for austenitic stainless steel. It is worth noting that the variation coefficient for the chord radius (R_0) has been assumed to be equal that recommended for the chord thickness (V_t), as the chord radius is usually defined in terms of t_0 (e.g., R_0=2·t_0). Additionally, the uncertainty derived from obtaining the reference results (r_e) by means of FE analysis were taken into consideration through the coefficient of variation V_{FE}. The values of the coefficients of variation, along with the values of b and V_δ, are presented in Table 5.5.

Table 5.5. Summary of the reliability analysis results for the two materials.

Material	b	V_δ	V_b	V_h	V_t	V_{fy}	V_{FE}	V_{rt}	V_r	Q	γ_M
S275	1.079	0.075	0.009	0.009	0.025	0.055	0.050	0.084	0.112	0.112	**1.05**
EN 1.4301	1.056	0.045	0.010	0.012	0.028	0.060	0.050	0.090	0.101	0.100	**1.06**

All the variability derived from the uncertainties associated with the basic variables and the scatter of the data was accounted for through the variation parameter V_r, obtained according to Eq. 5.13-Eq. 5.14 as recommended in Annex D of prEN 1990 (2022) for small values of $V_{x,i}$ and V_δ.

$$V_{rt}^2 = \sum V_{X_i}^2 \quad \text{Eq. 5.13}$$

$$V_r^2 = V_\delta^2 + V_{rt}^2 \quad \text{Eq. 5.14}$$

Finally, the partial resistance factor (γ_M) was calculated using Eq. 5.15-Eq. 5.16, as recommended for large number of results (n≥100).

$$Q = \sqrt{\ln(V_r^2 + 1)} \quad \text{Eq. 5.15}$$

$$\gamma_M = \frac{r_k}{b r_t \exp(-k_\infty Q - 0.5Q^2)} \quad \text{Eq. 5.16}$$

In these equations, k_∞=3.04 is the design fractile factor for n tending to infinity and the characteristic value r_k was obtained by dividing the theoretical resistance r_t by the overstrength factor (ratio between the mean and nominal yield stress) of the corresponding material, using a value of 1.25 for carbon steel and 1.22 for austenitic stainless steel, as per EN 1993-1-1 (2005) and Arrayago et al. (2020(a)). The obtained partial resistance factors are presented in Table 5.5, along with the additional variables needed to calculate them. The partial resistance factor (γ_M) obtained for carbon steel joints is 1.05, which is greater than the partial resistance factor prescribed in EN 1993-1-8 (2005) and prEN 1993-1-8 (2020) for joints between hollow section members γ_{M5}=1.00 mainly because the current formulation (Eq. 5.5) provides overly conservative estimations for certain geometries. On the other hand, prEN 1993-1-4 (2021) does not have a specific partial resistance factor γ_{M5} for stainless steel, mainly because the formulation for estimating the resistance of joints between hollow sections has not been yet adapted to this material. The value of γ_M obtained for stainless steel joints is 1.06, based on the study carried out on over 200 austenitic stainless steel welded joints, therefore the proposed partial resistance factor for this type of connections would be γ_{M5}=1.05. Alternatively, and considering that the partial factors for cross-section and member design prescribed in prEN 1993-1-4 (2021) are γ_{M0}= γ_{M1}=1.10, it can be safely recommended to adopt a γ_{M5} factor with the same value, and hence, a value of γ_{M5}=1.10 is proposed for the design of welded stainless steel tubular joints when using the formulation proposed in this study.

5.5. Concluding remarks

From Section 5.1 to 5.4 the behaviour of T-joints between tubular members showing chord face failure modes under bending loading is investigated, considering both steel and stainless steel connections. The study is based on a parametric study carried out in carbon steel and stainless steel welded joints using

finite element models previously validated against tests on similar joint configurations. In total 444 advanced FE models of RHS joints were analysed under pure bending conditions (243 corresponded to carbon steel joints, while 201 featured stainless steel alloys).

The assessment of the design provisions prescribed in current and upcoming standards for steel structures (EN 1993-1-8 (2005) and prEN 1993-1-8 (2020)) indicated that while for certain geometries (joints with β<0.45) the current formulation estimated accurately the bending resistance of the welded joints, with a mean value of the ratio M_{FE}/M_{Rk}equal to 1.03 and 88% of the joints assessed showing M_{FE}/M_{Rk} ratios between 0.9 and 1.15, the obtained results did not match those obtained by means of the FE models for joint geometries exhibiting β-values over 0.45. In this case, the mean value of the M_{FE}/M_{Rk} ratio raised up to 1.27 and only for 3% of the analysed cases the resistance estimation could be classified as accurate for the current design formulation, i.e., $M_{FE}/M_{Rk}\epsilon$(0.9,1.15). Therefore, the results derived from the parametric study suggested that a different yield line mechanism from the one considered by the formulation presented in current and upcoming standards (EN 1993-1-8 (2005) and prEN 1993-1-8 (2020)) occurs for high β-values, and alternative mechanism and design formulations are proposed and assessed in this section.

The new yield line mechanism (shown in Figure 5.8 and Figure 5.9) and associated new formulation (given by Eq. 5.7) proposed provided more accurate resistance estimations for high β-values (with a mean numerical-to-predicted ration of 1.06 and 82% of the data in the range of 0.9-1.15). On top of that, the new formulation considers additional geometric parameters that were found to influence the bending resistance of welded tubular joints and that are not included in the current formulation, such as the external radius of the chord and the weld thickness. Moreover, the proposed formulation can be used for low β-values without losing much accuracy thanks to the proposed effective length parameter b_0^* (Eq. 5.8), with a mean value of the M_{FE}/M_{Rk} ratio equal to 1.06 and 72% of the results lying between 0.9 and 1.15.

Additionally, the accuracy of the proposed formulation was also assessed for a set of joints made from the austenitic stainless steel grade EN 1.4301, characterized by having a high nonlinear stress–strain relationship and significant strain hardening. A total of 201 stainless steel joints were modelled and the results were compared with the resistance estimations provided by the proposed formulation (i.e., Eq. 5.7-Eq. 5.8 in conjunction with the CSM formulation (Eq. 2.45-Eq. 2.46) with very good agreement. The mean value of the M_{FE}/M_{Rk} ratios obtained with the new formulation was 1.07, with an 95% of the M_{FE}/M_{Rk} ratios between 0.9 and 1.15, whereas the current formulation provides unreliable estimations for stainless steel joints – mean M_{FE}/M_{Rk} ratios of 1.42 and 15% of results with $M_{FE}/M_{Rk}\epsilon$(0.9,1.15). Further research needs to be carried out for other stainless steel grades, but the obtained results suggest

that it is possible to combine the proposed formulation with the CSM formulation in order to account for strain hardening effects when estimating accurately the resistance of stainless steel joints.

Finally, the soundness and safety of the proposed formulation was statistically investigated, obtaining γ_M partial resistance factors of 1.05 and 1.06 for carbon steel and stainless steel connections, respectively. Hence, and based on the obtained results, values of γ_{M5}=1.05 and γ_{M5}=1.10 are proposed for carbon and stainless steel welded joints between tubular sections, respectively.

CHAPTER 6

Influence of joint modelling on the frame response

6.1. Introduction

As seen in Section 4, carbon and stainless steel frames with plastic cross-sections seem to be able to fail describing plastic collapse mechanisms and to redistribute internal forces. However, in order to fully form plastic collapse mechanisms, the designed joints must be able to withstand the increase in internal forces resulting from this redistribution, and to provide enough stiffness to prevent significant second order effects. According to European codes (prEN 1993-1-1 (2019)), full-strength joints can be modelled as perfectly rigid joints and, for structures with Class 1 cross-sections, plastic global analysis is allowed. Both statements have been widely studied at room temperature, but whether these assumptions are also valid under fire situation needs to be assessed yet.

With this goal in mind, a numerical study is first presented in this chapter, where the response of carbon and stainless steel frames for which the welded joints between members are explicitly modelled is compared with the response for frames with perfectly rigid numerical joints, both at room temperature and at elevated temperatures. The numerical studies are presented separately for carbon steel structures (Section 6.3) and for stainless steel frames (Section 6.4). Following the results and

conclusions extracted in this chapter, the redistribution capacity of the frames will be assessed in Section 7, at room temperature and at elevated temperatures.

6.2. Specific information of the FE models

Since in this study the influence of two alternative modelling techniques (i.e., explicitly modelled joints or perfectly rigid numerical joints) is analysed, one of which requires the detailed reproduction of the actual geometry of the welded connections, the solid element C3D10 available in the Abaqus (2020) library is employed for discretization purposes, as was also considered in Section 5. However, it should be noted that this decision does not invalidate the potential use of shell elements for meshing purposes for the remaining parts of this type of structures.

The heat transfer problem was solved as specified in Section 3.2, and the mechanical problem at room temperature was solved by means of the arc-length method, while the mechanical problem at elevated temperatures was solved by means of the Newton-Raphson method with a damping factor of 0.0002 for numerical convergence stability purposes. For more information on the developed FE models, the reader is referred to Section 3.

6.3. Influence of joint modelling on carbon steel frames

The influence of joint modelling on carbon steel frames focused on five single-bay, single-span carbon steel frames with plastic cross-sections and rigid welded connections. The overall frame geometry was defined with a span length (L) equal to 5 m and a column heigh (H) of 3 m, which are typical dimensions for building construction frames. All the analysed frames had fixed supports and the out-of-plane displacements were prevented, but the thermal expansion of the structural members was permitted in all directions. The adopted loading case included both vertical (q) and horizontal (P) loading, as depicted in Figure 6.1. The material considered for the analysed frames was the carbon steel grade S275.

A total of five different cross-section geometries were adopted, the main parameters of which are reported in Table 6.1, where b is the width, h is the height and t is the thickness of the cross-section; note that the subscript 0 corresponds to the column, whereas the subscript 1 refers to the beam, and the weld throat thickness is denoted by a. The loading case for each of the studied frames is defined by the parameter R, which is the ratio between the total vertical load (Q=$q \cdot L$) over the horizontal load (P).

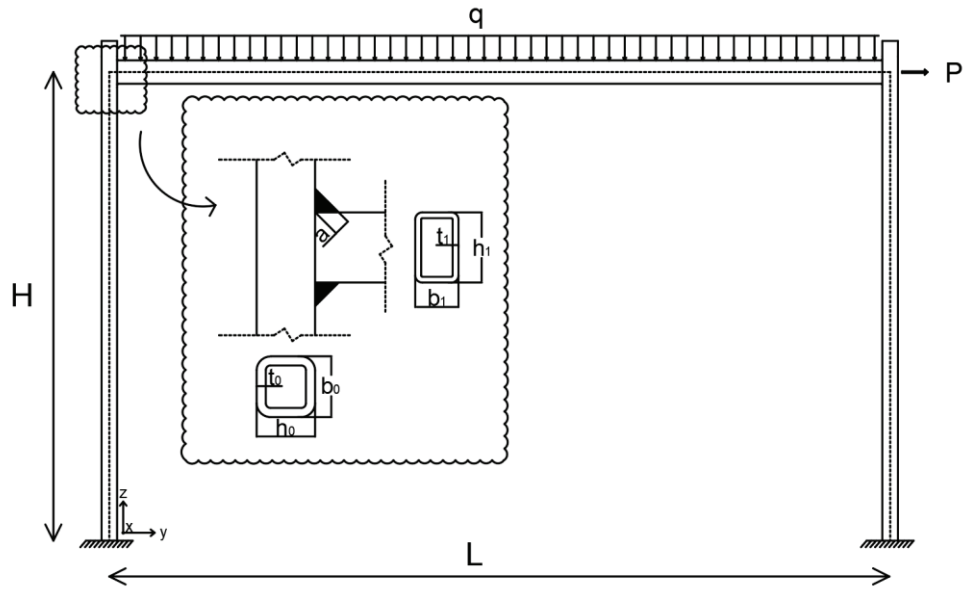

Figure 6.1. Overall frame geometry and loading pattern adopted.

The cross-sections were defined in order to produce the first plastic hinges on the beams by imposing $M_{pl,1}$<$M_{pl,0}$, where $M_{pl,1}$ and $M_{pl,0}$ are the plastic bending resistances of the beam and the column, respectively. According to the classical plastic theory, the welded joints were defined as full-strength joints, the welds had a 45º inclination, and a throat thickness (a) equal to the beam thickness (t_1), as recommended by CIDECT (Wardenier 2001) for S275 carbon steel. Since the cross-sections reported in Table 6.1 are classified as Class 1, the frames were expected to show a certain internal force redistribution capacity at room temperature. Moreover, all frames were classified as non-sway frames under the loading cases presented, exhibiting values of α_{cr}≥10 at room temperature.

Table 6.1. Main geometric parameters of the analysed frames.

Frame ID	α_{cr}	L [m]	H [m]	h_0 [mm]	b_0 [mm]	t_0 [mm]	h_1 [mm]	b_1 [mm]	t_1 [mm]	a [mm]	R
1	117.2	5	3	200	200	12.5	180	100	5	5	0.7
2	64.2	5	3	150	150	10	180	80	3.2	3.2	1.1
3	27.4	5	3	100	150	14.2	140	70	8	8	2.0
4	36.3	5	3	100	100	8	120	60	3.2	3.2	1.4
5	27.0	5	3	80	80	5	80	70	3.2	3.5	2.0

6.3.1. Response at room temperature

The ultimate load of each frame was obtained by means of the numerical model described in Section 3, considering explicit joints ($P_{u,FE,E}$) and numerical rigid joints ($P_{u,FE,N}$). The results are presented in Table 6.2, along with the bending moment resistances of the frame elements according to the current codes (prEN 1993-1-1 (2019)): the plastic bending moment resistance of the columns ($M_{pl,0}$), the plastic bending moment resistance of the beams ($M_{pl,1}$), and the bending moment resistance of

the joints according to the formulation included in prEN 1993-1-8 (2020) ($M_{2,EN}$) (i.e., Eq. 5.5) and the new formulation presented in Chapter 5 ($M_{2,PR}$) (i.e., Eq. 5.7-Eq. 5.8), along with the values of $\beta=b_1/b_0$ of the joints. All the analysed joints were expected to fail due to chord face failure ($\beta\leq0.85$), except for the joints in Frame 5, which was expected to fail due to a combination between chord face failure and chord side failure due to its geometry ($1.0\geq\beta>0.85$). However, for joints with $\beta>0.85$ no estimation of the bending resistance ($M_{2,PR}$) could be calculated based on the new formulation (Eq. 5.7-Eq. 5.8), because it exceeds the limits of applicability of the presented formulation, as explained in Section 5.4. Moreover, the analytical ultimate loads calculated according to global plastic analysis ($P_{u,PGA}$) are also presented, the detailed calculations of which can be found in Annex B. Note that resistances are presented in terms of the maximum horizontal load (P_u) that the frames could withstand under the loading case shown in Figure 6.1, with a concurrent vertical load corresponding to the horizontal load ratio R also reported in Table 6.1. For instance, Frame 1 could resist up to a theoretical horizontal load of $P_{u,PGA}$=131.8 kN and a total vertical load $Q_{u,PGA}$=131.8·0.7=92.3 kN applied simultaneously.

Table 6.2. Bending moment resistances of frame elements, and ultimate frame loads considering different joint modelling approaches and global plastic analysis at room temperature.

Frame ID	$M_{pl,0}$ [kN·m]	$M_{pl,1}$ [kN·m]	β	$M_{2,EN}$ [kN·m]	$M_{2,PR}$ [kN·m]	$P_{u,FE,E}$ [kN]	$P_{u,FE,N}$ [kN]	$P_{u,PGA}$ [kN]
1	170.6	42.4	0.5	40.1	43.4	135.8	138.6	130.4
2	77.5	25.0	0.53	29.3	29.7	58.7	57.8	58.0
3	55.8	34.1	0.47	39.0	43.3	45.0	46.4	44.9
4	26.5	11.4	0.6	13.9	17.7	20.2	19.5	20.6
5	11.4	6.8	0.88	7.6†	–	8.7	8.8	9.1

†The joint resistance was calculated as per the formulation provided in prEN 1993-1-8 (2020) for chord side wall failure.

Table 6.2 highlights that the difference on the ultimate load between the numerical models with explicit joints ($P_{u,FE,E}$) and with numerical rigid joints ($P_{u,FE,N}$) is nearly negligible for the analysed carbon steel frames. Besides that, both FE results show a good agreement with the analytical estimation of the ultimate load ($P_{u,PGA}$). Nevertheless, a slight difference on the response can be identified if the load–displacement curves of the models with explicit joints are compared to those corresponding to the models with numerical rigid joints. Figure 6.2 shows the evolution of the applied horizontal loads against the vertical displacements at midspan (negative displacements) and the horizontal displacements at the right joint (positive displacements) for the two joint modelling approaches for each frame.

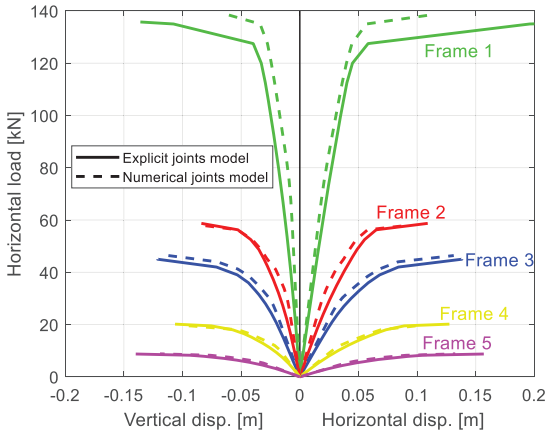

Figure 6.2. Vertical displacements (left) and horizontal displacements (right) of the analysed carbon steel frames with explicitly modelled joints (solid line) and with numerical rigid joints (dashed line).

Each pair of curves (corresponding to the explicit and numerical joint modelling approaches) show similar overall load–displacement responses: a first stage with a perfectly linear response, followed by a second stage characterized by a nonlinear response, ending with a third stage at which horizontal and vertical displacements increase rapidly due to the complete formation of the plastic mechanism. Small differences can be observed between the two modelling approaches: frames with numerical rigid joints show a slightly stiffer response under the applied loads, whereas the frames with explicit joints exhibit a more ductile behaviour enduring larger displacements before collapsing.

6.3.2. Response in fire situation

After assessing the correct performance of the designed joints, the same carbon steel frames were analysed under fire situation. The analysed frames were subjected to fire in all exposed faces by increasing the temperature of the air around the frames according to the normalised ISO-834 curve, introduced in Section 2.4 as per Eq. 2.18. Hence, the temperature field of the structure over time was obtained by solving the heat transfer problem numerically, as described in Section 3. The temperature evolution of the beams and columns of the analysed frames is shown in Figure 6.3 along with the evolution of the air temperature.

As it can be seen in Figure 6.3, the beams of all the frames showed a higher temperature than the columns at all time steps due to their higher section factor (S_m), which is the ratio between the exposed surface in contact with the heated air and the volume of steel. These non-uniform temperatures were observed at all time steps, with higher temperatures near the beams and lower temperatures in the parts closer to the columns.

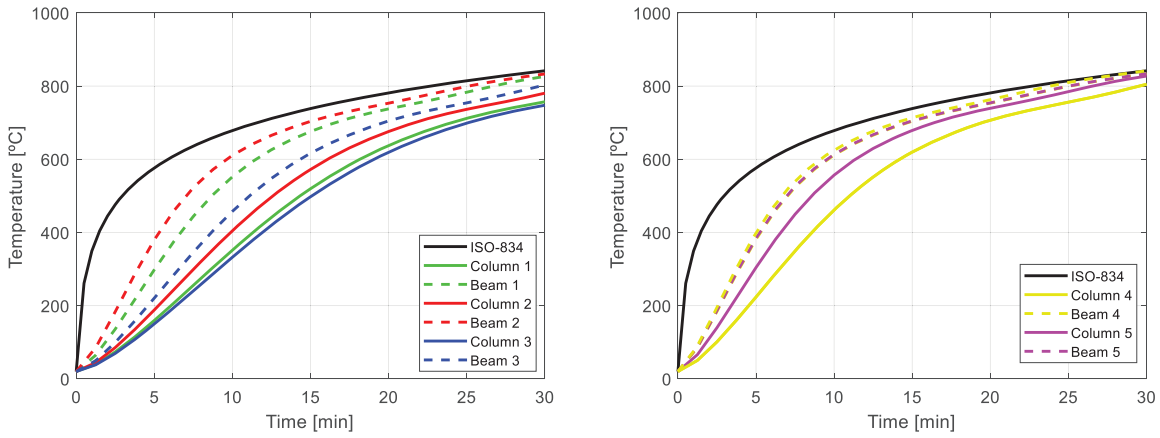

Figure 6.3. Temperature evolution of the beams and columns compared to the air temperature in a standard fire according to the normalized ISO-834 curve for (a) Frame 1 to Frame 3, and (b) Frames 4 and 5.

This non-uniform temperature field along the frames induced a faster degradation of the mechanical properties for the beams than for the columns, exacerbating the differences between the resistance and the stiffness of the beams and columns as fire built up. Likewise, the joint temperature (for those frames with explicitly modelled joints) was always lower than the beam temperature, meaning that the initial difference between the beam-to-joint resistance was increased under the fire situation for the analysed frames.

The investigated carbon steel frames were subjected to the loading case shown in Figure 6.1 considering degrees of utilisation (μ_0) equal to 0.3 and 0.7 (i.e., loaded with 30% and 70% of the ultimate loads causing the collapse of the frames at room temperature), in order to assess the performance of the joints with relatively low and high initial loads under fire situation. To estimate the frame response, the temperature evolution shown in Figure 6.3 was imposed at each time step while the initial loads were maintained constant, as described in Chapter 3. The vertical (negative) and horizontal (positive) displacement evolution over time are shown in Figure 6.4 for the analysed frames.

The curves show an initial displacement due to the loads already applied before the fire started, representing the normal operational situation of the frames. When the fire started, the thermal expansion resulted in an increase of the horizontal deflections – due to the beam elongation – and in a slight reduction of the vertical displacements. After that, the displacements increased rapidly until the collapse of the frames was reached. The main differences between the frames subjected to a degree of utilisation of μ_0=0.3 and those subjected to μ_0=0.7 can be observed in Figure 6.4(a) and (b), where frames subjected to lower initial loads show smaller initial displacements that lead to higher time fire resistances (TFR), while frames subjected to high initial loads describe larger initial displacements, resulting in lower TFRs.

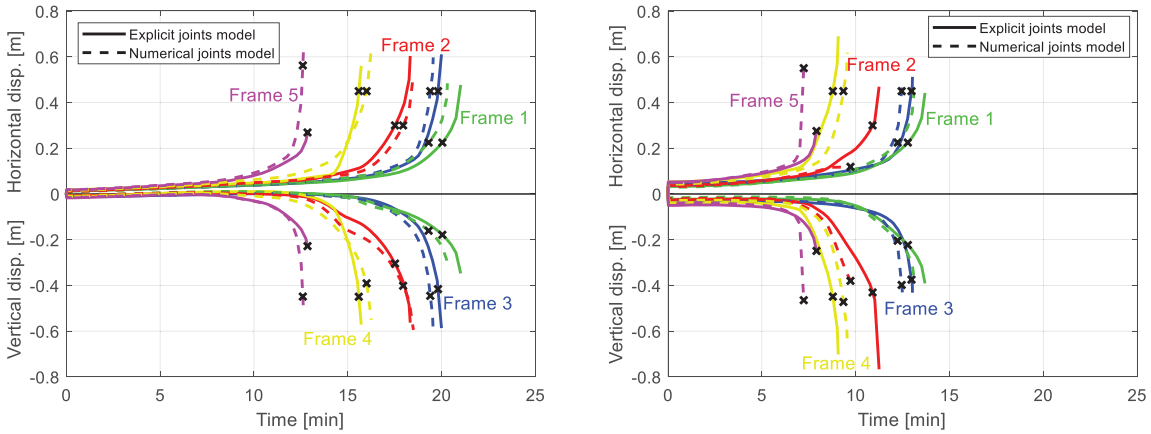

(a) (b)

Figure 6.4. Vertical displacements (bottom) and horizontal displacements (top) of carbon steel frames with explicitly modelled joints (solid line) and numerical rigid joints (dashed line) under fire situation for a degree of utilisation of (a) 0.3, and (b) 0.7.

Moreover, no clear pattern can be discerned between the response of the frames with numerical joints and the response of the frames with explicit joints. This suggests that it is possible to model welded full-strength joints – classified as so at room temperature – between carbon steel RHS elements as ideal rigid joints also at elevated temperatures for low and high initial load levels, resulting in a minimum difference in their predicted response. It should be pointed out that, however, a significant difference can be seen for the displacements of the two modelling approaches for Frame 2, as shown in Figure 6.4(b): the horizontal displacement does not exceed the value of 0.2 m for the frame with numerical rigid joints, while the horizontal displacement for the frame with explicit joints is over 0.4 m. This is because the frame with rigid joints ended forming a beam plastic mechanism, whereas the frame with detailed joints formed a global plastic mechanism.

Following the approach for advanced fire design discussed in Chapter 4, the failure of the analysed carbon steel frames was determined using the failure criteria presented in Section 4.3, which has already been verified against experimental data for carbon steel frames. The time fire resistance of the frames is marked with "×" in Figure 6.4. Likewise, Table 6.3 reports the time fire resistance (TFR) and the corresponding critical temperatures for the beams ($\theta_{cr,1}$) and columns ($\theta_{cr,0}$) for degrees of utilisation of 0.3 and 0.7, respectively, for the two joint modelling approaches considered.

From the results presented in Table 6.3, no clear pattern can be distinguished: in some cases, the frames with numerical rigid joints exhibited a slightly higher resistance under fire situation due to their stiffer response, whereas in other cases the frames with explicit joints were able to accommodate better the imposed thermal elongations, thus resisting longer under fire.

Table 6.3. Main results of the frames analysed under fire situation with the two joint modelling techniques.

		Carbon steel frames with explicit joints			Carbon steel frames with numerical joints		
Frame ID	μ_0	TFR [min]	$\theta_{cr,0}$ [°C]	$\theta_{cr,1}$ [°C]	TFR [min]	$\theta_{cr,0}$ [°C]	$\theta_{cr,1}$ [°C]
1	0.3	20.0	637	738	19.3	623	748
	0.7	12.8	449	632	12.2	549	661
2	0.3	17.6	631	731	17.9	640	736
	0.7	10.9	440	633	9.7	393	604
3	0.3	19.8	620	702	19.4	612	697
	0.7	13.0	441	562	12.5	424	547
4	0.3	15.6	636	711	16.0	641	717
	0.7	8.8	407	574	9.3	433	593
5	0.3	12.9	637	673	12.6	632	669
	0.7	7.9	469	542	7.2	435	514

6.3.3. Response under uniform temperature

The results presented in the previous section are promising, but the conditions under which the joints were capable of resisting and redistributing internal forces at elevated temperatures were multiple. One of these conditions was that the joints were always at a lower temperature than the beam cross-sections forming the first plastic hinges due to the different section factors of the beams and the columns. Consequently, the resistance deterioration of the beams was faster than the reduction of the resistance at the joints at elevated temperatures. This could be a reason why the analysed joints performed adequately under the fire situation, without showing any differences between the response of frames modelled with ideal rigid joints and frames modelled with explicit joints.

In order to evaluate this, the same frames with the same degrees of utilisation were subjected to an imposed temperature field that increased uniformly along the frames until collapse. The temperature–displacement curves for both degrees of utilisation (μ_0=0.3 and μ_0=0.7) for the uniform temperature field are shown in Figure 6.5.

These figures highlight the difference in critical temperatures between the frames under a low degree of utilisation (Figure 6.5(a)) compared to the frames with a higher degree of utilisation (Figure 6.5(b)). A higher initial load level put the frames at a more disadvantageous position to cope with fire, similar to the results presented for non-uniform temperature fields in the previous section.

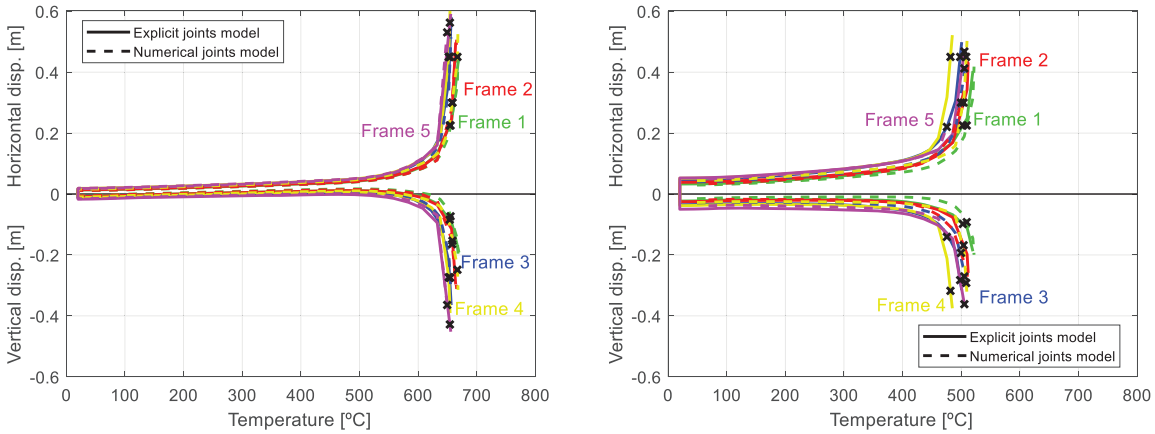

Figure 6.5. Vertical displacements (bottom) and horizontal displacements (top) of carbon steel frames with explicitly modelled joints (solid line) and numerical rigid joints (dashed line) under fire situation for a degree of utilisation of (a) 0.3, and (b) 0.7.

Again, no clear differences could be seen between the frames with numerical rigid joints and the frames with explicit joints, delivering a first hint about the fact that joints can be modelled as simplified joints at elevated temperatures, even under a uniform temperature field. Table 6.4 reports the critical temperatures of the analysed carbon steel frames under the different degrees of utilisation for the two types of joint modelling, frames with explicit joints ($\theta_{cr,E}$) and frames with numerical rigid joints ($\theta_{cr,N}$).

Table 6.4. Critical temperatures for the analysed carbon steel frames with imposed uniform temperature field and different degrees of utilisation.

	μ_0=0.3		μ_0=0.7	
Frame ID	$\theta_{cr,E}$ [°C]	$\theta_{cr,N}$ [°C]	$\theta_{cr,E}$ [°C]	$\theta_{cr,N}$ [°C]
1	654	655	498	505
2	654	655	503	509
3	658	658	504	499
4	652	667	482	508
5	654	649	505	475

Note that the critical temperatures reported in Table 6.4 were obtained imposing the displacement and displacement rate limits proposed in Section 4.3. As it can be seen, no significant differences can be observed between the frames with numerical rigid joints and explicit joints for a given degree of utilisation (μ_0). These results confirm that the performance of the designed joints was also adequate at the worst possible scenarios, and that they could be modelled as perfectly rigid joints even when the temperature field was uniform along the frames.

Another interesting result obtained from the analysis of carbon steel systems considering a uniform temperature field was that the critical temperature of the frames seemed to depend only on the degree of

utilisation considered, since the variations of the temperature values reported in Table 6.4 for a given degree of utilisation (μ_0) is low. This conclusion is in accordance with the results reported in Section 4 for similar carbon steel frames, which consisted on structures with constant cross-sections along the whole frames, which generated a uniform cross-section temperature distribution through the whole frame when subjected to fire. Figure 6.6 shows the reduction factors of the yield stress ($k_{y,\theta}$) at elevated temperatures side by side with the critical temperatures (θ_{cr}) of the analysed frames with uniform temperature fields plotted depending on their degree of utilisation (μ_0). In addition, the critical temperatures of the carbon steel frames analysed in Chapter 4 are also plotted for comparison.

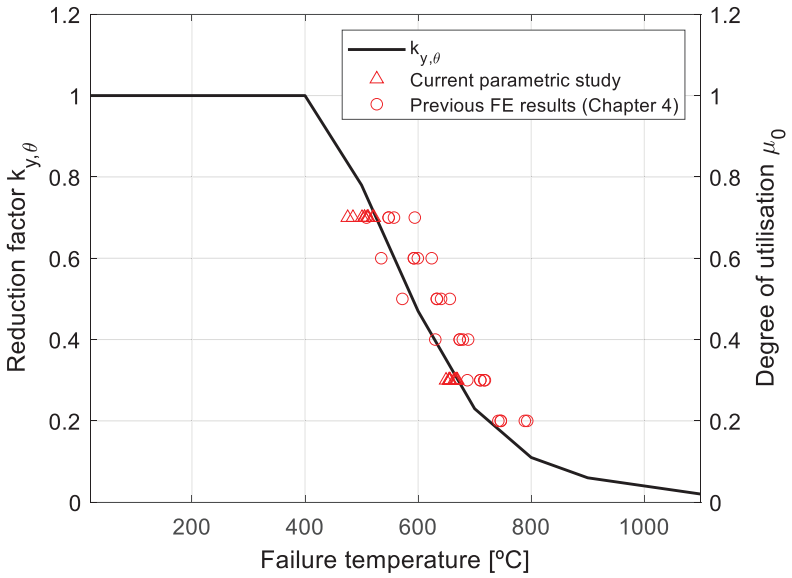

Figure 6.6. Critical temperatures of carbon steel frames under uniform temperature fields for carbon steel frames, including the results from Chapter 4.

It should be pointed out, however, that the frames analysed in Chapter 4 were not subjected to a perfectly uniform temperature distribution since the frames were exposed to the normalised ISO-834 curve and some were subjected to fire only on their three inner faces. Nevertheless, the cross-section temperature distribution was the same along the whole frame, and the obtained results match the reduction factor of the yield stress at elevated temperature reasonably well.

6.4. Influence of joint modelling on stainless steel frames

The equivalent study on the influence of joint modelling for stainless steel structures focused on ten single-bay, single-span stainless steel frames with plastic cross-sections and rigid welded connections. For this study, two overall frame geometries were defined, one with a span length (L) equal to 5 m and a column heigh (H) of 3 m, similar to that used for the carbon steel study, and the other one with a span length (L) of 4 m and a column height (H) of 2 m. All the analysed frames had fixed supports and the out-of-plane displacements were prevented, but the thermal expansion of the structural members was permitted in all directions. The adopted loading case also included both vertical (q) and horizontal (P)

loading, as depicted in Figure 6.1. The materials considered for the analysis were the commonly used austenitic stainless steel grades EN 1.4301 and EN 1.4401; both stainless steel grades exhibit the same mechanical properties at room temperature, but different performances under fire situation according to prEN 1993-1-2 (2021).

A total of ten different cross-section geometries were adopted, the main parameters of which are reported in Table 6.5. Frames 1 to 5 had the same geometry as the carbon steel frames presented in Table 6.1, while Frames 6 to 10 were new geometries with a different stainless steel grade in order to analyse the influence of different material degradation at elevated temperature, since EN 1.4301 (Austenitic I) and EN 1.4401 (Austenitic II) belong to different material subgroups according to prEN 1993-1-2 (2021). The frames were analysed under three different degrees of utilisation μ_0=0.3, μ_0=0.5 and μ_0=0.7.

Table 6.5. Main geometric parameters of the analysed stainless steel frames.

Frame ID	EN Grade	$\alpha_{cr,mod}$	L [m]	H [m]	h_0 [mm]	b_0 [mm]	t_0 [mm]	$\bar{\lambda}_{p,0}$	h_1 [mm]	b_1 [mm]	t_1 [mm]	$\bar{\lambda}_{p,1}$	a [mm]	R
1	1.4301	18.5	5	3	200	200	12.5	0.24	180	100	5	0.31	5	0.7
2	1.4301	14.9	5	3	150	150	10	0.24	180	80	3.2	0.42	3.2	1.1
3	1.4301	9.2	5	3	100	150	14.2	0.15	140	70	8	0.11	8	2.0
4	1.4301	11.4	5	3	100	100	8	0.19	120	60	3.2	0.28	3.2	1.4
5	1.4301	7.1	5	3	80	80	5	0.31	80	70	3.2	0.34	3.5	2
6	1.4401	8.6	4	2	100	100	8	0.25	120	85	5	0.26	5.3	2
7	1.4401	7.6	4	2	90	90	8	0.16	80	40	5	0.10	5	0.8
8	1.4401	11.0	4	2	100	140	10	0.22	130	90	5	0.28	5	1.5
9	1.4401	7.3	4	2	60	60	5	0.16	50	30	3.2	0.10	3.5	0.9
10	1.4401	6.7	4	2	120	110	10	0.16	90	60	5	0.16	5	0.7

On top of that, Table 6.5 reports the relative local slenderness ($\bar{\lambda}_p$) of each of the cross-sections adopted, which ranges from 0.1 to 0.42, all below the limit of $\bar{\lambda}_p \leq$ 0.58, which corresponds to the Class 1 limit in compression according to prEN 1993-1-4 (2021). Thus, the influence of strain hardening on the cross-section resistance was expected to play a major role in the performance of the analysed frames. The cross-sections were defined in order to produce the first plastic hinges on the beams, by imposing that $M_{pl,1}<M_{pl,0}$, according to plastic bending moment theory. Moreover, the frames investigated in this study were classified as both non-sway and sway frames under the loading cases adopted according to prEN 1993-1-4 (2021). Those frames with values of $\alpha_{cr,mod}\geq$10 at room temperature were classified as non-sway, otherwise they were classified as sway frames. For more information on the $\alpha_{cr,mod}$ factor prescribed for stainless steel structures, the reader is referred to Section 2.5.3.1. The load ratio (R) was defined in order to trigger the combined collapse mechanism for each of the analysed frames, which is a mechanism characterized by being a combination of the beam mechanism and the global sway mechanism, involving the resistance of

the beam and the two columns when forming the plastic collapse mechanism. Finally, all the joints were classified as full-strength joints according to the classical plastic bending moment theory and the current formulation provided in prEN 1993-1-8 (2020) (i.e., Eq. 5.5).

6.4.1. Remarks on strength classification of stainless steel joints

To better describe the analysed stainless steel frames, Table 6.6 reports the plastic bending moment resistance of the columns ($M_{pl,0}$) and the beams ($M_{pl,1}$) according to the traditional plastic theory (i.e., M_{pl}=W_{pl}·f_y, where W_{pl} is the plastic section modulus, and f_y equal to 280 MPa according to Afshan et al. (2019)), and the bending moment resistance of the columns ($M_{csm,0}$) and the beams ($M_{csm,1}$) predicted by the Continuous Strength Method (CSM) as explained in Section 2.5.2, which are reported along with the bending resistances of the joints obtained from the predictive expressions prescribed in prEN 1993-1-8 (2020) ($M_{2,EN}$) (using Eq. 5.5), and the joint resistance estimated as per the new formulation presented in Chapter 5 (Eq. 5.7-Eq. 5.8), ($M_{2,PR}$). It should be pointed out, that joints with β-values above 0.85 cannot be calculated using the new formulation due to their geometry (i.e., β=b_1/b_0>0.85), for more information the reader is referred to Section 5.4.

Table 6.6. Bending resistance of the main structural components comprising the analysed stainless steel frames at room temperature.

Frame ID	$M_{pl,0}$ [kN·m]	$M_{pl,1}$ [kN·m]	β	$M_{2,EN}$ [kN·m]	$M_{2,PR}$ [kN·m]	$M_{csm,0}$ [kN·m]	$M_{csm,1}$ [kN·m]
1	173.8	43.1	0.5	44.2	55.9	226.3	55.9
2	79.0	25.4	0.53	30.2	38.0	102.8	28.6
3	56.8	34.8	0.47	44.1	55.5	73.2	44.5
4	27.0	11.6	0.60	17.7	22.7	35.1	14.9
5	11.8	6.9	0.88	7.6†	–	15.4	8.7
6	28.6	21.1	0.85	28.1†	–	35.9	26.5
7	21.3	6.9	0.44	7.1	11.0	26.7	8.6
8	41.9	24.7	0.64	29.8	38.1	52.8	31.0
9	5.9	1.9	0.50	3.8	3.0	7.3	2.4
10	45.1	10.8	0.54	16.4	21.0	56.5	13.5

†The joint resistance was calculated as per prEN 1993-1-8 (2020).

Additionally, the ratios between the design resistance of the joint ($M_{2,EN}$) over the design plastic resistance of the beam ($M_{pl,1}$), or the CSM bending resistance of the beam ($M_{csm,1}$), $K_{EN/pl}$=$M_{2,EN}/M_{pl,1}$ and $K_{EN/csm}$=$M_{2,EN}/M_{csm,1}$ respectively, are also introduced in Table 6.7. Note that the joints with $K_{EN/pl}$>1.0 were classified as full-strength joints according to prEN 1993-1-8 (2020). Likewise, the ratio between the estimated resistance of the joint using the proposed new formulation (Eq. 5.7-Eq. 5.8) $M_{2,PR}$ – which accounts for the strain hardening of the material – and the CSM bending resistance of the beam cross-section ($M_{csm,1}$) $K_{PR/csm}$=$M_{2,PR}/M_{csm,1}$ is also reported in Table 6.7. Additionally, the β-values

of the joints are also presented. Recall that joints with $\beta \leq 0.85$ are expected to fail due to chord face failure, while those with $\beta \epsilon (0.85,1.0]$ are expected to fail due to a combination between chord face failure and chord side failure.

Table 6.7. Ratios between the bending moment resistance of the joints and the beams using different estimation approaches.

Frame ID	β	$K_{EN/pl}$	$K_{EN/csm}$	$K_{PR/csm}$
1	0.50	1.03	0.79	1.00
2	0.53	1.19	1.06	1.33
3	0.47	1.27	0.99	1.25
4	0.60	1.53	1.19	1.52
5†	0.88	1.10	0.87	–
6†	0.85	1.33	1.06	–
7	0.44	1.03	0.83	1.28
8	0.64	1.21	0.96	1.23
9	0.50	2.00	1.58	1.25
10	0.54	1.52	1.21	1.56

†The joint resistance was calculated as per the formulation provided in prEN 1993-1-8 (2020) for chord side wall failure.

As it has been already explained, the current formulation for estimating the bending moment resistance of welded joints between RHS elements included in prEN 1993-1-8 (2020) does not take into consideration the strength enhancement of stainless steel joints due to strain hardening. Hence, it would not be appropriate to compare the CSM bending moment resistance ($M_{csm,1}$) with the current joint resistance estimation ($M_{2,EN}$) when classifying joints as full- or partial-strength connections (i.e., using the $K_{EN/csm}$ ratio). For instance, all frames in the present study could be designed using a plastic global analysis, accounting for plastic redistribution and the development of a plastic collapse mechanism, according to European specifications (prEN 1993-1-8 (2020)) if the resistance of the different members comprising the structure is limited to the yield stress (f_y), since all connections would be classified as full-strength joints (i.e., $K_{EN/pl}$>1.0 in all cases).

However, if the CSM bending resistances are assumed as the cross-section design resistance, half of the presented frame geometries would not fulfil the requirement for full-strength joints ($K_{EN/csm}$ ratios below 1.0 reported in Table 6.7), and thus the resistance of these frames would be limited to the strength of the most critical element, without accounting for plastic internal force redistributions. This fact highlights the need to assess and derive additional design formulations for stainless steel in other parts of European standards if the CSM formulation becomes the norm for designing such structures, in order to ensure that research improvements such as the CSM formulation do not cause inconsistencies and issues in other aspects of the design.

This issue could be, nevertheless, solved for the studied cases with the new formulation presented in Section 5.4 for estimating the bending resistance of tubular T-joints in stainless steel structures that fail due to chord face yielding by using the CSM formulation. If the ratio $K_{PR^*/csm}$ is used for joint strength classification, all the analysed joints with $\beta \leq 0.85$ would be classified as full-strength joints, regardless of the approach adopted for the estimation of the bending resistance of the beams, which is in accordance with the response shown by the frames (and the joints).

6.4.2. Response at room temperature

With the aim of assessing the influence of joint modelling on stainless steel structures at room temperature, typical horizontal load–vertical/horizontal displacement curves measured at the beam midspan (vertical displacements) and at the right joint (horizontal displacements) of five representative stainless steel frames (Frames 3, 4, 5, 7, and 8) are presented in Figure 6.7, which correspond to FE models with explicitly modelled joints (solid lines) and numerically modelled joints (dashed lines). The frames were subjected to the loading case presented in Figure 6.1, increasing the applied loads incrementally – with a vertical to horizontal load ratio R according to Table 6.5 – until the frames reached the corresponding peak loads.

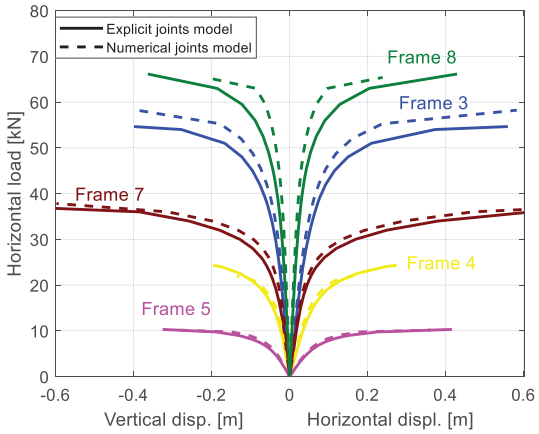

Figure 6.7. Representative horizontal load vs. vertical displacement (left) and horizontal displacement (right) curves of stainless steel frames with explicitly modelled joints (solid lines) and numerical rigid joints (dashed lines).

As it can be seen in Figure 6.7, frames with numerically modelled joints (i.e., ideal rigid joints) exhibit a slightly stiffer response, as it was also observed for carbon steel frames, but apart from that, results show little to no difference between the two joint modelling techniques in terms of the achieved ultimate loads and the predicted load–displacement paths, which is in agreement with the requirements prescribed in prEN 1993-1-8 (2020) for global plastic analysis (i.e., joints classified as full-strength). This means that the designed joints were able to resist the increase of internal loads arising from strain hardening as the ratio $K_{PR/csm}$ correctly predicted. Moreover, Figure 6.7 proves that stainless steel frames describe larger displacements before collapse than equivalent carbon steel frames: for instance, the ultimate displacements reached by carbon steel frames shown in Figure 6.2 were all below 0.2 m,

while most of the stainless steel frames analysed herein surpassed the 0.4 m in vertical and horizontal displacements, as Figure 6.7 highlights.

The ultimate loads obtained at room temperature by means of the FE models accounting for the two modelling techniques are shown in Table 6.8. The ultimate numerical resistances ($P_{u,FE}$) are presented along with the $\alpha_{cr,mod}$ values of the frames and the analytical collapse load estimations according to a plastic global analysis ($P_{u,PGA}$) that uses M_{pl} and M_{csm} as bending moment resistances.

Table 6.8. Ultimate loads ($P_{u,FE}$) for explicitly (E) and numerically (N) modelled joints, along with the resistance estimations from global plastic analyses ($P_{u,PGA}$) using M_{pl} and M_{csm} as bending moment resistances.

Frame ID	$\alpha_{cr,mod}$	$P_{u,FE,E}$ [kN]	$P_{u,FE,N}$ [kN]	$P_{u,PGA,pl}$ [kN]	$P_{u,PGA,csm}$ [kN]
1	18.5	168.4	171.6	132.8	174.1
2	14.9	67.3	70.1	59.1	73.1
3	9.2	54.7	58.2	45.7	59.1
4	11.4	25.0	23.2	21.0	27.4
5	7.1	10.3	10.2	9.3	11.9
6	8.6	41.1	43.1	35.2	44.5
7	7.6	37.6	37.8	24.9	31.2
8	11.0	65.0	65.4	51.8	65.6
9	7.3	8.4	8.9	6.6	8.3
10	6.7	68.2	70.5	49.3	62.0

As it can be seen from the results reported in Table 6.8, the analytical results ($P_{u,PGA}$) obtained by means of a plastic global analysis (Annex B) with the plastic bending moment resistances (M_{pl}) are far from the results predicted by the nonlinear numerical models ($P_{u,FE}$) because the plastic bending moment does not account for the additional resistance resulting from strain hardening effects, whereas this phenomenon is correctly reproduced by the numerical models. However, the fact that all the ultimate loads estimated by the advanced FE models are above the resistances obtained by means of traditional plastic global analysis considering the plastic bending moment resistance (M_{pl}) confirms that the analysed frames possess sufficient plastic redistribution capacity to form plastic collapse mechanism. This is in accordance with prEN 1993-1-4 (2021), where the redistribution capacity of Class 1 stainless steel frames is already recognised, and plastic global analysis is allowed under certain circumstances and for certain stainless steel types, including austenitic alloys.

Aiming at a more accurate estimation of the resistance of the frames, the ultimate loads derived from a plastic analysis using the CSM bending moment capacity (M_{csm}) were also calculated ($P_{u,PGA,csm}$), which are reported in Table 6.8. This is a rather simple but useful way of calculating the load required to form a plastic mechanism while accounting for strain hardening effects, although in order to obtain a more accurate estimation of the ultimate collapse load of sway frames ($\alpha_{cr,mod}$<10) second order

effects should be also included in the calculation. Nevertheless, it can be seen from the results reported in Table 6.8 that this simplified method in conjunction with the CSM formulation (M_{csm}) provides good results when compared to the ultimate loads estimated by means of the advanced numerical models ($P_{u,FE}$), indicating that strain hardening effects are very important in this type of frames and should be considered in design.

These results evidence that the loads needed to form the global plastic mechanisms could be estimated accurately for the frames classified as non-sway (i.e., Frames 1, 2, 4 and 8) using the CSM bending resistance in conjunction with the traditional global plastic analysis. The predicted resistances ($P_{u,PGA,csm}$) in these cases were always on the ±10% range of the expected resistances obtained by means of nonlinear FE analyses, indicating a reasonable prediction of the capacity of the frames (prEN 1993-1-4 (2021)). However, for frames classified as sway, this simple estimation of the collapse load was not accurate because it does not consider for second order effects, which can be significant in stainless steel structures. The results obtained for sway frames were varied, with ratios over and below the ±10% range: in some of the studied cases, the predicted resistance ($P_{u,PGA,csm}$) was above the resistance derived from the nonlinear analysis ($P_{u,FE}$) – e.g., for Frame 5 –, but in other cases the opposite was observed – e.g., Frame 7. These sway frame cases were more complex and, in order to provide a clear explanation, require a deeper analysis on the influence of second order effects on this type of structures, which will be assessed and discussed in Section 8.3.

6.4.3. Response in fire situation

The influence of the two joint modelling techniques on the response of the same stainless steel frames was also assessed under fire situation for three different degrees of utilisation, μ_0=(0.3,0.5,0.7). Their response in fire is directly governed by the evolution of the temperature field, which was obtained as explained in Section 3.2. The temperature–time curves of some representative beam and columns comprising the analysed frames (i.e., Frame 1, Frame 2, Frame 3, and Frame 10) are presented in Figure 6.8, in which the ISO-834 curve is also included for reference.

The main parameter governing the temperature increase, besides the thermal properties of the material – which are the same for the two analysed stainless steel grades according to prEN 1993-1-2 (2021) –, is the section factor (S_m), which compares the volume per unit of length of the cross-section with the exposed area in contact with the heated air per unit of length. The results in Figure 6.8 show that frames with higher section factors (S_m) are in worse conditions to cope with fire because they heat up faster, while frames with lower section factors should be able to withstand the fire effect during longer periods, as their temperature is increased slower.

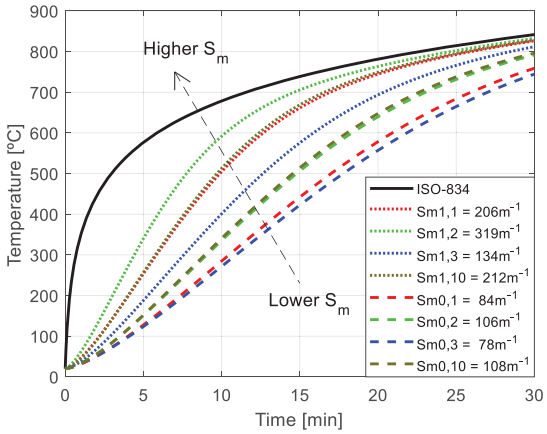

Figure 6.8. Evolution of the temperature at beams (dotted lines) and columns (dashed lines) over time for four representative stainless steel frames (Frame 1, Frame 2, Frame 3, Frame 10) and the ISO-834 standard curve.

Table 6.9 reports the section factors (S_m) of the analysed stainless steel frames and the temperatures reached at the columns (θ_0) and the beams (θ_1) after being exposed to the fire effect for 15 and 30 minutes. The results in Table 6.9 highlight that the section factor has a major impact in the temperature development of the structural member at the first stages of fire, although after a certain time the temperature of all the cross-sections tends to the ISO-834 curve, regardless of its section factor, as Figure 6.8 proves.

Table 6.9. Section factor S_m of the analysed frames and the temperatures reached at the columns (θ_0) and the beams (θ_1) after being exposed to the ISO-834 fire curve for 15 and 30 minutes.

Frame ID	Columns			Beams		
	$S_{m,0}$ [m^{-1}]	$\theta_{0,15m}$ [°C]	$\theta_{0,30m}$ [°C]	$S_{m,1}$ [m^{-1}]	$\theta_{1,15m}$ [°C]	$\theta_{1,30m}$ [°C]
1	84.4	442	759	206.0	661	826
2	105.8	506	791	318.8	706	832
3	77.9	422	745	133.6	575	812
4	133.9	573	812	321.8	705	832
5	213.3	666	827	323.8	706	832
6	135.9	578	814	208.3	666	827
7	135.0	578	814	215.2	671	828
8	107.4	514	796	207.7	664	827
9	215.2	671	828	335.3	711	834
10	107.8	514	796	211.8	669	828

With the initial load maintained constant through the entire thermo-mechanical analysis, as explained in Chapter 3, the vertical/horizontal displacement–time curves obtained for some representative stainless steel frames (i.e., Frames 1, 3, 5, 7, 8, and 10) are shown in Figure 6.9 for the two joint modelling approaches adopted. The analysed frames showed nearly identical displacement–time paths, only with slight differences, for the two modelling techniques under different degrees of utilisation (μ_0). On top of that, the results in Figure 6.9 suggest that lower degrees of utilisation led to higher time fire

resistances (TFR), whereas higher degrees of utilisation (i.e., higher initial loads) were aligned with lower time fire resistances.

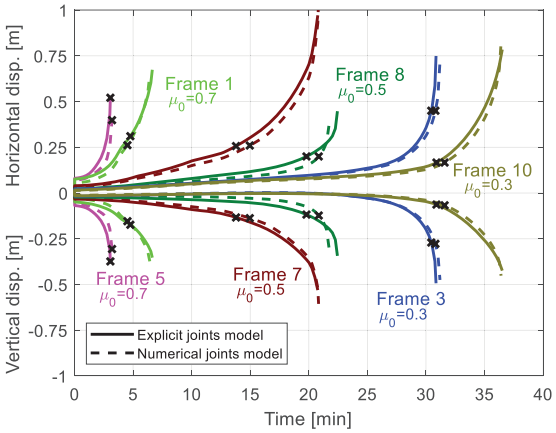

Figure 6.9. Representative vertical displacements (bottom) and horizontal displacements (top) vs. time curves of stainless steel frames under fire with explicitly modelled joints (solid lines) and numerically modelled joints (dashed lines).

Hence, the results in Figure 6.7 and Figure 6.9 indicate that it is possible to model welded full-strength joints between stainless steel RHS elements as numerical rigid joints both at room and elevated temperatures, resulting in a minimum difference in the predicted responses and frame resistances, which is in line with the results obtained for the carbon steel frames analysed in the previous section.

Note that the failure of the frames (and corresponding TFRs) is highlighted in Figure 6.9 with the marker "×" based on the failure criteria presented in Section 4.3 (i.e., Eq. 4.3-Eq. 4.6), which was validated against experimental data on carbon steel frames. However, based on the results shown in Figure 6.9, it may not seem appropriate to apply the same failure criteria defined for carbon steel frames to stainless steel frames, since it appears that for some of the analysed stainless steel frames the TFR (or collapse) is defined too early (e.g., Frame 7 with μ_0=0.5 and Frame 10 with μ_0=0.3) with the failure criteria defined in Section 4.3. For this reason, an in-depth analysis and a revision of these failure criteria for stainless steel frames is carried in out Section 8.2.

Nevertheless, these failure criteria can be preliminarily used to determine the collapse of the analysed stainless steel frames (and the corresponding TFRs) from the advanced FE models adopting the different joint modelling techniques separately, which are shown in Table 6.10 for different degrees of utilisation.

Based on the results reported in Table 6.10, it can be confirmed that the time fire resistances (TFR) obtained with the two joint modelling techniques and the failure criteria presented in Section 4.3 are in good agreement, with a mean value of TFR_E/TFR_N=0.96 and a value of the coefficient of variation COV=0.060 for the whole set of results. These results strengthen the idea that stainless steel frames

with full-strength joints (classified as such at room temperature) can be modelled using numerical rigid joints under fire situation also without affecting the predicted response of the structures.

Table 6.10. Time fire resistance (TFR) of frames with numerically modelled joints (N) and with explicitly modelled joints (E) based on the failure criteria presented in Eq. 4.3-Eq. 4.6 for stainless steel frames in fire under different degrees of utilisation (μ_0).

Frame	μ_0=0.7		μ_0=0.5		μ_0=0.3	
	TFR_E [min]	TFR_N [min]	TFR_E [min]	TFR_N [min]	TFR_E [min]	TFR_N [min]
1	4.8	4.5	13.4	14.5	28.1	30.1
2	4.0	4.1	13.6	13.9	31.3	28.9
3	5.7	5.7	18.0	19.1	30.5	30.8
4	4.8	4.8	15.5	16.6	28.4	29.3
5	3.1	3.2	11.3	12.1	23.8	24.9
6	6.2	7.2	19.2	20.0	35.3	36.4
7	8.0	8.0	13.8	15.0	30.5	31.1
8	8.3	7.4	19.8	20.8	35.9	37.1
9	6.5	7.0	12.0	12.9	30.4	33.5
10	8.3	8.0	15.3	16.3	30.9	31.6
$\frac{TFR_E}{TFR_N}$	mean	0.99	mean	0.93	mean	0.96
	COV	0.070	COV	0.049	COV	0.063

6.5. Concluding remarks

According to European structural codes (prEN 1993-1-8 (2020)), joints classified as full-strength can be modelled as perfectly rigid joints for numerical purposes with no major differences in the response of the structure. The results obtained in the study presented in this chapter, focused on multiple carbon and stainless steel frames at room temperature, support this simplification.

Moreover, the carbon and stainless steel frames modelled with explicit joints exhibited similar responses when compared to the same frames modelled with simplified rigid joints under fire situation too for different degrees of utilisation. The comparisons between the two joint modelling approaches confirm that this simplification could also be extended to fire situation for Class 1 carbon and stainless steel RHS frames that do not present any member instability issues. These results encourage the development and use of advance design FE models to assess the structural response of steel frames under fire situation more accurately, allowing more efficient designs than those resulting from simple calculation models prescribed in prEN 1993-1-2 (2021) for Class 1 frames.

Besides, this study has also proved that the new formulation provided in Chapter 5 for assessing the bending moment resistance of such welded joints can be used for more accurate joint strength classification (i.e., full- or partial-strength joints) when employing the CSM formulation in the design of stainless steel cross-sections, as it is capable of accounting for the effect of strain hardening too.

However, the results also highlight that the incorporation of the CSM formulation in the new generation of European structural codes (prEN 1993-1-4 (2021)) should come with a thorough revision of other parts of the specifications that may be affected for consistency and to guarantee an efficient design of stainless steel structures (e.g., the influence of strain hardening on the stainless steel joint resistance). Otherwise, full-strength joints could be misclassified as partial-strength joints, which will lead to non-optimal designs leading to a misuse of stainless steel as structural material.

Finally, in this chapter carbon and stainless steel frames proved to be able to redistribute internal forces at room temperature, since its ultimate load at room temperature could be estimated by means of a plastic global analysis as recognised by prEN 1993-1-1 (2019) and prEN 1993-1-4 (2021). However, if this capability is maintained at elevated temperatures is yet to be confirmed and will be studied in the subsequent chapter. Likewise, the influence of the second order effects on the frame's response at elevated temperature and the failure criteria for stainless steel frames needs to be analysed, this will be addressed in the Chapter 8.

CHAPTER 7

Redistribution capacity of carbon and stainless steel frames in fire

7.1. Introduction

The results presented in the previous chapter have proved that full-strength joints (classified as such at room temperature) are able to perform as good as ideal rigid joints even under fire situation, both for carbon and stainless steel frames. According to European standards (prEN 1993-1-1 (2019), prEN 1993-1-4 (2021) and prEN 1993-1-8 (2020)), plastic global analysis is allowed when designing carbon and stainless steel structures formed by Class 1 cross-sections and with full-strength joints at room temperature; however, whether this redistribution capacity and sufficiency of these two conditions can be extended to fire design is still unknown.

The requirements for the fire design of carbon and stainless steel structures in current standards is still primarily based on the resistance of individual members, disregarding strain hardening effects and the redistribution of internal forces that prevents the efficient design of highly redundant structures. On this basis, this chapter is devoted to analysing the redistribution capacity of carbon and stainless steel frames both at room temperature and at elevated temperatures, based on the parametric study presented in the previous Chapter 6.

7.2. Redistribution capacity of carbon steel frames

The redistribution capacity of carbon steel frames is investigated through the cases of study detailed in Section 6.3, the main characteristic of which are shown in Table 6.1, and the overall frame geometry and loading case are shown in Figure 6.1. The FE models employed are detailed in Chapter 3. The ratio between the total applied vertical load (Q) and the horizontal load (R=Q/P=q·L/P) of each frame was defined in order to trigger the combined plastic collapse mechanism, calculated as per Annex B.4. The combined plastic mechanism is characterized for being a combination of the beam mechanism (Annex B.2) and the sway mechanism (Annex B.3), forming four plastic hinges for the one bay frames with fixed supports analysed in this study (see Figure 6.1).

According to the first order plastic global analysis theory, the first plastic hinge forms at the most loaded cross-section, which is usually located at the right beam-to-column joint for the analysed loading case; for the present study cases, the first plastic hinge should form in the beam cross-section nearest to the right joint, since the plastic bending moment resistance of the beams is lower than that of the columns, $M_{pl,1}$<$M_{pl,0}$. In general, the next plastic hinges form at the right support or near the beam midspan, depending on the relationship between the second moments of inertia (I_0/I_1) and the combination of the applied loads (R). The fourth and last plastic hinge usually appears at the left support, completing the global plastic mechanism, and causing the frame collapse. This global mechanism involves all the frame elements and allows assessing the influence of the joints on the redistribution capacity of the frame.

7.2.1. Redistribution capacity at room temperature

All the analysed carbon steel frames failed describing a combined plastic mechanism, according to Figure 7.1, where the bending moment evolution at the four critical cross-sections (i.e., right joint, area near the midspan section, and column supports) is plotted as the applied horizontal load increases for Frame 3. The plastic bending moment resistances of the beam ($M_{pl,1}$) and the columns ($M_{pl,0}$) are also shown for reference. Note that although the internal forces plotted in Figure 7.1 correspond to Frame 3 with explicit joints, all the analysed frames described a similar response for the two joint modelling alternatives, as demonstrated in Chapter 6.

The first stage of the curves in Figure 7.1 is characterized by a linear increase of the bending moment at the four critical cross-sections. As the applied loads increased, the stiffness of the right joint cross-section was reduced due to the yielding of the outer fibres, which caused a reduction of the bending moment increase rate. As the loads increased and the stiffness of the right joint cross-section was

further reduced, a significant redistribution of the bending moments at the right joint and the left support could be seen. Once the plastic hinge was formed at the right joint, the bending moment at the left support started to increase rapidly until all four plastic hinges were formed and the plastic mechanism was fully developed.

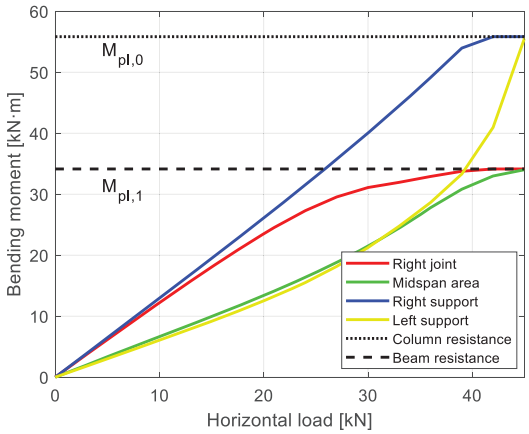

Figure 7.1. Evolution of bending moments at the four cross-sections expected to form a plastic hinge as the applied load increases according to a FE analysis.

This confirms the redistribution capacity of Class 1 structures at room temperature, a well-known capability of carbon steel frames that prEN 1993-1-2 (2019) acknowledge by allowing for plastic global analyses to be performed for frames with Class 1 cross-sections under certain situations. However, this capacity has not been yet confirmed under fire situation, and therefore, current structural codes do not allow carrying out global plastic analyses under fire situation.

After proving that the global response of the analysed carbon steel frames with explicit joints was similar to the response of the same frames with perfectly rigid joints under fire situation, the next step is to assess whether carbon steel frames are capable of redistributing internal forces at elevated temperatures, and to which extent this redistribution happens.

7.2.2. Redistribution capacity in fire situation

Figure 7.2 shows the typical response of the analysed carbon steel frames under fire situation, which corresponds to Frame 3 under a degree of utilisation of 0.3. All the analysed frames failed describing what could be defined as a global plastic mechanism, except for Frame 4 with simplified joints, which failed forming a beam plastic mechanism as it has been already stated. Note that the grey zones depicted in Figure 7.2 correspond to finite elements with plastic deformations (ε_{pl}) larger than 0.01.

Figure 7.2 shows how the deformed shape matches the expected configuration in a combined plastic mechanism, and the plastic hinges formed at the four critical cross-sections (i.e., right joint, near the midspan section, and the two column supports). Moreover, joints did not suffer any plastic deformations, resulting in an elastic response of the joints even under fire situations.

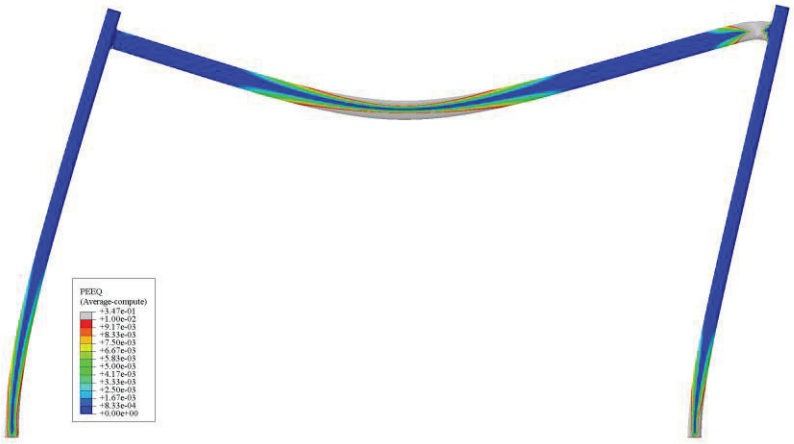

Figure 7.2. Inelastic deformation field and deformed shape just before the collapse of Frame 3 under fire situation for a degree of utilisation of 0.3.

The full development of the plastic mechanism at elevated temperatures can be verified by checking the evolution of bending moments at the four critical cross-sections. Figure 7.3 shows the evolution of these bending moments as the fire advanced in time for Frame 3, considering a degree of utilisation equal to 0.3, and explicit joint modelling. The plastic bending moment resistances of the beam ($M_{pl,1,\theta}$) and the columns ($M_{pl,0,\theta}$) at elevated temperatures are also indicated for comparison purposes.

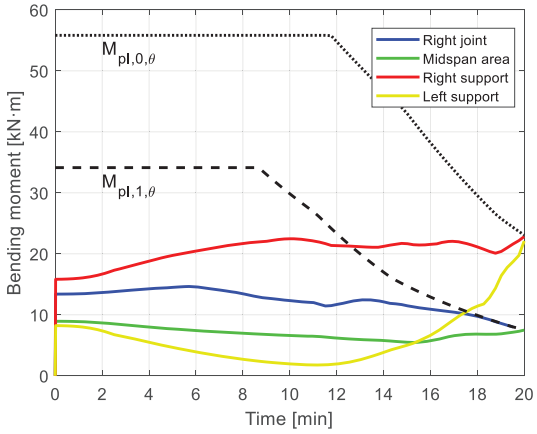

Figure 7.3. Bending moment [kN·m] evolution at the critical cross-sections over time under fire situation for Frame 3 subjected to the applied loads adopting a degree of utilisation equal to 0.3.

The starting points of the bending moments at each critical cross-section were far from the plastic resistance because the operational situation of the frame analysed in Figure 7.3 corresponds to a degree of utilisation of 0.3. As fire developed and the temperature of the frame increased, producing its thermal elongation, the right support began to withstand more load, whereas the left support unloaded. Once the member temperature surpassed 400°C —temperature that is reached at different times for the beam and the columns due to their different section factor— the plastic resistance of the members decreased. Shortly before this happened, the beam section next to the right joint reached its plastic bending moment capacity, and the left support saw its internal forces increased due to second order effects. Once the

plastic moment at the right joint was reached, the other critical cross-sections suffered a rapid increase in their internal forces until all of them reached their corresponding plastic moment resistances and the frame collapsed.

The starting points of the internal forces at the critical cross-sections for a degree of utilisation of 0.3 were low (approximately 20-40% of the corresponding plastic bending capacities). On the contrary, the adoption of a degree of utilisation of 0.7 for the same frame resulted in some cross-section exhibiting plastic deformations before the fire started. The bending moment evolution over time for the same frame (Frame 3) under a degree of utilisation of 0.7 is presented in Figure 7.4. As for μ_0=0.3, the plastic bending capacity was reached at the four critical cross-sections forming a global plastic mechanism at collapse.

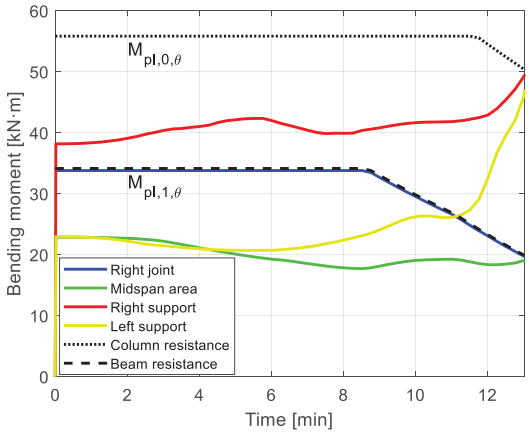

Figure 7.4. Bending moment [kN·m] evolution over time at the critical cross-sections under fire situation for Frame 3 subjected to the applied loads adopting a degree of utilisation equal to 0.7.

Figure 7.4 highlights that the right joint beam cross-section was already fully yielded when the fire started, leaving the frame in a worse position in front of an accidental fire event. Nevertheless, this frame could withstand the applied loads for 13 minutes due to its capacity for redistributing internal forces before failure. It finally collapsed after forming plastic hinges at its four critical cross-sections, describing a combined plastic mechanism similar to that presented in Figure 7.2. It is worth noting that the results presented in Figure 7.3 and Figure 7.4 correspond to Frame 3. Nevertheless, all the analysed frames formed fully developed plastic mechanisms under fire situation and exhibited similar responses too.

All carbon steel frames analysed under a degree of utilisation (μ_0) equal to a value of 0.7 started with a fully developed plastic hinge on the right joint (at room temperature). In accordance with the prEN 1993-1-2 (2021) for simplified fire design methods, the frames would not be able to withstand any increase in temperature, because the load bearing capacity of the critical elements was exhausted before the fire even started. However, according to the results obtained by means of the advanced

numerical models, the frames resisted temperatures over 500°C for the beams and over 400°C for the columns, resulting in time fire resistances ranging between 7 and 12 minutes.

The results presented in this section suggest that the investigated frames were capable of redistributing internal forces and forming plastic collapse mechanisms even under fire situations. At this stage, these results cannot be extended to all Class 1 carbon steel frames, although they suggest a new way to assess the response of steel frames under fire situation more accurately, which is further analysed and exploited in Chapter 8.

It is also worth mentioning that the investigated frames were designed with RHS members and full-strength joints, were classified as non-sway frames at room temperature, and were characterized by having no member stability issues. Obviously, frames which are susceptible of presenting member instabilities or are designed with partial strength joints will be highly dependent on the joint stiffness reduction at elevated temperatures, and may not be able to fully develop a plastic mechanism.

7.3. Redistribution capacity of stainless steel frames

As already introduced, the upcoming European code for the design of structural stainless steel prEN 1993-1-4 (2021) recognises the capacity of such structures to redistribute internal forces at room temperature, and allows the use of plastic global analysis if certain conditions are fulfilled (i.e., Class 1 cross-sections and full-strength joints). However, whether these assumptions are still valid for stainless steel frames under elevated temperatures, as it were for carbon steel frames, needs to be assessed yet and is addressed in this section.

In previous sections a first step towards the extension of plastic design for stainless steel structures in fire was carried out. Based on the results obtained from Chapter 6, welded joints between RHS members with $\beta \leq 0.85$ that are classified as full-strength joints (adopting the CSM bending resistance of the weakest connected member and using the new formulation for assessing the bending resistance of such joints presented in Section 5.4 for such classification) were found to be able to resist the increase of internal forces derived from strain hardening, and thus can be modelled as perfectly rigid joints even under fire situation.

The next step is to assess how much redistribution capacity stainless steel frames with Class 1 cross-section and full-strength joints exhibit under elevated temperatures, and whether this is sufficient to justify the adoption of plastic global analysis in design. With this in mind, the redistribution capacity of the stainless steel frames presented in Section 6.4 is assessed in this section. The main characteristics of the analysed frames are shown in Table 6.5, and the overall frame geometries and loading cases are shown in Figure 6.1. The FE models employed are detailed in Chapter 3.

7.3.1. Redistribution capacity at room temperature

As for the carbon steel frames analysed, the load ratios (R) adopted for stainless steel frames and reported in Table 6.5 were defined in order to trigger the combined collapse mechanism (Annex B) in all frames. This type of global mechanism allows assessing the influence of the joints on the redistribution capacity of the frames, because it involves all frame components, and thus is useful to assess the plastic redistribution capacity of stainless steel frames under fire situation.

As explained for carbon steel frames in Section 7.2, the expected development of the combined collapse mechanism in the investigated structures is the following: the first plastic hinge should form at the beam cross-section nearest to the right joint (since $M_{csm,1}$<$M_{csm,0}$). Then, the next plastic hinges should form at the right support or near the beam midspan, depending on the relationship between the second moments of inertia (I_0/I_1), the bending moment resistances ($M_{csm,0}/M_{csm,1}$) and the applied loading case (R). Finally, the fourth and last plastic hinge should appear at the left support, completing the combined plastic mechanism and causing the collapse of the frame.

The redistribution capacity of the analysed stainless steel frames is assessed and discussed below through the analysis of the evolution of the bending moments at the four key cross-sections expected to form a plastic hinge (i.e., at the beam cross-section closest to the right joint, at the midspan zone of the beam and at both supports). This bending moment evolution is shown in Figure 7.5 for Frame 3 and Frame 8, which exhibit performances representative of all the analysed stainless steel frames. The bending moment evolutions at the four key cross-sections were obtained by means of the FE models with explicitly modelled joints at room temperature, and the plastic bending resistance and the CSM bending resistance of the columns ($M_{pl,0}$ and $M_{csm,0}$) and the beam ($M_{pl,1}$ and $M_{csm,1}$) are also plotted in these figures for comparison.

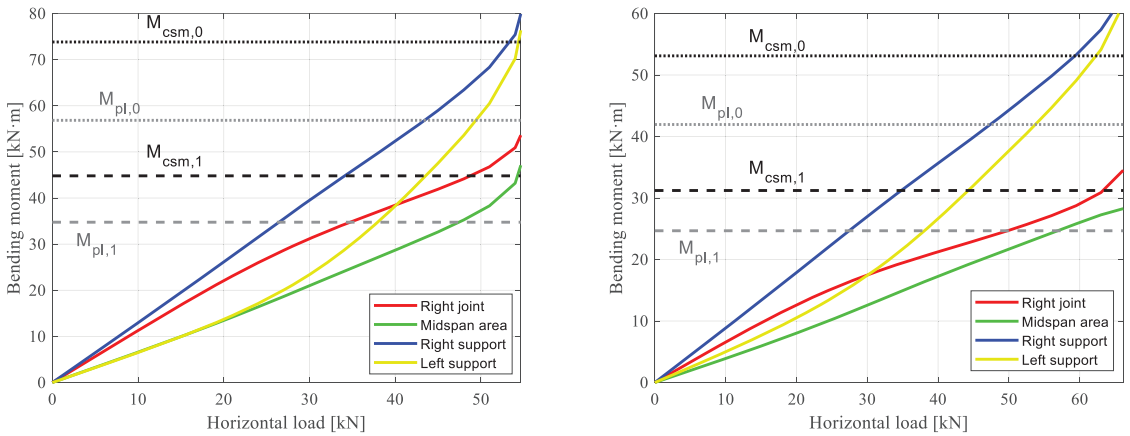

Figure 7.5. Evolution of bending moments in (a) Frame 3 and (b) Frame 8 at the four cross-sections expected to develop plastic hinges for increasing loading at room temperature.

The evolution of internal forces depicted in Figure 7.5 represent the perfect development of a combined collapse mechanism. During the first load increments, the bending moment at all four cross-sections increased linearly, with a stiffness that depended on the loading case assumed, the frame geometry, and the relationship between the second moments of inertia (I_0/I_1). But as the bending moments at the right joints corresponding to the beams approached their theoretical plastic bending moment (M_{pl}=$W_{pl}\cdot f_y$), the effects of the material nonlinearity become more relevant and the increase rate of the bending moment reduced. The load applied after that was redistributed towards the left supports, which saw an intensification at their bending moment increase rate, while the midspan zones and the right supports kept increasing their bending moment linearly. At the end, when all four cross-sections had exceeded their corresponding plastic bending moment resistances (M_{pl}), the bending moments increased rapidly until the ultimate load ($P_{u,FE}$) of the frames was reached, developing a combined collapse mechanism, and reaching the CSM bending resistance (M_{csm}) at each cross-section.

It is worth noting that, for all the analysed stainless steel frames, the plastic hinges expected to form at the beam midspan areas were always subjected to bending moments lower than those of the plastic hinges formed at the beam cross-sections near the right joints when subjected to the corresponding ultimate loads ($P_{u,FE}$). This is because the midspan area in which the "plastic hinges" were formed was far from being an ideal hinge, with all the rotation concentrated at a single cross-section, but represented a clear example of a plastic zone that spread over 1/3 of the beam length at the midspan area according to the FE model results. A representative deformed shape of the analysed frames and the Von Misses stress [N/m^2] field distribution is shown in Figure 7.6. Grey parts correspond to zones surpassing the yield stress (i.e., $\sigma > f_y = f_{0.2}$).

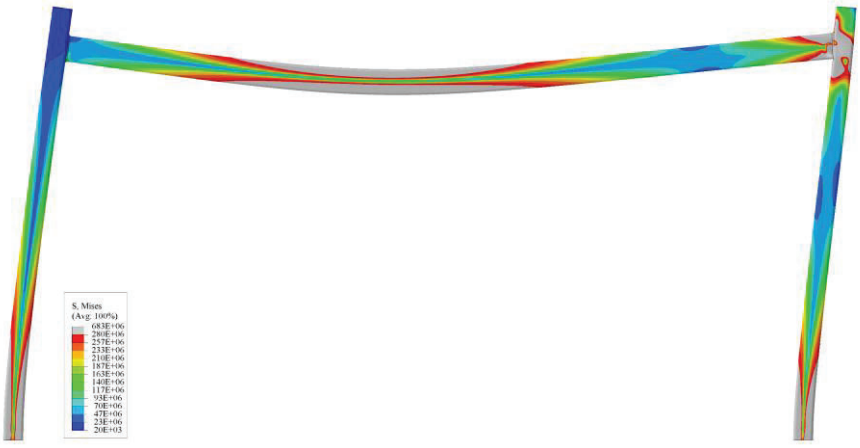

Figure 7.6. Deformed shape and Von Misses [N/m^2] field distribution of Frame 8 at room temperature according to FE models with explicit joints.

Overall, all the analysed stainless steel frames were able to form a combined collapse mechanism and showed a great redistribution capacity at room temperature, reaching or exceeding the CSM bending resistance in most of the critical cross-sections. Moreover, the welded joints were capable of resisting

the increase of internal forces arising from strain hardening effects, and proved to provide the required redistribution capacity to develop complete plastic failure mechanisms. The results also proved that the overstrength of stainless steel welded joints due to strain hardening is at least as good as the overstrength occurring at the cross-sections, which can be estimated using the CSM formulation (prEN 1993-1-4 (2021)). Otherwise, the observed failure of the frames would have been governed by the joint failure, which would occur before the first plastic hinge formed at the beam near the right joint. If that was the case, the plastic hinge formed at the right joint would have not been able to reach the CSM bending resistance of the beam ($M_{csm,1}$), and would have failed once the bending resistance of the joint was reached, which was not the behaviour observed in the analysed frames, as shown in Figure 7.5.

As it can be also seen in Figure 7.5, most cross-sections were able to reach higher bending moments than the predicted CSM bending moment capacities (given by Eq. 2.50). This is due to the cut-off adopted in the CSM approach, which is a limitation of the current formulation of the CSM base curve (Eq. 2.45) included in prEN 1993-1-4 (2021), where the maximum deformation is limited by $C_1 \cdot \varepsilon_u/\varepsilon_y$ and the parameter Ω. While the $C_1 \cdot \varepsilon_u/\varepsilon_y$ limit is related to the adopted stress–strain material model, and ensures no significant over-predictions of the resistance occurs, the parameter Ω controls the maximum permissible level of plastic strain in the structure (i.e., $\varepsilon_{csm}/\varepsilon_y \leq \Omega$), and it is usually assumed to be equal to 15 (prEN 1993-1-4 (2021)). Of course, these limitations only affect cross-sections that are very stocky (i.e., $\overline{\lambda}_p$<0.33 at room temperature for the materials employed in this study), but most of the cross-sections used in this study corresponded to this case. Due to this limitation, the analytical estimation of the bending moment capacity based on the CSM formulation (M_{csm}) was always below the reached bending moment (M_{FE}) according to FE analysis, except for the "plastic hinge" developing at the midspan area that was spread through 1/3 of the beam length.

7.3.2. Redistribution capacity in fire situation

As it has been already introduced in Chapter 6, two different stainless steel grades (EN 1.4301 and EN 1.4401) were assessed in this study, which have the same stress–strain relationship at room temperature since their main mechanical properties were obtained from the literature (Afshan et al. 2019). However, their response at elevated temperature differs, because according to prEN 1993-1-2 (2021) they belong to different subgroups of reduction factors (Austenitic I and Austenitic II).

As it happens for the performance of stainless steel frames at room temperature, one may expect strain hardening to play a major role on the response of these structures at elevated temperatures too, as a result of the large deformations developed. This could be addressed by using a modified Continuous Strength Method approach for fire design, but the extension of the Continuous Strength Method formulation has not been addressed yet for the design at elevated temperatures. For this reason, a preliminary adaptation of the current CSM formulation for room temperature is proposed in this thesis

to estimate the resistance of stainless steel cross-sections at elevated temperatures accounting for strain hardening.

In this new formulation, the CSM strain limit at elevated temperatures ($\varepsilon_{csm,\theta}$) is calculated as per Eq. 7.1, based on the original equation Eq. 2.45, while the CSM bending moment capacity at elevated temperatures is estimated as per in Eq. 7.2, which is based on the original formulation for room temperature too (see Eq. 2.50). Since the topic of this study is the plastic design of structures in fire, the extension of the two equations is only carried out for plastic cross-sections (Class 1).

$$\frac{\varepsilon_{csm,\theta}}{\varepsilon_{y,\theta}} = \frac{0.25}{\bar{\lambda}_{p,\theta}^{\,3.6}} \leq \min\left(\Omega, C_1 \cdot \frac{\varepsilon_{u,\theta}}{\varepsilon_{y,\theta}}\right) \qquad for\ \bar{\lambda}_{p,\theta} \leq 0.68 \qquad \text{Eq. 7.1}$$

$$M_{csm,\theta} = W_{pl} f_{0.2,\theta} \cdot \left[1 + \frac{E_{sh,\theta}}{E_\theta} \cdot \frac{W_{el}}{W_{pl}} \cdot \left(\frac{\varepsilon_{csm,\theta}}{\varepsilon_{y,\theta}} - 1\right) - \left(1 - \frac{W_{el}}{W_{pl}}\right) \cdot \left(\frac{\varepsilon_{csm,\theta}}{\varepsilon_{y,\theta}}\right)^{-\alpha}\right] \qquad for \frac{\varepsilon_{csm,\theta}}{\varepsilon_{y,\theta}} \geq 1.0 \qquad \text{Eq. 7.2}$$

The ultimate strain at elevated temperatures was calculated as per $\varepsilon_{u,\theta}$=C_1(1-$f_{2.0,\theta}/f_{u,\theta}$), following the prEN 1993-1-2 (2021) prescriptions (where the 2.0% proof stress is used to estimate the ultimate strain of the stress–strain curves for stainless steel alloys), and the same C_1 material parameter codified in prEN 1993-1-2 (2021) for room temperature. In contrast, the proof stress at a 0.2% strain ($f_{0.2,\theta}$) was used to calculate the strain hardening modulus at elevated temperatures ($E_{sh,\theta}$) and in the CSM bending moment resistance ($M_{csm,\theta}$), as shown in Eq. 7.2. More information on the CSM resistance equations at room temperature can be found in Section 2.3. Likewise, the 0.2% proof stress ($f_{0.2,\theta}$) was used to calculate the relative local slenderness ($\bar{\lambda}_{p,\theta}$) as shown in Eq. 7.3, updating the values of the proof stress ($f_{0.2,\theta}$) and the Young modulus (E_θ) according to the temperature (θ).

$$\bar{\lambda}_{p,\theta} = \sqrt{\frac{f_{0.2,\theta}}{\sigma_{cr,\theta}}} \qquad \text{Eq. 7.3}$$

As it has been already demonstrated in the previous section, the investigated stainless steel frames were able to form the four expected plastic hinges (or plastic zones) and form global plastic failure mechanisms at room temperature exhibiting significant strain hardening. Similarly, this section investigates the plastic redistribution capacity of the same stainless steel frames at elevated temperatures, assessing the evolution of bending moments at the four critical cross-sections over time.

The results are presented for degrees of utilisation of 0.7 and 0.3 for Frame 3 (in Figure 7.7(a) and Figure 7.7(b), respectively) and Frame 8 (in Figure 7.7(c) and Figure 7.7(d), respectively). As in the previous section, the plotted curves correspond to the FE models with explicitly modelled joints, and the bending moment resistances of the beams and columns corresponding to the plastic section capacity ($M_{pl,\theta}$) and the CSM ($M_{csm,\theta}$) are also shown as function of the temperature. Following the prEN 1993-

1-2 (2021) recommendations, the plastic moment at elevated temperatures was calculated using the proof stress $f_{2.0}$ as per $M_{pl,\theta}=W_{pl}\cdot f_{2.0}\cdot k_{2.0,\theta}$. This approach already considers part of the strain hardening inherent to stainless steels at elevated temperatures, but introduces some inconsistences with the European code (prEN 1993-1-4 (2021)) for the design of stainless steel structures at room temperature, as explained in Section 2.5.2.

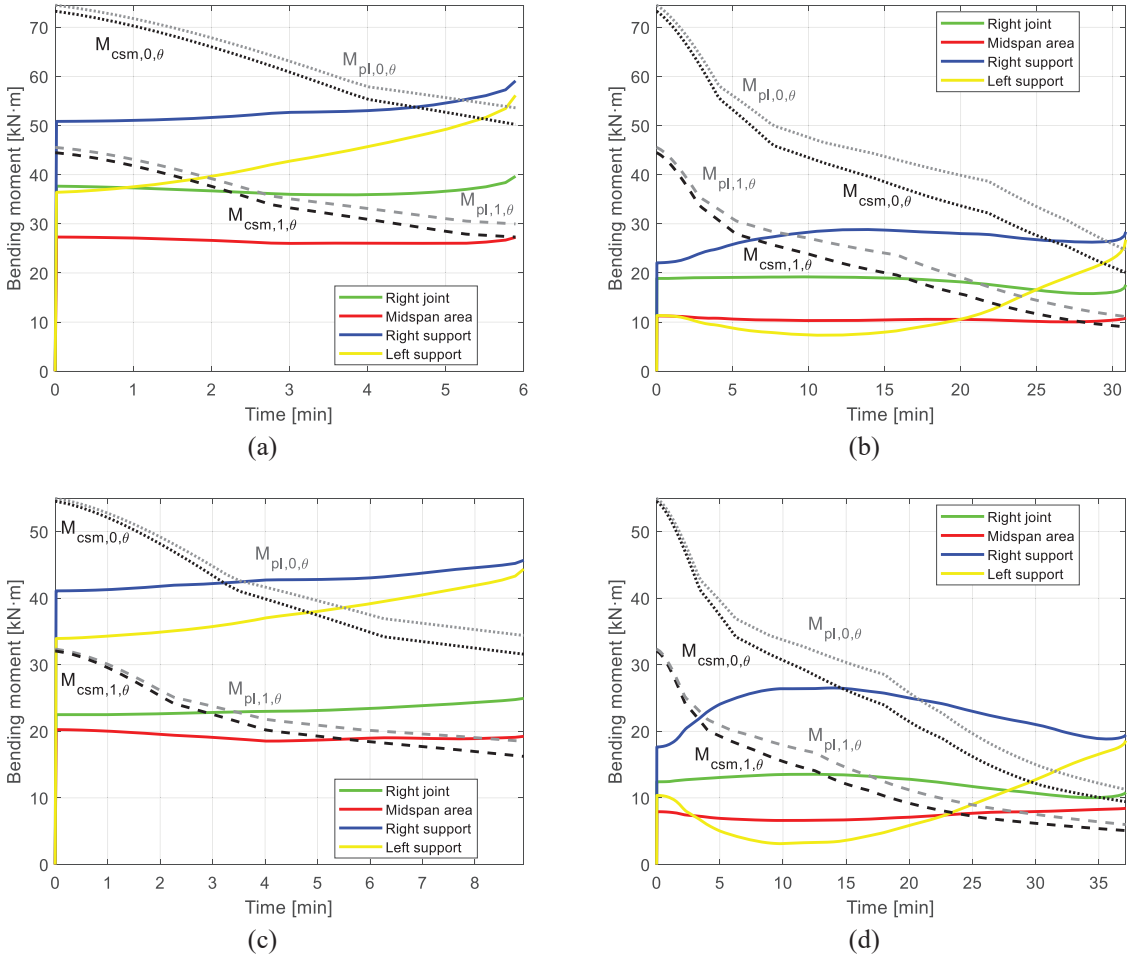

Figure 7.7. Evolution of bending moments over time at the four cross-sections expected to develop plastic hinges for Frame 3 (a) with μ_0=0.7 and (b) with μ_0=0.3, and for Frame 8 (c) with μ_0=0.7 and (d) with μ_0=0.3 under fire situation.

In contrast to what happens at room temperature for stainless steel structures, where the plastic bending resistance (M_{pl}) is calculated using the $f_{0.2}$ proof stress as the yield stress – thus disregarding all strain hardening effects (see Figure 7.5)–, at elevated temperatures the European code for fire design (prEN 1993-1-2 (2021)) recommends the use of the $f_{2.0}$ proof stress as the yield stress for simplified design methods. Therefore, the plastic bending resistance at elevated temperatures ($M_{pl,\theta}$) considers to some extend the over-strength derived from strain hardening, and provides bending moment resistance estimations similar to those obtained using the adapted CSM formulation for elevated temperatures (Eq. 7.1-Eq. 7.2). Nevertheless, both formulations failed at providing accurate bending moment resistance estimations at elevated temperatures for the cross-sections shown in Figure 7.7, where the bending

moments obtained from the FE analyses exceed both predictions. This is because most of the adopted cross-sections were very stocky (i.e., $\overline{\lambda}_p \leq 0.33$ at room temperature), and the additional resistance arising from strain hardening (represented by the $\varepsilon_{csm}/\varepsilon_y$ ratio) was limited by the deformation limit $\Omega=15$ in the CSM formulation, underestimating to some extent the cross-section resistance. Likewise, and although the plastic bending resistance based on the $f_{2.0}$ proof stress is a useful linear approach to a more complex nonlinear phenomenon, it was found to fail accounting for the relative local slenderness ($\bar{\lambda}_p$) of the cross-sections.

As it can be seen in Figure 7.7(a) and Figure 7.7(c), for both Frame 3 and Frame 8 the four critical cross-sections were heavily loaded when the fire started when a degree of utilisation of $\mu_0=0.7$ was assumed; for instance, for Frame 3 (Figure 7.7(a)) the bending moment at the beam cross-section nearest to the right joint already exceeded the plastic bending moment capacity at room temperature calculated as $M_{pl,1}=W_{pl,1}\cdot f_{0.2}$ (equal to 34.8 kN·m according to Table 6.6). Similar results were observed for the other stainless steel frames analysed in this study too when high degrees of utilisation were adopted. As the fire developed and the temperature increased, the bending resistances of the beam and the columns decreased due to the loss of mechanical properties, until all four critical cross-sections exceeded their CSM bending resistances ($M_{csm,\theta}$) and the plastic bending resistances ($M_{pl,\theta}$), both calculated as explained above.

Conversely, when the results corresponding to a degree of utilisation of $\mu_0=0.3$ are analysed in Figure 7.7(b) and Figure 7.7(d), it can be seen that the initial bending moment at each critical cross-section was far from the cross-section bending resistance at the beginning. Once the fire started, the bending moments remained constant at the beam cross-section near the right joint and at the beam cross-section located near the midspan area, whereas both supports suffered a variation on bending moments as a result of the thermal expansion, which was prevented to some extent due to the stiffness provided by the columns. Not allowing the beam to freely expand produced further axial forces at the beam, which generated additional bending moments at the frame supports. Then, once the beam cross-section near the right joint yielded, the bending moments redistributed towards the left support until failure, which occurred once all four cross-sections surpassed the CSM bending resistance and the plastic bending resistance, similar to what happened at room temperature (see Figure 7.5).

It should be pointed out, once again, that the bending moment at the beam cross-section near the midspan zone was always lower than the bending moment reached at the beam cross-section near the right joint (see Figure 7.7), as it happened at room temperature (see Figure 7.5 and Figure 7.6). This phenomenon occurred because the "plastic hinge" expected to form near the midspan area developed into a plastic zone according to the obtained FE results. This phenomenon can be clearly observed in Figure 7.8, where the Von Misses stress [N/m^2] field is plotted onto the deformed shape of Frame 3

before collapse under a degree of utilisation of 0.5, where the four plastic zones can be clearly identified. Zones marked in grey correspond to areas that exceed the proof stress corresponding to a plastic deformation of 2% ($f_{2.0,\theta}$).

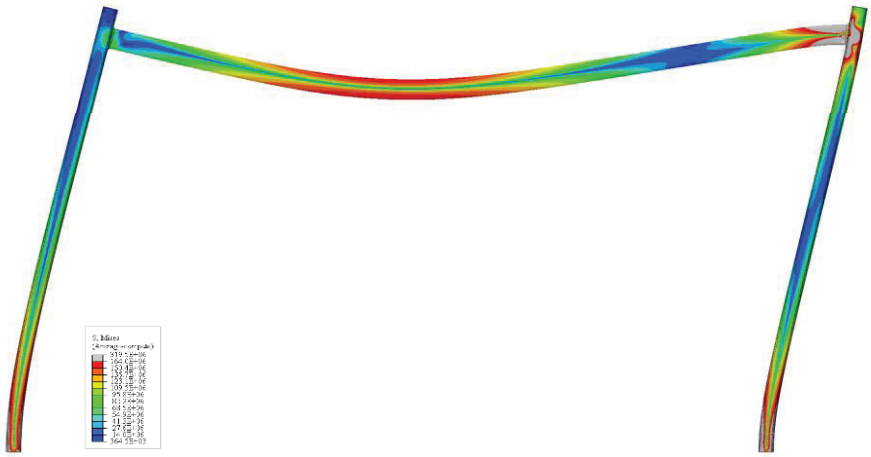

Figure 7.8. Von Misses stress field [N/m^2] and deformed shape just before the collapse of Frame 3 under fire situation for a degree of utilisation of μ_0=0.5.

In any event, Frame 3 formed a plastic mechanism before collapsing, as shown in Figure 7.8, as well as all the other analysed stainless steel frames, and they were capable of redistributing internal forces before failure at elevated temperatures for different degrees of utilisation, as Figure 7.7 proved for Frame 3 and Frame 8 as representatives for the analysed frames.

The fact that stainless steel frames are able to redistribute internal forces at elevated temperatures is promising. At this stage, these results cannot be extended to all Class 1 stainless steel frames, since the upcoming codes (prEN 1993-1-2 (2021)) do not allow for plastic analyses to be carried out under fire situation for stainless steel frames – neither do they for carbon steel frames –, but the results presented herein suggest a new procedure to assess the response of stainless steel frames under fire situation more accurately. It is also worth mentioning that the investigated frames were designed with RHS and full-strength joints, and were characterized by having no member stability issues, as for the carbon steel frames analysed in this chapter. Obviously, frames susceptible of presenting member instabilities or which are designed with partial strength joints will be highly dependent on the reduction of the mechanical properties of the joint at elevated temperatures, and may not be able to fully develop plastic mechanisms.

7.4. Concluding remarks

The redistribution capacity of carbon and stainless steel structures at room temperature, already acknowledged by prEN 1993-1-1 (2019) and prEN 1993-1-4 (2021), has been confirmed by means of numerical simulations, and the results obtained in the present study confirm the capability of these structures to redistribute forces and form plastic collapse mechanisms.

Furthermore, the analyses presented in this section suggest that carbon and stainless steel frames exhibit excellent redistribution capacity at elevated temperatures also, being capable of forming plastic collapse mechanisms even when subjected to high initial loads (i.e., degrees of utilisation of μ_0=0.7). This redistribution capacity suggests the possibility of developing more accurate analytical formulations for estimating the resistance of carbon and stainless steel frames under fire situation accounting for their redistribution capacity.

In this regard, the assessment of the plastic redistribution capacity of stainless steel frames reported in this section has demonstrated that the CSM formulation is capable of accounting for strain hardening effects at room temperature and at elevated temperatures, by adopting the adaptation of the current CSM formulation to elevated temperatures proposed in this chapter. However, the results also showed that further research is needed for remarkably stocky cross-sections – i.e., those sections affected by the maximum CSM plastic deformation limit of Ω=15. Likewise, the plastic bending resistance at elevated temperatures based on the $f_{2.0}$ proof stress, as currently prescribed in prEN 1993-1-2 (2021), proved to be able to partially account for strain hardening effects of stainless steel alloys.

CHAPTER 8

New proposals for the plastic design of carbon and stainless steel frames in fire

8.1. Introduction

Throughout this document, it has been demonstrated that both carbon and stainless steel structures are capable of redistributing internal forces and developing plastic collapse mechanisms in fire if the analysed structure is formed by full-strength joints and Class 1 cross-sections.

As demonstrated in Chapter 6, full-strength joints (classified as such at room temperature) provide enough stiffness under fire situation so that their response can be compared to the response of perfectly rigid joints. Moreover, full-strength joints have been proved to exhibit enough resistance under fire situation and could withstand the increase of internal forces derived from strain hardening – for those made of stainless steel – even at elevated temperatures. Therefore, the analysed joints could be modelled as perfectly rigid joints under fire situation without modifying the frame fire resistance.

Likewise, carbon and stainless steel Class 1 cross-sections have proved their capacity of redistributing internal forces under fire situation, as demonstrated in Chapter 7. The rotation capacity exhibited by the analysed cross-sections was sufficient to accommodate the displacements needed to develop a plastic collapse mechanism even under fire situation.

Nevertheless, the upcoming design code (prEN 1993-1-2 (2021)) for fire design disregard the potential redistribution capacity of carbon and stainless steel structures when the simplified design methods are adopted under fire situation, and leave to the designers' experience the assessment of the structural collapse in fire when employing advanced design methods. It is hence fundamental to develop new proposals for the plastic design of carbon and stainless steel frames in fire to guarantee safe and efficient structures. With this in mind, this chapter carries out an in-depth revision of the failure criteria to determine the structural collapse by means of FE analysis for stainless steel frames in Section 8.2, based on the failure criteria proposed and validated in Section 4.3 for carbon steel frames in fire. In addition, a new analytical approach to assess the fire resistance of carbon and stainless steel frames in fire is presented in Section 8.3, which is based on plastic global analysis and accounts for their redistribution capacity at elevated temperatures.

8.2. Fire design based on advanced numerical models

In contrast with the response of carbon and stainless steel frames at room temperature, where the ultimate load can be commonly identified as the peak load of the load–displacement curve, the procedure for defining the time fire resistance and the corresponding critical temperature of such frames is unclear under fire situation when advanced numerical models are used for the design. To address this issue, new failure criteria were presented in Section 4.3 for determining the time fire resistance (TFR) and its correspondent critical temperature (θ_{cr}) for such structures, but they were only validated for carbon steel frames since no stainless steel frames have been tested in fire up to date.

Stainless steel structures are known for describing larger displacements than carbon steel structures before collapsing, which was confirmed in Chapter 6 by comparing the ultimate displacements reached by stainless steel frames and carbon steel frames at room and elevated temperatures. For more information, the reader is referred to the results presented in Figure 6.2 vs. Figure 6.7, and Figure 6.4 vs. Figure 6.9. Therefore, it may not be reasonable to apply the same displacement limits and displacement rate limits to carbon and stainless steel structures in fire when defining their collapse in Ultimate Limit State.

The failure criteria for carbon steel structures presented in Section 4.3 are reproduced in Eq. 8.1-Eq. 8.4. These failure criteria were validated for carbon steel frames against experimental data of

laboratory tests carried out obtained from the literature, for more information the reader is referred to Section 4.3.

For vertical displacements:

$$D_v = \frac{L^2}{400 \cdot h_1} \text{ [mm]} \quad \text{Eq. 8.1}$$

$$\frac{dD_v}{dt} = \frac{L^2}{9000 \cdot h_1} \cdot 10\mu_0 \text{ [mm/min]} \quad \text{Eq. 8.2}$$

For horizontal displacements:

$$D_h = 2 \cdot \frac{H^2}{400 \cdot h_0} \text{ [mm]} \quad \text{Eq. 8.3}$$

$$\frac{dD_h}{dt} = \frac{H^2}{9000 \cdot h_0} \cdot 10\mu_0 \text{ [mm/min]} \quad \text{Eq. 8.4}$$

After assessing the stainless steel frames in previous chapters, it could be determined that the limiting failure criterion for stainless steel frames was the displacement rate limit. Therefore, in order to analyse the accuracy of the failure criteria shown in Eq. 8.1 to Eq. 8.4 for the analysed stainless steel frames, the displacement rate [mm/min] was normalized to a comparable variable [min^{-1}] that was independent of the geometry of the frame and the cross-sections used. These normalized comparable variables are shown in Eq. 8.5-Eq. 8.6, and the evolution over time of these two new variables $const_v$ and $const_h$ is shown in Figure 8.1 for some representative stainless steel frames under different degrees of utilisation. Note that these frames correspond to the parametric study presented in Chapter 6; for more information on these frames, please see Table 6.5 in Chapter 6. The limiting value of the variables $const_v$ and $const_h$ is, according to the original failure criteria, $10 \cdot \mu_0/9000$ (see Eq. 8.2 and Eq. 8.4).

$$const_h = \frac{dD_h}{dt} \cdot \frac{h_0}{H^2} \text{ [min}^{-1}\text{]} \quad \text{Eq. 8.5}$$

$$const_v = \frac{dD_v}{dt} \cdot \frac{h_1}{L^2} \text{ [min}^{-1}\text{]} \quad \text{Eq. 8.6}$$

Figure 8.1 shows, along with the evolution of $const_h$ (Eq. 8.5) and $const_v$ (Eq. 8.6), the normalized displacement rate limits calculated using the original failure criteria, as per equations Eq. 8.2 and Eq. 8.4. According to the results presented in Figure 8.1, these original limits seem to be too conservative for the analysed frames, since stainless steel frames are characterized by describing larger displacements – and large displacement rates – before collapsing (González-de-León 2022).

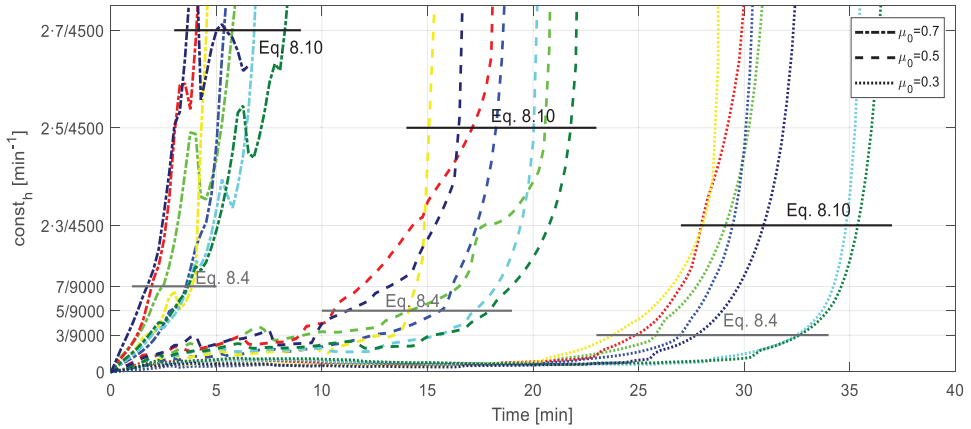

(a)

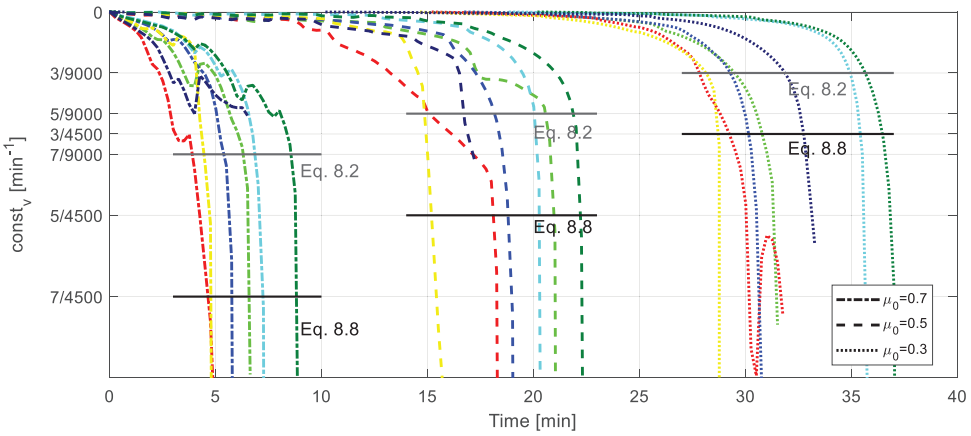

(b)

Figure 8.1. Development over time of the variables (a) $const_h$ and (b) $const_v$ for some representative stainless steel frames under different degrees of utilisation, calculated according to Eq. 8.5 and Eq. 8.6, respectively.

Figure 8.1 suggests that the original normalized displacement rate limits cut the normalized displacement rate–time curves too soon for certain degrees of utilisation (e.g., μ_0=0.3), even before the vertical asymptotes that reflect the rapid collapse of the frames due to the attainment of their critical temperature are reached. This indicates that new limits are necessary for stainless steel frames, and therefore it is proposed that the displacement rate limits are doubled compared to previous limits for stainless steel structures (i.e., from $10 \cdot \mu_0/9000$ to $10 \cdot \mu_0/4500$). The proposed failure criteria are reproduced in Eq. 8.7 to Eq. 8.10. Note that the displacement limits have been keep equal, while the displacement rate limits have been modified and are shown in Figure 8.1. The reason behind keeping the displacement limits equal is that this failure criterion was not determining the collapse of stainless steel frames in fire (since both failure criteria should be surpassed), but the displacement rate criterion was the limiting condition. Therefore, after a comprehensive analysis of the displacements rates in stainless steel frames in fire, a new proposal was presented that captures the collapse of such structures in fire in a more accurate way.

For large vertical displacements:

$$D_v = \frac{L^2}{400 \cdot h_1} \text{ [mm]} \quad \text{Eq. 8.7}$$

$$\frac{dD_v}{dt} = \frac{L^2}{4500 \cdot h_1} \cdot 10\mu_0 \text{[mm/min]} \quad \text{Eq. 8.8}$$

For large horizontal displacements:

$$D_h = 2 \cdot \frac{H^2}{400 \cdot h_0} \text{ [mm]} \quad \text{Eq. 8.9}$$

$$\frac{dD_h}{dt} = 2 \cdot \frac{H^2}{4500 \cdot h_0} \cdot 10\mu_0 \text{[mm/min]} \quad \text{Eq. 8.10}$$

It is worth noting that the original horizontal displacement limit (Eq. 8.3) was assumed to be twice the vertical displacement limit (Eq. 8.1). The reason behind this is that for the type of frames analysed, the horizontal displacement is measured at the top end of the column – which works as a cantilever under bending forces –, while the vertical displacement is measured at the beam midspan. Thus, it was deemed reasonable to double the limit for vertical displacement when proposing the horizontal displacement limit. However, this increase on the horizontal displacement limits was not originally applied to the horizontal displacement rate limit, inconsistency that has been corrected in this final proposal (see Eq. 8.10). Therefore, the failure of stainless steel frames shall be assumed to be reached when both criteria – i.e., Eq. 8.7 and Eq. 8.8 for vertical deflections, or Eq. 8.9 and Eq. 8.10 for horizontal displacements – have been exceeded. For frames describing large horizontal and vertical displacements (e.g., frames forming a combined collapse mechanism), the most restrictive pair of limits should be used.

Based on these redefined failure criteria, the time fire resistances (TFR) of the frames presented in Chapter 6 can be obtained. The typical vertical and horizontal displacement–time curves of some representative stainless steel frames are shown in Figure 8.2, where the TFRs corresponding to the proposed failure criteria are highlighted with the "×" marker.

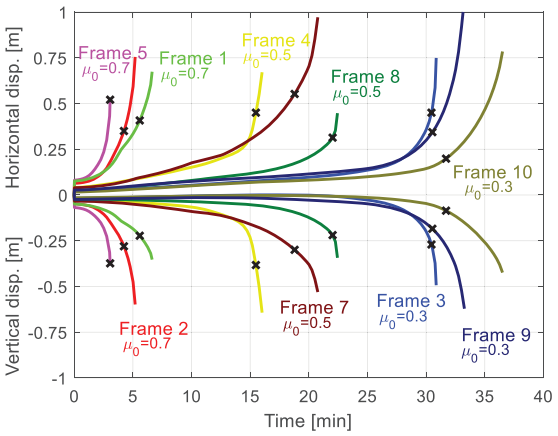

Figure 8.2. Vertical displacements (bottom) and horizontal displacements (top) vs. time curves of representative stainless steel frames under fire situation, along with their corresponding failure (Eq. 8.7-Eq. 8.10).

Moreover, for those frames not describing a monotonically increasing displacement slope (see the horizontal displacement–time curve for Frame 1 under μ_0=0.7 in Figure 8.2), the TFR should be assumed as the first time step in which the displacement rate limit is exceeded after the local minimum. It should be bear in mind that the proposed failure criteria should only be applied to determine the failure of stainless steel frames analysed by means of advanced FE modelling. And that for those frames not reaching the failure criteria before the last converged step, the time fire resistance – and its associated critical temperature – needs to be assumed as the last converged time step.

The time fire resistances (TFR) obtained with the new proposed failure criteria, marked with "×" for the stainless steel frames presented in Figure 8.2, are reported in Table 8.1 for the entire dataset, along with the corresponding critical temperatures at the columns ($\theta_{cr,0}$) and the beams ($\theta_{cr,1}$) corresponding to the FE analyses with explicitly modelled joints.

Table 8.1. Time fire resistance (TFR) of stainless steel frames with explicitly modelled joints (E), along with the corresponding critical temperatures (θ_{cr}) under different degrees of utilisation (μ_0).

Frame	μ_0=0.7			μ_0=0.5			μ_0=0.3		
	TFR_E [min]	$\theta_{cr,0}$ [°C]	$\theta_{cr,1}$ [°C]	TFR_E [min]	$\theta_{cr,0}$ [°C]	$\theta_{cr,1}$ [°C]	TFR_E [min]	$\theta_{cr,0}$ [°C]	$\theta_{cr,1}$ [°C]
1	5.6	149	287	20.5	589	748	28.9	746	818
2	4.2	129	284	17.8	590	741	31.3	802	837
3	5.7	149	220	18.6	521	666	30.5	751	815
4	4.8	178	328	15.5	587	712	28.4	799	823
5	3.1	175	234	11.8	549	608	24.2	752	768
6	6.9	268	362	20.1	698	748	35.3	847	855
7	8.0	305	415	18.8	673	735	30.9	820	833
8	8.6	287	444	22.0	688	767	35.9	840	857
9	9.5	332	430	16.3	697	728	30.5	831	836
10	9.0	306	467	21.5	681	764	31.7	812	837

Table 8.1 highlights the big influence that the degree of utilisation has on the time fire resistance of stainless steel frames, as Figure 8.2 suggested. Frames subjected to high initial loads (i.e., μ_0=0.7) could not withstand the fire action beyond the 10 minutes mark, while most frames subjected to a degree of utilisation of 0.5 could resist the effect of the fire for nearly 20 minutes. Alternatively, most of the investigated stainless steel frames subjected to μ_0=0.3 could resist more than 30 minutes without using any protection, which is, for example, the required time fire resistance for detached houses according to the Spanish building construction code (CTE 2006). This feature is one of the main competitive advantages of stainless steel structures against traditional carbon steel structures – which could not withstand the fire effects for, since the latter could not reach TFR near the 30 minutes mark even for low initial load thus they need to be protected to meet the most basic fire safety requirements, while

stainless steel structures are often capable of meeting these fire safety prescriptions without any protection under certain conditions.

Needless to say, the response of stainless steel frames under fire situation differs depending on the stainless steel type conforming the structure (i.e., austenitic, ferritic or duplex) and the grade selected, due to the differences in thermal and mechanical properties at elevated temperatures of each particular grade, and the results obtained in this study using the two most common austenitic stainless steel grades (EN 1.4301 and EN 1.4401) cannot be extended to all stainless steel alloys. Nevertheless, the stainless steel grades considered are not characterized for having the best mechanical properties at elevated temperatures; quite the opposite – especially for the grade EN 1.4301 – when compared to other stainless steel grades according to prEN 1993-1-2 (2021). For more information, the reader is referred to Section 2.5.1.

As demonstrated in Section 6.3.3 for carbon steel frames subjected to a uniform temperature field, the critical temperature (and its corresponding TFR) of a frame describing a plastic collapse mechanism follows the evolution curve of the reduction factor of the yield stress relative to their degree of utilisation (Figure 6.6). This trend is further analysed in Figure 8.3, where the critical temperatures of the investigated carbon and stainless steel frames are plotted together with the corresponding reduction factors of the yield stress ($k_{y,\theta}$). From Figure 8.3, similar conclusions to those highlighted in Section 6.3.3 can be drawn for carbon and stainless steel frames. In previous results shown the frames had a uniform cross-section distribution along the whole structure, however in the presented cases in Figure 8.3 the beam and the columns were at different temperatures when subjected to fire due to their different section factor (S_m).

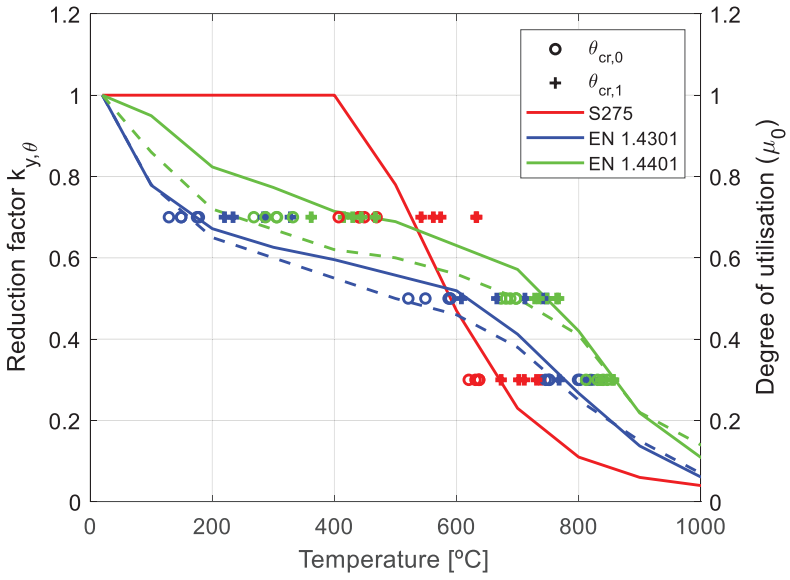

Figure 8.3. Critical temperature of the beam ($\theta_{cr,0}$) and the columns ($\theta_{cr,1}$) for different degrees of utilisation (μ_0) along with the yield stress reduction factors ($k_{y,\theta}$) at elevated temperatures for several carbon and stainless steel materials. For stainless steels, both $k_{0.2,\theta}$ (dashed line) and $k_{2.0,\theta}$ (solid line) reduction factors are plotted.

As it can be seen, the pair of critical temperatures ($\theta_{cr,0}$ for the columns and $\theta_{cr,1}$ for the beam) of each of the analysed frames follow the yield stress reduction factor ($k_{y,\theta}$) curve of their corresponding material. This can be clearly observed for the carbon steel frames (in red) analysed under the degrees of utilisation μ_0=0.7 and μ_0=0.3, where the obtained critical temperatures (based on the proposed failure criteria, Eq. 8.1-Eq. 8.4) follow the curve described by the yield stress reduction factor at elevated temperatures. The critical temperatures reached by the columns – which had lower section factors (S_m) and contributed to the resistance of the plastic collapse mechanism in a higher proportion than the beams – were always below the curve described by $k_{y,\theta}$ at elevated temperatures, whereas the critical temperatures achieved by the beams were always located over the $k_{y,\theta}$ curve.

A similar phenomenon is described by the analysed stainless steel frames, where the critical temperatures of the beam ($\theta_{cr,0}$) and the columns ($\theta_{cr,1}$) lie in between the curves corresponding to the reduction factors of the proof stress $f_{0.2}$ and $f_{2.0}$ of their corresponding stainless steel grade. The exact location of the critical temperature relative to these two curves mainly depends on the capacity of the cross-section to use its inherent strain hardening (i.e., how stocky the cross-section is); for thinner cross-sections, the evolution of its critical temperature will be closer to the evolution of $k_{0.2,\theta}$, while the critical temperature of stockier cross-sections follows the $k_{2.0,\theta}$ curve.

In general, the results presented in Figure 8.3 suggest that carbon steel structures may be in a better position to cope with fire when subjected to high degrees of utilisation, while austenitic stainless steels seem to outperform carbon steel frames for low degrees of utilisation. These differences in reduction path of mechanical properties at elevated temperatures between stainless steel grades are reflected on the critical temperatures of the analysed stainless steel frames, as Table 8.1 evidences. For a degree of utilisation equal to 0.7, frames made of the austenitic EN 1.4301 stainless steel grade (Frames 1 to 5) failed when the column temperatures were around 150℃ and before reaching temperatures of 300℃ at the beams, whereas frames with the austenitic EN 1.4401 stainless steel grade (Frames 6 to 10) failed when the column temperatures were around 300℃ and the beam temperatures surpassed 400ºC. Similar differences in the critical temperatures can be found for a degree of utilisation of 0.5, where the EN 1.4301 frames failed for temperatures comprised between 520 and 750℃, while frames made of EN 1.4401 stainless steel failed for higher temperatures, being the lowest critical temperature equal to 673℃, reached at the column. For μ_0=0.3, the differences in the critical temperatures between the two stainless steel grades were less significant, but still frames modelled with the austenitic EN 1.4401 stainless steel failed for critical temperatures around 30-60℃ higher, on average, than the EN 1.4301 frames.

Another important factor influencing the critical temperature of the members comprising the frame is their contribution to the frame's resistance. If the frame's resistance only depended on the resistance of

one of its members (e.g., failure by member buckling), the TFR of the frame would be easily calculated as the time needed for the member to reach its critical temperature, as the simplified design methods provided in prEN 1993-1-2 (2021) recommend. However, the analysed frames were characterized for forming a plastic collapse mechanism before failure under fire situation, and the overall frame resistance depended on the contribution of each of the members comprising the frame to the overall resistance, which was remarkably not uniform; see the calculations detailed in Annex B for more information.

8.3. New analytical approach accounting for plastic redistribution for fire design

The complex response described by carbon and stainless steel frames under fire situation, where the material and geometric nonlinearities, as well as the plastic redistribution of design forces, play a major role on the frame response, can be correctly reproduced by means of advanced numerical models, as validated in Section 3.5 and recognised by the upcoming European code for structural design in fire (prEN 1993-1-2 (2021)). However, no simplified design methods based on analytical calculations capable of accounting for these plastic redistributions have been yet developed to estimate the resistance of such structures under fire. In this section, a novel analytical approach accounting for the plastic redistribution of internal forces is presented for the design of carbon and stainless steel frames under fire situation, which is assessed against the models presented in the previous chapters and an extended parametric study presented herein.

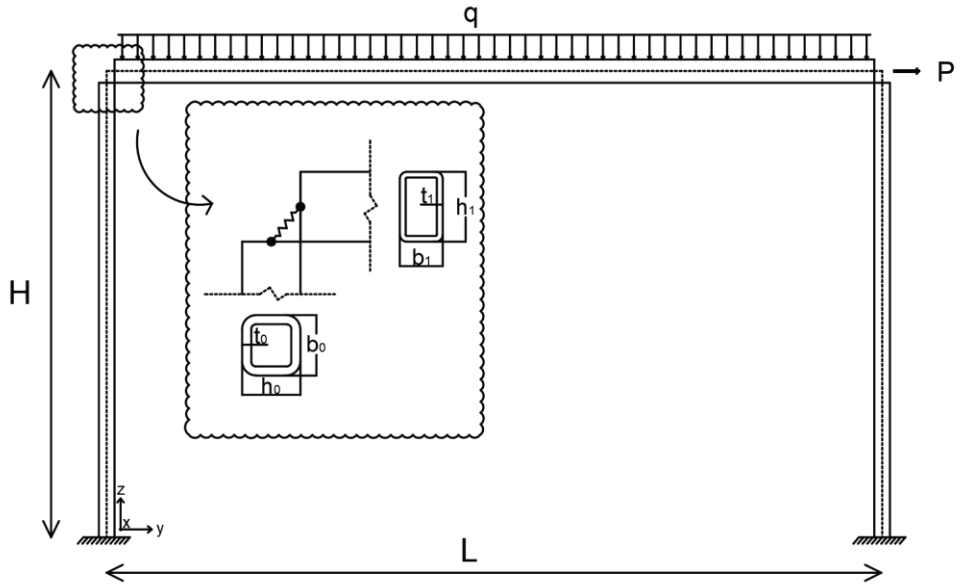

Figure 8.4. Overall frame geometry and loading pattern adopted in the extended parametric study.

The extended parametric study developed to assess the new developed analytical approach for fire design was based on the considerations described in Chapter 3, and studied the response of 60 frames under fire situation. These frames were characterized by being single-bay, single-span portal frames with plastic cross-sections, rigid numerical connections and fixed column supports (see Figure 8.4). Two additional overall frame geometries were defined, one with a span length (L) equal to 5 m and a

column height (H) of 3 m, which are typical dimensions for building construction frames, and the other one with a span length (L) of 2 m and a column height (H) of 6 m, a rather uncommon geometry that was only included in the parametric study in order to assess the applicability of the analytical methodology to a wider range of geometries.

All the analysed frames had the out-of-plane displacements prevented, but the thermal expansion of the structural members was permitted in all directions. The adopted loading cases included both vertical (q) and horizontal (P) loading, as depicted in Figure 8.4; the loading cases for each of the studied frames was defined by the parameter R, which is the ratio between the total vertical load (Q=$q \cdot L$) over the horizontal load (P). For each overall frame geometry, two different loading cases were analysed, each of them with their corresponding cross-section geometries. The materials considered for the analysed frames were the austenitic stainless steel grades EN 1.4301, EN 1.4401 and EN 1.4571 and the duplex stainless steel EN 1.4062, along with the carbon steel S275. On top of that, each frame was analysed under fire situation subjected to three different degrees of utilisation μ_0=(0.3,0.5,0.7), which correspond to the typical ratios between the two combinations of actions under fire situation ($E_{fi,d}$) and at room temperature (E_d). The main parameters of the analysed frames are reported in Table 8.2.

Table 8.2. Main geometric parameters of the analysed frames.

Frame ID	Material	α_{cr} or $\alpha_{cr,mod}$	L [m]	H [m]	h_0 [mm]	b_0 [mm]	t_0 [mm]	$\bar{\lambda}_{p,0}$	h_1 [mm]	b_1 [mm]	t_1 [mm]	$\bar{\lambda}_{p,1}$	R
1	EN 1.4301	12.8	2	6	200	200	8	0.41	200	80	5	0.30	1.0
2	EN 1.4401	12.8	2	6	200	200	8	0.41	200	80	5	0.30	1.0
3	EN 1.4571	12.8	2	6	200	200	8	0.41	200	80	5	0.30	1.0
4	EN 1.4062	14.9	2	6	200	200	8	0.57	200	80	5	0.41	1.0
5	EN S275	42.0	2	6	200	200	8	0.40	200	80	5	0.29	1.0
6	EN 1.4301	7.0	2	6	250	250	10	0.41	200	100	8	0.19	4.0
7	EN 1.4401	7.0	2	6	250	250	10	0.41	200	100	8	0.19	4.0
8	EN 1.4571	7.0	2	6	250	250	10	0.41	200	100	8	0.19	4.0
9	EN 1.4062	5.4	2	6	250	250	10	0.56	200	100	8	0.26	4.0
10	EN S275	16.9	5	3	250	250	10	0.40	200	100	8	0.18	4.0
11	EN 1.4301	10.3	5	3	160	120	8	0.22	120	60	8	0.10	1.25
12	EN 1.4401	10.3	5	3	160	120	8	0.22	120	60	8	0.10	1.25
13	EN 1.4571	10.3	5	3	160	120	8	0.22	120	60	8	0.10	1.25

14	EN 1.4062	10.4	5	3	160	120	8	0.30	120	60	8	0.13	1.25
15	EN S275	39.7	5	3	160	120	8	0.21	120	60	8	0.09	1.25
16	EN 1.4301	9.4	5	3	100	100	10	0.12	160	80	8	0.14	3.0
17	EN 1.4401	9.4	5	3	100	100	10	0.12	160	80	8	0.14	3.0
18	EN 1.4571	9.4	5	3	100	100	10	0.12	160	80	8	0.14	3.0
19	EN 1.4062	6.7	5	3	100	100	10	0.16	160	80	8	0.19	3.0
20	EN S275	17.2	5	3	100	100	10	0.11	160	80	8	0.11	3.0

Different cross-sections were considered for the columns and the beams conforming each frame. Likewise, Table 8.2 reports the relative local slenderness ($\overline{\lambda}_p$) under bending forces of each of the cross-sections adopted. It should be pointed out that stainless steel cross-sections with low relative local slenderness were expected to have their bending resistances highly influenced by strain hardening. The connections between the members comprising the frame were modelled as rigid joints, both at room temperature and under fire situation, and the joints were classified as full-strength – a requirement needed to use plastic global analysis.

Moreover, the frames investigated in this study were classified as non-sway and sway frames under the loading cases adopted at room temperature, according to the criteria prescribed in prEN 1993-1-1 (2019) for carbon steel frames and according to prEN 1993-1-4 (2021) for stainless steel frames. Carbon steel frames were classified as non-sway when $\alpha_{cr} \geq 10$, whereas for stainless steel frames those meeting $\alpha_{cr,mod} \geq 10$ at room temperature were classified as non-sway. Otherwise, the frames were classified as sway. The frames presented in Table 8.2 were also defined in order to exhibit global failure modes following sway collapse mechanisms or the combined collapse mechanism.

Besides the extended parametric study presented in this section, the data on carbon steel frames and stainless steel frames analysed in the previous sections (i.e., Chapters 6 and 7) have also been used in this study in order to further calibrate the developed methodology. Since this study focuses on the assessment of a new methodology developed to determine the fire resistance of carbon and stainless steel frames under fire situation, the frames presented in Table 8.2 were modelled with rigid numerical joints. This simplification was done in agreement with the conclusions obtained in Chapter 6, which also allowed a FE discretization of the frame geometry employing the S4R shell elements available in the ABAQUS library, reducing the computational effort significantly.

The heat transfer problem was solved as specified in Section 3.2, and the mechanical problem at room temperature was solved by means of the arc-length method, while the mechanical problem at elevated temperatures was solved by means of the Newton-Raphson method with a damping factor of 0.0002 for numerical convergence stability purposes. For more information, the reader is referred to Chapter 3.

8.4. Development and assessment of a new design procedure accounting for plastic redistribution at elevated temperatures

8.4.1. General remarks on first and second order plastic global analysis

Plastic global analysis can be carried out at room temperature to estimate the plastic resistance of the lowest energy mechanism, if the conditions of Class 1 cross-sections and full-strength joints are fulfilled. In order to carry out a plastic global analysis, a suitable plastic collapse mechanism should be defined, where all plastic deformations are concentrated in plastic hinges. Then, based on the principle of virtual works (PVW), where the work produced by the external forces is equated to the work produced by the internal forces ($\sum W_{ext}$=$\sum W_{int}$), the resistance of the proposed mechanism $P_{k,1,i}$ can be obtained.

At room temperature, for the loading case presented in Figure 8.4 and the geometries presented in Table 8.2, only three different plastic mechanisms are feasible: the beam collapse mechanism (given by Eq. 8.11), the sway collapse mechanism (Eq. 8.12), and the combined collapse mechanism (Eq. 8.13), which is a combination of the two previous mechanisms. The development of these equations can be found in Annex B.

$$P_{k,1,beam} = \frac{4 \cdot (2M_1 + 2M_2)}{R \cdot L} \quad \text{Eq. 8.11}$$

$$P_{k,1,sway} = \frac{2 \cdot (M_0 + M_2)}{H} \quad \text{Eq. 8.12}$$

$$P_{k,1,combined} = \frac{2M_0 + (M_1 + M_2) \cdot \frac{L}{L - x}}{H + \frac{R \cdot x}{2}} \quad \text{Eq. 8.13}$$

In these equations, M_0 and M_1 are the bending moment resistances of the columns and beam, respectively, and M_2 is the bending resistance of the beam-to-column joints – which was assumed to be equal to the lowest of the bending moment resistances of the connected beam and column –, and x is the distance between the plastic hinge formed at the beam midspan area and the left joint, because its optimum position may not be exactly at the beam midspan section. The optimised position (x_o) of the plastic hinge at the beam midspan area was calculated as the one corresponding to the plastic collapse mechanism with the lowest associated energy for the geometries analysed, and the derivation of the solution is also presented in Annex B.

This design approach, which adopts a first order plastic global analysis, is accurate enough to estimate the resistance of non-sway frames at room temperature, because when α_{cr}≥10 (or $\alpha_{cr,mod}$≥10), the amplification of internal forces due to sway second order effects is no more than 10% of the internal forces according to a first order analysis (prEN 1993-1-1 (2019) and prEN 1993-1-4 (2021)). Conversely, when the analysed frame is classified as sway, second order effects should be accounted for in the resistance estimation of the plastic mechanism, which is more complex to formulate.

In a first order plastic global analysis, the resistance of the mechanism does not depend on the rotation (θ) described by the mechanism (as Eq. 8.11-Eq. 8.13 reproduce), because the rotations and displacements described by the frame are assumed to be small enough to be neglected (i.e., the length of the members is assumed to be constant through the development of the plastic collapse mechanism). However, this assumption cannot be extended to second order plastic global analysis, and thus the effects produced by the lengthening or shortening of the structural members should be incorporated in the calculations. The bases for incorporating second order effects on plastic global analysis are presented in Annex C, which are based on the assumption that after a certain rotation threshold of the members (θ) is exceeded, all the additional rotations ($\delta\theta$) produce displacements large enough so that they cannot be neglected.

Naturally, an initial distribution of internal forces must be obtained in order to estimate the influence of the lengthening or shortening of the structural members on the frame plastic resistance, which can be determined from a first order elastic global analysis corresponding to the structural configuration of the proposed plastic collapse mechanism (Plastic Theory of Structures (Horne 1976), Plastic Design and Second-Order Analysis (Chen and Sohal 1995)). It is necessary, however, that the proposed plastic collapse mechanism is classified as a complete mechanism, where the plastic hinges required to develop the plastic collapse mechanism should be equal to the degree of redundancy of the analysed frame plus one; otherwise, obtaining the internal force distribution is not feasible. For this reason, the analysed frames were defined in order to trigger the sway or combined collapse mechanisms at room temperature, because the beam collapse mechanism is not a complete plastic mechanism, and the corresponding internal forces cannot be calculated.

In Annex D, the resistances $P_{k,2,i}$ of the two plastic collapse mechanisms producing complete mechanisms (i.e., the sway collapse mechanism and the combined collapse mechanism) are calculated according to a second order plastic global analysis. The resulting resistance predictions for the sway collapse mechanism and the combined collapse mechanism are as given in Eq. 8.14 and Eq. 8.15, respectively, where the second order effects are taken into consideration by means of the parameter *dθ,* which corresponds to the additional rotations that produce non-neglectable displacements, and which can be directly related to the horizontal displacements (d_h) described by the frame as $d\theta \approx d_h/H$.

$$P_{k,2,sway} = \frac{2 \cdot (M_0 + M_2)}{H \cdot (1 + R \cdot d\theta)} \quad \text{Eq. 8.14}$$

$$P_{k,2,complete} = \frac{2M_0 + (M_1 + M_2) \cdot \frac{L}{L-x}}{H + \frac{R \cdot x}{2} + \left(R \cdot H - \frac{x \cdot L}{L-x}\right) \cdot d\theta} + \frac{\left(\frac{M_0 + M_2}{H} \cdot \frac{x \cdot L}{L-x}\right) \cdot d\theta}{H + \frac{R \cdot x}{2} + \left(R \cdot H - \frac{x \cdot L}{L-x}\right) \cdot d\theta} \quad \text{Eq. 8.15}$$

As it can be seen, when second order effects are included in the calculation of the plastic collapse load, the frame resistance is directly dependant on the horizontal displacement of the frame ($d\theta \approx d_h/H$). This means that the plastic resistance of the frame changes with the assumed horizontal drift, and even the plastic collapse mechanism with the lowest collapse load may change depending on the value of the horizontal displacement (d_h).

8.4.2. Second order plastic global analysis at room temperature

As it has been already mentioned, plastic global analysis is allowed as a suitable design method at room temperature for carbon and stainless steel structures that meet the necessary requirements. In this section, the accuracy of this methodology and the relevance of second order effects is assessed at room temperature for carbon and stainless steel frames by comparing the predicted resistances with those obtained from advanced numerical modelling, where the stress–strain nonlinearities are explicitly contemplated along with the second order effects by means of advanced FE analysis.

The accuracy of the estimated frame resistances depends, however, on the capability of basic design equations to predict the actual bending resistance of stainless steel cross-sections, the accuracy of which has been found to be insufficient as highlighted in Chapter 7. To minimize the effect of the inaccuracies related to this, when estimating the resistance of the stainless steel frames using the analytical plastic global analysis approach the bending moment resistance of the columns (M_0) and the beam (M_1) comprising the analysed stainless steel frames were estimated using advanced FE analysis. The models comprised simply supported beams of the analysed cross-sections, which were subjected to point bending moments at both ends of the beam until failure – produced by local buckling after yielding. In contrast, for carbon steel cross-sections the bending moment resistance could be accurately estimated with the traditional plastic bending moment (M_{pl}), since carbon steel is characterized by its bilinear stress–strain curve.

Once the FE bending moment resistances of the investigated cross-sections was estimated, the plastic resistance of the analysed non-sway frames (i.e., frames with $\alpha_{cr} \geq 10$ or $\alpha_{cr,mod} \geq 10$) was assumed to be the lowest of the resistances obtained from Eq. 8.11-Eq. 8.13. However, for sway frames (i.e., frames with $\alpha_{cr} < 10$ or $\alpha_{cr,mod} < 10$), the frame resistance depended on the horizontal displacement (d_h) and the plastic collapse mechanism with the lowest associated energy varied depending on the horizontal drift of the frame. This phenomenon is illustrated in Figure 8.5, where the load–displacement curves of two representative

frames are shown: Frame 19 (stainless steel, sway $\alpha_{cr,mod}$=6.7) and Frame 20 (carbon steel, non-sway α_{cr}=17.2). The numerical reference curves were obtained from GMNA analyses (solid lines), and the predicted load–displacement paths by means of second order plastic global analyses for the sway collapse mechanism (dashed lines) and the combined collapse mechanism (dotted lines). It can be seen that the analytical load–displacement curves obtained using the FE bending resistances ($M_{FE,0}$ and $M_{FE,1}$) showed good agreement with the load–displacement curves obtained with advanced numerical models.

As it can be seen in Figure 8.5, both frames were expected form a combined collapse mechanism according to a first order plastic global analysis, as the results of the second order plastic global analysis for a horizontal displacement equal to zero correspond to the solution of the first order plastic global analysis.

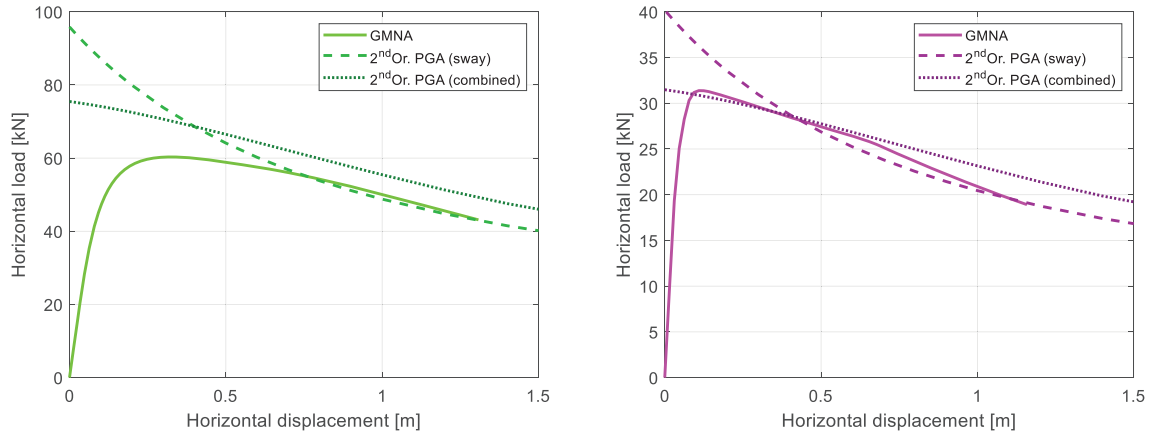

Figure 8.5. Horizontal load–displacement curves for (a) Frame 19 and (b) Frame 20 obtained from GMNA (solid lines) and second order plastic global analyses for sway (dashed lines) and complete (dotted lines) plastic mechanisms.

However, as the horizontal displacement of the frames increases, and second order effects play a major role on the frame response, the sway collapse mechanism becomes the dominant plastic mechanism (i.e., the mechanism with the lowest associated energy). This phenomenon was observed for all the analysed frames defined to trigger combined collapse mechanisms: after a certain horizontal displacement, the dominant mechanism was always the sway collapse mechanism.

Since the GMNA resistance was assumed to be equal to the peak load of the numerical load–displacement curve, from Figure 8.5(b) it can be seen that the ultimate GMNA load (P_{GMNA}=31.4 kN) for Frame 20 (with α_{cr}=17.2) is in accordance with the first order plastic global analysis estimation (P_{1PGA}=31.5 kN), as expected for a non-sway frame. Results in line with those obtained for Frame 20 were also observed for all the analysed non-sway frames, for which the GMNA resistance P_{GMNA} could be estimated accurately (with errors below 10%) by means of a first order plastic global analysis, as reported in Chapter 7. However, Figure 8.5(a) shows that the ultimate GMNA load (P_{GMNA}=60.3 kN) for Frame 19 (with $\alpha_{cr,mod}$=6.7) is far from the analytical estimation calculated from a first order plastic global analysis (P_{1PGA}=75.5 kN), as expected for a sway frame in which second order effects are relevant (prEN 1993-1-

1 (2019) and prEN1993-1-4 (2021)). Likewise, Frame 19 can be considered as representative of most of the sway frames analysed, whose resistances could not be estimated with accuracy based on first order plastic global analyses only.

Based on plastic global analysis (PGA) the carbon and stainless steel frame resistances could be estimated at room temperature and are reported in Table 8.3. The resistance of the analysed frames was calculated with a first order PGA and compared to the results obtained with a GMNA, where the mean value of the ratio P_{GMNA}/P_{1PGA} equal to 0.91 and a COV of 0.10. Likewise, the estimation based on a second order PGA is also reported, with a mean value of P_{GMNA}/P_{1PGA} equal to 1.04 and a COV of 0.09.

Table 8.3. Main geometric, material and loading parameters of the frames considered in the presented parametric study and previous sections, and estimated frame resistances from GMNA and different plastic global analyses at room temperature.

Frame ID	Material grade	L [m]	H [m]	α_{cr} or $\alpha_{cr,mod}$	R	Bending moment resistance* [kN·m]		Frame plastic resistance [kN]			Error [%]	
						M_0	M_1	P_{GMNA}	$P_{1PGA,FE}$	$P_{2PGA,FE}$	P_{GMNA}/P_{1PGA}	P_{GMNA}/P_{2PGA}
1	EN 1.4301	2	6	12.8	1.0	141.4	59.6	62.6	67.0	59.8	0.93	1.05
2	EN 1.4401	2	6	12.8	1.0	141.4	59.6	62.6	67.0	59.8	0.93	1.05
3	EN 1.4571	2	6	12.8	1.0	141.4	59.6	62.6	67.0	59.8	0.93	1.05
4	EN 1.4062	2	6	14.9	1.0	247.8	101.2	101.9	116.3	106.7	0.88	0.96
5	EN S275	2	6	42.0	1.0	117.3	45.1	55.4	54.1	52.9	1.02	1.05
6	EN 1.4301	2	6	7.0	4.0	274.3	108.8	98.5	119.3	85.5	0.83	1.15
7	EN 1.4401	2	6	7.0	4.0	274.3	108.8	98.5	119.3	85.5	0.83	1.15
8	EN 1.4571	2	6	7.0	4.0	274.3	108.8	98.5	119.3	85.5	0.83	1.15
9	EN 1.4062	2	6	5.4	4.0	483.0	178.8	168.8	204.9	160.1	0.82	1.05
10	EN S275	2	6	16.9	4.0	229.0	76.5	90.6	93.7	92.9	0.97	0.98
11	EN 1.4301	5	3	10.3	1.25	80.2	40.2	60.4	69.3	62.5	0.87	0.97
12	EN 1.4401	5	3	10.3	1.25	80.2	40.2	60.4	69.3	62.5	0.87	0.97
13	EN 1.4571	5	3	10.3	1.25	80.2	40.2	60.4	69.3	62.5	0.87	0.97
14	EN 1.4062	5	3	10.4	1.25	134.4	61.7	104.2	111.6	107.1	0.93	0.97
15	EN S275	5	3	39.7	1.25	59.4	24.9	49.2	47.4	47.4	1.04	1.04
16	EN 1.4301	5	3	9.4	3.0	45.2	71.7	34.3	47.5	27.4	0.72	1.25
17	EN 1.4401	5	3	9.4	3.0	45.2	71.7	34.3	47.5	27.4	0.72	1.25
18	EN 1.4571	5	3	9.4	3.0	45.2	71.7	34.3	47.5	27.4	0.72	1.25
19	EN 1.4062	5	3	6.7	3.0	71.9	113.9	60.3	75.5	50.6	0.80	1.19
20	EN S275	5	3	17.2	3.0	30.1	47.2	31.4	31.5	31.5	1.00	1.00
21[1]	EN 1.4301	5	3	18.5	0.7	228.0	53.7	168.4	171.6	163.9	0.98	1.03
22[1]	EN 1.4301	5	3	14.9	1.1	102.1	26.7	67.3	71.0	69.6	0.95	0.97
23[1]	EN 1.4301	5	3	9.2	2.0	80.1	53.7	54.7	67.6	54.1	0.81	1.01
24[1]	EN 1.4301	5	3	11.4	1.4	37.8	13.5	25.0	27.3	25.0	0.92	1.00
25[1]	EN 1.4301	5	3	7.1	2	15.1	7.9	10.3	11.2	10.5	0.92	0.98
26[1]	EN 1.4401	4	2	8.6	2	37.8	27.5	41.1	46.2	42.2	0.89	0.97
27[1]	EN 1.4401	4	2	7.6	0.8	30.5	11.0	37.6	37.1	33.6	1.01	1.12
28[1]	EN 1.4401	4	2	11.0	1.5	56.8	31.7	65.0	68.3	65.3	0.95	1.00
29[1]	EN 1.4401	4	2	7.3	0.9	8.4	2.8	8.4	9.6	8.7	0.88	0.97
30[1]	EN 1.4401	4	2	6.7	0.7	64.9	15.6	68.2	70.9	66.2	0.96	1.03
31[2]	EN S275	5	3	64.2	1.1	170.6	42.4	135.8	130.4	130.4	1.04	1.04
32[2]	EN S275	5	3	27.4	2.0	77.5	25.0	58.7	58.0	58.0	1.01	1.01
33[2]	EN S275	5	3	117.2	0.7	55.8	34.1	45	44.9	44.9	1.00	1.00
34[2]	EN S275	5	3	36.3	1.4	26.5	11.4	20.2	20.6	20.6	0.98	0.98
35[2]	EN S275	5	3	27.0	2	11.4	6.8	8.7	9.1	9.0	0.96	0.97
										mean†	0.91	1.04
										COV†	0.10	0.09

* The bending moment resistances (for columns M_0 and beams M_1) of stainless steel cross-sections were estimated by means of advanced numerical FE models. For carbon steel cross-sections, the plastic moment (M_{pl}) was employed.

† At room temperature all austenitic stainless steel grades exhibit the same mechanical properties, their results are exactly the same. Duplicated results were left out of the statistical calculations.

[1] These frames were originally analysed in Chapters 6 and 7.

[2] These frames were originally analysed in Chapters 6 and 7.

Another interesting phenomenon observed during the assessment of the response of the frames presented in Table 8.3 was that some frames would describe load–displacement curves with positive slope when calculated by means of a plastic global analysis (PGA) with second order effects (i.e., increasing the frame resistance as the horizontal drift increased), at least for low values of the horizontal displacement. This response is theoretically possible, since when a structural element is subjected to tension forces, the produced external work has the opposite sign to that of the work produced by the external forces applied (P and q). This means that, under certain geometries and loading cases, second order effects stabilize the frame and the resulting load–displacement curve can exhibit a positive slope. This phenomenon was observed for Frame 21 ($\alpha_{cr,mod}$=18.5) and Frame 22 ($\alpha_{cr,mod}$=14.9), for example, which are presented in Figure 8.6.

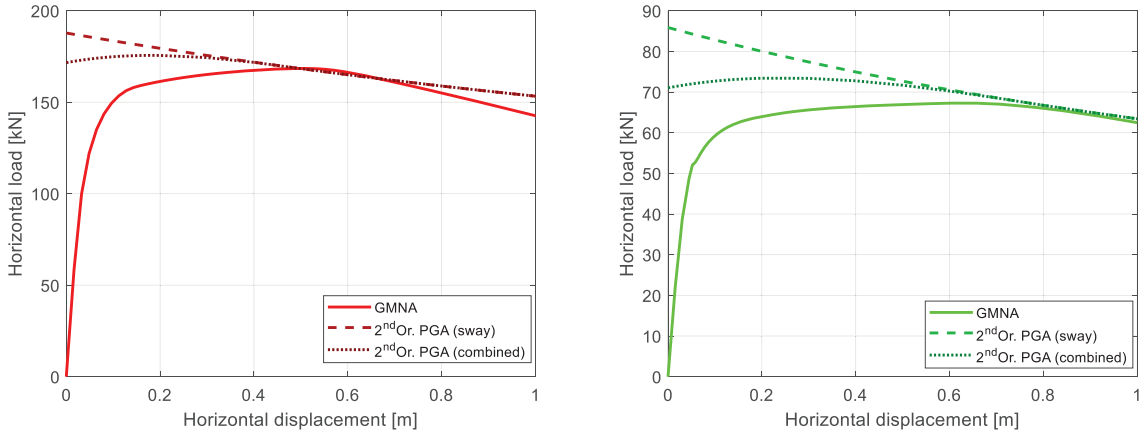

Figure 8.6. Horizontal load–displacement curves for (a) Frame 21 and (b) Frame 22 obtained from GMNA (solid lines) and second order plastic global analyses for sway (dashed lines) and complete (dotted lines) plastic mechanisms.

The obtained load–displacement curves for sway frames (e.g., see Figure 8.5(a)) evidence a new matter: in order to correctly estimate the second order plastic global resistance a target design horizontal displacement (d_h^*) must be defined, because the ultimate resistance of such frames is highly dependent on the frame's horizontal drift. After assessing the response of the frames analysed at room temperature in the extended parametric study and in the previous Chapters 6 and 7, a first formulation to estimate the target design horizontal displacement is proposed, as shown in Eq. 8.16.

$$d_h^* = C \cdot \frac{H}{\bar{\lambda}_{p,0}} \qquad \text{Eq. 8.16}$$

In this equation, H is the frame height, $\bar{\lambda}_{p,0}$ is the relative local slenderness of the column cross-section, and C is a constant that was calibrated based on the numerical frame results, which is equal to 0.05 for stainless steel frames and 0.01 for carbon steel frames. This is a first approximation to the definition of

the target displacement, and further research is needed on this complex topic, although the obtained results are remarkably accurate, as shown herein.

Once the target design horizontal drift was calculated for each particular frame as per Eq. 8.16, the ultimate resistance (P_{2PGA}) of the frames accounting for second order effects could be estimated (see Eq. 8.14 and Eq. 8.15), assuming that $d\theta \approx d_h/H$. When comparing the analytical estimations with a first order analysis (P_{1PGA}) and with a second order analysis (P_{2PGA}) reported in Table 8.3, for non-sway frames it could be confirmed that the influence of the geometry nonlinearly could be neglected. The two approaches showed an estimation resistance difference below the 10%, as prEN 1993-1-1 (2019) recognizes. Whereas, for sway frames it could be evidenced that second order effects played a major role on the frame resistance – with difference with the first order estimation above the 10% –, in line with the recommendations codified in prEN 1993-1-1. Moreover, the accuracy shown by the analytical approach for stainless steel frames when employing bending moment resistances obtained with FE analysis was similar to the one shown for carbon steel frames.

In summary, the results showed that the plastic response of Class 1 carbon and stainless steel frames can be estimated accurately at room temperature with second order plastic global analysis if the proposed target design horizontal displacement is used. Even for non-sway frames the target design horizontal displacement could be employ to determine the frame resistance, since the influence of the second order effects is negligible for this type of frames.

In the following section, this methodology is extended to fire situation, and it is compared against the frame responses obtained from advanced numerical models, where all the nonlinearities derived from the stress–strain relationship and second order effects were considered along with the degradation of the mechanical properties due to the increase of temperature.

8.4.3. Extension and applicability of second order plastic global analysis for fire design

The parametric study carried out in this investigation under fire situation consisted of the same frames analysed at room temperature, but they were exposed to standardized fire actions considering three different degrees of utilisation μ_0=(0.3,0.5,0.7). Under fire situation, the temperature of the frames increases due to their exposure to fire, and thus the mechanical properties of the members deteriorate over time, meaning that at each time increment the bending moment resistance of the cross-sections decreases. Therefore, the frame resistance is not only dependant on the lateral displacements (due to second order effects) as it occurred at room temperature, but also on the time the frame has been exposed to the fire action. This fact has been included in the developed analytical methodology by using the bending moment resistance ($M_{Rk,t}$) at each time increment t for the corresponding temperature,

resulting in a different load–displacement curve equivalent to those described in the previous section for each calculated time increment.

The bending moment resistances ($M_{Rk,t}$) were calculated once the temperature field of each frame was known, which was obtained by means of a numerical heat transfer analysis, as explained in Chapter 3. Then, the bending moment resistance of each cross-section was estimated at different temperatures by means of advanced numerical models, where simply supported beams comprising the analysed cross-sections were subjected to pure bending moment at both ends under a uniform temperature distribution (isothermal analysis) for a given temperature. This procedure was carried out for all the stainless steel cross-sections analysed in this parametric study and for the stainless steel cross-sections analysed in Chapters 6 and 7. Each cross-section was analysed for 11 different uniform temperature fields (20, 100, 200, …1000ºC), and a total of 572 cross-section bending moment resistances were obtained with this procedure. Conversely, for carbon steel cross-sections the bending moment resistance was estimated according to the traditional plastic bending moment ($M_{pl,\theta}$).

Once the development of the temperature field of each analysed frame was obtained, the resistance of all the analysed frames was estimated for time increments of 5 seconds using the procedure explained in the previous section and interpolating between bending moment resistances at different temperatures, obtaining a different load–displacement curve at each time increment. Following this approach, the estimated fire resistance of frames depends both on the lateral drift and on the time the frame has been exposed to the fire effect. This means that, for each of the analysed frames under fire situation, the resistance can be estimated from a load–displacement–time surface.

At room temperature depending on the frame geometry and loading case the plastic global analysis could result in a load–displacement curve with a positive slope due to the tensile force, as shown in Figure 8.6. However, some structural members that were subjected to tension forces at room temperature were actually under compression forces at elevated temperatures due to the thermal expansion of the members, according to the thermo-mechanical analysis. In the FE analyses, this expansion was prevented to some extent as a result of the stiffness provided by the other structural members, as explained in Chapter 7 by means of the assessment of the bending moment evolution of the critical cross-sections. Hence, with the aim of avoiding the overestimation of the capacity of the frames at elevated temperatures, under fire situation the external work produced by the enlargement of the beam was not considered when estimating the frame fire resistance, as explained in Annex D.

Figure 8.7 shows the 3D load–displacement–time evolution curves for Frame 8 under fire situation when subjected to different degrees of utilisation (μ_0=0.3,0.5,0.7) obtained from GMNA analyses (solid lines), along with the estimated resistance surface (in grey) according to the second order plastic global analysis proposed in this thesis. In addition, the projected displacement–time curves of the original

GMNA 3D paths are also shown, along with the proposed design curves corresponding to the intersection between the analytical resistance surface and the design load that corresponded to each analysed degree of utilisation ($P_{fi,Ed}$=$\mu_0 \cdot P_{u,FE}$); when the two projected lines intersect, the frame theoretically collapses. It should be noted that, although only the results corresponding to one frame are presented, the response of Frame 8 is representative of all the carbon and stainless steel frames analysed under fire situation.

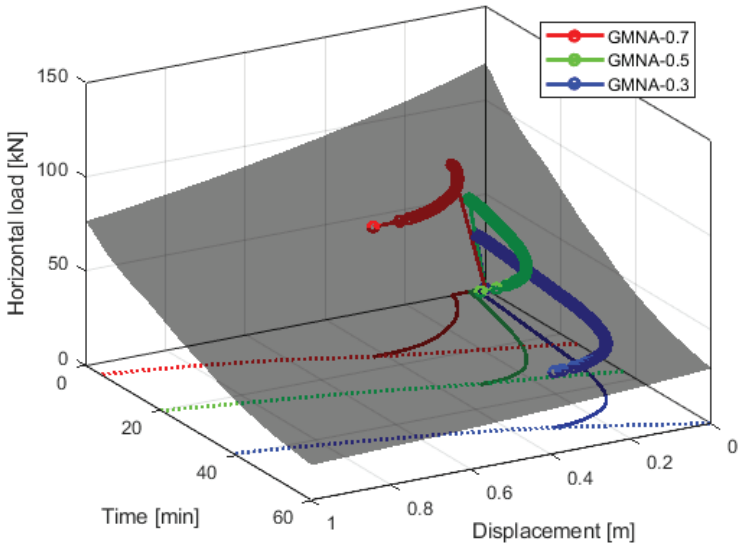

Figure 8.7. Load–displacement–time curves from GMNA (grey surface) and second order plastic global analysis (using M_{FE}) for Frame 8 and different degrees of utilisation (μ_0) under fire situation.

As for room temperature design, the analytical methodology for fire design also requires a target design horizontal displacement ($d^*_{h,fi}$) to be defined in order to estimate the fire resistance of the frame. Following the approach taken at room temperature, Eq. 8.17 presents the new formulation to estimate the target design horizontal displacement ($d^*_{h,fi}$) to be used for second order plastic global analyses under fire situation, based on the FE results derived from the extended parametric study and the previous Chapters 6 and 7.

$$d^*_{h,fi} = C \cdot \frac{H}{\bar{\lambda}_{p,0}} \cdot \mu_0 \qquad \text{Eq. 8.17}$$

In this equation, C is equal to 0.05 and 0.01 for stainless steel and carbon steel frames, respectively, which are the same values proposed for room temperature analysis too. Moreover, the GMNA curves displayed in Figure 8.7 are projected onto the time–displacement, load–time and load–displacement planes in Figure 8.8, alongside with the fire resistance estimations according to the second order plastic global analysis. For Figure 8.8(a), the analytical curves were obtained by intersecting the analytical load–displacement–time resistance surface with the TFRs obtained from the GMNA analyses. On the

contrary, the analytical curves shown in Figure 8.8(b) were calculated using the target design horizontal displacement ($d^*_{h,fi}$) for fire design (Eq. 8.17). Note that larger target design horizontal displacements are obtained for higher initial loads μ_0 according to Eq. 8.17, leading to more conservative estimations for higher degrees of utilisation, as in the design load–displacement curve the resistance usually decreases for increasing horizontal drifts (see Figure 8.8(a)).

If Eq. 8.17 is used in conjunction with Eq. 8.14 and Eq. 8.15, the frame fire resistance becomes only dependent on the time the structure is being exposed to the fire effect, which means that a resisted load–time curve can be derived for each analysed frame, as shown in Figure 8.8(c). Since the load applied onto the frame is maintained constant along time in fire design, the TFR of the analysed frame can be calculated analytically as the intersection between the theoretical resisted load–time curve and the applied design load ($P_{fi,Ed}$). For the case presented in Figure 8.8(c), the TFRs of Frame 8 according to the advanced numerical model were 15.8 minutes (μ_0=0.7), 31.9 minutes (μ_0=0.5), and 51.1 minutes (μ_0=0.3), respectively, while the TFRs estimated from the proposed second order plastic global analysis were 13.5 minutes (μ_0=0.7), 30.8 minutes (μ_0=0.5), and 53.5 minutes (μ_0=0.3).

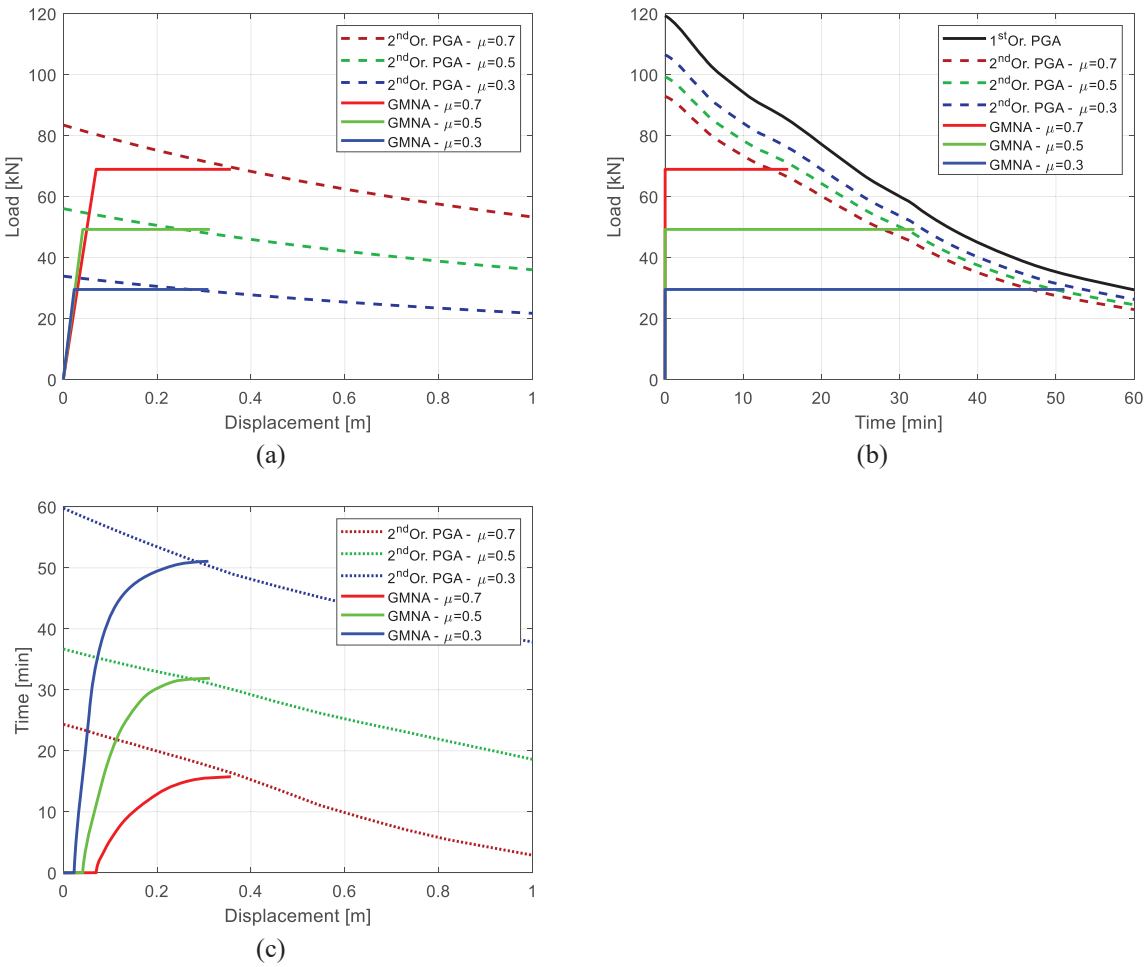

Figure 8.8. Fire response curves obtained according to a GMNA and second order plastic global analysis for Frame 8 projected onto: (a) the load–displacement plane, (b) the load–time plane, and (c) the time–displacement plane.

Similar results were obtained for all the analysed frames, which are fully reported in Table 8.5. The predicted time fire resistance (TFR) obtained by means of advanced numerical models (i.e., GMNA) are reported for the frames analysed under different degrees of utilisation. Likewise, the analytical predictions obtained according to the upcoming European code (prEN 1993-1-2 (2021)) are presented along with the fire resistance estimations obtained by means of a second order plastic global analysis at elevated temperatures, where the bending moment resistance of carbon steel cross-section was estimated with the plastic bending moment ($M_{pl,\theta}$), while for stainless steel frames the bending moment resistance were calculated using advanced numerical models (M_{FE}) in order estimate the frames fire resistance as accurate as possible. Finally, the absolute differences (ΔTFR) between the obtained fire resistance with advanced numerical methods and the two analytical approaches are also presented.

Note that the analytical time fire resistance estimations reported in Table 8.5 were calculated accounting for second order effects for all the analysed frames (i.e., using a second order plastic global analysis), despite some of them being classified as non-sway at room temperature. From the obtained results, it was not clear whether second order effects under fire situation could be disregarded based on the sway/non-sway classification at room temperature, and thus it is recommended that a second order plastic global analysis approach is adopted when designing carbon and stainless steel frames in fire using the approach proposed in this thesis.

A summary of the accuracy of the results obtained using the proposed design approach under fire situation is presented in Table 8.4. The analytical estimations based on prEN 1993-1-2 are far from the fire resistances obtained with advanced numerical methods, since current simplified design methods do not consider the redistribution capacity of such structures in fire. The mean value of the absolute difference ($\overline{\Delta TFR}$) between the time fire resistance obtained with a GMNA and estimated based on prEN 1993-1-2 recommendations is 7.3 minutes for carbon steel frames and 14.6 minutes for stainless steel frames.

Table 8.4. Summary of the assessment of the different approaches for fire design.

	ΔTFR	Carbon steel				Stainless steel			
	[min]	$\mu_0 = 0.7$	$\mu_0 = 0.5$	$\mu_0 = 0.3$	All	$\mu_0 = 0.7$	$\mu_0 = 0.5$	$\mu_0 = 0.3$	All
prEN 1993-1-2* (2021)	Mean	9.3	6.0	5.9	**7.3**	8.3	17.3	18.2	**14.6**
	σ	3.7	5.2	3.0	**3.9**	3.3	5.9	7.6	**7.3**
2nd Or. PGA* $\theta_{FE} + M_{FE}$	Mean	-0.9	-1.1	-0.7	**-0.9**	0.2	0.4	0.0	**0.2**
	σ	1.0	0.7	1.0	**0.9**	2.0	2.1	2.3	**2.1**
2nd Or. PGA† $\theta_{ISO834} + M_{pl}$	Mean	-0.5	-0.5	-0.1	**-0.4**	3.5	3.9	2.7	**3.4**
	σ	1.0	0.8	0.9	**0.9**	3.4	3.7	2.6	**3.3**

* Detailed results presented in Table 8.5.
† Detailed results presented in Table 8.6.

Table 8.5. Time fire resistances (TFR) [min] of steel and stainless steel frames under fire situation for different degrees of utilisation obtained from GMNA, prEN 1993-1-2 (2021) and the new proposed methodology, and differences relative to GMNA estimations.

Frame ID	Material grade	GMNA			prEN 1993-1-2 (2021)*			2nd Or. PGA†			ΔTFR (prEN 1993-1-2 (2021))			ΔTFR (2nd Or. PGA)		
		μ_0=0.7	μ_0=0.5	μ_0=0.3	μ_0=0.7	μ_0=0.5	μ_0=0.3	μ_0=0.7	μ_0=0.5	μ_0=0.3	μ_0=0.7	μ_0=0.5	μ_0=0.3	μ_0=0.7	μ_0=0.5	μ_0=0.3
1	EN 1.4301	5.3	16.4	27.1	0	2.1	13.9	5.1	17.0	27.6	5.3	14.3	13.2	0.2	-0.6	-0.5
2	EN 1.4401	8.5	22.3	38.2	0	3.4	18.7	8.3	22.1	37.7	8.5	18.9	19.5	0.2	0.2	0.5
3	EN 1.4571	13.9	29.8	50	0	5.1	26.1	13.2	28.8	50.3	13.9	24.7	23.9	0.7	1.0	-0.3
4	EN 1.4062	8.8	15.3	21.9	0	3.7	12.8	9.4	15.7	22.4	8.8	11.6	9.1	-0.6	-0.4	-0.5
5	EN S275	9.3	12.2	15.3	0	7.5	10.6	11.1	13.4	17.0	9.3	4.7	4.7	-1.8	-1.2	-1.7
6	EN 1.4301	6.0	18.4	29.2	0	1	9.9	5.2	19.7	31.0	6	17.4	19.3	0.8	-1.3	-1.8
7	EN 1.4401	9.4	24.6	40.2	0	0	13.5	8.6	24.8	40.7	9.4	24.6	26.7	0.8	-0.2	-0.5
8	EN 1.4571	15.8	31.9	51.1	0	1.6	18.1	13.5	30.8	53.5	15.8	30.3	33	2.3	1.1	-2.4
9	EN 1.4062	9.0	17.1	23.7	0	0	9.4	9.7	18.0	25.2	9	17.1	14.3	-0.7	-0.9	-1.5
10	EN S275	10.3	13.6	16.8	0	0	12.3	13.1	15.5	19.4	10.3	13.6	4.5	-2.8	-1.9	-2.6
11	EN 1.4301	6.0	18.2	28	0	1.9	13.2	7.2	19.2	29.3	6	16.3	14.8	-1.2	-1.0	-1.3
12	EN 1.4401	10.0	23.4	37.9	0	2.8	17.6	13.4	23.8	38.9	10	20.6	20.3	-3.4	-0.4	-1.0
13	EN 1.4571	16.0	29.7	49.6	0	3.6	23.7	16.8	28.6	50.0	16	26.1	25.9	-0.8	1.1	-0.4
14	EN 1.4062	9.1	16.1	22.3	0	2	11.4	10.2	16.7	23.3	9.1	14.1	10.9	-1.1	-0.6	-1.0
15	EN S275	11.5	13.7	17.3	0	9.8	13.3	11.7	14.0	17.6	11.5	3.9	4	-0.2	-0.3	-0.3
16	EN 1.4301	6.0	19	29.3	2.2	8.7	23.6	6.3	21.0	32.6	3.8	10.3	5.7	-0.3	-2.0	-3.3
17	EN 1.4401	9.6	23.1	39.8	2.6	14.2	30.2	12.4	25.7	42.2	7	8.9	9.6	-2.8	-2.6	-2.4
18	EN 1.4571	16.0	30.5	51.3	3.7	18.9	37.8	16.7	30.1	54.4	12.3	11.6	13.5	-0.7	0.4	-3.1
19	EN 1.4062	8.3	15.5	23.5	0.9	10.3	19.4	10.7	18.4	26.1	7.4	5.2	4.1	-2.4	-2.9	-2.6
20	EN S275	11.5	14.2	17.7	10.7	12.5	15.9	12.8	15.3	19.0	0.8	1.7	1.8	-1.3	-1.1	-1.3
21[1]	EN 1.4301	6.4	21.1	34.8	0	0.0	8.4	3.8	15.7	30.0	6.4	21.1	26.4	2.7	5.3	4.8
22[1]	EN 1.4301	5.3	18.4	32.2	0	0.6	10.3	3.0	13.4	27.6	5.3	17.7	21.9	2.3	5.0	4.6
23[1]	EN 1.4301	6.0	20.0	31.2	0	2.0	13.5	5.3	20.6	32.2	6.0	18.0	17.7	0.6	-0.6	-1.0
24[1]	EN 1.4301	4.9	16.8	30.3	0	2.5	13.8	6.8	17.6	27.9	4.9	14.3	16.5	-2.0	-0.8	2.4
25[1]	EN 1.4301	3.2	12.1	24.9	0	3.0	15.1	4.4	13.5	24.9	3.2	9.1	9.8	-1.2	-1.4	0.0
26[1]	EN 1.4401	7.2	20.2	36.5	0	3.9	19.7	6.4	18.8	34.6	7.2	16.3	16.8	0.8	1.4	1.9
27[1]	EN 1.4401	9.0	20.8	34.9	0	0.0	8.9	6.0	18.5	33.1	9.0	20.8	26.0	3.0	2.4	1.8
28[1]	EN 1.4401	8.0	21.7	37.3	0	3.0	17.8	6.1	20.0	35.2	8.0	18.7	19.5	1.9	1.7	2.1
29[1]	EN 1.4401	7.0	17.5	33.5	0	0.0	10.7	5.6	16.4	32.9	7.0	17.5	22.8	1.4	1.1	0.6
30[1]	EN 1.4401	10.0	23.0	36.4	0	0.0	5.5	4.5	18.4	32.3	10.0	23.0	30.9	5.5	4.7	4.2
31[2]	EN S275	13.1	–	20.30	0	–	9.95	12.4	–	19.9	13.1	–	10.4	0.7	–	0.4
32[2]	EN S275	9.7	–	18.50	0	–	8.07	10.8	–	17.9	9.7	–	10.4	-1.1	–	0.6
33[2]	EN S275	12.5	–	19.6	0	–	13.44	12.9	–	20	12.5	–	6.2	-0.4	–	-0.4
34[2]	EN S275	9.6	–	16.20	0	–	8.67	9.9	–	16.4	9.6	–	7.5	-0.3	–	-0.2
35[2]	EN S275	7.2	–	12.60	0	–	9.01	8.2	–	13.7	7.2	–	3.6	-1.0	–	-1.1
										Mean	8.6	15.7	15.0	-0.1	0.2	-0.2
										σ	3.4	6.9	8.6	1.8	2.1	2.0

* The bending moment ($M_{0,\theta}$ and $M_{1,\theta}$) resistances were estimated according to prEN 1993-1-2 (2021).

† The bending moment resistances ($M_{0,\theta}$ and $M_{1,\theta}$) of stainless steel cross-sections were estimated by means of advanced numerical models. For carbon steel cross-sections the plastic moment ($M_{pl,\theta}$) was employed.

[1] These frames were originally analysed in Chapter 6 and 7.

[2] These frames were originally analysed in Chapter 6 and 7.

However, the results obtained with the new methodology presented (see Table 8.4) show a great improvement on the statistical values where the mean value of the ΔTFR=TFR_{GMNA}-$TFR_{\text{2PGA,FE}}$ difference is equal to -0.9 minutes for carbon steel frames and equal to 0.2 minutes for stainless steel frames. Moreover, the new methodology shows a remarkably low standard deviation (σ) of 0.9 and 2.1 minutes for carbon steel frames and stainless steel frames, respectively. Hence, the accuracy of the proposed methodology is found to be consistent through the different degrees of utilisation, in contrast to the estimations provided by the upcoming design specifications (prEN 1993-1-2 (2021)), whose accuracy varied depending on the degree of utilisation in addition to providing inaccurate TFR estimations.

The results presented in Table 8.4 prove the capability of the proposed methodology to estimate the resistance of carbon and stainless steel frames – accounting for their redistribution capacity at elevated temperatures, the influence of second order effects derived from the lateral deflections of the frame, and the loss of mechanical properties due to the fire effect – with an accuracy equivalent to that provided by the advanced numerical models (GMNA). It should be pointed out, however, that the results reported for the developed analytical methodology were based on the cross-section bending resistances (M_{FE}) obtained from GMNA analyses and the temperature field (θ_{FE}) predicted from a numerical heat transfer analysis, which would not be typically available to engineers in everyday design practice. Hence, in the following section the accuracy of the proposed methodology is assessed when the temperature evolution and the bending moment resistance are estimated using provisions available in the upcoming codes (prEN 1993-1-2 (2021)), following a fully analytical design approach in the prediction of the resistance of carbon and stainless steel frames in fire.

8.4.4. Assessment of the proposed methodology using current knowledge and specifications

As explained in Chapter 2, the evolution of the temperature in a steel member can be estimated with great accuracy using the simplified formulation (Eq. 2.25) provided in prEN 1993-1-2 (2021) for the heat transfer between the heated air and the steel structure.

The error introduced when estimating the frame temperature with this analytical approach is nearly zero when compared to the estimations obtained with advanced numerical models (i.e., proper heat transfer analysis), as shown in Figure 8.9 for Frame 20. Hence, the advanced FE heat transfer analyses can be replaced by the prEN 1993-1-2 (2021) simplified formulation in the proposed design approach without losing accuracy in the final result for everyday design practice.

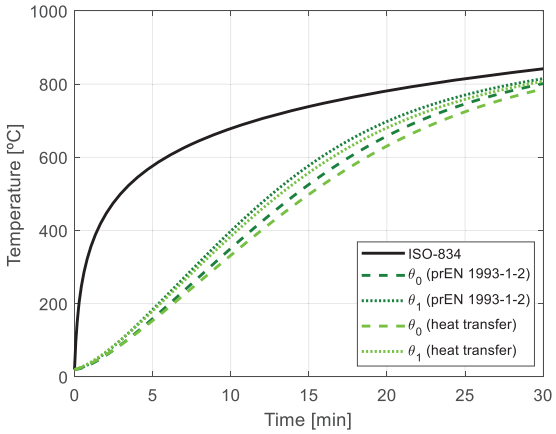

Figure 8.9. Temperature–time curves of the beam (θ_1) and the column (θ_0) for Frame 20 obtained from a FE heat transfer analysis (light green) and for the prEN 1993-1-2 (2021) formulation (dark green), compared with the ISO-834 curve (black).

However, the inaccuracy derived from estimating the bending moment resistance of cross-section using the currently codified formulation for stainless steel cross-sections is significant, as introduced in previous chapters and as Figure 8.10(a) proves.

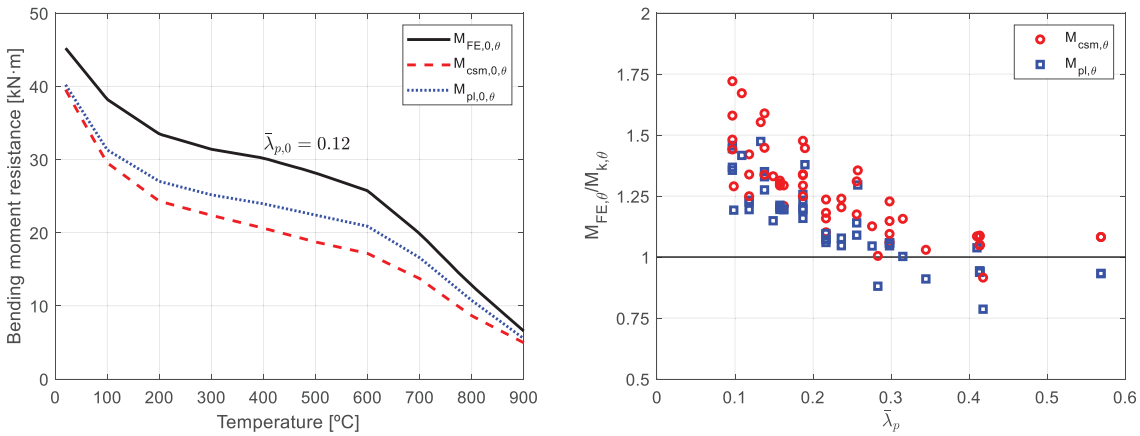

(a) (b)

Figure 8.10. (a) Bending moment evolution at different temperatures for the column in Frame 16 considering: GMNA, CSM, and plastic moment for the 2% proof stress; (b) Ratio between the GMNA and the CSM (or the plastic) bending moment resistances against the relative local slenderness ($\bar{\lambda}_p$) for the analysed stainless steel cross-sections.

This figure shows the evolution of the bending moment resistance at elevated temperatures for the column cross-section corresponding to Frame 16 (with $\bar{\lambda}_{p,0}$=0.12) calculated using different approaches: advanced numerical models (GMNA) ($M_{FE,0,\theta}$), the Continuous Strength Method approach applied at elevated temperatures ($M_{csm,0,\theta}$) (see Section 2.5.2), and the plastic bending moment capacity ($M_{pl,0,\theta}$) as the product of the plastic section modulus and the $f_{2.0}$ proof stress, as recommended in prEN 1993-1-2 (2021). As it can be seen, the differences between the analytical estimations and the resistance obtained with advanced numerical models is significant, with the

analytical approaches underestimating the cross-section resistance by 40% on average if the CSM formulation is employed, and by 20% if the plastic bending resistance is used.

The inaccuracy of the current analytical formulations for stainless steel cross-sections was found to be higher for lower relative local slenderness values, because strain hardening played a major role in the bending moment response of such cross-sections. This is evident from Figure 8.10(b), where the ratios between the numerical and analytical bending moment resistances (CSM formulation and the traditional plastic moment capacity) of the investigated stainless steel cross-sections (both columns and beams) are plotted against their relative local slenderness ($\bar{\lambda}_p$). As it can be seen, for lower $\bar{\lambda}_p$ values the accuracy of the analytical estimations decreased. It should be noted that these results considered a simplified application of the CSM for fire design (detailed in Section 2.5.2), highlighting that further research is necessary, as proposed by Murtaza and Kucukler (2023).

According to these results, the accuracy of the proposed fire design methodology was expected to be reduced when the analytical bending moment resistances were employed instead of the numerically estimated ones. Obviously, this issue only affected stainless steel frames, since for carbon steel Class 1 cross-sections the bending moment resistance can be accurately estimated based on the plastic section modulus, since no strain hardening should be considered for carbon steel structures after temperatures of 400ºC (prEN 1993-1-2 (2021)).

The final assessment of the proposed fire design approach using second order plastic global analysis and the target design horizontal displacement when adopting the analytical temperature evolution formulation (Eq. 2.25) and the bending moment resistance ($M_{\theta,Rk}$=$W_{pl}\cdot f_{2.0}\cdot k_{2.0,\theta}$) provided in prEN 1993-1-2 (2021) is presented in Table 8.6, where the TFRs of all carbon and stainless steel frames are compared for the new methodology and the advanced numerical models (GMNA), and which also reports the differences between the two time resistances. As it can be seen, the accuracy of the proposed approach is lower in comparison with the adoption of the same methodology with the bending moment resistances obtained from GMNA analyses, as Table 8.4 reports. Nevertheless, and considering that the minimum TFR for this type of frames is 30 minutes according to the Spanish building construction (CTE 2006), the results are remarkably good: it can be assumed that a mean error of 3.4 minutes and a standard deviation (σ) of 3.3 minutes is a good approximation of the actual response of the stainless frames, especially considering the limitations in current knowledge for the bending resistance of very stocky stainless steel cross-sections. For carbon steel frames, the difference in accuracy when employing the temperature field obtained with the analytical formulation (Eq. 2.25) is negligible, as expected. Since the cross-section resistance can be correctly predicted by means of the traditional plastic bending moment, the accuracy of the presented fully analytical methodology shows a mean error of -0.4 minutes and a standard deviation (σ) of 0.9 minutes.

Table 8.6. Time fire resistances (TFR) [min] of carbon steel and stainless steel frames under fire situation for different degrees of utilisation obtained from GMNA and the new methodology for the theoretical temperature evolution (Eq. 2.25) and bending resistances according to prEN 1993-1-2 (2021), and differences relative to GMNA estimations.

Frame ID	Material grade	GMNA			2nd Or. PGA *			ΔTFR (2nd Or. PGA)		
		μ_0=0.7	μ_0=0.5	μ_0=0.3	μ_0=0.7	μ_0=0.5	μ_0=0.3	μ_0=0.7	μ_0=0.5	μ_0=0.3
1	EN 1.4301	5.3	16.4	27.1	5.6	17.2	27.5	-0.3	-0.8	-0.4
2	EN 1.4401	8.5	22.3	38.2	9.3	22.2	37.5	-0.8	0.1	0.7
3	EN 1.4571	13.9	29.8	50	14.1	29.1	51.2	-0.2	0.7	-1.2
4	EN 1.4062	8.8	15.3	21.9	10.3	15.9	22.3	-1.5	-0.6	-0.4
5	EN S275	9.3	12.2	15.3	10.7	12.9	16.4	-1.4	-0.7	-1.1
6	EN 1.4301	6.0	18.4	29.2	4.8	18.1	29.5	1.2	0.3	-0.3
7	EN 1.4401	9.4	24.6	40.2	7.4	23.4	39.1	2.0	1.2	1.1
8	EN 1.4571	15.8	31.9	51.1	11.7	29.4	52.9	4.1	2.5	-1.8
9	EN 1.4062	9.0	17.1	23.7	8.8	16.2	23.7	0.2	0.9	0.0
10	EN S275	10.3	13.6	16.8	12.6	15.0	18.7	-2.3	-1.4	-1.9
11	EN 1.4301	6.0	18.2	28	3.0	13.3	24.4	3.0	4.9	3.6
12	EN 1.4401	10.0	23.4	37.9	4.7	17.6	33.6	5.3	5.8	4.3
13	EN 1.4571	16.0	29.7	49.6	7.2	22.7	45.0	8.8	7.0	4.6
14	EN 1.4062	9.1	16.1	22.3	4.5	12.7	19.4	4.6	3.4	2.9
15	EN S275	11.5	13.7	17.3	11.2	13.3	16.7	0.3	0.4	0.6
16	EN 1.4301	6.0	19	29.3	2.4	13.3	26.7	3.6	5.7	2.6
17	EN 1.4401	9.6	23.1	39.8	3.6	17.9	35.8	6.0	5.2	4.0
18	EN 1.4571	16.0	30.5	51.3	5.0	23.2	47.5	11.0	7.3	3.8
19	EN 1.4062	8.3	15.5	23.5	3.7	13.5	21.5	4.6	2.0	2.0
20	EN S275	11.5	14.2	17.7	12.1	14.4	18.0	-0.6	-0.2	-0.3
21[1]	EN 1.4301	6.4	21.1	34.8	3.1	13.3	28.4	3.3	7.7	6.4
22[1]	EN 1.4301	5.3	18.4	32.2	3.7	14.9	27.7	1.6	3.5	4.5
23[1]	EN 1.4301	6.0	20.0	31.2	2.0	12.4	27.5	4.0	7.5	3.7
24[1]	EN 1.4301	4.9	16.8	30.3	5.1	16.7	26.8	-0.3	0.1	3.5
25[1]	EN 1.4301	3.2	12.1	24.9	3.7	13.7	24.8	-0.4	-1.6	0.1
26[1]	EN 1.4401	7.2	20.2	36.5	3.3	15.0	32.0	3.9	5.1	4.5
27[1]	EN 1.4401	9.0	20.8	34.9	0.0	10.5	28.3	9.0	10.4	6.6
28[1]	EN 1.4401	8.0	21.7	37.3	4.5	17.6	33.8	3.5	4.2	3.5
29[1]	EN 1.4401	7.0	17.5	33.5	2.1	10.9	28.5	4.9	6.6	5.0
30[1]	EN 1.4401	10.0	23.0	36.4	0.0	10.0	28.6	10.0	13.0	7.8
31[2]	EN S275	13.1	–	20.3	12.4	–	19.9	0.9	–	0.7
32[2]	EN S275	9.7	–	18.5	10.8	–	17.9	-0.8	–	1.0
33[2]	EN S275	12.5	–	19.6	12.9	–	20	-0.1	–	0.1
34[2]	EN S275	9.3	–	16.2	9.9	–	16.4	-0.1	–	0.3
35[2]	EN S275	7.2	–	12.6	8.2	–	13.7	-0.8	–	-0.6
							Mean	2.5	3.3	2.0
							σ	3.5	3.7	2.6

* The bending moment ($M_{0,\theta}$ and $M_{1,\theta}$) resistances were estimated according to prEN 1993-1-2 (2021).

[1] These frames were originally analysed in Chapter 6 and 7.

[2] These frames were originally analysed in Chapter 6 and 7.

Finally, Figure 8.11 shows the difference between the TFRs obtained by means of advanced numerical models (GMNA) and the analytical estimations according to the simplified design approach prescribed in prEN 1993-1-2 (2021) (in red), or based on the proposed analytical methodology for two different scenarios: first, using the bending moment resistances and temperature distribution obtained from advanced FE analyses (light blue), and second, using the plastic bending moment resistances and the temperature field according to prEN 1993-1-2 (2021) (dark blue) for carbon steel frames (Figure 8.11(a)) and for stainless steel frames (Figure 8.11(b)).

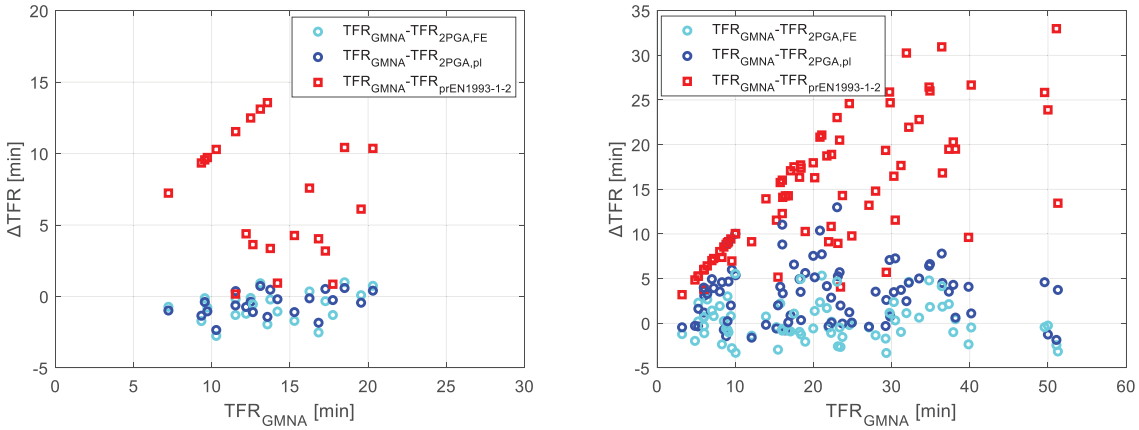

Figure 8.11. Differences between TFRs obtained from GMNA and estimated with the proposed second order plastic global analysis methodology or prEN 1993-1-2 (2021) provisions for (a) carbon steel frames, and (b) stainless steel frames.

As it can be seen in Figure 8.11(a), the proposed methodology provides better estimations of the numerical TFRs than the simplified prEN 1993-1-2 (2021) approach, as reported in Table 8.4, with a mean absolute error of -0.4 minutes and a standard deviation (σ) of 0.9 minutes. This is because the new design approach is able to consider the redistribution capacity of carbon steel frames, while the current code estimates the frame capacity based on the resistance of its critical member. On top of that, it can be seen that estimating the temperature of a uniformly heated frame using the analytical formulation (Eq. 2.25) included in prEN 1993-1-2 (2021) does not have a meaningful impact on the accuracy of the estimations obtained with the new methodology presented, as the two blue datasets plotted in Figure 8.11(a) are very similar. Note that the CSM formulation at elevated temperature introduced in Section 7.3.2 was not employed for this final assessment, since it was observed that it does not remarkably improved the bending moment estimations, while requiring more complex calculations compared to the prEN 1993-1-2 (2021) based on the traditional bending moment capacity.

For stainless steel frames, results of which are presented in Figure 8.11(b), the estimations provided by the proposed methodology when using the plastic bending moment resistances result in less accurate predictions – with a mean difference of the TFR estimation between the two approaches of $\overline{\Delta TFR}$=3.4

minutes –, while those based on the bending moment resistance obtained from advanced numerical models result in nearly no error ($\overline{\Delta TFR}$=0.2 minutes). In any event, both approaches provide significantly more accurate estimations than the member-based simplified methodologies prescribed in the upcoming codes (prEN 1993-1-2 (2021)), which exhibit an average error of 14.6 minutes for the analysed stainless steel frames.

8.5. Concluding remarks

In this chapter two different approaches for estimating the time fire resistance of carbon and stainless steel frames have been introduced. The first one, based on FE analysis, where the new failure criteria presented in Chapter 4 and validated for carbon steel frames have been revised for stainless steel frames; addressing the problem that existed when using advanced design methods following prEN 1993-1-2 (2021) recommendations, where the upcoming European fire code fail providing adequate failure criteria to determine the collapse of such structures in fire. The second approach presented, it is an analytical approach, where the redistribution capacity of carbon and stainless steel frames can be accounted for under fire situation included the influence of the second order effects based on a plastic global analysis.

8.5.1. Design based on advanced numerical models

In contrast with the response of stainless steel frames at room temperature, where the ultimate load can be commonly identified as the peak load of the load–displacement curve, the procedure for defining the time fire resistance of such frames and the corresponding critical temperature is unclear under fire situation. In this section a revision of the failure criteria presented and validated in Section 4 for carbon steel frames was carried out, since the failure of this type of structures cannot be easily identified when using the advanced calculation models codified in prEN 1993-1-2 (2021). A new proposal has been developed and assessed for determining the failure of stainless steel frames under fire situation. In particular, the criterion related to the displacement rate, which is based on the results derived from the parametric study carried out in this throughout this document.

The proposed failure criteria for assessing the collapse of carbon and stainless steel frames in fire situation by means of FE analysis are reproduced in Eq. 8.18-Eq. 8.25.

For carbon steel frames with predominant vertical displacements:

$$D_v = \frac{L^2}{400 \cdot h_1} \ [\text{mm}] \qquad \text{Eq. 8.18}$$

$$\frac{dD_v}{dt} = \frac{L^2}{9000 \cdot h_1} \cdot 10\mu_0 \ [\text{mm/min}] \qquad \text{Eq. 8.19}$$

For carbon steel frames with predominant horizontal displacements:

$$D_h = 2 \cdot \frac{H^2}{400 \cdot h_0} \text{ [mm]} \quad \text{Eq. 8.20}$$

$$\frac{dD_h}{dt} = \frac{H^2}{9000 \cdot h_0} \cdot 10\mu_0 \text{ [mm/min]} \quad \text{Eq. 8.21}$$

For stainless steel frames with predominant vertical displacements:

$$D_v = \frac{L^2}{400 \cdot h_1} \text{ [mm]} \quad \text{Eq. 8.22}$$

$$\frac{dD_v}{dt} = \frac{L^2}{4500 \cdot h_1} \cdot 10\mu_0 \text{[mm/min]} \quad \text{Eq. 8.23}$$

For stainless steel frames with predominant horizontal displacements:

$$D_h = 2 \cdot \frac{H^2}{400 \cdot h_0} \text{ [mm]} \quad \text{Eq. 8.24}$$

$$\frac{dD_h}{dt} = 2 \cdot \frac{H^2}{4500 \cdot h_0} \cdot 10\mu_0 \text{[mm/min]} \quad \text{Eq. 8.25}$$

8.5.2. Analytical design based on plastic global analysis

This section presents a numerical study to assess the plastic redistribution capacity of carbon and stainless steel frames at room temperature and under fire situation with the aim of developing more efficient design procedures that account for system effects at elevated temperatures. A total of 60 carbon and stainless steel frames were analysed under fire situation by means of advanced numerical models (GMNA) while subjected to different degrees of utilisation.

On the basis of the results obtained in parametric study and based on the results presented in Section 6 and 7 on the response of Class 1 carbon and stainless steel frames under fire situation, a thorough revision of the simplified design methods included in prEN 1993-1-2 (2021) is carried out. The assessment of the design provisions prescribed in prEN 1993-1-2 (2021) indicated that current simplified design methods for fire design – based on the critical member resistance – could not estimate accurately the response of Class 1 carbon and stainless steel frames, since their response is determined by their redistribution capacity. Moreover, the current simplified design methods could not provide any fire resistance for most frames (~85%) subjected to high initial loads (μ_0=0.7), because according to the upcoming design guidelines the frames had already failed even before the fire started, despite the results obtained with GMNA showed that these same frames could withstand the fire effect up to 20 minutes. Therefore, a new methodology based on plastic global analysis is proposed with the aim of accounting for the redistribution capacity of such structures under fire situation.

The new design methodology was evaluated against the results obtained by means of a GMNA of 100 carbon and stainless steel frames under fire situation with promising results. The second order plastic

global analyses of these frames provided accurate estimations when compared to the results obtained by means of advanced numerical models, with a nearly null mean absolute error (i.e., $\overline{\Delta TFR}$=0.2 minutes) and a standard deviation (σ) of 2.1 minutes for stainless steel frames when based on the cross-section bending resistances obtained from GMNA analyses and the temperature field predicted from a numerical heat transfer analysis. Likewise, for carbon steel frames the obtained mean absolute error was equal to 0.9 minutes and a standard deviation (σ) of 0.9 minutes, when using the temperature field predicted by the numerical heat transfer.

Moreover, the new methodology presented was assessed in conjunction with the provisions provided in prEN 1993-1-2 (2021) for cross-section resistance and temperature estimation. The fire resistance estimations were a significant improvement to those obtained based on the simplified design methods included in the upcoming European codes, with a mean absolute error of 3.4 minutes and a standard deviation (σ) equal to 3.3 minutes for stainless steel frames, while the main statistical indicators when assessing the current design guidelines were $\overline{\Delta TFR}$=14.6 minutes and σ=7.3 minutes. For carbon steel frames estimations based on current design guidelines provided a mean absolute error of 7.3 minutes and σ=3.9 minutes, while the estimations based on the new methodology in conjunction with the temperature estimation formulation provided in prEN 1993-1-2 (2021) provided better statistical indicators: $\overline{\Delta TFR}$=0.4 minutes and σ=0.9 minutes.

CHAPTER 9

Conclusions and suggestions for future research

9.1. General conclusions

Carbon steel and stainless steel structures are characterized by their inherent capacity to redistribute internal forces. With a good structural design, this characteristic leads to the development of plastic collapse mechanisms, which are classified as ductile failure modes. This type of failure is highly recommended for the design of steel structures, as they are non-fragile collapses that show signs of deterioration before collapse. From the studies carried out and presented in this thesis, it has been possible to demonstrate that carbon and stainless steel frames able to develop plastic collapse mechanisms at room temperature maintain such capacity under fire situation too. Moreover, based on several numerical studies, it has been possible to propose novel recommendations for the fire design of carbon and stainless steel frames with plastic cross-sections (i.e., Class 1) and full-strength joints, which take into account the plastic redistribution capacity of such structures.

To date, studies investigated the response of carbon and stainless steel structures at elevated temperatures have focused on isolated members (i.e., beams, columns or beam-columns). Data available at system level is scarce, but necessary to study the development of plastic collapse mechanisms, as it

involves the whole structure. For this reason, an extensive parametric numerical study is presented in Chapter 4 to carry out a preliminary analysis of the behaviour of carbon and stainless steel frames in fire. In this analysis the main basic design parameters influencing the frame response in fire are identified, along with the main existing drawbacks for the implementation of advanced system-based design approaches. Moreover, a first proposal of objective failure criteria for defining the collapse of carbon steel frames in fire is presented and validated against experimental data available in the literature.

Following the results found in Chapter 4, the subsequent Chapter 5 presents a new formulation to estimate the bending resistance of welded joints between rectangular hollow sections (RHS), cross-sections typically employed in the construction of stainless steel structures. This new formulation provides more accurate resistance estimations than current design recommendations, and considers the influence of strain hardening on the joint resistance for stainless steel connections.

Once the design of the frame connections was established, the influence of such joints on the response of carbon and stainless steel frames in fire is analysed in Chapter 6. The response of multiple frames with explicitly modelled joints is compared with the response of the same frames with ideal rigid joints. From the results obtained in this chapter it could be concluded that full-strengths joints (classified as such at room temperature) can also be modelled as ideal rigid joints in fire situation without influencing the frame fire resistance, which is in line with the recommendations given in current European codes (prEN 1993-1-8 (2020)) for full-strength joints at room temperature.

The analysis of the influence of welded joints on the frame response showed that carbon and stainless steel frames with plastic cross-section and full-strength joints exhibit certain redistribution capacity under fire situation. In Chapter 7, this redistribution capacity is analysed in depth for carbon and stainless steel frames using advanced finite element tools. Based on the results obtained in this chapter, it could be concluded that carbon and stainless steel frames develop plastic collapse mechanisms before failure in fire situation, if they fulfil the requirements established for the plastic design at room temperature (i.e., full-strength joints and plastic cross-sections). These results suggest the possibility of developing more accurate analytical formulations for estimating the resistance of such frames under fire situation that account for the overall resistance provided by the whole structure. In contrast to current simplified design methods codified in prEN 1993-1-2 (2021) that are member-based, where the whole structure resistance is based on the fire resistance of the weakest member, disregarding any capacity of redistributing internal forces.

To address these shortcomings, Chapter 8 presents a new design proposal for estimating the fire resistance of carbon and stainless steel frames based on advanced design methods. If advanced design methods (i.e., nonlinear numerical FE analysis) are employed, revised failure criteria are proposed for

estimating the fire resistance of stainless steel frames, similar to the failure criteria validated for carbon steel frames presented in Chapter 4.

Likewise, a new design method is presented in Chapter 8, from which the fire resistance of carbon and stainless steel frames can be estimated analytically based on a plastic global analysis. This new methodology considers the influence of second order effects derived from the horizontal drift of the structures, and accounts for the over-strength provided by strain hardening for stainless steel frames. The results obtained with this new analytical approach have been found to be in good agreement with the fire resistance estimations obtained with advanced numerical models, and provide a remarkable improvement on the design of carbon and stainless steel structures in fire if compared to the accuracy of the current design guidelines included in the European codes (prEN 1993-1-2 (2021)).

9.2. Specific conclusions

This section reports the specific conclusions derived from the studies presented in this thesis. Although each chapter has a final section where the main conclusions are highlighted, a summary of the most relevant conclusions and contributions derived from this thesis is presented herein.

9.2.1. Bending moment resistance of welded joints

The main cross-section typology analysed throughout this thesis has been the rectangular hollow section (RHS), because it is the most common cross-section employed in the design of stainless steel structures due to the excellent strength-to-weight ratio exhibited by this product type. However, the analysis presented in this thesis regarding the resistance of joints between RHS members demonstrated that current design guidelines fail to estimate accurately the bending moment resistance of welded joints between RHS members comprising typical frame geometries employed in building construction, since the formulation was thought and developed to be applied to smaller connections, more common in truss joints.

Therefore, based on a large parametric study, a new formulation for estimating the bending resistance of such connections has been developed in this thesis, which is reproduced in Eq. 9.1. This new formulation covers welded joints failing due to chord face yielding, and considers the influence of additional geometric parameters (i.e., the chord radius and the weld throat thickness) which are not considered in current design specifications (prEN 1993-1-8 (2020)).

$$M_{Rk} = f_y h_1 {t_0}^2 \left(\frac{1+\beta^*}{4\eta^*} + \frac{2}{\sqrt{1-\beta^*}} + \frac{\eta^*}{2(1-\beta^*)} \right) k_n / \gamma_{M5} \qquad \text{Eq. 9.1}$$

The proposed formulation is derived from a new yield line mechanism and provides better resistance predictions than current formulations for carbon steel connections, as Figure 9.1 confirms. Furthermore, this new formulation is also able to consider the over-strength provided by strain hardening in stainless steel connections thanks to the consideration of the Continuous Strength Methods (CSM). The new formulation (Eq. 9.1), along with the CSM provisions, is a considerable improvement (Figure 9.1) for estimating the bending moment resistance of stainless steel joints between RHS members.

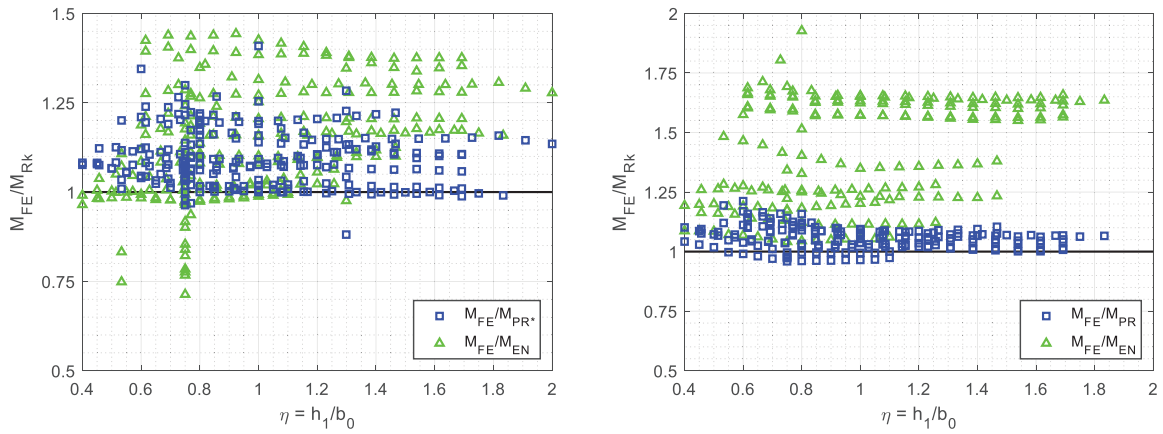

(a) (b)

Figure 9.1. Assessment of the new proposal (in blue) and the current design recommendations (prEN 1993-1-8 (2020)) (green) for estimating the bending moment resistance of welded joints between RHS (a) carbon steel and (b) stainless steel members with $\beta \leq 0.85$.

Finally, the soundness and safety of the proposed formulation has been statistically investigated, obtaining γ_M partial resistance factors of 1.05 and 1.06 for carbon steel and stainless steel connections, respectively. Hence, and based on the obtained results, values of γ_{M5}=1.05 and γ_{M5}=1.10 are proposed for carbon and stainless steel welded joints between tubular sections, respectively.

9.2.2. Comparison of the response of carbon and stainless steel frames in fire

Throughout this thesis, it has been proved that the response of carbon and stainless steel frames with plastic cross-sections in fire should be analysed considering structures as whole systems if a safe and efficient design is aimed. Their response is directly influenced by the boundary conditions, the loading case, and the relative resistances and stiffnesses of the columns and the beams. Moreover, it has been proved that the estimation of the fire resistance of such structures based on the resistance of their critical member is inadequate, as it results in overly conservative time fire resistance estimations.

The degree of utilisation (μ_0) – calculated as the ratio between the design load for fire design over the ultimate load resistance of the structure at room temperature – plays a major role on the frame's response. This parameter usually ranges from 0.3 to 0.7, being 0.3 the most favourable case and 0.7 the most disadvantageous situation. The results showed that high initial loads ($\mu_0 \geq 0.6$) generally lead to low critical temperatures (and low time fire resistances), situations in which carbon steel performs better than most

stainless steel grades due to its capacity to retain mechanical properties better at low-to-intermediate temperatures (mechanical properties of carbon steel suffer a sudden reduction at temperatures ≥400ºC). In contrast, stainless steel grades (and, in particular, austenitic stainless steels) outperform carbon steel for structures under mid-to-low degrees of utilisation ($\mu_0 \leq 0.5$), because most stainless steel grades retain mechanical properties better than carbon steel at high-to-very high temperatures (i.e., ≥600ºC).

Traditionally, carbon steel structures are provided with some additional fire protection to resist the fire effect for the required timespans. The results obtained in this thesis are in line with this common practice, since unprotected carbon steel structures were found to not be able to withstand the effect of fire for 30 minutes, which is the minimum requirement according to fire safety codes (CTE 2006). However, if designed appropriately, the unprotected stainless steel structures investigated in this thesis (and, in particular, austenitic stainless steel structures) were found to be able to withstand the effect of fire for over 30 minutes. In the case of frames made of the stainless steel grade EN 1.4571 – characterized by having the highest retention factors at elevated temperatures – exceptionally high time fire resistances were observed, reaching time fire resistances of over 50 minutes. This particularity of stainless steel alloys is a clear advantage, in addition to their corrosion resistance, which could lead to the design of unprotected stainless steel structures that meet the government requirements for fire safety.

9.2.3. Redistribution capacity of carbon and stainless steel frames in fire

Based on the numerical analyses carried out in the different studies presented in this document, it has been demonstrated that carbon steel and stainless steel frames maintain a high internal force redistribution capacity even at elevated temperatures. By checking the bending moment evolution at the critical cross-sections expected to develop plastic hinges (or plastic zones), it could be confirmed that carbon and stainless steel critical cross-sections reach their plastic bending capacities before the frames collapse at elevated temperatures, as shown in Figure 9.2.

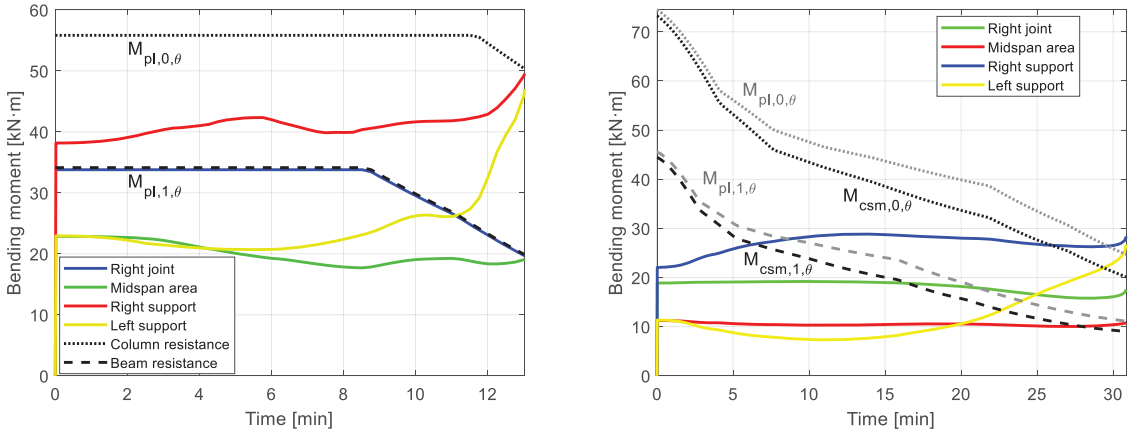

(a) (b)

Figure 9.2. Bending moment [kN·m] evolution at the critical cross-sections over time under fire situation for (a) carbon steel frame with μ_0=0.7, and (b) stainless steel frame μ_0=0.3.

Moreover, it could be confirmed that carbon and stainless frames with full-strength joints and plastic cross-sections failed describing plastic collapse mechanisms in fire situation. This phenomenon could be clearly observed from the plastic deformation field of carbon steel frames moments before the frames collapse, where all inelastic deformations are concentrated at the four critical cross-sections expected to develop plastic hinges, as Figure 9.3 shows.

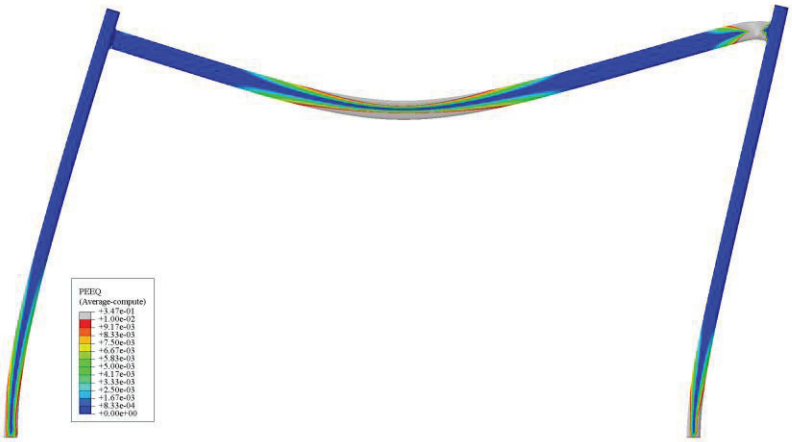

Figure 9.3. Inelastic deformations of a carbon steel frame in fire before collapsing.

9.2.4. Failure criteria for carbon and stainless steel frames in fire

The upcoming European codes for fire design (prEN 1993-1-2 (2021)) allow employing advanced design methods (i.e., advanced finite element analysis) for estimating the fire resistance of steel structures. However, European codes (prEN 1993-1-2 (2021)) do not provide any information on how to determine the failure of such structures under fire situation. For this reason, a set of failure criteria have been proposed in this thesis for estimating the collapse of carbon and stainless steel frames objectively when using advanced design methods.

The defined failure criteria include limiting values for the vertical and horizontal displacements occurring at the structures, as well as for the corresponding displacements rates, and they have been validated against laboratory data from multiple tests carried out on carbon steel frames subjected to fire (Rubert and Schaumann 1986). The proposed failure criteria for carbon steel frames are reproduced in Eq. 9.2-Eq. 9.5.

For large vertical displacements:

$$D_v = \frac{L^2}{400 \cdot h_1} \text{ [mm]} \qquad \text{Eq. 9.2}$$

$$\frac{dD_v}{dt} = \frac{L^2}{9000 \cdot h_1} \cdot 10\mu_0 \text{ [mm/min]} \qquad \text{Eq. 9.3}$$

For large horizontal displacements:

$$D_h = 2 \cdot \frac{H^2}{400 \cdot h_0} \text{ [mm]} \quad \text{Eq. 9.4}$$

$$\frac{dD_h}{dt} = \frac{H^2}{9000 \cdot h_0} \cdot 10\mu_0 \text{ [mm/min]} \quad \text{Eq. 9.5}$$

Since no stainless steel frames have been tested in fire yet, the assessment of the proposed failure criteria for stainless steel frames was based on the numerical results obtained from the multiple frames analysed in this thesis. After a comprehensive analysis of the failure criteria, and especially the displacement rates for stainless steel frames in fire, a new limiting criteria was proposed, which capture the collapse of such structures in fire more accurately, and which are reproduced in Eq. 9.6-Eq. 9.9.

For large vertical displacements:

$$D_v = \frac{L^2}{400 \cdot h_1} \text{ [mm]} \quad \text{Eq. 9.6}$$

$$\frac{dD_v}{dt} = \frac{L^2}{4500 \cdot h_1} \cdot 10\mu_0 \text{[mm/min]} \quad \text{Eq. 9.7}$$

For large horizontal displacements:

$$D_h = 2 \cdot \frac{H^2}{400 \cdot h_0} \text{ [mm]} \quad \text{Eq. 9.8}$$

$$\frac{dD_h}{dt} = 2 \cdot \frac{H^2}{4500 \cdot h_0} \cdot 10\mu_0 \text{[mm/min]} \quad \text{Eq. 9.9}$$

The failure of carbon and stainless steel frames under the applied loads is considered to occur when both failure criteria have been exceeded (e.g., Eq. 9.6 and Eq. 9.7 for stainless steel frames describing large vertical displacements, and Eq. 9.8 and Eq. 9.9 for stainless steel frames with predominantly horizontal displacements). For frames describing large horizontal and vertical displacements (e.g., frames failing in a combined collapse mechanism), the most restrictive pair of limits should be used. The same procedure should be applied for carbon steel frames.

9.2.5. Second order plastic global analysis in fire

The final and most relevant contribution of this thesis is a new approach for estimating the fire resistance of carbon and stainless steel frames with plastic cross-sections. This analytical design method is based on a plastic global analysis, and it accounts not only for the redistribution capacity of carbon and stainless steel frames, but also for the influence of second order effects resulting from the horizontal drift of the frames in fire situation.

This new methodology to assess the frame fire resistance requires to solve a complete plastic mechanism by means of a second order plastic global analysis to accurately predict the fire resistance of carbon and

stainless steel frames. The equations predicting the frame resistance are time dependant, and vary depending on the analysed loading case and frame geometry. Consequently, this new approach provides fire resistance estimations with a significantly improved accuracy compared with the current simplified design methods, as Figure 9.4 corroborates. The red markers represent the absolute error committed in the prediction of the time fire resistance of carbon and stainless steel frames following the design guidelines codified in prEN 1993-1-2 (2021) when compared to advanced FE models, while the results in blue indicate the absolute error corresponding to the new methodology presented.

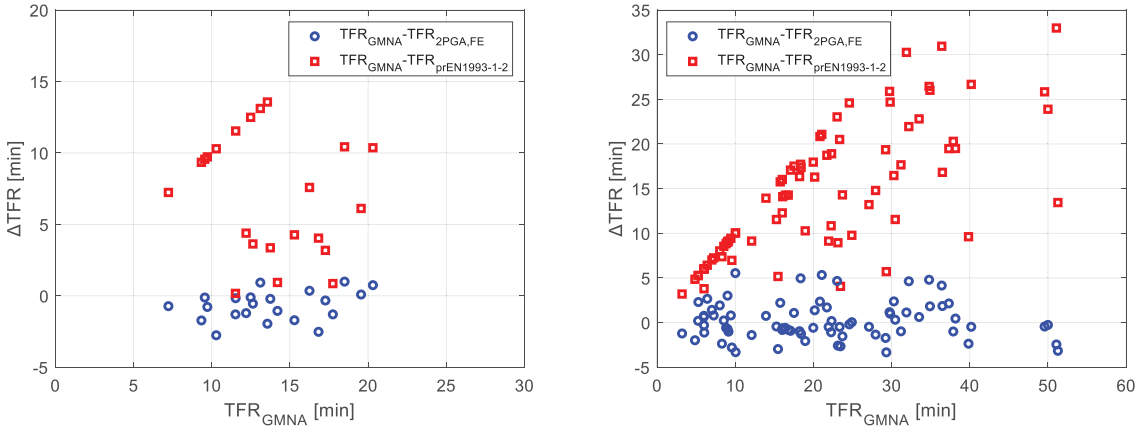

Figure 9.4. Differences between *TFR*s obtained from GMNA and estimated with the proposed second order plastic global analysis methodology or prEN 1993-1-2 (2021) provisions for (a) carbon steel frames, and (b) stainless steel frames.

This new approach for calculating the fire resistance of carbon and stainless steel structures by means of an analytical design method, which allows to account for the plastic redistribution capacity of such structures, opens a new way of fire design in steel structures. This is especially relevant for stainless steel structures, which due to their unique mechanical and thermal properties at elevated temperatures, can be potentially left unprotected and still fulfil the fire safety requirements based on the presented simplified design method. This feature, combined with the exceptional corrosion resistance and ductility exhibited by stainless steels, poise these alloys as excellent alternatives to more traditional structural materials in the paradigm of making the construction sector safer and more sustainable.

9.3. Future works

This final section provides a list of future lines of research that will allow to extend the studies carried out in this thesis on the different research paths addressed.

1. The conclusions presented in this thesis are limited to frames that do not show instability failure modes. Hence, assessing the influence of member buckling on the overall frame response requires further investigation. By analysing frames comprised of members prompt to buckle, the limiting relative member slenderness from which the redistribution capacity of the frames

is affected in fire situation could be determined, or establish whether the member slenderness does not have any influence on the development of plastic collapse mechanisms at elevated temperatures.

2. The study of this thesis solely focused on rectangular hollow section (RHS) members, mainly because RHS are the most used cross-sections in the design of stainless steel structures. However, it would be necessary to assess the applicability of the proposed analytical methodology to predict the fire resistance of steel structures exhibiting other section types, where the shadow effect may play a major role on the temperature evolution at the cross-sections.
3. Likewise, only frames with one bay and one storey have been analysed throughout this thesis. Other configurations with more complex geometries should be also analysed to investigate the applicability of the new method to more redundant structures, and to assess the influence of second order effects in fire for other frame geometries. Moreover, studying buildings with multiple bays and storey would allow analysing diverse fire scenarios (e.g., fire appearing on an isolated frame or fire spreading along a whole building storey), and their influence on the overall structural response in fire.
4. Different fire cases (e.g., localized fires or full chamber fires) directly affect the temperature field evolution over time. Determining the influence of these different fire cases on the structural response would be a fundamental path of investigation to consolidate the proposed design approach. Moreover, determining if the redistribution capacity shown by the assessed frames is influenced by the fire scenario the structure is subjected to could be further analysed.
5. Another necessary path of investigation is to assess the accuracy of the fire resistance estimations based on a first order plastic global analysis for carbon and stainless steel structures that fail describing partial plastic mechanisms (e.g., beam or column plastic mechanism), since this type of structures cannot be solved accounting for second order effects analytically. However, a first order analysis may be sufficient to accurately predict the fire resistance of such structures.
6. The proposed failure criteria to be used in conjunction with advanced design methods (i.e., FE analysis) should be extended and revised for other frame typologies and fire situations. Other fire situations (i.e., external, hydrocarbon or localized fires) may lead to faster or slower heat transfer rates, which would directly influence the displacement rates described by the structure. The extension and revision of the proposed failure criteria to more general fire cases and structure types could be a great advance for the fire design based on FE analysis.
7. The target horizontal displacements proposed in this thesis can be considered as preliminary, as they have been calibrated based on a limited amount of data. The extension of this parameter to other frame typologies and materials would be relevant, because analytically determining the ultimate horizontal drift a steel structure can reach before collapsing is difficult when yielding

occurs throughout the structure. However, providing a target horizontal displacement that could be used in multiple design cases (both at room temperature and in fire situation) would be a great advance for plastic design. This parameter should be estimated statistically based on large parametric studies, where multiple frame geometries, loading cases and different materials are analysed.

8. Lastly, a goal that multiple researchers have tried to achieve is to relate the curvature (χ) of a critical cross-section with the rotation (θ) required to form the plastic collapse mechanism. If this is achieved, it would allow to track the exact evolution of the bending moment at each critical cross-section (even for nonlinear materials such as stainless steel), and to determine the maximum displacements the structure can describe before fully forming the plastic collapse mechanism.

REFERENCES

Abaqus Documentation. Abaqus 2020. Abaqus, Version 6.20. Dassault Systems Simulia Corp. USA.

Afshan, S. Structural Behaviour of Cold-Formed Stainless Steel Tubular Members. PhD thesis, Imperial College London, 2013.

Afshan, S.; Gardner, L. *The continuous strength method for structural stainless steel design*. Thin-Walled Structures 68, 42-49, 2013.

Afshan, S.; Zhao, O.; Gardner, L. *Standardised material properties for numerical parametric studies of stainless steel structures and buckling curves for tubular columns*. Journal of Constructional Steel Research 152, 2–11, 2019.

ANSI/AISC 360-10. Specification for structural steel buildings. American Institute of Steel Construction (AISC), Chicago, USA, 2010.

ANSI/AISC 370-21. Specification for structural stainless steel buildings. American Institute of Steel Construction (AISC), Chicago, USA, 2016.

Arrayago, I.; Rasmussen, K.; Real, E. *Statistical analysis of the material, geometrical and imperfection characteristics of structural stainless steels and members*. Journal of Constructional Steel Research 175, 106378, 2020.

Arrayago, I.; Rasmussen, K.J.R. *Influence of the imperfection direction on the ultimate response of steel frames in advanced analysis*. Journal of Constructional Steel Research 190, 107137, 2022.

Arrayago, I.; Rasmussen, K.J.R. *Reliability of stainless steel frames designed using the Direct Design Method in serviceability limit states*. Journal of Constructional Steel Research 196, 107425, 2022.

Arrayago, I.; Rasmussen, K.J.R.; Zhang, H. *System-based reliability analysis of stainless steel frames subjected to gravity and wind loads*. Structural Safety 97, 102211, 2022.

Arrayago, I.; Real, E.; Gardner, L.; Mirambell, E. *The Continuous Strength Method for the design of stainless steel hollow section beam-columns*. Engineering Structures 238, 111981, 2021.

Arrayago, I.; Real, E.; Mirambell, E.; Gardner, L. *The Continuous Strength Method for the design of stainless steel hollow section columns*. Thin-Walled Structures 154, 106825, 2020.

Bock, M.; Gardner, L., Real, E. *Material and local buckling response of ferritic stainless steel sections.* Thin-Walled Structures 89, 131–141, 2015.

Bock, M.; Gardner, L.; Real, E. *Material and local buckling response of cold-formed ferritic stainless steel sections*. Thin-Walled Structures 89, 131–41, 2015.

Chen, W.F.; Sohal, I. Plastic Design and Second-Order Analysis of Steel Frames. Springer-Verlag, 1995. ISBN 10: 1461384303

Código Técnico de la Edificación, Documento Básico, Seguridad ante Incendio. CTE-BD-SI. Ministerio de Fomento, España, 2006.

Couto, C.; Vila Real, P.; Lopes, N.; Rodrigues, J.P. *Buckling analysis of braced and unbraced steel frames exposed to fire.* Engineering Structures 49, 514-559, 2013.

Design Manual of Structural Stainless Steel. 4th Edition. Ascot, United Kingdom, 2017. ISBN: 978-1-85942-226-7.

Dundu M.; Van Tonder P. *Local buckling strength of stainless steel beam webs subjected to a stress gradient*. Thin-Walled Structures 77, 48-5, 2014.

Elflah, M.; Theofanous, M.; Dirar, S. *Behaviour of stainless steel beam-to-column joints-part 2: Numerical modelling and parametric study*. Journal of Constructional Steel Research 152, 194–212, 2019.

Elflah, M.; Theofanous, M.; Dirar, S.; Yuan, H. *Structural behaviour of stainless steel beam-to-tubular column joints.* Engineering Structures 184, 158–175, 2019.

Espinós, A. Numerical analysis of the fire resistance of circular and elliptical slender concrete filled tubular columns. PhD thesis, Universitat Politècnica de València, 2012.

Espinós, A.; Romero, M.; Hospitaler, A. *Simple calculation model for evaluating the fire resistance of unreinforced concrete filled tubular columns*. Engineering Structures 42, 231-244, 2012.

European Committee for Standardization (CEN). EN 1363-1:2020. Fire resistance tests – Part 1: General Requirements. Brussels, Belgium, 2020.

European Committee for Standardization (CEN). EN 1990:2002. Eurocode 0: Basis of structural and geotechnical design. Brussels, Belgium, 2002.

European Committee for Standardization (CEN). EN 1991-1-2:2002. Eurocode 1: Action on structures – Part 1-2: General actions. Actions on structures exposed to fire. Brussels, Belgium, 2002.

European Committee for Standardization (CEN). EN 1993-1-4:2006. Eurocode 3: Design of Steel Structures – Part 1-4: General Rules. Supplementary Rules for Stainless Steels. Brussels, Belgium, 2006.

European Committee for Standardization (CEN). EN 1993-1-8:2005. Eurocode 3: Design of Steel Structures – Part 1-8: Design of Joints. Brussels, Belgium, 2011.

European Committee for Standardization (CEN). EN 1994-1-2:2005. Eurocode 4: Design of Composite Steel and Concrete Structures – Part 1-2: General rules. Structural fire design. Brussels, Belgium, 2005.

European Committee for Standardization (CEN). prEN 1990:2022. Eurocode: Basis of structural and geotechnical design. Draft, 2022.

European Committee for Standardization (CEN). prEN 1993-1-1:2019. Eurocode 3: Design of Steel Structures – Part 1-1: General rules and rules for buildings. Brussels, Belgium, 2019.

European Committee for Standardization (CEN). prEN 1993-1-14:2021. Eurocode 3: Design of steel structures – Part 1-14: Design assisted by finite element analysis. Brussels, Belgium, 2021.

European Committee for Standardization (CEN). prEN 1993-1-2:2021. Eurocode 3: Design of Steel Structures – Part 1-2: General Rules. Structural fire design. Brussels, Belgium, 2021.

European Committee for Standardization (CEN). prEN 1993-1-4:2021. Eurocode 3: Design of Steel Structures – Part 1-4: General Rules. Supplementary Rules for Stainless Steels. Brussels, Belgium, 2021.

European Committee for Standardization (CEN). prEN 1993-1-8:2020. Eurocode 3: Design of Steel Structures – Part 1-8: Design of Joints. Brussels, Belgium, 2020.

European Committee for Standardization (CEN).EN 1993-1-1:2005. Eurocode 3: Design of Steel Structures – Part 1-1: General rules and rules for buildings. Brussels, Belgium, 2005.

Feng, R.; Huang, Z.; Chen, Z.; Roy, K.; Chen, B.; Lim, J.B.P. *Finite-element analysis and design of stainless-steel CHS-to-SHS hybrid tubular joints under axial compression*. Thin-Walled Structures 151, 106728, 2020.

Feng, R.; Liu, Y.; Zhu, J. *Tests of CHS-to-SHS tubular connections in stainless steel*. Engineering Structures 199, 109590, 2019.

Feng, R.; Young, B. *Experimental investigation of cold-formed stainless steel tubular T-joints*. Thin-Walled Structures 46 (10), 1129–1142, 2008.

Feng, R.; Young, B. *Theoretical analysis of cold-formed stainless steel tubular joints*. Engineering Structures 83, 99–115, 2015.

Franssen, J.M.; Vila Real, P. Fire Design of Steel Structures. ECCS Eurocode Design Manuals. ECCS and Ernst & Sohn, 2010. ISBN: 978-92-9147-099-0 and 978-3-433-02974-9.

Gardner, L. *Stability and design of stainless steel structures – Review and outlook*. Thin-Walled Structures 141, 208-216, 2019.

Gardner, L.; Insausti, A.; Ng, K.T.; Ashraf, M. *Elevated temperature material properties of stainless steel alloys*. Journal of Constructional Steel Research 66, 634-647, 2010.

González-de-León, I.; Arrayago, I.; Real, E.; Mirambell, E. *A stiffness reduction method for the in-plane design of stainless steel members and frames according with EN 1993-1-4*. Engineering Structures 253, 113740, 2022.

González-de-León, I.; Arrayago, I.; Real, E.; Nastri, E. *Rotation capacity of cold-formed stainless steel RHS beams under cyclic loading*. Journal of Constructional Steel Research 192, 107199, 2022.

Han, L.H. *Fire performance of concrete filled steel tubular beam-columns.* Journal of Constructional Steel Research 57(6), 697-711, 2001.

Horne, M.R. Plastic theory of structures. 2nd Edition in SI/Metric Units. Pergamon, 1979. ISBN: 0080227384.

International Institute of Welding (IIW) Subcommission XV-E, XV-1281-08: Static Design Procedure for Welded Hollow Section Joints-Recommendations, 3rd Ed., 2008.

ISO 14346:2013: Static design procedure for welded hollow-section joints – Recommendations. ISO/FDIS 14346:2013(E), Geneva, 2013.

Johansen, K.W. *Yield-line formulae for slabs*. CRC Press, 1972. ISBN: 9780721008196.

Kožich, M.; Wald, F.; Ding Bu, X.; Packer, J. A. *The strain limit state criterion for hollow section joints.* Steel Construction: Design and Research, 15, Issue S1 Supplement: Hollow Sections, 2-9, 2022.

Kucukler, M.; Xing, Z.; Gardner, L. *Behaviour and design of stainless steel I-section columns in fire.* Journal of Constructional Steel Research 165, 105890, 2020.

Lan, X.; Chan, T.M.; Young, B. *Structural behaviour and design of chord plastification in high strength steel CHS X-joints.* Construction and Building Materials 191, 1252-1267, 2018.

Lie, T.T. *A procedure to calculate fire resistance of structural members*. Fire and Materials 8(1), 40-48, 1984.

Liu, W.; Zhang, H.; Rasmussen, K.J.R. *System reliability-based Direct Design Method for space frames with cold-formed steel hollow sections*. Engineering Structures 166, 79–92, 2018.

Lopes, N.; Vila Real, P.; Simões da Silva, L.; Franssen, J.M. *Numerical analysis of stainless steel beam-columns in case of fire.* Fire Safety Journal 50, 35-50, 2012.

Lu, L.H.; de Winkel, G.D.; Yu, Y.; and Wardenier, J. *Deformation limit for the ultimate strength of hollow section joints*. Proceedings 6th International Symposium on Tubular Structures, 341-347. Melbourne, Australia. Tubular Structures VI, Balkema, Rotterdam, The Netherlands, 1994.

Manninen, T.; Säynäjäkangas, J. *Mechanical Properties of Ferritic Stainless Steels at Elevated Temperatures.* Stainless Steel in Structures, Fourth International Experts Seminar, Ascot, UK, 2012.

Medall, D.; Espinós, A.; Albero, V.; Romero, M. *Simplified proposal for the temperature field of steel-reinforced CFST columns exposed to fire.* Engineering Structures 273, 115083, 2022.

Murtaza, H.; Kucukler, M. *Fire Design of steel columns trough second-order inelastic analysis with strain limits.* Thin-Walled Structures 184, 110458, 2023.

Nethercot, D.A.; Gardner, L. *Exploiting the special features of stainless steel in structural design*. Proceedings of the Third Conference on Advances in Steel Structures (ICASS02), Volume 1, 43-55. Hong Kong, China 2002.

Ng, K. T.; Gardner, L. *Buckling of stainless steel columns and beams in fire.* Engineering Structures 29(5), 717–730, 2007.

Ozyurt, E.; Wang, Y.C.; *A numerical investigation of static resistance of welded planar steel tubular joints under in-plane and out-of-plane bending at elevated temperatures.* Engineering Structures 199, 109622, 2019.

Ozyurt, E.; Wang, Y.C.; *Effect of truss behavior on critical temperatures of welded steel tubular truss members exposed to uniform fire*. Engineering Structures 88, 225-240, 2015.

Ozyurt, E.; Wang, Y.C.; Tan, K.H. *Elevated temperature resistance of welded tubular joints under axial load in the brace member*. Engineering Structures 59, 574-586, 2014.

Packer, J.A. *Theoretical behaviour and analysis of welded steel joints with RHS chord sections*. PhD thesis, University of Nottingham, U.K., 1978.

Packer, J.A.; Wardenier, J.; Zhao, X.L.; van der Vegte, G.J.; Kurobane, Y. Design Guide for Rectangular Hollow Section (RHS) Joints under Predominantly Static Loading. CIDECT, Verlag TUV Rheinland, Germany, 2009. ISBN-10: 3824900890.

Rossi, B. Stainless steel in structures in view of sustainability. In: Fourth international stainless steel experts seminar. Ascot, UK, 2012.

Rubert, A.; Schaumann, P. *Structural Steel and Plane Frame Assemblies under Fire Action*. Fire Safety Journal 10, 173-184, 1986.

Segura, G.; Pournaghshband, A.; Afshan, S.; Mirambell, E. *Influence of the degree of utilisation on the structural behaviour of stainless steel frames subject to fire*. Proceedings of the European Conference on Steel and Composite Structures (Eurosteel 2020), Sheffield, UK, 2021.

Todini, N.; Rossi, B.; Franssen, J.M. *Experimental investigation of ferritic stainless steel columns in fire*. Fire Safety Journal 62, 238–248, 2013.

Togo, T. *Experimental study on mechanical behaviour of tubular joints*. PhD thesis, Osaka University, Japan, 1967 (in Japanese).

UNE-EN 10088-1:2015: Stainless steels - Part 1: List of stainless steels.

Walport, F.; Chan, H.U.; Nethercot, D.A.; Gardner, L. *Design of stainless steel structural systems by GMNIA with strain limits*. Engineering Structures 276, 115339, 2023.

Walport, F.; Gardner, E.; Real, E.; Arrayago, I.; Nethercot, D.A. *Effects of material nonlinearity on the global analysis and stability of stainless steel frames*. Journal of Constructional Steel Research 152, 173–182, 2019.

Wardenier, J. *Hollow section joints*. PhD thesis, Delft University Press, The Netherlands, 1982.

Wardenier, J. Hollow Sections in Structural Applications. CIDECT. John Wiley & Sons Ltd, 2001. ISBN-10: 0471499137.

Wardenier, J.; Kurobane, Y.; Packer, J.A.; van der Vegte, G.J.; Zhao, X.L. Design Guide for Circular Hollow Section (CHS) Joints under Predominantly Static Loading, CIDECT, Verlag TUV Rheinland, Germany, 2008. ISBN-10: 3885859750.

Young, B. *Research on cold-formed steel columns*. Thin-Walled Structures 46(7–9), 731–740, 2008.

Yu, Y. *The static strength of uniplanar and multiplanar connections in rectangular hollow sections*. PhD thesis, Delft University Press, The Netherlands, 1997.

Yun, X.; Zhu, Y.; Wang, Z.; Gardner, L. *Benchmark tests on high strength steel frames*. Engineering Structures 258, 114108, 2022.

Zhang H.; Shayan S.; Rasmussen K.J.R; Ellingwood B.R. *System-based design of planar steel frames, II: Reliability results and design recommendations*. Journal of Constructional Steel Research 807 123, 154–161, 2016.

Zhao XL. *Deformation limit and ultimate strength of welded T-joints in cold-formed RHS sections*. Journal of Constructional Steel Research 53(2), 149–65, 2000.

Zhao, O.; Afshan, S.; Gardner, L. *Structural response and continuous strength method design of slender stainless steel cross-sections*. Engineering Structures 140, 14-25, 2017.

Zhao, O.; Gardner, L.; Young, B. *Buckling of ferritic stainless steel members under combined axial compression and bending*. Journal of Constructional Steel Research 117, 35-48, 2016.

Zhao, X.L. *The behaviour of cold formed RHS beams under combined actions*. PhD thesis, The University of Sydney, Australia, 1992.

ANNEX A

Development of the new formulation for the bending resistance of RHS welded joints based on a proposed yield line mechanism

A.1.Notation

YL_i: yield line i.

A-H: main points of the mechanism geometry.

M: bending moment.

h_1: brace height.

b_1: brace width.

b_0: chord width.

R_0: chord radius.

b_0^*: effective length as defined in Eq. 5.8.

m_{pl}: plastic moment.

l_i: length of the yield line i.

θ: joint rotation.

φ_i: rotation of the yield line i.

α: angle between yield line 6 and yield line 7.

δ: maximum out-of-plane displacement produced by the bending moment.

β^*: b_1/b_0^*.

η^*: h_1/b_0^*.

A.2.Basic calculations

The resistance of a yield line mechanism is based on the principle of virtual works (PVC), which can be expressed as per Eq. A. 1,

$$W_{ext} = W_{int} \quad \text{Eq. A. 1}$$

where W_{int} and W_{ext} are the work produced by the internal and external forces, and can be calculated as shown in Eq. A. 2 and Eq. A. 3

$$W_{ext} = M \cdot \theta \quad \text{Eq. A. 2}$$

$$W_{int} = \varphi_i l_i m_{pl} \quad \text{Eq. A. 3}$$

and θ and m_{pl} are obtained according to Eq. A. 4 and Eq. A. 5, respectively.

$$\theta = \frac{2 \cdot \delta}{h_1} \quad \text{Eq. A. 4}$$

$$m_{pl} = \frac{t_0^2}{4} \cdot f_y \quad \text{Eq. A. 5}$$

In order to obtain the bending moment resistance (M) of the proposed yield line mechanism, the internal work ($W_{int,i}$) of each yield line (YL_i) shown in Figure A. 1 needs to be derived, which is presented in detail in the following sub-sections of this Annex.

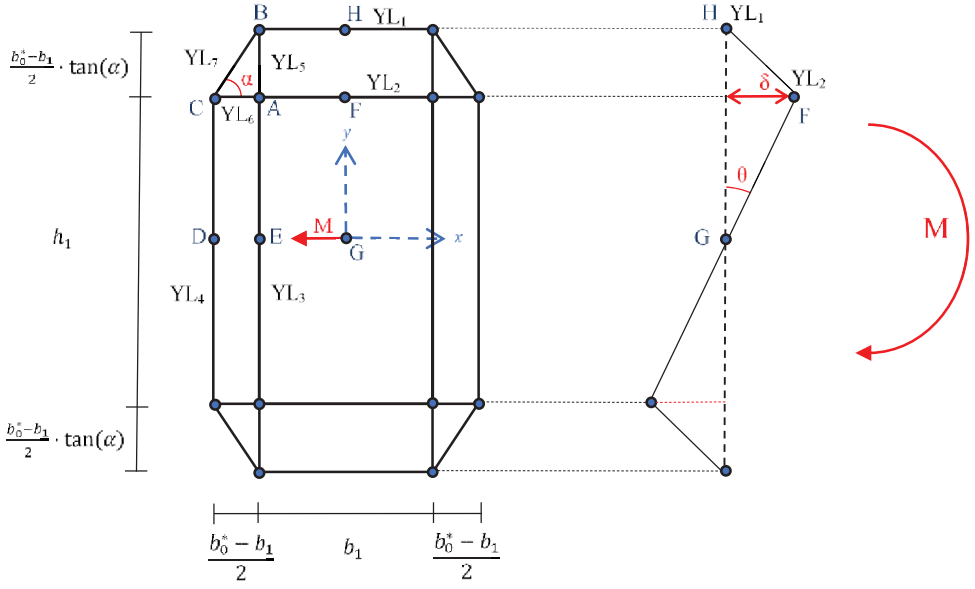

Figure A. 1. Geometry and basic information of the proposed yield line mechanism.

For all the upcoming calculations presented in this Annex, it has been assumed that the deformations (δ) produced by the bending moment (M) are small enough so that expressions Eq. A. 6-Eq. A. 8 are applicable for all the angles out of the x–y plane.

$$\sin(x) \approx x \qquad \text{Eq. A. 6}$$

$$\cos(x) \approx 1 \qquad \text{Eq. A. 7}$$

$$\tan(x) \approx x \qquad \text{Eq. A. 8}$$

On top of that, it is important to note that the rotations of yield lines 5 and 6 have been assumed to be equal to the projected rotation into the y–z and x–z planes, respectively, as previous studies did (Wardenier 1982) when deriving formulations using yield line mechanisms. Nevertheless, this assumption is on the safe side because the projected angle will always be lower than the real angle, and thus this simplification reduces the work produced by the internal forces and, consequently, the estimated bending moment resistance (see Eq. A. 1 to Eq. A. 3).

A.3.Internal work of yield lines 1 and 2

The internal work done by the yield lines 1 and 2 can be calculated in accordance with Figure A. 2.

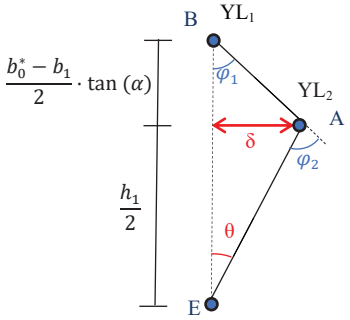

Figure A. 2. Geometric description of the rotations for yield line 1 and yield line 2.

The rotations of the yield lines 1 and 2 can be defined as per in Eq. A. 9 and Eq. A. 10, respectively.

$$\varphi_1 = \frac{2 \cdot \delta}{(b_0^* - b_1) \cdot \tan(\alpha)} \quad \text{Eq. A. 9}$$

$$\varphi_2 = \frac{2 \cdot \delta}{(b_0^* - b_1) \cdot \tan(\alpha)} + \frac{2 \cdot \delta}{h_1} \quad \text{Eq. A. 10}$$

Likewise, the length of the yield lines 1 and 2 is given in Eq. A. 11 and Eq. A. 12.

$$l_1 = b_1 \quad \text{Eq. A. 11}$$

$$l_2 = b_1 \quad \text{Eq. A. 12}$$

Therefore, the internal work (Eq. A. 3) done by each of these yield lines can be calculated as per in Eq. A. 13 and Eq. A. 14:

$$W_1 = \varphi_1 \cdot l_1 \cdot m_{pl} = \frac{2 \cdot \delta \cdot b_1}{(b_0^* - b_1) \cdot \tan(\alpha)} \cdot m_{pl} \quad \text{Eq. A. 13}$$

$$W_2 = \varphi_2 \cdot l_2 \cdot m_{pl} = \left[\frac{2 \cdot \delta}{(b_0^* - b_1) \cdot \tan(\alpha)} + \frac{2 \cdot \delta}{h_1}\right] \cdot b_1 \cdot m_{pl} \quad \text{Eq. A. 14}$$

A.4.Internal work of yield lines 3 and 4 (ruled surface)

The points A-E-D-C shown in Figure A. 1 do not form a plane, but a ruled surface. Thus, the rotation of yield line 3 and yield line 4 is not equal through their entire lengths, because it changes depending on the position on the y-axis. This phenomenon is clarified in Figure A. 3

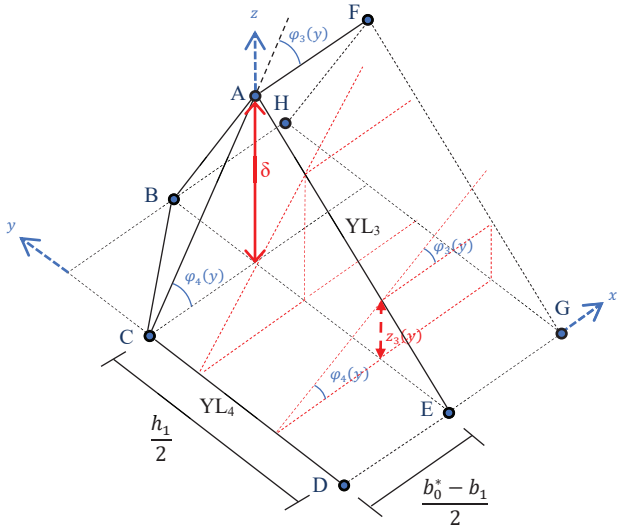

Figure A. 3. Detail of the geometry involving yield line 3 and yield line 4.

As it can be seen in Figure A. 3, the rotation of yield lines 3 and 4 depends on the position in respect to the y-axis, being zero at the points D and E, and maximum at the points C and A. On top of that, the rotation of yield lines 3 and 4 is equal for a fixed y-value (see Eq. A. 15).

$$\varphi_3(y) = \varphi_4(y) \qquad \text{Eq. A. 15}$$

This rotation can be calculated as per in Eq. A. 16,

$$\varphi_3(y) = \varphi_4(y) = \frac{z_3(y)}{(b_0^* - b_1)/2} \qquad \text{Eq. A. 16}$$

where $z_3(y)$ stands for the difference in height between the line A-E and the plane x–y, which can be expressed as shown in Eq. A. 17.

$$z_3(y) = \frac{2 \cdot \delta}{h_1} \cdot y \qquad \text{Eq. A. 17}$$

Thus, the rotations φ_3 and φ_4 can be expressed as per in Eq. A. 18.

$$\varphi_3(y) = \varphi_4(y) = \frac{2 \cdot z_3(y)}{b_0^* - b_1} = \frac{4 \cdot \delta \cdot y}{h_1 \cdot (b_0^* - b_1)} \qquad \text{Eq. A. 18}$$

Since the rotation of yield lines 3 and 4 depends on the position along the y-axis, the integral presented in Eq. A. 19 needs to be solved in order to obtain the internal work done by these yield lines.

$$W_3 = W_4 = m_{pl} \cdot 2 \cdot \int_0^{\frac{h_1}{2}} \frac{4 \cdot \delta \cdot y}{h_1 \cdot (b_0^* - b_1)} dy \qquad \text{Eq. A. 19}$$

Finally, the internal work of yield lines 3 and 4 can be calculated as shown in Eq. A. 20 to Eq. A. 22.

$$W_3 = W_4 = m_{pl} \cdot 2 \frac{4 \cdot \delta}{h_1 \cdot (b_0^* - b_1)} \cdot \frac{y^2}{2}\Big|_0^{\frac{h_1}{2}} \qquad \text{Eq. A. 20}$$

$$W_3 = W_4 = m_{pl} \cdot \frac{8 \cdot \delta}{h_1 \cdot (b_0^* - b_1)} \cdot \frac{h_1^2}{8} \qquad \text{Eq. A. 21}$$

$$W_3 = W_4 = \frac{h_1 \cdot \delta}{(b_0^* - b_1)} \cdot m_{pl} \qquad \text{Eq. A. 22}$$

Additionally, the length (Eq. A. 23) and the rotation (Eq. A. 24) of the yield lines can be obtained independently as:

$$l_3 = l_4 = h_1 \qquad \text{Eq. A. 23}$$

$$\varphi_3 = \varphi_4 = \frac{\delta}{(b_0^* - b_1)} \qquad \text{Eq. A. 24}$$

A.5.Internal work of yield line 5

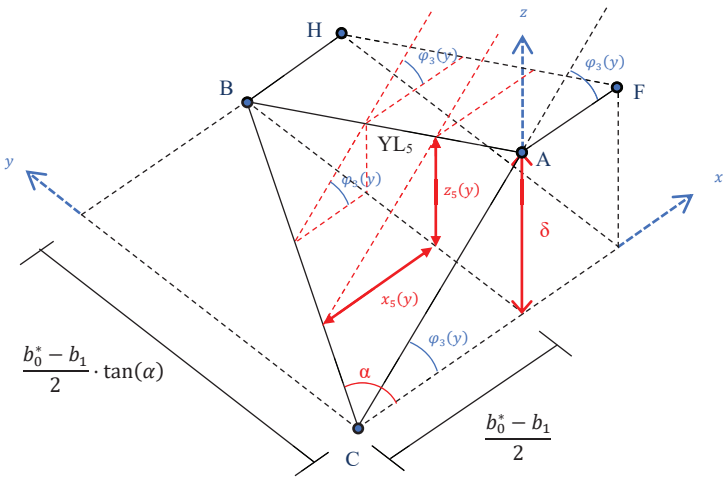

Figure A. 4. Detail of the geometry involving yield line 5.

The internal work done by yield line 5 can be calculated from the geometry shown in Figure A. 4.The rotation of yield line 5 is equal along its entire length, which is proved in Eq. A. 25-Eq. A. 29.

$$\varphi_5(y) = \frac{z_5(y)}{x_5(y)} \quad \text{Eq. A. 25}$$

$$z_5(y) = \frac{2 \cdot \delta \cdot y}{(b_0^* - b_1) \cdot \tan(\alpha)} \quad \text{Eq. A. 26}$$

$$x_5(y) = \frac{y}{\tan(\alpha)} \quad \text{Eq. A. 27}$$

$$\varphi_5(y) = \frac{z_5(y)}{x_5(y)} = \frac{2 \cdot \delta \cdot y \cdot \tan(\alpha)}{(b_0^* - b_1) \cdot \tan(\alpha) \cdot y} \quad \text{Eq. A. 28}$$

$$\varphi_5 = \frac{2 \cdot \delta}{b_0^* - b_1} \quad \text{Eq. A. 29}$$

Additionally, the length of yield line 5 is given in Eq. A. 30.

$$l_5 = \frac{b_0^* - b_1}{2} \cdot \tan(\alpha) \quad \text{Eq. A. 30}$$

Therefore, the internal work done by yield line 5 can be calculated as per in Eq. A. 31-Eq. A. 32.

$$W_5 = \varphi_5 \cdot l_5 \cdot m_{pl} = \frac{2 \cdot \delta}{b_0^* - b_1} \cdot \frac{b_0^* - b_1}{2} \cdot \tan(\alpha) \cdot m_{pl} \quad \text{Eq. A. 31}$$

$$W_5 = \delta \cdot \tan(\alpha) \cdot m_{pl} \quad \text{Eq. A. 32}$$

A.6.Internal work of yield line 6

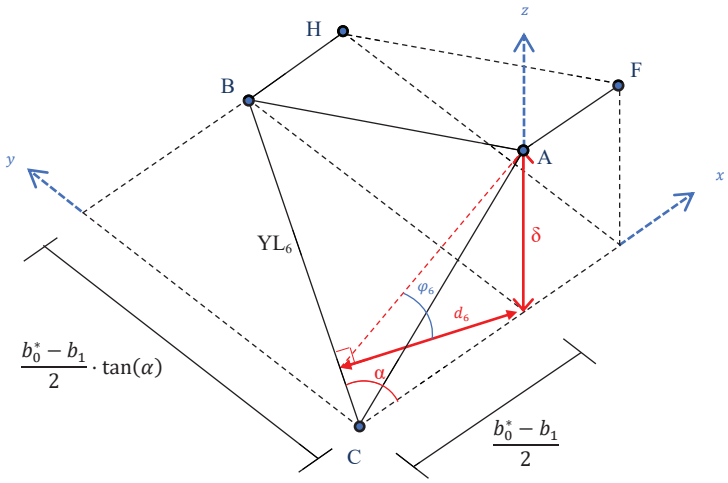

Figure A. 5. Detail of the geometry involving yield line 6.

The internal work done by yield line 6 can be calculated based on the geometry shown in Figure A. 5. The rotation of yield line 6 can be calculated as per in Eq. A. 33-Eq. A. 34.

$$d_6 = \frac{b_0^* - b_1}{2} \cdot \sin(\alpha) \quad \text{Eq. A. 33}$$

$$\varphi_6 = \frac{\delta}{d_6} = \frac{2 \cdot \delta}{(b_0^* - b_1) \cdot \sin(\alpha)} \quad \text{Eq. A. 34}$$

The length of yield line 6 is given in Eq. A. 35,

$$l_6 = \frac{b_0^* - b_1}{2 \cdot \cos(\alpha)} \quad \text{Eq. A. 35}$$

and therefore, the internal work done by this yield line can be calculated as per in Eq. A. 36-Eq. A. 37.

$$W_6 = \varphi_6 \cdot l_6 \cdot m_{pl} = \frac{2 \cdot \delta}{(b_0^* - b_1) \cdot \sin(\alpha)} \cdot \frac{b_0^* - b_1}{2 \cdot \cos(\alpha)} \cdot m_{pl} \quad \text{Eq. A. 36}$$

$$W_6 = \frac{\delta}{\sin(\alpha) \cdot \cos(\alpha)} \cdot m_{pl} \quad \text{Eq. A. 37}$$

Expanding the internal work done by yield line 6 in terms of $\tan(\alpha)$ will be useful for deriving a final compact formulation, the development of which is shown from Eq. A. 38 to Eq. A. 43.

$$W_6 = \frac{\delta}{\sin(\alpha)} \cdot \frac{1}{\cos(\alpha)} \cdot m_{pl} \quad \text{Eq. A. 38}$$

$$W_6 = \frac{\delta}{\sin(\alpha)} \cdot \left[\frac{1}{\cos(\alpha)} + \cos(\alpha) - \cos(\alpha)\right] \cdot m_{pl} \quad \text{Eq. A. 39}$$

$$W_6 = \frac{\delta}{\sin(\alpha)} \cdot \left[\cos(\alpha) + \frac{1 - \cos^2(\alpha)}{\cos(\alpha)}\right] \cdot m_{pl} \quad \text{Eq. A. 40}$$

$$W_6 = \frac{\delta}{\sin(\alpha)} \cdot \left[cos(\alpha) + \frac{\sin^2(\alpha)}{cos(\alpha)}\right] \cdot m_{pl} \quad \text{Eq. A. 41}$$

$$W_6 = \delta \cdot \left[\frac{\cos(\alpha)}{\sin(\alpha)} + \frac{\sin(\alpha)}{\cos(\alpha)}\right] \cdot m_{pl} \quad \text{Eq. A. 42}$$

$$W_6 = \delta \cdot \left[\frac{1}{\tan(\alpha)} + \tan(\alpha)\right] \cdot m_{pl} \quad \text{Eq. A. 43}$$

A.7.Internal work of yield line 7 (rules surface)

As for yield lines 3 and 4, the points A-E-D-C do not form a plane, but a ruled surface, and thus the rotation of yield line 7 is not equal through its entire length, as it changes depending on the position in respect to the x-axis. This phenomenon is clarified in Figure A. 6.

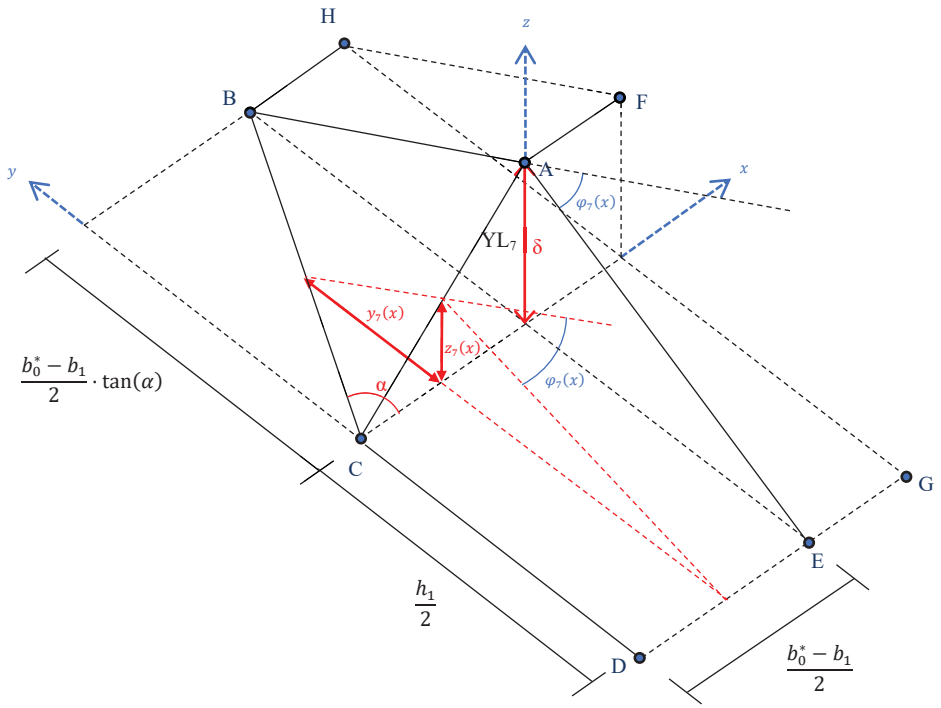

Figure A. 6. Detail of the geometry involving yield line 7.

As it can be seen in Figure A. 6, the rotation of yield line 7 depends on the position in respect of the x-axis. Being minimum at point C and maximum at point A. The rotation can be calculated as per Eq. A. 44-Eq. A. 47.

$$\varphi_7(x) = \frac{z_7(x)}{y_7(x)} + \frac{z_7(x)}{h_1/2} \quad \text{Eq. A. 44}$$

$$z_7(x) = \frac{2 \cdot \delta \cdot x}{b_0^* - b_1} \quad \text{Eq. A. 45}$$

$$y_7(x) = \tan(\alpha) \cdot x \quad \text{Eq. A. 46}$$

$$\varphi_7(x) = \frac{2 \cdot \delta}{(b_0^* - b_1) \cdot \tan(\alpha)} + \frac{4 \cdot \delta \cdot x}{(b_0^* - b_1) \cdot h_1} \quad \text{Eq. A. 47}$$

Since the rotation of the yield line 7 is dependent on the position along the x-axis, the integral presented in Eq. A. 48 needs to be solved in order to obtain its internal work.

$$W_7 = m_{pl} \cdot \int_0^{\frac{b_0^* - b_1}{2}} \frac{2 \cdot \delta}{(b_0^* - b_1) \cdot \tan(\alpha)} + \frac{4 \cdot \delta \cdot x}{(b_0^* - b_1) \cdot h_1} dx \quad \text{Eq. A. 48}$$

Developing the integral, the internal work done by yield line 7 can be calculated, as shown in Eq. A. 49-Eq. A. 52.

$$W_7 = \frac{2 \cdot \delta}{b_0^* - b_1} \cdot m_{pl} \cdot \int_0^{\frac{b_0^* - b_1}{2}} \frac{1}{\tan(\alpha)} + \frac{2 \cdot x}{h_1} dx \quad \text{Eq. A. 49}$$

$$W_7 = \frac{2 \cdot \delta}{b_0^* - b_1} \cdot m_{pl} \cdot \left[\frac{x}{\tan(\alpha)} + \frac{x^2}{h_1} \right]_0^{\frac{b_0^* - b_1}{2}} \quad \text{Eq. A. 50}$$

$$W_7 = m_{pl} \cdot \frac{2 \cdot \delta}{b_0^* - b_1} \cdot \left[\frac{b_0^* - b_1}{2 \cdot \tan(\alpha)} + \frac{(b_0^* - b_1)^2}{4 \cdot h_1} \right] \quad \text{Eq. A. 51}$$

$$W_7 = m_{pl} \cdot \delta \cdot \left[\frac{1}{\tan(\alpha)} + \frac{b_0^* - b_1}{2 \cdot h_1} \right] \quad \text{Eq. A. 52}$$

Additionally, the length (Eq. A. 53) and the rotation (Eq. A. 54) of yield line 7 can be obtained independently as:

$$l_7 = \frac{b_0^* - b_1}{2} \quad \text{Eq. A. 53}$$

$$\varphi_7 = \delta \cdot \left[\frac{2}{(b_0^* - b_1) \cdot \tan(\alpha)} + \frac{1}{h_1} \right] \quad \text{Eq. A. 54}$$

A.8.Total internal work

The obtained internal work done by each of the yield lines is summarized in Eq. A. 55 to Eq. A. 61.

$$W_1 = \frac{2 \cdot \delta \cdot b_1}{(b_0^* - b_1) \cdot \tan(\alpha)} \cdot m_{pl} \quad \text{Eq. A. 55}$$

$$W_2 = \left[\frac{2 \cdot \delta}{(b_0^* - b_1) \cdot \tan(\alpha)} + \frac{2 \cdot \delta}{h_1} \right] \cdot b_1 \cdot m_{pl} \quad \text{Eq. A. 56}$$

$$W_3 = \frac{h_1 \cdot \delta}{(b_0^* - b_1)} \cdot m_{pl} \quad \text{Eq. A. 57}$$

$$W_4 = \frac{h_1 \cdot \delta}{(b_0^* - b_1)} \cdot m_{pl} \quad \text{Eq. A. 58}$$

$$W_5 = \delta \cdot \tan(\alpha) \cdot m_{pl} \quad \text{Eq. A. 59}$$

$$W_6 = \delta \cdot \left[\frac{1}{\tan(\alpha)} + \tan(\alpha)\right] \cdot m_{pl}$$ Eq. A. 60

$$W_7 = \delta \cdot \left[\frac{1}{\tan(\alpha)} + \frac{b_0^* - b_1}{2 \cdot h_1}\right] \cdot m_{pl}$$ Eq. A. 61

Therefore, the total internal work can be obtained by adding all of the internal works and accounting for the number of yield lines of each type present in the proposed mechanism, as per in Eq. A. 62-Eq. A. 63.

$$W_{int} = 2W_1 + 2W_2 + 2W_3 + 2W_4 + 4W_5 + 4W_6 + 4W_7$$ Eq. A. 62

$$W_{int} = \delta \cdot \left[2\frac{2 \cdot b_1}{(b_0^* - b_1) \cdot \tan(\alpha)} + 2\left(\frac{2}{(b_0^* - b_1) \cdot \tan(\alpha)} + \frac{2}{h_1}\right) \cdot b_1 + 2\frac{h_1}{(b_0^* - b_1)} + 2\frac{h_1}{(b_0^* - b_1)} + 4\tan(\alpha) + 4 \cdot \left(\frac{1}{\tan(\alpha)} + \tan(\alpha)\right) + 4 \cdot \left(\frac{1}{\tan(\alpha)} + \frac{b_0^* - b_1}{2 \cdot h_1}\right)\right] \cdot m_{pl}$$ Eq. A. 63

A.9.Adaptation to current code nomenclature (β* and η*)

To adapt the previous expression to the nomenclature adopted in current codes, the bending resistance of the proposed yield line mechanism is separated in terms that are dependent and independent respect to the angle α, as presented in Eq. A. 64-Eq. A. 68.

$$W_{ext} = M \cdot \frac{2 \cdot \delta}{h_1}$$ Eq. A. 64

$$M \cdot \frac{2 \cdot \delta}{h_1} = \delta \cdot \left[2\frac{2 \cdot b_1}{(b_0^* - b_1) \cdot \tan(\alpha)} + 2\left(\frac{2}{(b_0^* - b_1) \cdot \tan(\alpha)} + \frac{2}{h_1}\right) \cdot b_1 + 2\frac{h_1}{(b_0^* - b_1)} + 2\frac{h_1}{(b_0^* - b_1)} + 4\tan(\alpha) + 4 \cdot \left(\frac{1}{\tan(\alpha)} + \tan(\alpha)\right) + 4 \cdot \left(\frac{1}{\tan(\alpha)} + \frac{b_0^* - b_1}{2 \cdot h_1}\right)\right] \cdot m_{pl}$$ Eq. A. 65

$$M = \frac{h_1}{2 \cdot \delta} \cdot m_{pl} \cdot \delta \cdot \left[2b_1 \cdot \frac{2}{(b_0^* - b_1) \cdot \tan(\alpha)} + 2b_1\left(\frac{2}{(b_0^* - b_1) \cdot \tan(\alpha)} + \frac{2}{h_1}\right) + 2h_1 \cdot \frac{1}{b_0^* - b_1} + 2h_1 \cdot \frac{1}{b_0^* - b_1} + 4 \cdot \tan(\alpha) + 4\left(\frac{1}{\tan(\alpha)} + \tan(\alpha)\right) + 4\left(\frac{1}{\tan(\alpha)} + \frac{b_0^* - b_1}{2 \cdot h_1}\right)\right]$$ Eq. A. 66

$$M = \frac{h_1}{2} \cdot \frac{t_0^2 \cdot f_y}{4} \cdot \left[\frac{4b_1}{b_0^* - b_1} \cdot \operatorname{cotan}(\alpha) + \frac{4b_1}{b_0^* - b_1} \cdot \operatorname{cotan}(\alpha) + \frac{4b_1}{h_1} + \frac{4h_1}{b_0^* - b_1} + 4\tan(\alpha) + 4\operatorname{cotan}(\alpha) + 4\tan(\alpha) + 4\operatorname{cotan}(\alpha) + \frac{2(b_0^* - b_1)}{h_1}\right]$$ Eq. A. 67

$$M = f_y \frac{h_1}{2} t_0^2 \cdot \left[\frac{b_0^*}{2h_1} + \frac{b_1}{2h_1} + \frac{h_1}{b_0^* - b_1} + \frac{2b_1}{b_0^* - b_1} \cdot \operatorname{cotan}(\alpha) + 2\tan(\alpha) + 2\operatorname{cotan}(\alpha)\right]$$ Eq. A. 68

Furthermore, the formulations provided in current codes are expressed in terms of the geometric parameters β=b_1/b_0 and η=h_1/b_0. Following this criterion, the bending resistance of the proposed yield line mechanism should be expressed in terms of the modified geometric parameters β^*=b_1/b_0^* and η^*=h_1/b_0^*, based on the effective length term b_0^* (see Section 5.4.2). Some basic relationships of b_1, h_1 and b_0^* expressed in terms of β^* and η^* used for this are shown in Eq. A. 69-Eq. A. 74.

$$\beta^* = \frac{b_1}{b_0^*} \quad \text{Eq. A. 69}$$

$$\eta^* = \frac{h_1}{b_0^*} \quad \text{Eq. A. 70}$$

$$1 - \beta^* = \frac{b_0^* - b_1}{b_0^*} \leftrightarrow \frac{1}{1 - \beta^*} = \frac{b_0^*}{b_0^* - b_1} \quad \text{Eq. A. 71}$$

$$\frac{\eta^*}{1 - \beta^*} = \frac{h_1}{b_0^* - b_1} \leftrightarrow \frac{1 - \beta^*}{\eta^*} = \frac{b_0^* - b_1}{h_1} \quad \text{Eq. A. 72}$$

$$\frac{b_1}{h_1} = \frac{\beta^*}{\eta^*} \quad \text{Eq. A. 73}$$

$$\frac{\beta^*}{1 - \beta^*} = \frac{b_1}{b_0^* - b_1} \quad \text{Eq. A. 74}$$

The final expression of the bending moment resistance $M(\alpha)$ in terms of β^* and η^* is given in Eq. A. 75.

$$M(\alpha) = f_y \cdot \frac{h_1}{2} \cdot t_0^2 \left[\frac{1}{2\eta^*} + \frac{\beta^*}{2\eta^*} + \frac{\eta^*}{1 - \beta^*} + \frac{2\beta^*}{1 - \beta^*} \cdot \operatorname{cotan}(\alpha) + 2\tan(\alpha) + 2\operatorname{cotan}(\alpha) \right] \quad \text{Eq. A. 75}$$

A.10.Energy minimization

From Eq. A. 75, it can be seen that the proposed yield line mechanism can be optimized in terms of α in order to obtain the geometry that requires the lowest energy to develop. This can be done by obtaining the roots (α_o) of the function presented in Eq. A. 75. But first, the change of variable shown in Eq. A. 76 is applied to simplify the upcoming calculations.

$$x = \tan(\alpha) \leftrightarrow \frac{1}{x} = \operatorname{cotan}(\alpha) \quad \text{Eq. A. 76}$$

Therefore, the bending moment resistance can be rewritten in terms of x, as shown in Eq. A. 77 and Eq. A. 78.

$$M(x) = f_y \cdot \frac{h_1}{2} \cdot t_0^2 \left[\frac{1}{2\eta^*} + \frac{\beta^*}{2\eta^*} + \frac{\eta^*}{1-\beta^*} + \frac{2\beta^*}{(1-\beta^*)\cdot x} + 2x + \frac{2}{x}\right] \quad \text{Eq. A. 77}$$

$$M(x) = f_y \cdot \frac{h_1}{2} \cdot t_0^2 \left[\frac{1}{2\eta^*} + \frac{\beta^*}{2\eta^*} + \frac{\eta^*}{1-\beta^*}\right] + f_y \cdot \frac{h_1}{2} \cdot t_0^2 \cdot 2\left[x + \frac{1}{x} \cdot \left(\frac{\beta^*}{1-\beta^*} + 1\right)\right] \quad \text{Eq. A. 78}$$

Then, the equation can be derived and equated to 0, obtaining the roots (x_o) of the equation, as shown in Eq. A. 79-Eq. A. 82.

$$\frac{dM(x)}{dx} = 0 \leftrightarrow f_y \cdot \frac{h_1}{2} \cdot t_0^2 \cdot 2\left[1 - \frac{1}{x^2} \cdot \left(\frac{\beta^*}{1-\beta^*} + 1\right)\right] = 0 \quad \text{Eq. A. 79}$$

$$\frac{dM(x)}{dx} = 0 \leftrightarrow 1 - \frac{1}{x^2} \cdot \left(\frac{\beta^*}{1-\beta^*} + 1\right) = 0 \quad \text{Eq. A. 80}$$

$$\frac{1}{x^2} \cdot \left(\frac{\beta^*}{1-\beta^*} + 1\right) = 1 \leftrightarrow \frac{\beta^* + 1 - \beta^*}{1-\beta^*} = x^2 \quad \text{Eq. A. 81}$$

$$x_o = \pm\sqrt{\frac{1}{1-\beta^*}} = \pm\frac{1}{\sqrt{1-\beta^*}} \quad \text{Eq. A. 82}$$

Undoing the change of variable shown in Eq. A. 76, the obtained roots can be expressed as per in Eq. A. 83 and Eq. A. 84.

$$\tan(\alpha_0) = \pm\frac{1}{\sqrt{1-\beta^*}} \quad \text{Eq. A. 83}$$

$$\alpha_0 = \pm\operatorname{atan}\left(\frac{1}{\sqrt{1-\beta^*}}\right) \quad \text{Eq. A. 84}$$

However, according to the geometry presented in Figure A. 1 the angle α cannot be negative, thus the only possible root for this energy minimization problem is given in Eq. A. 85.

$$\alpha_0 = \operatorname{atan}\left(\frac{1}{\sqrt{1-\beta^*}}\right) \quad \text{Eq. A. 85}$$

A.11.Final expression

Implementing the angle (α_o) that minimizes the energy needed to form the yield mechanism proposed in Figure A. 1 (i.e., Eq. A. 85), the following calculations (see Eq. A. 86-Eq. A. 88) can be done in order to obtain a compact formulation.

$$M = f_y \cdot \frac{h_1}{2} \cdot t_0^2 \left[\frac{1+\beta^*}{2\eta^*} + \frac{\eta^*}{1-\beta^*} + \frac{2\beta^*}{1-\beta^*} \cdot \sqrt{1-\beta^*} + 2\sqrt{1-\beta^*} + \frac{2}{\sqrt{1-\beta^*}} \right] \quad \text{Eq. A. 86}$$

$$M = f_y \cdot h_1 \cdot t_0^2 \left[\frac{1+\beta^*}{4\eta^*} + \frac{\eta^*}{2(1-\beta^*)} + \frac{\beta^*}{\sqrt{1-\beta^*}} + \sqrt{1-\beta^*} + \frac{1}{\sqrt{1-\beta^*}} \right] \quad \text{Eq. A. 87}$$

$$M = f_y \cdot h_1 \cdot t_0^2 \left[\frac{1+\beta^*}{4\eta^*} + \frac{\eta^*}{2(1-\beta^*)} + \frac{\beta^*+1}{\sqrt{1-\beta^*}} + \frac{1-\beta^*}{\sqrt{1-\beta^*}} \right] \quad \text{Eq. A. 88}$$

Finally, the new formulation for the bending resistance of welded joints between RHS members based on the proposed yield line mechanism can be derived, which is given in Eq. A. 89.

$$M = f_y \cdot h_1 \cdot t_0^2 \left[\frac{1+\beta^*}{4\eta^*} + \frac{\eta^*}{2(1-\beta^*)} + \frac{2}{\sqrt{1-\beta^*}} \right] \quad \text{Eq. A. 89}$$

ANNEX B

First order plastic global analysis

B.1.Notation

L: Frame span length.

H: Frame height

K: Geometry ratio. $K = H/L$.

q: Uniformly distributed vertical load at the beam.

P: Horizontal point load.

R: Load ratio. $R = q \cdot L/\ P$.

x: Distance between the plastic hinge formed at the beam midspan area and the left column.

d_v: Virtual vertical displacement produced by the vertical applied load q.

d_h: Virtual horizontal displacement produced by the horizontal applied load P.

θ: Virtual rotations produced by the internal forces.

$\delta\theta$: Additional virtual rotations that produce non-negligible second order effects.

N: Axial load applied.

M_0: Bending moment resistance of the column cross-section.

M_1: Bending moment resistance of the beam cross-section.

M_2: Bending moment resistance of the joint. Considered as the minimum resistance among the beam, the column, and the connection itself.

B.2.Beam collapse mechanism

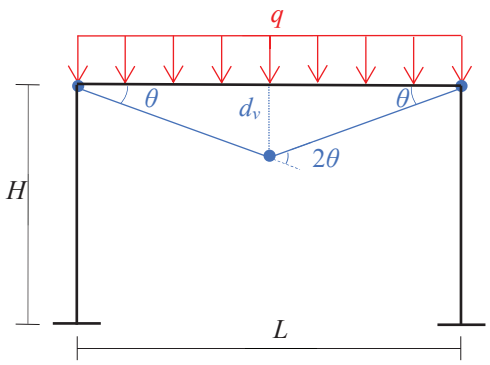

Figure B. 1. Graphic scheme of the beam collapse mechanism.

Based on the beam collapse mechanism defined in Figure B. 1, the work produced by the applied external loads can be calculated as per Eq. B.1, while the work produced by the internal forces can be obtained according to Eq. B.2, where d_v can be calculated according to the geometry described in Figure B. 1, as per in Eq. B.3.

$$\sum W_{ext} = q \cdot \frac{d_v L}{2} \quad \text{Eq. B.1}$$

$$\sum W_{int} = 2\theta M_1 + 2\theta M_2 \quad \text{Eq. B.2}$$

$$d_v = \theta \cdot L/2 \quad \text{Eq. B.3}$$

Then, based on the (PVW) Principle of Virtual Works ($\sum W_{ext} = \sum W_{int}$), the maximum load that the frame can withstand according to the beam collapse mechanism can be calculated, which is given in Eq. B.4. The frame resistance can be also expressed in terms of an equivalent horizontal load P, based on the load ratio R, as per Eq. B.5.

$$q = \frac{8(M_1 + M_2)}{L^2} \quad \text{Eq. B.4}$$

$$P = \frac{8(M_1 + M_2)}{R \cdot L} \quad \text{Eq. B.5}$$

B.3.Sway collapse mechanism

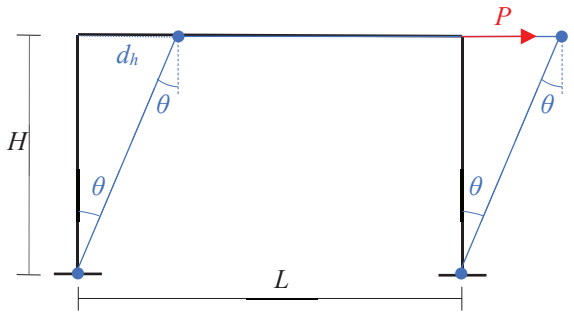

Figure B. 2. Graphic scheme of the sway collapse mechanism.

Likewise, based on the sway collapse mechanism defined in Figure B. 2, the work produced by the applied external loads can be calculated as per Eq. B.6, while the work produced by the internal forces can be obtained from Eq. B.7, where d_h can be calculated according to the geometry described in Figure B. 2, as per in Eq. B.8.

$$\sum W_{ext} = P \cdot d_h \quad \text{Eq. B.6}$$

$$\sum W_{int} = 2\theta M_0 + 2\theta M_2 \quad \text{Eq. B.7}$$

$$d_h = \theta \cdot H \quad \text{Eq. B.8}$$

Then, based on the PVW ($\sum W_{ext} = \sum W_{int}$), the maximum load that the frame can withstand according to the sway collapse mechanism can be calculated, and it is given by Eq. B.9.

$$P = \frac{2 \cdot (M_0 + M_2)}{H} \quad \text{Eq. B.9}$$

B.4.Combined collapse mechanism

Based on the combined collapse mechanism defined in Figure B. 3, the work produced by the applied external loads can be calculated as per Eq. B.10, while the work produced by the internal forces can be obtained from Eq. B.11, where d_h and d_v can be calculated as per Eq. B.12 and Eq. B.13, respectively.

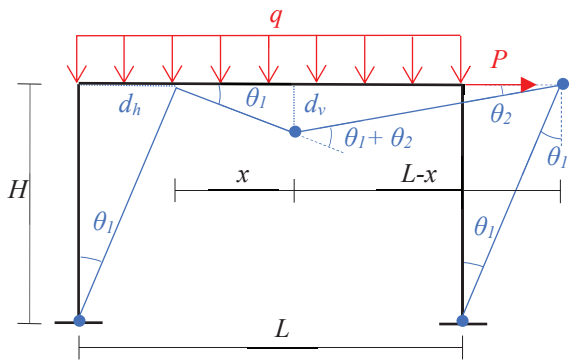

Figure B. 3. Graphic scheme of the combined collapse mechanism.

$$\sum W_{ext} = q \cdot \frac{d_v L}{2} + P \cdot \delta_h \quad \text{Eq. B.10}$$

$$\sum W_{int} = 2M_0\theta_1 + (M_1 + M_2) \cdot \frac{\theta_1 L}{L - x} \quad \text{Eq. B.11}$$

$$d_h = \theta_1 \cdot H \quad \text{Eq. B.12}$$

$$d_v = \theta_1 \cdot x = \theta_2 \cdot (L - x) \quad \text{Eq. B.13}$$

Then, based on the PVW ($\sum W_{ext} = \sum W_{int}$), the maximum load that the frame can withstand according to the combined collapse mechanism can be calculated, which is given by Eq. B.14.

$$P(x) = \frac{2M_0 + (M_1 + M_2) \cdot \frac{L}{L - x}}{H + \frac{R \cdot x}{2}} \quad \text{Eq. B.14}$$

As it can be seen, this maximum load depends on the location of the plastic hinge formed at the beam midspan area. Therefore, the resistance function $P(x)$ can be optimized in order to obtain the mechanism geometry that requires the lowest energy to develop. By solving the problem $dP(x)/dx$=0, the optimized location (x_o) of the plastic hinge formed at the beam midspan area can be calculated, as per Eq. B.15.

$$x_o = L \cdot \left[1 + \frac{M_1 + M_2}{2 \cdot M_0} \cdot \left(1 - \sqrt{1 + \frac{2M_0}{M_1 + M_2} \cdot \left(1 + \frac{2K}{R}\right)}\right)\right] \quad \text{Eq. B.15}$$

ANNEX C

Basics for second order plastic global analysis

C.1.Assumptions for second order plastic global analysis

In first order plastic global analysis, the rotations (θ) described by the structure are assumed to be small enough to produce a negligible lengthening or shortening of the structural members. This phenomenon is represented graphically in Figure C. 1, where the initial rotation (θ) produces small initial vertical displacements (d_v).

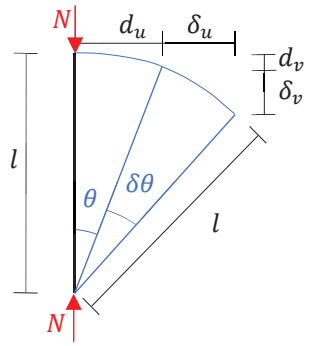

Figure C. 1. Influence of the member rotation on the structural member length.

However, after a certain rotation (θ) is reached, all further rotation ($\delta\theta$) produces non-dismissible vertical displacements (δ_v). This means that the axial load (N) applied onto a structural member of length l produces additional external work, which can be calculated approximating $\cos(\theta)$ by the first

three terms of the Maclaurin series expansion (Plastic Theory of Structures (Horne 1976), Plastic Design and Second-Order Analysis (Chen and Sohal 1995)) (Eq. C.1-Eq. C.2).

$$f(x) \approx f(0) + f'(0) \cdot x + f''(0) \cdot \frac{x^2}{2!} \quad \text{Eq. C.1}$$

$$\cos(\theta) \approx 1 - \frac{\theta^2}{2} \quad \text{Eq. C.2}$$

Finally, the external work produced by the axial load (*N*) applied onto the structural member of length *l*, can be calculated considering second order effects, as per Eq. C.3-Eq. C.5.

$$d_v(\theta) = l - l \cdot \cos(\theta) = l \cdot \frac{\theta^2}{2} \quad \text{Eq. C.3}$$

$$\delta_v = \frac{\partial(d_v)}{\partial\theta} = l \cdot \theta \cdot \delta\theta \quad \text{Eq. C.4}$$

$$W_{ext,2} = N \cdot \delta_v = N \cdot l \cdot \theta \cdot \delta\theta \quad \text{Eq. C.5}$$

ANNEX D

Second order plastic global analysis

D.1.Notation

The additional notation necessary to calculate the internal forces of the plastic collapse mechanism considered, and the loading case of all the analysed frames, are shown in Figure D. 1.

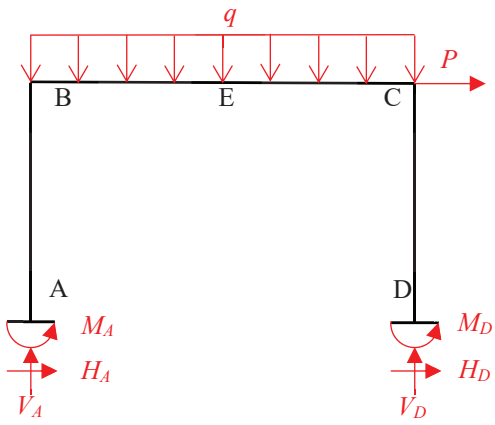

Figure D. 1. Additional notation for second order plastic global analysis.

D.2.Sway collapse mechanism

Once the sway collapse mechanism (Figure B. 2) is determined, the internal force distribution can be calculated as for in a first order elastic global analysis. Although the distributed vertical load (q) does not affect the frame resistance (see Annex B.3) according to a first order plastic global analysis, it influences the internal force distribution of the frame once the sway collapse mechanism is formed. Considering this, the internal force distribution can be obtained member by member based on the equilibrium equations, as in Figure D. 2.

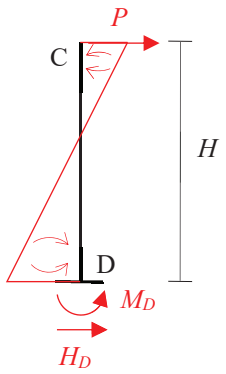

Figure D. 2. Internal forces at the right column once the sway collapse mechanism is formed.

According to Figure D. 2, and knowing that $M_D = M_0$ and $M_C = M_2$, the horizontal reactions at both supports can be obtained as per Eq. D.1 and Eq. D.2.

$$H_D = -\frac{M_0 + M_2}{H} \quad \text{Eq. D.1}$$

$$H_A = -P - H_D = \frac{M_0 + M_2}{H} - P \quad \text{Eq. D.2}$$

Likewise, according to Figure D. 3 the vertical reactions at both supports can be obtained, as per Eq. D.3-Eq. D.5, knowing that $M_B = -M_C = M_2$.

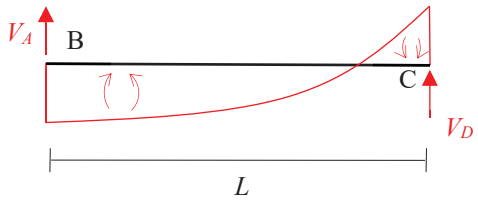

Figure D. 3. Internal forces at the beam once the sway collapse mechanism is formed

$$M_2 = -M_2 + V_D \cdot L - \frac{q \cdot L^2}{2} \quad \text{Eq. D.3}$$

$$V_D = \frac{2M_2}{L} + \frac{q \cdot L}{2} = \frac{2M_2}{L} + \frac{P \cdot R}{2} \quad \text{Eq. D.4}$$

$$V_A = q \cdot L - V_D = P \cdot R - \frac{2M_2}{L} - \frac{P \cdot R}{2} = \frac{P \cdot R}{2} - \frac{2M_2}{L} \quad \text{Eq. D.5}$$

Therefore, based on the obtained reactions, the axial force and bending moment distributions of the analysed frames are shown in Figure D. 4(a) and Figure D. 4(b), respectively.

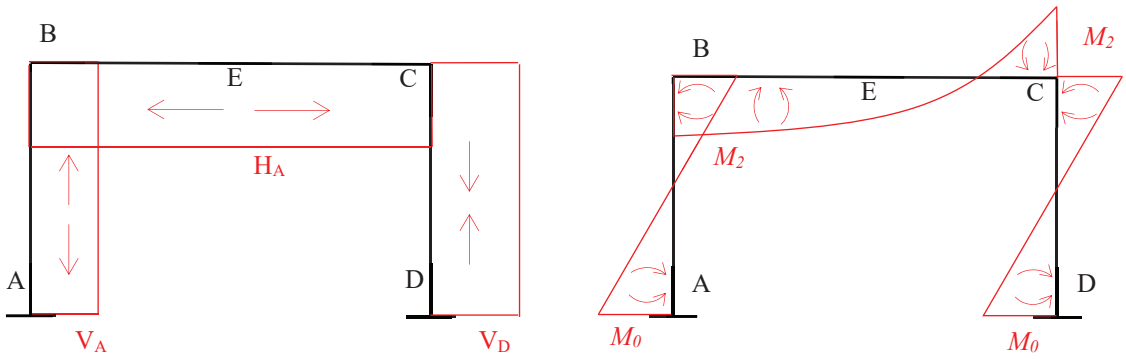

(a) (b)

Figure D. 4. (a) Axial force and (b) bending moment distributions once the sway collapse mechanism is formed.

Then, based on the obtained internal force distribution, the additional external work produced due to the consideration of second order effects can be calculated based on the theory explained in Annex C. It should be noted that the beam does not produce any additional external work since it does experience additional relative rotations according to Figure B. 2. A summary of the additional external works due to second order effects can be found in Table D.1.

Table D.1. Additional external works accounting for second order effects in a sway collapse mechanism.

Member	N_k	l_k	θ_k	$\delta\theta_k$
AB	$\frac{P \cdot R}{2} - \frac{2M_2}{L}$	H	θ	$\delta\theta$
CD	$\frac{P \cdot R}{2} + \frac{2M_2}{L}$	H	θ	$\delta\theta$

Therefore, the additional external work produced due to second order effects can be calculated according to Eq. D.6.

$$\sum W_{ext,2} = \left(\frac{P \cdot R}{2} - \frac{2M_2}{L}\right) \cdot H \cdot \theta \cdot \delta\theta + \left(\frac{P \cdot R}{2} + \frac{2M_2}{L}\right) \cdot H \cdot \theta \cdot \delta\theta = P \cdot R \cdot H \cdot \theta \cdot \delta\theta \qquad \text{Eq. D.6}$$

Finally, the internal and external works based on a second order plastic global analysis can be calculated as per Eq. D.7-Eq. D.8.

$$\sum W_{ext,1} + \sum W_{ext,2} = P \cdot \theta \cdot H + P \cdot R \cdot H \cdot \theta \cdot \delta\theta = P \cdot \theta \cdot H(1 + R \cdot \delta\theta) \qquad \text{Eq. D.7}$$

$$\sum W_{int} = 2\theta(M_0 + M_2) \qquad \text{Eq. D.8}$$

And thus, the overall resistance corresponding to the sway collapse mechanism according to a second order plastic global analysis is that shown in Eq. D.9.

$$P(\delta\theta) = \frac{2(M_0 + M_2)}{H(1 + R \cdot \delta\theta)} \qquad \text{Eq. D.9}$$

with $\delta\theta \approx dU_3/H$, and where dU_3 is the horizontal displacement of the frame.

D.3.Combined collapse mechanism

Once the combined collapse mechanism (Figure B. 3) is determined, the internal force distribution can be calculated as per in a first order elastic global analysis. Based on the equilibrium equations, the internal force distribution can be obtained for each member.

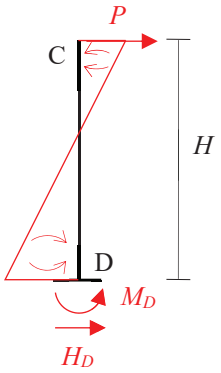

Figure D. 5. Internal forces at the right column once the combined collapse mechanism is formed.

According to Figure D. 5, and knowing that $M_D = M_0$ and $M_C = M_2$, the horizontal reactions at both supports can be obtained as per Eq. D.10-Eq. D.11.

$$H_D = -\frac{M_0 + M_2}{H} \qquad \text{Eq. D.10}$$

$$H_A = -P - H_D = \frac{M_0 + M_2}{H} - P \qquad \text{Eq. D.11}$$

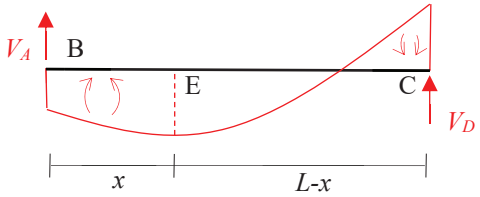

Figure D. 6. Internal forces at the beam once the combined collapse mechanism is formed.

Likewise, from Figure D. 6 the vertical reactions at both supports can be calculated as per in Eq. D.12-Eq. D.14, knowing that $M_C = M_2$ and $M_E = M_1$.

$$M_1 = -M_2 + V_D \cdot (L - x) - \frac{q \cdot (L - x)^2}{2} \quad \text{Eq. D.12}$$

$$V_D = \frac{(M_1 + M_2)}{L - x} + \frac{q \cdot (L - x)^2}{2(L - x)} = \frac{M_1 + M_2}{L - x} + \frac{P \cdot R}{2} \cdot \left(1 - \frac{x}{L}\right) \quad \text{Eq. D.13}$$

$$V_A = q \cdot L - V_D = P \cdot R - \frac{M_1 + M_2}{L - x} - \frac{P \cdot R}{2} \cdot \left(1 - \frac{x}{L}\right) = \frac{P \cdot R}{2}\left(1 + \frac{x}{L}\right) - \frac{M_1 + M_2}{L - x} \quad \text{Eq. D.14}$$

The value of M_B can be calculated according to Figure D. 7, as per Eq. D.15, knowing that $M_A = M_0$.

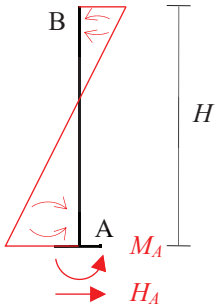

Figure D. 7. Internal forces at the beam once the combined collapse mechanism is formed.

$$M_B = -M_0 + H_A \cdot H = P \cdot H - 2M_0 - M_2 \quad \text{Eq. D.15}$$

Therefore, based on the obtained reactions, the axial force and bending moment distributions of the frame can be determined, which are shown in Figure D. 8(a) and Figure D. 8(b), respectively.

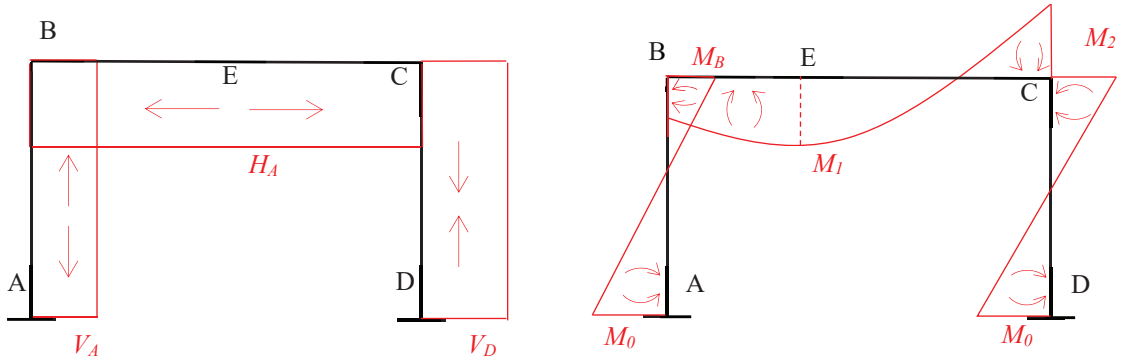

(a) (b)

Figure D. 8. (a) Axial force and (b) bending moment distributions once the combined collapse mechanism is formed.

Then, based on the obtained internal force distributions, the additional external work produced due to the consideration of second order effects can be calculated based on the theory explained in Annex C

summary of the additional external works produced due to second order effects can be found in Table D.2.

Table D.2. Additional external works accounting for second order effects in a combined collapse mechanism.

Member	N_k	l_k	θ_k	$\delta\theta_k$
AB	$\frac{P \cdot R}{2}\left(1+\frac{x}{L}\right)-\frac{M_1+M_2}{L-x}$	H	θ_1	$\delta\theta_1$
BE	$\frac{M_0+M_2}{H}-P$	x	θ_1	$\delta\theta_1$
EC	$\frac{M_0+M_2}{H}-P$	$L-x$	θ_2	$\delta\theta_2$
CD	$\frac{M_1+M_2}{L-x}+\frac{P \cdot R}{2}\cdot\left(1-\frac{x}{L}\right)$	H	θ_1	$\delta\theta_1$

Some basic relationships between θ_1 and θ_2 (or $\delta\theta_1$ and $\delta\theta_2$) are shown in Eq. D.16-Eq. D.18.

$$\theta_2 = \frac{\theta_1 \cdot x}{L-x} \quad \text{Eq. D.16}$$

$$\delta\theta_2 = \frac{\delta\theta_1 \cdot x}{L-x} \quad \text{Eq. D.17}$$

$$\theta_2 \cdot \delta\theta_2 = \frac{\theta_1 \cdot \delta\theta_1 \cdot x^2}{(L-x)^2} \quad \text{Eq. D.18}$$

Therefore, the additional external work produced due to second order effects can be calculated according to Eq. D.19-Eq. D.23.

$$W_{ext,2}|_{AB} = \left[\frac{P \cdot R}{2}\left(1+\frac{x}{L}\right)-\frac{M_1+M_2}{L-x}\right] \cdot H \cdot \theta_1 \cdot \delta\theta_1 \quad \text{Eq. D.19}$$

$$W_{ext,2}|_{BE} = \left(\frac{M_0+M_2}{H}-P\right) \cdot x \cdot \theta_1 \cdot \delta\theta_1 \quad \text{Eq. D.20}$$

$$W_{ext,2}|_{EC} = \left(\frac{M_0+M_2}{H}-P\right) \cdot \frac{\theta_1 \cdot \delta\theta_1 \cdot x^2}{L-x} \quad \text{Eq. D.21}$$

$$W_{ext,2}|_{CD} = \left[\frac{M_1+M_2}{L-x}+\frac{P \cdot R}{2}\cdot\left(1-\frac{x}{L}\right)\right] H \cdot \theta_1 \cdot \delta\theta_1 \quad \text{Eq. D.22}$$

$$W_{ext,2} = \theta_1 \cdot \delta\theta_1 \cdot \left[P\left(R \cdot H-\frac{xL}{L-x}\right)+\frac{M_0+M_2}{H}\cdot\frac{xL}{L-x}\right] \quad \text{Eq. D.23}$$

Thus, the final internal and external works based on a second order plastic global analysis can be calculated as per in Eq. D.24-Eq. D.26, and the overall resistance of the combined collapse mechanism according to a second order plastic global analysis can be determined, which is shown in Eq. D.27.

$$\sum W_{int} = 2M_0\theta_1 + (M_1+M_2)\cdot\frac{\theta_1 L}{L-x} \quad \text{Eq. D.24}$$

$$\sum W_{ext,1} + \sum W_{ext,2} = \theta_1 \left(P \cdot H + \frac{P \cdot Rx}{2} \right) + \theta_1 \cdot \delta\theta_1 \cdot \left[P \left(R \cdot H - \frac{xL}{L-x} \right) + \frac{M_0 + M_2}{H} \cdot \frac{xL}{L-x} \right] \quad \text{Eq. D.25}$$

$$\sum W_{ext} = \theta_1 P \left[H + \frac{Rx}{2} + \left(R \cdot H - \frac{xL}{L-x} \right) \cdot \delta\theta_1 \right] + \theta_1 \cdot \delta\theta_1 \left(\frac{M_0 + M_2}{H} \cdot \frac{xL}{L-x} \right) \quad \text{Eq. D.26}$$

$$P(x, \delta\theta_1) = \frac{2M_0 + (M_1 + M_2) \cdot \frac{L}{L-x}}{H + \frac{Rx}{2} + \left(R \cdot H - \frac{xL}{L-x} \right) \cdot \delta\theta_1} + \frac{\left(\frac{M_0 + M_2}{H} \cdot \frac{xL}{L-x} \right) \cdot \delta\theta_1}{H + \frac{Rx}{2} + \left(R \cdot H - \frac{xL}{L-x} \right) \cdot \delta\theta_1} \quad \text{Eq. D.27}$$

with $\delta\theta \approx dU_3/H$, and where dU_3 is the horizontal displacement of the frame. Note that for each increase of rotation ($\delta\theta_1$), the position (x) of the plastic hinge at the beam midspan area producing the collapse mechanism with the minimum associated energy can be optimized, as described in Annex B.4.

D.3.1.Under fire situation

Moreover, when frames prone to develop a combined collapse mechanism under fire situation, the thermal expansion of the members may produce additional internal forces if these are prevented in some degree, which should be considered in the calculations. For the analysed frames, the beams were the only structural members that had their thermal expansion prevented to some extent due to the stiffness of the columns. After assessing the response of the frames analysed in this study, it was deemed appropriate to disregard the external work produced by the beam due to second order effects because the compressive forces resulting from the prevented thermal expansion at the beam outweighed the tensile axial loads introduced by the initial applied loads. Therefore, under fire situation, the additional external works considered due to second order effects are summarized in Table D.3.

Table D.3. Additional external works accounting for second order effects in a combined collapse mechanism under fire situation.

Member	N_k	l_k	θ_k	$\delta\theta_k$
AB	$\frac{P \cdot R}{2}\left(1 + \frac{x}{L}\right) - \frac{M_1 + M_2}{L-x}$	H	θ_1	$\delta\theta_1$
CD	$\frac{M_1 + M_2}{L-x} + \frac{P \cdot R}{2} \cdot \left(1 - \frac{x}{L}\right)$	H	θ_1	$\delta\theta_1$

Therefore, the resistance of the plastic collapse mechanism under fire situation can be calculated as per Eq. D.28-Eq. D.30.

$$\sum W_{int} = 2M_0\theta_1 + (M_1 + M_2) \cdot \frac{\theta_1 L}{L-x} \quad \text{Eq. D.28}$$

$$\sum W_{ext,1} + \sum W_{ext,2} = \theta_1 \left(P \cdot H + \frac{P \cdot R \cdot x}{2} \right) + \theta_1 \cdot \delta\theta_1 \cdot P \cdot R \cdot H \quad \text{Eq. D.29}$$

$$P_{fi}(x,\delta\theta_1)=\frac{2M_0+(M_1+M_2)\cdot\frac{L}{L-x}}{H+\frac{Rx}{2}+R\cdot H\cdot\delta\theta_1} \quad \text{Eq. D.30}$$

with $\delta\theta \approx dU_3/H$, and where dU_3 is the horizontal displacement of the frame. For each increase of rotation ($\delta\theta_1$), the position (x) of the plastic hinge at the beam midspan area that produces the collapse mechanism with the minimum associated energy can be optimized according to Eq. D.31-Eq. D.36.

$$\frac{\partial P_{fi}}{\partial x}=\frac{\left(H+\frac{Rx}{2}+R\cdot H\cdot\delta\theta_1\right)\cdot(M_1+M_2)\cdot\frac{L}{(L-x)^2}-\left[2M_0+(M_1+M_2)\cdot\frac{L}{L-x}\right]\cdot\frac{R}{2}}{\left(H+\frac{Rx}{2}+R\cdot H\cdot\delta\theta_1\right)^2}=0 \quad \text{Eq. D.31}$$

$$\frac{\partial P_{fi}}{\partial x}=C+x\cdot B+x^2A=0 \quad \text{Eq. D.32}$$

with

$$A=-M_0R \quad \text{Eq. D.33}$$

$$B=R\cdot L\cdot(M_1+M_2+2M_0) \quad \text{Eq. D.34}$$

$$C=L^2\cdot\left[(M_1+M_2)\cdot\left(K-\frac{R}{2}+K\cdot R\cdot\delta\theta_1\right)-M_0R\right] \quad \text{Eq. D.35}$$

and thus,

$$x_0=L\cdot\left[1+\frac{M_1+M_2}{2M_0}\cdot\left(1-\sqrt{1+\frac{2M_0}{M_1+M_2}\cdot\left(\frac{2K}{R}+1+2K\cdot\delta\theta_1\right)}\right)\right] \quad \text{Eq. D.36}$$